Nottingham Trent University

# Debris-covered glaciers:

# Assessing dynamics of European Alpine and Nepalese Himalayan examples

Anne Marie Stefaniak

March 2021

A thesis submitted in partial fulfilment of the requirements of Nottingham Trent University for the degree of Doctor of Philosophy

The candidate confirms that the work submitted is his/her own, except where work that has formed part of a co-authored publication has been included. The contributions of the candidate and other authors has been detailed below.

The work presented in Chapters one, two and three, which focus on Miage Glacier has appeared in the following publication:

> Stefaniak, A.M., Robson, B.A., Cook, S.J., Clutterbuck, B., Midgley, N.G., Labadz, J.C., (2021). Mass balance and surface evolution of the debris-covered Miage Glacier, 1990–2018. Geomorphology 373, 107474. DOI: 10.1016/j.geomorph.2020.107474.

Anne Stefaniak designed the study and carried out all data processing and analysis, figure preparation and development of the manuscript. Ben Robson helped provide support and guidance on using the geodetic approach and all authors contributed to drafts of the manuscript.

# Abstract

Many glaciers in high-mountain regions exhibit a debris cover that moderates their response to climatic change compared to clean-ice glaciers. Studies that integrate long-term observations of debris-covered glacier mass balance, velocity, surface debris evolution and geomorphological changes (such as ponds and ice cliffs) are relatively few. This thesis aims to investigate temporal and spatial changes in the dynamics of debris-covered glaciers in the European Alps and the Himalayan Manaslu region. A range of *in situ* data collection methods and remotely sensed data was analysed to further understand debris-covered glacier evolution and future response to climatic change.

Glacier surface evolution was mapped at Miage Glacier, Italian Alps, over the period 1952 – 2018 and at three easterly-flowing glaciers in the Manaslu region of the Nepalese Himalaya from 1970 to 2019; namely Punggen Glacier, Hinang Glacier and Himal Chuli Glacier. Surface elevation change was quantified over the 28-year and 49-year time periods respectively based on digital elevation model (DEM) differencing, in addition to surface velocity analysis. Bathymetric and ground-based photogrammetry surveys were undertaken to assess glacial lakes (inclusive of supraglacial ponds and ice-marginal lakes) and adjacent ice cliff evolution at Miage Glacier in 2017 and 2018, and at Hinang Glacier in 2019.

Sustained negative mass balance observed at both Miage Glacier (−0.86 ± 0.27 m w.e. $a^{-1}$ from 1990 – 2018) and the Manaslu glaciers (mean of −0.29 ± 0.05 m w.e. $a^{-1}$, 1970 – 2019) has coincided with similar stages of debris-covered glacier evolution regarding increased in debris-cover extent, limited reduction in terminal position, substantial reductions in surface velocity (−46%) and increasing development of supraglacial ponds and ice cliffs. Supraglacial ponds and ice cliffs have important roles in overall ablation at all surveyed glaciers accounting for up to eight times the mean surface lowering rates. Despite these broad similarities between regional responses, nonlinear variability was observed at both Miage Glacier and the Manaslu glaciers, which showed highly variable patterns of surface elevation change and dynamic flow behaviour. Glacier hypsometry and local variability in precipitation in addition to topographic controls, which regulate ice flux, are considered to account for individual glacier response providing further uncertainties when modelling future debris-covered glacier response to climatic change.

The inconsistency of these glacier dynamics highlight the complex, nonlinear changes of debris-covered glaciers over differing spatial and temporal scales. The results of this thesis add to the current knowledge base and offer a unique and valuable insight into the variability of debris-covered glacier evolution in two comparatively different environmental settings.

# Acknowledgements

I would like to thank all those who have helped and supported this research. Firstly, I would like to thank my supervisory team for their help and support during the PhD process. Many thanks to Dr Nicholas Midgely, Dr Ben Clutterbuck and Dr Jillian Labadz for their continued support, advice and encouragement over the past five years. I also owe a big thank you to Dr Simon Cook and Dr Benjamin Robson for their hard work and input into this research. Thank you all for the time and effort you have put into helping me throughout this project. A number of reviewers have provided useful insight and critique of this work and their comments were highly appreciated and led to a significant improvement in the quality of this research.

I would also like to thank those who have made this research possible including those who helped with fieldwork at Miage Glacier; Guaduneth Chico, Daniel Fitter, Miles Shirtcliffe, Bethany Bird, Mark Chaney-Baxter, and Emma Higginbotham. I would also like to thank those who helped collect GPR data on Miage Glacier in March 2018 and allowed me to accompany them on their fieldwork; Matt Westoby, Catriona Fyffe, Remy Veness, Philip Deline, and Allan-Philippe.

Thank you to Nottingham Trent University for funding this research. I would also like to thank the British Society for Geomorphology, Quaternary Research Association, Mount Everest Foundation and the European Space Agency ESA (grants 35359/ 53656) for providing funding grants and access to data without which this research would not have been possible. I would also like to thank Asha Rai whose help and guidance in Nepal was invaluable during our fieldwork in the Himalaya.

To the PhD candidates of Brackenhurst, you have been a pleasure to work alongside and made my time here highly enjoyable! Before COVID somewhat changed things, I relished our lunchtime conversations, social events and of course cake day! The support and friendships that you have all provided along the way are invaluable. Anthony, Aurelie, Dalton, Dinish, Ellen, Esther, Guaduneth, Helen, Jess, Josh, Kat, Kate, Kym, Niamh, Rae – thank you for everything, Brackenhurst would not have been the same without you!

Finally, I would like to thank my family and friends for their support and for putting up with me throughout this PhD. Thank you to my parents for always encouraging me to do my best, Emma, James, Oscar and Grandma for always supporting me. Finally, thank you to Hazzy and Teddy who have continually been there for me and kept me sane. Thank you for everything.

# Table of Contents

Abstract ..... V
Acknowledgements ..... VI
Table of Contents ..... VII
List of Figures ..... XI
List of Tables ..... XV
List of Equations ..... XVII
Chapter 1 : Introduction and research context ..... 1
1.1. Introduction ..... 1
1.2. Background ..... 1
1.3. Aims and objectives ..... 5
1.4. Structure of thesis ..... 5
Chapter 2 : Debris-covered glaciers: a literature review ..... 7
2.1. Introduction ..... 7
2.2. Glacier response to climatic change ..... 7
2.2.1. Global glacier change ..... 7
2.2.2. Glacier surface energy balance ..... 8
2.3. Characteristics of debris-covered glaciers ..... 9
2.4. Surface and structural evolution of debris-covered glaciers ..... 14
2.5. Debris-covered glacier surface features ..... 19
2.5.1. Glacial lakes ..... 21
2.5.2. Ice cliffs ..... 24
2.6. Commonly used techniques to assess debris-covered glaciers ..... 26
2.7. Research gaps ..... 27
2.8. Summary ..... 28
Chapter 3 : Study sites ..... 29
3.1. Introduction and rationale for study site selection ..... 29
3.2. European Alps ..... 30
3.2.1. Regional and climatic setting ..... 30
3.2.2. Mont Blanc massif ..... 31
3.2.3. Miage Glacier ..... 32
3.3. Himalaya ..... 39
3.3.1. Regional and climatic setting ..... 39
3.3.2. Manaslu region ..... 41
3.3.3. Hinang Glacier ..... 41
Chapter 4 : Surface evolution of Miage Glacier ..... 46

4.1. Introduction ..... 46
4.2. Methods and data accuracy assessment ..... 46
4.2.1. Data sources ..... 46
4.2.2. Glacier mapping ..... 49
4.3. Results ..... 52
4.3.1. Structural evolution 1952 – 2018 ..... 52
4.3.2. Surface change 1952 – 2018 ..... 58
4.4. Discussion ..... 66
4.4.1. The evolution of Miage Glacier ..... 66
4.4.2. Decay of Miage Glacier since 1990s ..... 67
4.4.3. The development of surface features ..... 68
4.5. Summary ..... 70
Chapter 5 : Mass balance and surface velocity of Miage Glacier ..... 72
5.1. Introduction ..... 72
5.2. Methods ..... 72
5.2.1. Digital Elevation Models (DEM) extraction ..... 73
5.2.2. Surface velocity ..... 76
5.2.3. Longitudinal profile and surface gradient ..... 78
5.3. Results ..... 78
5.3.1 Surface elevation change and geodetic mass balance 1990 – 2018 ..... 78
5.3.2. Surface velocity change 1990 – 2018 ..... 81
5.3.3. Longitudinal profiles and surface gradients ..... 82
5.3.4. Analysis of supraglacial ponds and ice cliffs ..... 83
5.4. Discussion ..... 84
5.4.1. Recent and long-term evolution of Miage Glacier ..... 84
5.4.2. Regional and global comparisons ..... 85
5.5. Summary ..... 87
Chapter 6 : Morphological analysis of glacial lakes and ice cliffs ..... 89
6.1. Introduction ..... 89
6.2. Methods ..... 89
6.2.1. Bathymetric surveys ..... 90
6.2.2. Photogrammetry surveys ..... 92
6.2.3. Quantification of change ..... 93
6.3. Results ..... 95
6.3.1. Glacial lakes bathymetry ..... 95
6.3.2. Ice cliff characteristics ..... 101
6.3.3. Supraglacial pond morphology and cliff interactions ..... 101
6.3.4. Quantification of ice cliff change ..... 102

6.3.5. Ablation season pond dynamics ..... 103
6.4. Discussion ..... 106
6.4.1. The evolution of Miage Glacier ..... 106
6.4.2. Glacial lake variability and pond dynamics ..... 106
6.4.3. V-A scaling relationships ..... 107
6.4.4. Ice cliff dynamics ..... 109
6.4.5. Morphological relationships between ponds and adjacent ice cliffs ..... 110
6.5. Summary ..... 112
Chapter 7 : Debris-covered glacier dynamics in Manaslu, Nepal 1970 – 2019 ..... 114
7.1. Introduction ..... 114
7.2. Methods ..... 115
7.2.1. Glacier mapping ..... 116
7.2.2. Digital Elevation Model (DEM) analysis ..... 117
7.2.3. Surface velocity ..... 117
7.2.4. Bathymetric surveys ..... 118
7.2.5. Photogrammetry surveys ..... 119
7.3. Results ..... 120
7.3.1. Surface mapping ..... 120
7.3.2. Surface elevation change 1970 – 2019 ..... 125
7.3.3. Surface velocity change 1991 – 2019 ..... 134
7.3.4. Photogrammetry and bathymetry analysis ..... 135
7.3.5. Monsoon season pond variability ..... 137
7.4. Discussion ..... 140
7.4.1. Glacier evolution and variability of the eastern Manaslu glaciers ..... 140
7.4.2. Himal Chuli Glacier flow behaviour ..... 142
7.4.3. Importance of surface features ..... 143
7.4.4. Regional comparisons ..... 145
7.5. Summary ..... 146
Chapter 8 : Debris-covered glacier evolution in the European Alps and Nepalese Himalaya: Overall discussion ..... 148
8.1. Overview of thesis ..... 148
8.2. Discussion of study objectives ..... 149
8.2.1. Debris-covered glacier surface evolution ..... 149
8.2.2. Temporal analysis of debris-covered glacier dynamics ..... 150
8.2.3. The importance of surface features on topographic evolution ..... 152
8.3. Implications and importance of study ..... 155
8.3.1. Future prognosis of Miage Glacier ..... 155
8.3.2. Future prognosis of the Manaslu glaciers ..... 156

8.3.3. Conceptual model of debris-covered glacier evolution ..... 157
8.3.4. Importance of this research ..... 159
8.4. Limitations and future work ..... 160
8.4.1. Methodological considerations for remote sensing techniques ..... 160
8.4.2. Logistical considerations with fieldwork ..... 162
Chapter 9 : Conclusions ..... 164
References ..... 167
Appendix ..... 189

# List of Figures

Figure 1.1: Global glacier distribution based on data from the RGI6.0 (RGI Consortium, 2017). .....2
Figure 1.2: Flow chart of the thesis structure. .....6
Figure 2.1: Global cumulative mass change relative to 1976 from 30 global reference glaciers with continuous observations as compiled by the World Glacier Monitoring Service (WGMS, 2019). Cumulative values relative to 1976 are represented on the y-axis. .....8
Figure 2.2: Energy balance and inputs and outputs within a glacier system, which affect the resulting glacier mass balance. .....9
Figure 2.3: The Østrem curve as derived from empirical measurements of the relationship between debris thickness and ice ablation rates on sample glaciers (redrawn from Mattson et al. (1993) as shown in Nicholson and Benn (2006)). .....10
Figure 2.4: Regions of the Hindu Kush Himalaya based on ICIMOD (2014). .....11
**Figure 2.5:** A conceptual model of the development of a Himalayan debris-covered glacier (a) in balance with climate, and (b) during net mass loss under a warming climate with an upglacier migration of the elevation line altitude (ELA). *Source:* Rowan et al. (2015). .....13
Figure 2.6: Schematic diagram of the structural evolution of Haut Glacier d'Arolla, Switzerland. A: Flow-units each with its own pattern of primary stratification, separated by structural discontinuities. B: Primary stratification gradually folded as it flows into the glacier tongue. Cut by open crevasses. C: Continued deformation and formation of longitudinal foliation. Closure and rotation of crevasse traces. D: Reactivation of crevasse traces and opening of splaying crevasses. *Source:* Goodsell et al.(2005b). .....15
Figure 2.7: Crevasse patterns in a valley glacier and associated stress regimes. A: Effect of shear stress exerted by valley walls, B: shear stress and extending flow, C: shear stress and compressive flow. *Source:* Benn and Evans (2010); adapted from Nye (1952). .....16
Figure 2.8: A: Main elements and succession of zones on a debris-covered glacier. B: Concept of medial moraine height evolution down-glacier and over time. *Source:* Mölg et al. (2020). .....25
Figure 3.1: A: Location of the Mont Blanc massif within the European Alps with Europe DEM for background. B: Miage Glacier looking up the valley towards Bionnassay Glacier at the back, highlighting the northern and southern lobes and Lake Miage. *Photo credit*: S. Nappa, (2009). ....29
Figure 3.2: A: Location of Manaslu conservation area within Nepal situated between the Annapurna conservation area to the west and Langtang national park to the east. B: Hinang Glacier highlighting the undulating surface topography with numerous ice cliffs, taken September 2019. .....30
Figure 3.3: ERA5 climate data for Miage Glacier from 1990 – 2020 showing daily average temperature (top), and amount of snowfall (bottom). Data from www.meteoblue.com, (Hersbach et al., 2018). .....31
Figure 3.4: A: Glacierised regions of the European Alps; red box indicates the Mont Blanc massif as shown in B. Background shows DEM of Europe. B: Glaciers of the Mont Blanc massif showing extent of debris-covered glaciers and main glaciers based on RGI6.0 data with 2018 Planet satellite imagery as background. .....32
Figure 3.5: Location of Miage Glacier and tributary glaciers located on the southwest flank of Mont Blanc in the Italian Alps and debris cover from the RGI6.0 Sentinel analysis (Scherler et al., 2018) with deposits from rockfall events in 1945 and 1988 and the 2015 TerraItaly orthophoto as background. Projection in UTM Zone 32N. .....33
Figure 3.6: Ice thickness of Miage Glacier as derived from the RGI6.0 data (Farinotti et al., 2019). Background consists of Planet data, 2018. .....34
Figure 3.7: The six stages of debris cover development since 1770. Key: (1) 'clean' ice, (2) discontinuous debris, (3) continuous debris cover, (4) medial moraine, (5) local rock-avalanche deposit. *Source:* Deline (2005). .....35

Figure 3.8: A: View upglacier with the proglacial lake in the foreground and Lake Miage behind in July 2017. B: View east over Lake Miage. ....37
Figure 3.9: Timeline of drainage events classified as per information from previous studies. Red – complete drainage, Yellow – partial drainage resulting in multiple basins, Blue – no information on level of drainage provided. ....38
Figure 3.10: A: Glaciers and debris cover across the Himalaya based on the RGI6.0 datasets, boxed area refers to the Manaslu conservation area as shown in B. B: Glaciers and debris cover in the Manaslu region (shown by black outline) with glaciers of interest noted. Background shows DEM for Manaslu region, Nepal. ....39
Figure 3.11: ERA5 climate data for Hinang Glacier from 1990 – 2020 showing daily average temperature (top), and amount of snowfall (bottom). Note heavy snowfall in 2015. Data from www.meteoblue.com. ....40
Figure 3.12: Glaciers on the eastern side of Manaslu including Punggen Glacier, Hinang Glacier and Himal Chuli Glacier. Background shows Planet data from October 2019. ....42
Figure 3.13: Ice thickness of the easterly flowing Manaslu glaciers, A: Punggen Glacier; B: Hinang Glacier; C: Himal Chuli Glacier, as derived from the RGI6.0 data. Background shows Landsat satellite data. ....44
Figure 3.14: A: Hinang Glacier looking upglacier to the west with a supraglacial pond; B: The Budhi Gandaki river in the lower reaches. Photos taken in September 2019. ....45
Figure 4.1: The use of NDWI to aid mapping of glacial lakes and streams with an example of those mapped in 2015. ....51
Figure 4.2: Mapping of structural and surface features from 1952. Background imagery shows the orthophoto derived from the 1952 aerial images. The 1945 rockfall was not visible in the imagery. ....53
Figure 4.3: Mapping of structural and surface features from 2018. Background shows the SPOT 2018 satellite imagery used for digitisation of structures. ....54
Figure 4.4: Structural mapping from 1952 to 2018. TC - Tête Carrée Glacier, BG – Bionnassay Glacier, DG – Dome Glacier, MB – Mont Blanc Glacier. ....56
Figure 4.5: Glacier extent, crevasse length and ogive length from 1952 – 2018. ....58
Figure 4.6: Variability of glacial lakes at Miage Glacier in area ($m^2$). Data show the overall number of glacial lakes present (grey bar) inclusive of proglacial lakes, ice-marginal lakes and supraglacial ponds, and area of supraglacial ponds (purple dots). *Data covering the area of Lake Miage in 1993 was not available from the imagery. ....60
Figure 4.7: A: Glacial lake change from 1952 – 2018, manually digitised from aerial and satellite imagery. B: Glacial lake density derived from the number of years water has been present. C: Ice thickness derived from the RGI6.0 (Farinotti et al., 2019). ....62
Figure 4.8: Development of S1 located at the top of the northern terminal lobe. ....63
Figure 4.9: The debris-covered Miage Glacier in 2017 looking southeast from the southern lateral moraine. S3 (~22 m across, along red line) and a smaller melt pond can be observed in the photo. ....64
Figure 4.10: Development of S4 along the northern margin of the valley tongue. ....65
Figure 4.11: Development of S5 from 2004 – 2018. ....65
Figure 5.1: Example plots of the coregistration method showing slope normalised terrain elevation differences between two DEMs over stable (non-glacier) terrain A: before co-registration, and B: after 3 iterations. The co-registration shifts that were applied during the processing are shown in red text. ....75
Figure 5.2: Mean annual surface elevation change in metres with a hillshaded elevation model as background. A: 1990 – 2018, B: 1990 – 2008, C: 2008 – 2018, D: 2012 – 2014, E: 2014 – 2016, F: 2016 – 2018. Note uncertainty associated with the nunatak at the base of Mont Blanc Glacier due to shadow in input data. ....79

Figure 5.3: Debris inputs onto Miage Glacier from Dome Glacier. A: Image of the area before deposition. B: Area of deposition after the event. C: Amount of surface change between 2012 and 2014. .....80
Figure 5.4: Landsat derived surface velocity displacements. A: 1990 – 1991, B: 2008 – 2009, , C: 2017 – 2018 with velocity transects used in Figure 5.5 and Figure 5.6. Contours at 200 m intervals. .....81
Figure 5.5: Landsat derived ice flow velocity fields with longitudinal profiles along the centreline to the top of the terminal lobes.....81
Figure 5.6: Downstream surface velocities along the northern lobe (left) and southern lobe (right) as shown in Figure 5.4C. .....82
Figure 5.7: Longitudinal profile of the glacier centreline in 1990 and 2018.....82
Figure 5.8: A: Total surface change from 2012 – 2014, B: Surface change from 2014 – 2016, and C: Surface change from 2016 – 2018, and D: Locations of supraglacial ponds from 2012 – 2018 and E: Locations of ice cliffs from 2012 – 2018. .....83
Figure 6.1: A: Location of Miage Glacier and the glacial lakes surveyed. Black box represents area in B: glacial lakes and ice cliffs present in 2017 and 2018. .....90
Figure 6.2: Bathymetric maps of Lake Miage, P1, P2 and Lac Vert (P3) in 2017 and 2018. Background images are SPOT satellite images from 2017 and 2018, and TerraItaly OrthoPhoto from 2015 (P3). .....97
Figure 6.3: Lake Miage taken on 29/09/2018 facing east looking towards Val Veny. Blue line refers to the previous water line. *Photo credit:* Connor Downes (2018). .....98
Figure 6.4: Left column A1-E1: Mean annual elevation change from 2016 – 2018 derived in Chapter 5. Central column A2-E2: Bathymetry and photogrammetry surveys in 2017 with SPOT7 orthophoto background. Right column A3-E3: Bathymetry and photogrammetry surveys in 2018 with SPOT7 orthophoto background. .....100
Figure 6.5: A-F: Ice cliff and bathymetric change between the two survey periods in 2017 and 2018. Units in m. Photogrammetry models displayed for context.....103
Figure 6.6: Water bodies at Miage Glacier from June – October 2017 (top row) and June – October 2018 (bottom row).....105
Figure 6.7: Lake and pond area plotted against mean depths for 2017 and 2018 surveys.....109
Figure 7.1: Locations of the ponds that were surveyed on Hinang Glacier in September 2019 and additional ponds that were identified using Planet satellite imagery. Purple dot indicates the location where the time-lapse camera was installed in 2019. .....119
Figure 7.2: Surface mapping in 1970 of A: Punggen Glacier, B: Hinang Glacier and C: Himal Chuli Glacier. Background images show Landsat imagery. .....121
Figure 7.3: Surface mapping in 2013 of A: Punggen Glacier, B: Hinang Glacier and C: Himal Chuli Glacier. Background images show Landsat imagery from the corresponding year. .....122
Figure 7.4: Surface mapping in 2019 of A: Punggen Glacier, B: Hinang Glacier and C: Himal Chuli Glacier Background images show Landsat imagery from the corresponding year. .....123
Figure 7.5: Surface elevation change in 1970 – 2019 covering Punggen Glacier, Hinang Glacier and Himal Chuli Glacier. .....125
Figure 7.6: Surface elevation change in 2013 – 2019 covering Punggen Glacier, Hinang Glacier and Himal Chuli Glacier. .....126
Figure 7.7: Surface elevation change in 2013 – 2016 covering Punggen Glacier, Hinang Glacier and Himal Chuli Glacier. .....127
Figure 7.8: Surface elevation change in 2016 – 2019 covering Punggen Glacier, Hinang Glacier and Himal Chuli Glacier. .....128
Figure 7.9: Surface elevation change m $a^{-1}$ and supraglacial pond locations 2013 – 2016 for Punggen Glacier (A1), Hinang Glacier (B1) and Himal Chuli Glacier (C1). Elevation change and pond locations between 2016 – 2019 for Punggen Glacier (A2), Hinang Glacier (B2) and Himal Chuli

Glacier (C2). Supraglacial pond distribution between 2013 and 2019 for Punggen Glacier (A3), Hinang Glacier (B3) and Himal Chuli Glacier (C3). .....132
Figure 7.10: Longitudinal profiles of Punggen Glacier, Hinang Glacier and Himal Chuli Glacier with the overall change in surface gradient and change over the regions associated with supraglacial ponding. Greyed out section indicates the regions where supraglacial ponding was observed. ..133
Figure 7.11: Surface velocity in A: 1991/1992, B: 2013/2014, and C: 2018/2019.....134
Figure 7.12: Bathymetric surveys of the supraglacial ponds and SfM photogrammetry models of the adjacent ice cliffs. .....136
Figure 7.13: Seasonal variability of supraglacial ponds over Punggen Glacier, Hinang Glacier and Himal Chuli Glacier.....138
Figure 8.1: Supraglacial ponds at Miage Glacier and Hinang Glacier plotted alongside results from Cook and Quincey (2015) on logarithmic scales. Ponds gathered within this study are consistent with growing supraglacial ponds. .....154
Figure 8.2: Revised conceptual model of debris-covered glacier evolution developed from the Benn et al. (2012) model.....159

# List of Tables

Table 1.1: Glacierised area (km$^2$) excluding ice sheets from the Randolph Glacier Inventory (RGI Consortium, 2017) ≥1 km$^2$ taken from Herreid and Pellicciotti (2020) based on the distribution of mountain areas based on the IPCC (Hock et al., 2019) and derived percentage of debris cover per region. ....3
Table 2.1: Identification of glaciological and surface structures derived from aerial and field observations from Goodsell et al. (2005b). ....18
Table 2.2: Summary of quantification of ice cliffs to total glacier ablation rates studies highlighting the disproportionate influence on ablation. ....20
Table 2.3: Refined relationship between glacier surface gradients, glacier velocity and supraglacial pond development. *Source:* Quincey et al. (2007). ....22
Table 4.1: Registration errors and uncertainty derived from data used. Dates in bold are those which the structural evolution and surface change was undertaken. Additional dates were for analysis of glacial lake evolution only. (NB: 1993, 2001 and 2004 georeferenced in ArcMap). ....48
Table 4.2: Summary of structures as derived from the mapping in Figure 4.2 to Figure 4.4. ....57
Table 4.3: Summary of ice cliff and glacial lakes on from 1952 to 2018. Glacial lakes and pond uncertainty is given at the upper value of 10% and uncertainty of ice cliffs at 8%. ....59
Table 5.1: Data sets used within this study (SPOT and Pleiades data provided by ESA, 2008 LiDAR DEM from Valle d'Aosta). All datasets used the panchromatic band for DEM extraction and SWIR for surface velocity analysis. ....73
Table 5.2: Summary of the GCPs and tie-points used to enhance the alignment of the imagery prior to DEM extraction. ....74
Table 5.3: DEM co-registration shifts and DEM differencing uncertainty. The mean deviation, standard deviation and uncertainty are based on the co-registered DEM pairs. Statistics are based on stable (non-glacier) terrain. DEM differencing uncertainty represents the sum of standard errors for each 100 m elevation band. ....75
Table 5.4: Accuracy assessment of the surface velocity feature tracking (m a$^{-1}$). ....77
Table 5.5: Vertical surface elevation change and geodetic mass balance of Miage Glacier from 1990 to 2018 based on DEM differencing. Standard errors for elevation change and uncertainty values for geodetic mass balance provided. ....78
Table 5.6: Variations in ablation rates associated with supraglacial ponds and ice cliffs, and density as a percentage of the debris-covered area from RGI6.0 analysis. Proportions of pond and ice cliff contributions to the total ablation rates are also calculated. Uncertainty was calculated at 5% for ice cliffs and 7% for supraglacial ponds. ....84
Table 6.1: Number of depth measurements, mean XY GNSS accuracy and RMSE for the IDW interpolations for the bathymetric maps. ....92
Table 6.2: Errors of the photogrammetry SfM ice cliff models during processing and summary of GCPs, check points and accuracy. ....93
Table 6.3: Area, depth, lake levels and volume of lakes surveyed July 2017 and 2018. *S5 area in 2017 estimated from satellite imagery rather than bathymetric survey. ....96
Table 6.4: Changes in lake properties from 2017 to 2018. Values for Lake Miage post drainage are estimated assuming the bathymetry has not changed since the 2018 survey. ....99
Table 6.5: Summary of 2017 and 2018 ice cliff geometry results. ....101
Table 6.6: Mean ice cliff retreat rates between 2017 and 2018 assessed through the M3C2 algorithm. ....102
Table 6.7: Summary of ponds mapped throughout the ablation season from 2017 – 2018. ....104
Table 6.8: Regression values ($R^2$) relationships for supraglacial ponds and proglacial lake area-volume and comparisons with data from Cook and Quincey (2015) and Watson et al. (2018b). .108

Table 7.1: Characteristics of the easterly flowing Manaslu glaciers. Data collated from GLIMs and Robson et al. (2018). ..... 114
Table 7.2: Data sets used within this study (SPOT and Pleiades data provided by ESA). Some snow cover exists in the 2016 data and must be interpreted with caution. All datasets used the panchromatic band for DEM extraction and SWIR for surface velocity analysis. ..... 116
Table 7.3: Accuracy and uncertainty estimates associated with the mapped components. Ranges show the maximum and minimum values for Punggen Glacier, Hinang Glacier and Himal Chuli Glacier. ..... 117
Table 7.4: Summary of the GCPs and tie-points used to enhance the alignment of the imagery prior to DEM extraction. ..... 117
Table 7.5: Accuracy assessment of the surface velocity feature tracking calculated for each glacier based on stable ground. ..... 118
Table 7.6: Number of depth measurements, mean XY GPS accuracy and RMSE for the IDW interpolations for the bathymetric maps ..... 118
Table 7.7: Errors of the photogrammetry SfM ice cliff models during processing and summary of GCPs, check points and accuracy. ..... 119
Table 7.8: Glacier surface change derived from mapping of the orthophotos in 1970, 2013 and 2019 as shown in Figure 7.2 to Figure 7.4. ..... 124
Table 7.9: Glacier surface elevation change per year and calculated geodetic mass balance of Punggen Glacier, Hinang Glacier and Himal Chuli Glacier from 1970 to 2019. *Care should be taken when interpreting the results associated with the 2016 DEM data as snow cover in the upper reaches incorporates mass loss from seasonal snow cover. ..... 129
Table 7.10: Summary of surface elevation change on regions associated with debris cover, supraglacial ponds and ice cliffs. Uncertainty of supraglacial ponds and ice cliffs was estimated <8%. ..... 131
Table 7.11: Mean surface velocity change from 1991 to 2019 for Punggen Glacier, Hinang Glacier and Himal Chuli Glacier calculated from regions shown in Figure 7.11. ..... 135
Table 7.12: Area, depth, lake levels and volume of supraglacial ponds surveyed in September 2019. Uncertainties were calculated from RMSE. ..... 136
Table 7.13: Summary of 2019 ice cliff geometry results. ..... 136
Table 7.14: Changes in supraglacial pond number, area and volumes over the monsoon season from May to November 2019 at Hinang Glacier. ..... 139
Table 7.15: Changes in supraglacial pond properties over the monsoon season from May 2019 to November 2019 for Punggen Glacier and Himal Chuli Glacier. Imagery was not available covering Himal Chuli Glacier in September 2019. ..... 139
Table 8.1: Volume-area relationships for supraglacial ponds and glacial lakes represented by regression values ($R^2$) when combined with data from Cook and Quincey (2015) and Watson et al. (2018b). ..... 153
Table 8.2: Correlation and GLM analysis of pond area and glacier dependant variables. ..... 155

# List of Equations

Equation 2.1: Net energy balance at glacier surface..... 8
Equation 4.1: Uncertainty calculation for termini position .....50
Equation 4.2: Normalised Difference Water Index (NDWI).....51
Equation 5.1: Standard error calculation.....76
Equation 5.2: Number of pixels in DEM differencing .....76
Equation 5.3: Sum of volume change uncertainty.....76
Equation 5.4: Root square mean sum.....76
Equation 6.1 : Refinement of rescaled measure of normals scale .....94
Equation 6.2: V-A relationships .....103
Equation 7.1: Glacier hypsometry index calculation.....117

# Chapter 1 : Introduction and research context

## 1.1. Introduction

Most glaciers around the world are receding or thinning due to climatic change, but local topographic and dynamic factors can exert a strong influence on the rate of glacier change (IPCC, 2014; Zemp et al., 2015). This thesis investigates the evolution of debris-covered glaciers; a sub-set of glaciers, the study of which has risen to prominence in recent years because of their importance as water resources in regions of the world that depend on glaciers for meltwater supply (e.g. Immerzeel et al., 2010, 2019; Irvine-Fynn et al., 2017; Biemans et al., 2019; Wood et al., 2020). Despite this, debris-covered glacier response to climatic variability remains poorly understood. Further investigation of the dynamics and evolutionary processes are required to better understand the ablation patterns and future response to climatic change.

This chapter will introduce the background to the project and rationale for this research leading to the study aims and objectives as presented in Section 1.3, and full structure of the thesis presented in Section 1.4. Further detailed analysis of the existing research will be examined in 'Chapter 2 – Debris-covered glaciers: a literature review' to further highlight gaps in the research and the existing knowledge of debris-covered glaciers.

## 1.2. Background

There are *c.*198,000 glaciers across the globe (excluding ice sheets) covering a total of 726,800 $km^2$ ± 34,000 $km^2$ (Pfeffer et al., 2014) according to the Randolph Glacier Inventory v.6.0 (RGI6.0) (RGI Consortium, 2017) with 271,760 $km^2$ associated with high-mountain regions (Figure 1.1, Table 1.1). Although glaciers cover just 0.5% of the Earth's land surface, meltwater and runoff are important contributors to global sea level rise and influence both global and local communities (Radić et al., 2014).

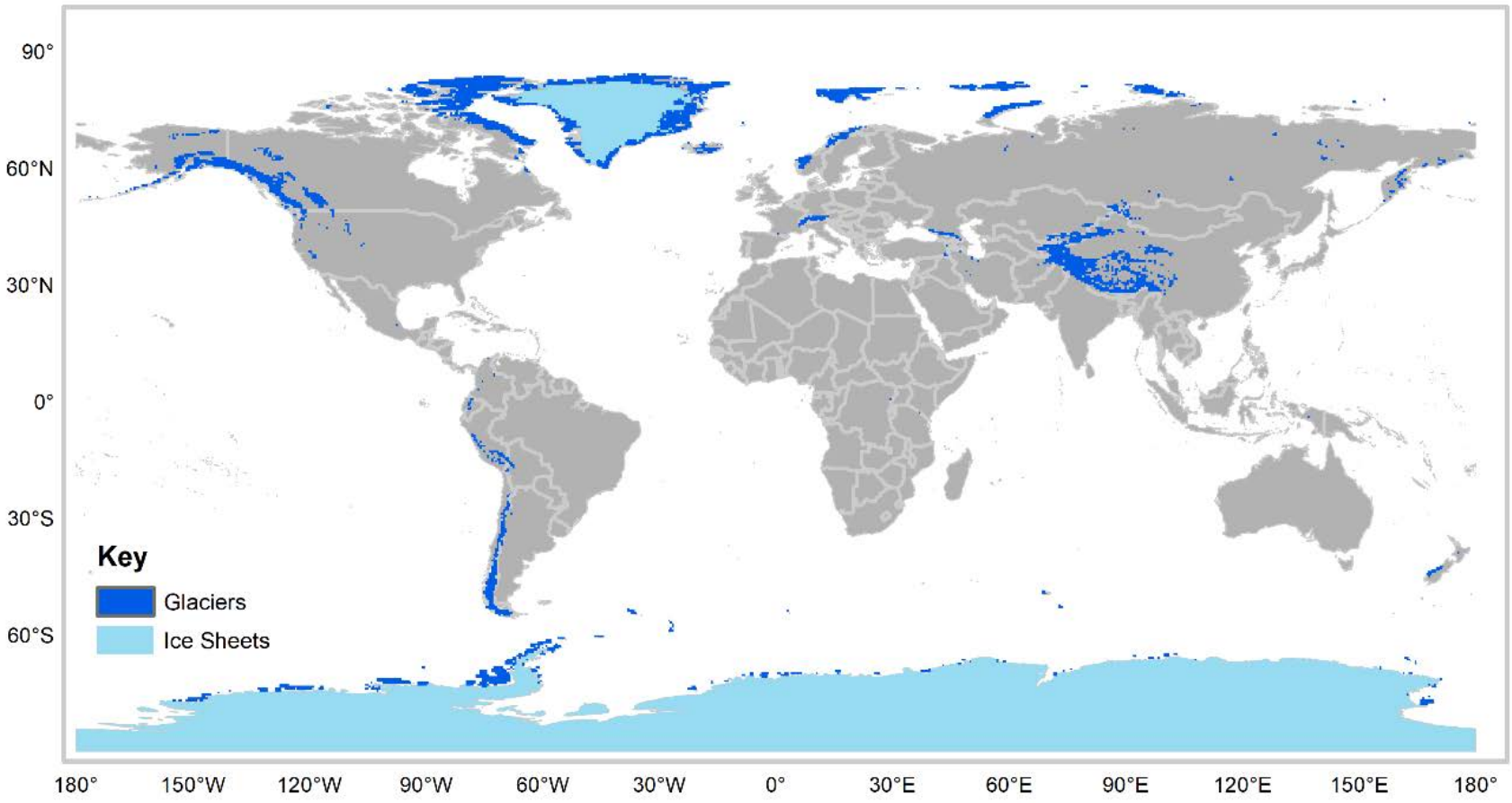


**Figure 1.1:** Global glacier distribution based on data from the RGI6.0 (RGI Consortium, 2017).

**Table 1.1:** Glacierised area ($km^2$) excluding ice sheets from the Randolph Glacier Inventory (RGI Consortium, 2017) ≥1 $km^2$ taken from Herreid and Pellicciotti (2020) based on the distribution of mountain areas based on the IPCC (Hock et al., 2019) and derived percentage of debris cover per region.

| Region | Glacierised area extent ($km^2$) | Percent debris-covered (%) |
|---|---|---|
| Alaska | 79280 | 14.2 |
| Western Canada and US | 10678 | 5.2 |
| Iceland | 10601 | 10.0 |
| Central Europe | 1471 | 15.7 |
| Scandinavia | 2155 | 3.5 |
| Caucasus and Middle East | 777 | 14.0 |
| North Asia | 1497 | 6.1 |
| High Mountain Asia | 75557 | 11.5 |
| Low Latitudes | 1511 | 3.5 |
| Southern Andes | 23948 | 2.8 |
| New Zealand | 580 | 19.6 |

Mountain glaciers have been experiencing sustained negative mass balance in response to recent climate change, resulting in overall recession and thinning (Huggel et al., 2002; Diolaiuti et al., 2005; Reid and Brock, 2014; Zemp et al., 2015). Local topographic and dynamic factors can cause substantial variations in the response of individual glaciers to this climatic trend (Pachauri et al., 2014; Zemp et al., 2015). The role of supraglacial debris cover is one such factor that can have a profound impact on glacier response to climatic forcing (Scherler et al., 2011; Benn et al., 2012). There has been an increase in the number and extent of debris-covered glaciers globally since the Little Ice Age (*c.* 1400 - 1900) (Yamada, 1998; Röhl, 2008; Carrivick and Tweed, 2013; Westoby et al., 2014; Rowan, 2017). As shown in Figure 1.1, debris cover is now present on 4.4% of the global glacier area (Scherler et al., 2018) and 7.3% of the mountain glacier area (Herreid and Pellicciotti, 2020). Debris-covered glaciers are increasingly prevalent in high-mountain regions owing to the increased weathering rates and rockfall activity within tectonically active regions resulting in a high rate of debris being transported to glacier surfaces through direct deposition and melt out of englacial debris septa (Goodsell et al., 2005a; Kirkbride and Deline, 2013; Rowan et al., 2015). As a result of such processes, debris-covered glaciers are prevalent in regions such as New Zealand (Anderson and Mackintosh, 2012; Dunning et al., 2015), Alaska (Herreid and Pellicciotti, 2020), Patagonia (Glasser et al., 2016), Andes (Reynolds, 1992), European Alps (Huggel et al., 2002; Diolaiuti et al., 2005; Paul et al., 2011; Reid and Brock, 2014) and the Pamirs, Karakorum and Himalaya (Reynolds, 1998; Scherler et al., 2011; Bolch et al., 2012; Gardelle et al., 2013). A substantial proportion (17.2%) of glaciers with debris cover are located within the South East Asia region (Table 1.1).

The presence of supraglacial debris cover alters glacier ablation and typically retards ablation under a thick debris layer (Østrem, 1959; Mattson et al., 1993; Nicholson and Benn, 2006). However, some comparisons with clean-ice glaciers have shown that debris-covered glaciers exhibit similar thinning rates at comparable elevations to clean-ice glaciers (e.g. Pellicciotti et al., 2015; Vincent et al., 2016). Recent studies have shown variable melt rates result in an undulating glacier surface topography and supraglacial features that commonly develop on debris-covered glaciers, such as supraglacial ponds and ice cliffs, which act as localised ablation hotspots and, therefore, contribute disproportionally to total ablation rates (e.g. Sakai et al., 2000; Buri et al., 2016b; Miles et al., 2016; Thompson et al., 2016). Yet, long-term studies of glacier surface evolution and topography are limited. Thus, it is important to assess the number, location and size of supraglacial ponds and ice cliffs in relation to surface evolution when considering the overall mass balance, glacier surface energy balance and response of debris-covered glaciers to future climatic change.

The relationship between glacier dynamics and supraglacial pond formation is complex and remains unclear as quantitative measurements are both limited spatially and temporally (Quincey et al., 2007; Watson et al., 2016). This highlights the need for more research to better understand the evolution of debris-covered glaciers and the development of surface features including supraglacial ponds and ice cliffs. This would provide detailed information regarding the state of debris-covered glaciers worldwide in the current climate and inform models for predicting future response, to aid water resource management and prediction and mitigation of Glacial Lake Outburst Floods (GLOF) events.

This research investigates debris-covered glacier dynamics in the European Alps and in the Manaslu region of the Nepalese Himalaya. Miage Glacier in the European Alps is a well-studied and easily accessed debris-covered glacier; accessibility was important for the deployment of several data collection techniques and multi-annual repeat surveys. Research methodologies were optimised at Miage Glacier before undertaking fieldwork at Hinang Glacier in the Manaslu region, which has not been studied extensively and is situated in a less accessible location where deployment of field equipment was more challenging. Comparison of results between the two locations will also help determine whether the evolution of debris-covered glaciers is strongly controlled by regional or environmental factors.

## 1.3. Aims and objectives

The overall aim of this research is to investigate debris-covered glacier evolution and dynamics in the European Alps and the Himalayan Manaslu region using a range of *in situ* data collection methods and remotely sensed data. The following objectives are identified to fulfil the overall aim of this thesis:

**Objective 1:** To complete glacier surface mapping including surface structures, development of debris cover, supraglacial ponds and ice cliffs on the Alpine Miage Glacier (1952 – 2018) and Himalayan Hinang Glacier (1970 – 2019).

**Objective 2:** To assess changing glacier dynamics through quantification of glacier surface elevation change and surface velocity at Miage Glacier (1990 – 2018) and Hinang Glacier (1970 – 2019).

**Objective 3:** To examine the impact of supraglacial ponds, and ice-marginal lakes and adjacent ice cliffs on glacier ablation rates at Miage Glacier and Hinang Glacier.

## 1.4. Structure of thesis

Figure 1.2 illustrates the structure of the thesis. Chapter 2 will provide an in-depth literature review of the current state of research regarding debris-covered glacier dynamics. Chapter 3 will describe the specific study sites highlighting previous research conducted at each of the sites and rationale for selection. Four data chapters present the distinct components of research and data collection, which fulfil the above aims and objectives. Methods and accuracy assessment will be discussed in each of the chapters to which they relate. Chapter 4 presents the surface evolution of Miage Glacier from 1952 to 2018. Chapter 5 details the glacier dynamics of Miage Glacier from 1990 to 2018 based on analysis of Digital Elevation Model (DEM) differencing and surface velocity. Chapter 6 details the impacts of glacial lakes and ice cliffs on ablation rates assessed through bathymetric and photogrammetry surveys carried out at Miage Glacier over two summer survey periods in 2017 and 2018. The final data chapter (Chapter 7) presents analysis of glacier dynamics and evolution of Hinang Glacier, and the two neighbouring glaciers, in the Manaslu region of the Nepalese Himalaya. A discussion chapter is presented in Chapter 8 to identify key debris-covered glacier dynamics and evolutionary processes followed by conclusions in Chapter 9.

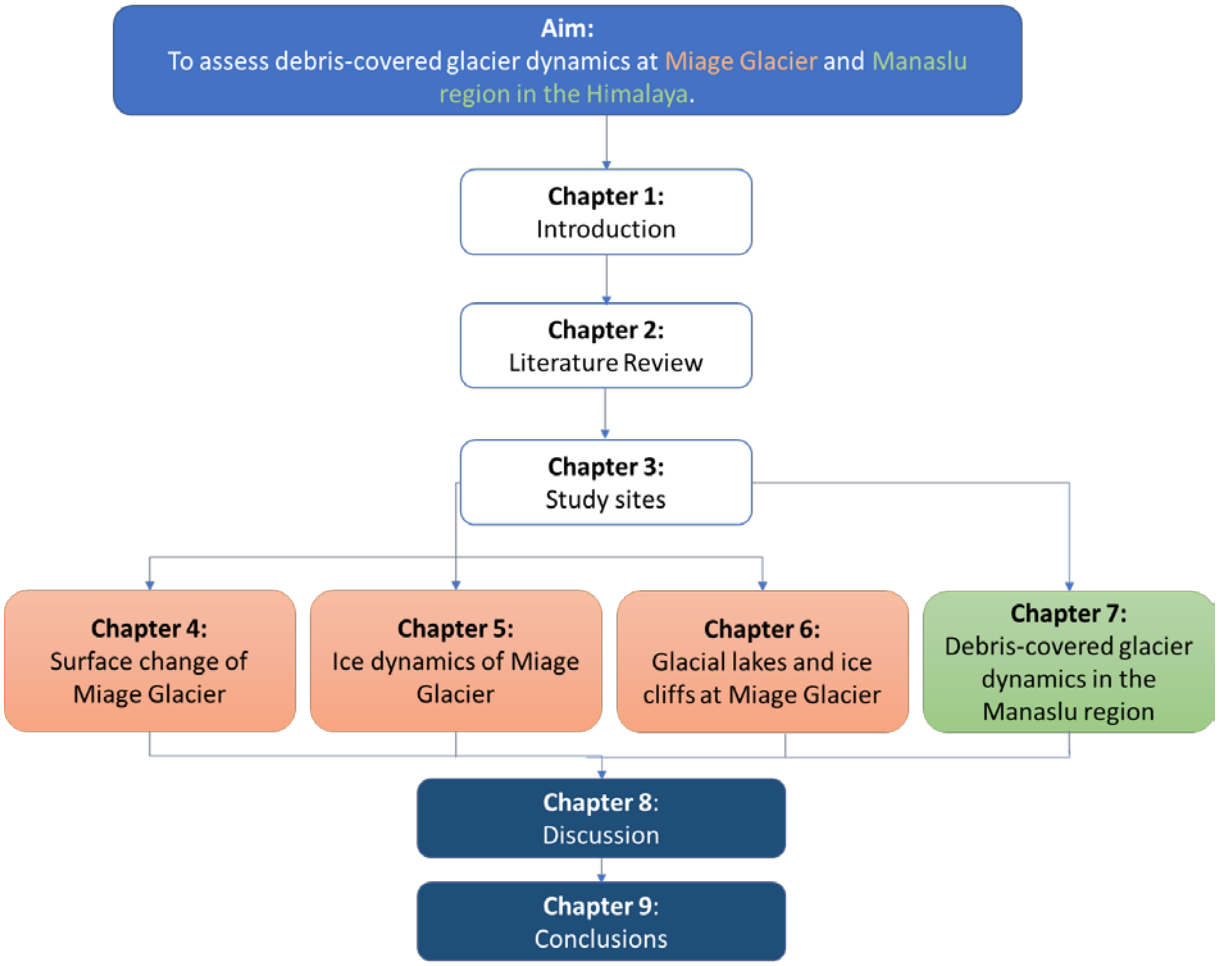


**Figure 1.2:** Flow chart of the thesis structure.

# Chapter 2 : Debris-covered glaciers: a literature review

## 2.1. Introduction

Accumulated rock debris on glacier surfaces can substantially influence glacier dynamics (Benn et al., 2012; Rowan et al., 2015). Debris cover is present on 44% of Earth's glaciers and is fundamental to include in global glacier models to better understand future response to a changing climate (Herreid and Pellicciotti, 2020). This chapter will provide a review of the existing literature to date, relevant to the three core objectives of the thesis (Section 1.3). This assessment of the current research situation will highlight the characteristics and evolution of debris-covered glaciers, and the impacts of supraglacial ponds and ice cliffs on their mass balance. This review will highlight where further research is required to aid our understanding and advance modelling efforts to accurately assess the future response of debris-covered glaciers. The research gaps identified from the literature review are then discussed.

This thesis uses the term 'glacial lakes' to refer to all water bodies inclusive of supraglacial, proglacial and ice-marginal ponds and lakes, regardless of size or location. Specification of water bodies will then be referred to by the terms as used above. The distinction between supraglacial ponds and lakes has not previously been well defined and are often used interchangeably (Watson et al., 2016). However, Watson et al. (2016) quantified the areal limit of supraglacial ponds as 20,000 $m^2$ and lakes are thus accepted to represent water bodies larger than this. The terms will be used in this way throughout this thesis for clarity and comparison with similar studies.

## 2.2. Glacier response to climatic change

Globally, glaciers are receding in response to climatic warming (Zemp et al., 2015; Huss and Hock, 2018). Rising global temperatures have resulted in the disappearance of numerous glaciers (Vaughan et al., 2013), particularly small mountain glaciers, which are highly sensitive to environmental change. Observed glacier change and variability is representative of the glacier surface energy balance and combined influence of the components.

### 2.2.1. Global glacier change

Since the early twentieth century, glaciers around the world have been experiencing negative mass balances (Figure 2.1) with reduced accumulation from snowfall, and increased ablation from warming temperatures albeit with a few exceptions (Benn and Evans, 2010; Zemp et al., 2015). Enhanced glacier ablation, inclusive of mass loss from the system through melt, sublimation, and avalanching in a terrestrial setting and by calving of ice blocks and icebergs in marine and lacustrine environments (Figure 2.2), in combination with reduced ice flux from the accumulation zones has resulted in negative mass balances on a global scale (Figure 2.1). The global mean annual value of

−0.54 metres per year water equivalent (m w.e. $a^{-1}$), between 2000 and 2010 shows a strong global signal (Zemp et al., 2015). Glaciers typically respond to negative mass balance by terminal retreat or downwasting, or both. Increased rates of terminal retreat have been observed at unprecedented rates since the early 21st century in response to the prolonged periods of negative mass balance (Zemp et al., 2015). The changing state of glaciers affect seasonal runoff, which provides valuable water resources in remote communities and are therefore important to monitor (Irvine-Fynn et al., 2017; Burger et al., 2019).

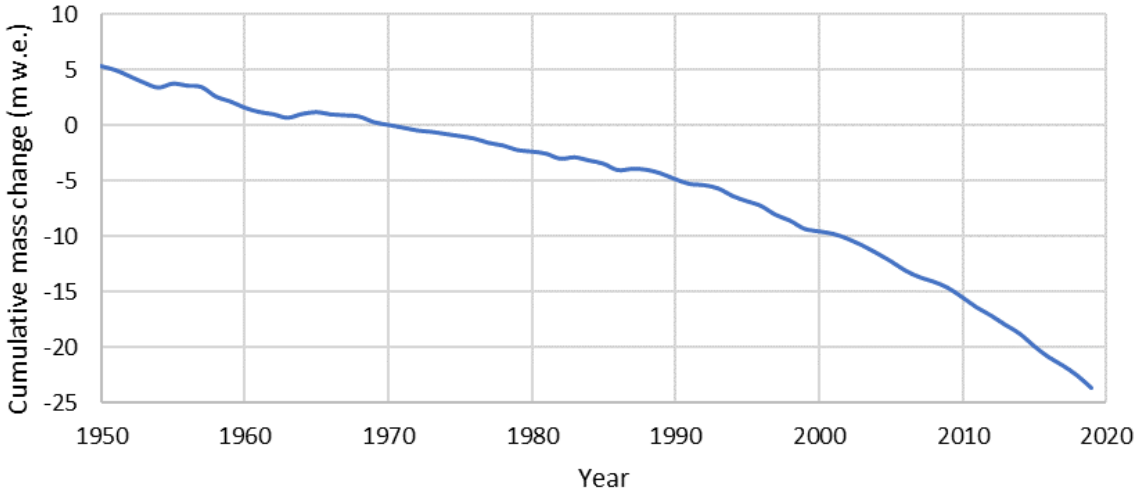


**Figure 2.1:** Global cumulative mass change relative to 1976 from 30 global reference glaciers with continuous observations as compiled by the World Glacier Monitoring Service (WGMS, 2019). Cumulative values relative to 1976 are represented on the y-axis.

### 2.2.2. Glacier surface energy balance

The glacier surface energy balance is dependent upon the interactions of the ice surface with long and shortwave incident radiation, sensible heat flux, and latent heat flux (Benn and Evans, 2010). The energy balance ultimately controls the amount of energy available for ablation and is therefore a fundamental component in the resulting mass balance and observed response of glaciers to climatic change (Figure 2.2). The net energy balance at a glacier surface is calculated as in Equation 2.1.

$$SEBnet = (SWin - SWout + LWin - LWout) + (QH + QE) + QG + QR - QT \quad \textbf{Equation 2.1}$$

Where SWin represents incoming shortwave radiation, SWout outgoing radiation, LWin incoming longwave radiation, LWout outgoing radiation, QH sensible heat transfer, QE latent heat transfer, QG ground heat flux, QR energy from precipitation, and QT is energy required for the phase change of ice (Cuffey and Paterson, 2010). Thus, the surface energy balance denotes the energy available

for glacier ablation. As such, glacier fluctuations, such as change in length, area, volume and mass, provide a useful indication of the energy balance and thus, climate (Figure 2.2).

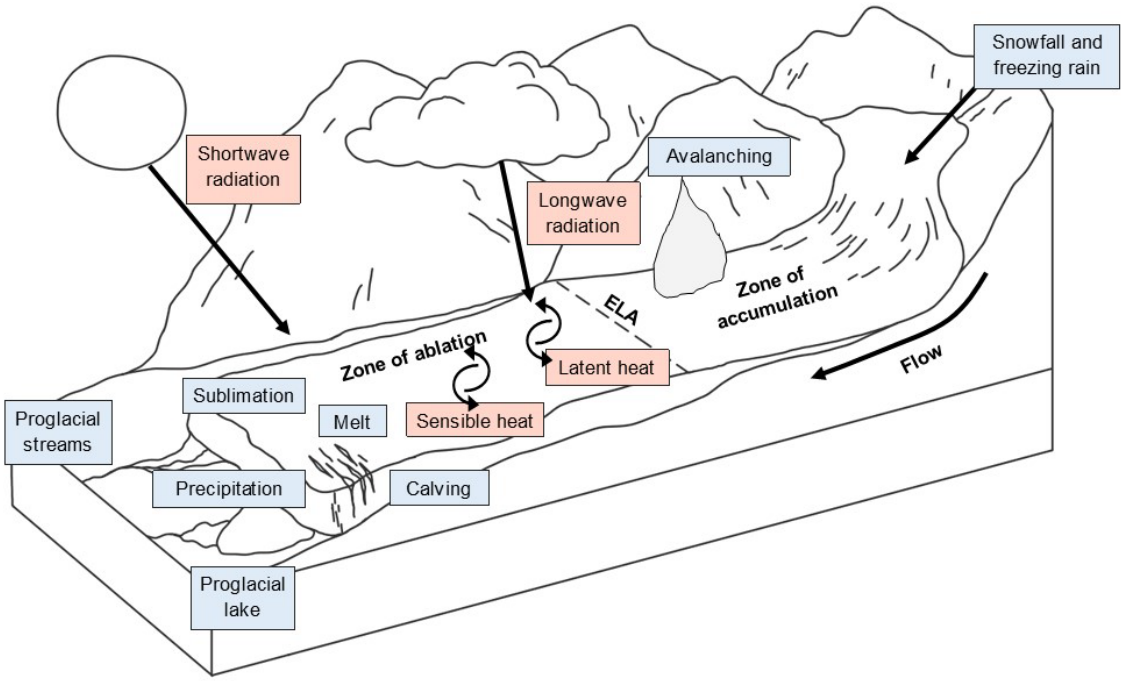


**Figure 2.2:** Energy balance and inputs and outputs within a glacier system, which affect the resulting glacier mass balance.

The presence of a supraglacial debris layer slows the transfer of energy between the atmosphere and the ice surface, ultimately delaying the response to either positive or negative surface energy balances. Properties of the debris layer provide additional controls on the rate of energy transfer between the atmosphere and ice surface (Rowan et al., 2021). Such properties include the debris thickness, lithology, porosity, grain size, moisture content and thermal capacity of the debris (Nicholson and Benn, 2006; Evatt et al., 2015). Thus, the debris properties result in high levels of variability between glaciers with a debris cover.

## 2.3. Characteristics of debris-covered glaciers

Debris-covered glaciers are prevalent in tectonically active, high-mountain regions due to the provision of debris from valley sides to glacier surfaces. Debris-covered glaciers therefore exist in a number of locations as highlighted in Table 1.1, including both the European Alps (Huggel et al., 2002; Diolaiuti et al., 2005; Paul et al., 2011; Reid and Brock, 2014; Berthier et al., 2016) and across the Himalaya (Reynolds, 1998; Scherler et al., 2011; Bolch et al., 2012; Gardelle et al., 2013; Herreid and Pellicciotti, 2020). Evidence has shown that debris cover is increasing in area in multiple regions as climate driven destabilisation of valley sides results in increased rockfall events (Ravanel et al.,

2017). Such increases in debris-cover extent have been observed in the European Alps (Deline, 2005; Kellerer-Pirklbauer et al., 2008; Mazué et al., 2009), and across the Himalaya (Scherler et al., 2011; Gibson et al., 2017a). Debris cover in the Everest region increased by 17.6 ± 3.1% between 1962 and 2011 (Thakuri et al., 2014) and is expected to continue to increase in the future (Rowan et al., 2015; Herreid and Pellicciotti, 2020).

The presence of debris cover affects glacier ablation rates and alters ablation patterns. Thick debris (>5 cm) restricts conduction of surface heat to the ice and acts to insulate the underlying ice, reducing ablation rates (Østrem, 1959; Nakawo and Rana, 1999; Nicholson and Benn, 2006). The critical thickness for debris to have an insulating effect has been found to vary from glacier to glacier and even from one point to another on the same glacier (Kirkbride and Dugmore, 2003). However, once debris thickness exceeds ~40 cm, ablation has been shown to reduce substantially at a number of sites (Mattson et al., 1993; Nicholson and Benn, 2006). Conversely, a thin debris layer (<2 cm) lowers albedo, thereby increasing the amount of energy conducted to the ice surface enhancing ablation rates. This relationship of increased ablation under an increasing debris thickness to a critical thickness followed by a substantial reduction in ablation rate was first identified by Østrem (1959) and is often referred to as the Østrem Curve (Figure 2.3). Glacier-scale mass balance is therefore strongly influenced by the presence, extent, and thickness of debris on the glacier surface (e.g. Gibson et al., 2017a).

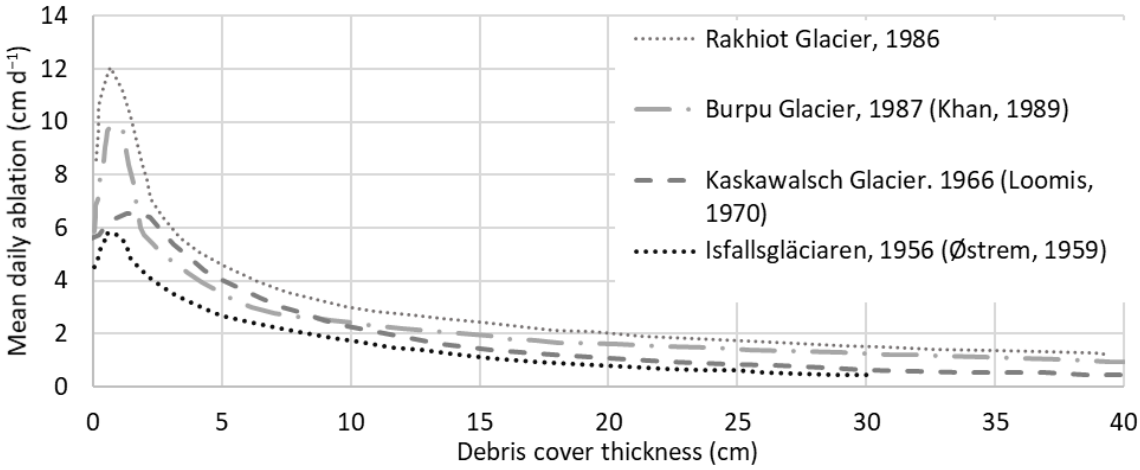


Figure 2.3: The Østrem curve as derived from empirical measurements of the relationship between debris thickness and ice ablation rates on sample glaciers (redrawn from Mattson et al. (1993) as shown in Nicholson and Benn (2006)). Reprinted from the Annals of Glaciology with permission of the International Glaciological Society.

The development of a thick debris cover has been identified on a number of glaciers during periods of sustained negative mass balance (Deline, 2005; Stokes et al., 2007; Kirkbride and Deline, 2013; Vincent et al., 2016; Gibson et al., 2017a). Once a thick debris cover develops (>40 cm) the insulating effect shields against increasing temperatures and debris-covered glaciers typically exhibit a

nonlinear response to climatic warming (Benn et al., 2001) and have been considered to be less sensitive to climatic changes than clean-ice glaciers (Scherler et al., 2011; Nuimura et al., 2012). Consequently, Rowan et al. (2015) suggested that, irrespective of any potential current climatic warming slowdowns, debris-covered glaciers will continue to experience a period of less negative mass balance resulting in longer, decadal response times compared to clean-ice glaciers. Thus, a number of debris-covered glaciers are observed at lower elevations with comparatively lower ablation rates in comparison to neighbouring clean-ice glaciers at similar elevations (Gardelle et al., 2012, 2013).

Although studies showed that significant glacier retreat was observed in the eastern and central Himalaya in line with the global trend during the early 21st century (Kääb et al., 2012; Gardelle et al., 2013), spatial variability in mass balance has been observed across the Himalaya with an east to west gradient in mass loss. Despite moderate to high mass losses in the eastern, central, and western Himalaya respectively, stable or slightly positive mass balances were observed in the Karakoram region (Figure 2.4) since the 1990s, referred to in the literature as the 'Karakoram anomaly' (Hewitt, 2005). The 'Karakoram anomaly' is attributed to local meteorological conditions and the influence of the Indian monsoon and predominant wind systems resulting in higher accumulation rates in the Karakoram (Bolch et al., 2012; Kääb et al., 2012; Farinotti et al., 2020).


**Figure 2.4:** Regions of the Hindu Kush Himalaya based on ICIMOD (2014).

Debris-covered glaciers often exhibit a delayed response to climatic change resulting from the insulation provided by their thick surface debris layers, yet a number of remote sensing studies have observed similar ablation rates to that of clean-ice glaciers (Bolch et al., 2012; Pellicciotti et al., 2015). The hitherto unexplained variability of ablation patterns on debris-covered glacier tongues at comparable rates to clean-ice glaciers has since been referred to in the literature as the 'debris-covered glacier anomaly' (Pellicciotti et al., 2015; Ragettli et al., 2016; Vincent et al., 2016; Salerno et al., 2017; Brun et al., 2019). The role of supraglacial debris cover in glacier mass balance thus drew further attention and highlighted a lack of long-term or *in situ* studies.

Debris cover is rarely homogenous as it is deposited intermittently either directly through rockfall and avalanche events, lateral moraine derived deposits (van Woerkom et al., 2019), or arrives at the surface through debris septa melt out (Kirkbride and Deline, 2013). It is then subject to redistribution via meltwater and gravity falls (Rowan et al., 2015; Gibson et al., 2017a). Debris-covered glaciers are therefore typically observed with varying thickness across the glacier surface (Zhang et al., 2011; Anderson and Anderson, 2018). As debris distribution and thickness varies, ablation is enhanced in regions of dirty ice or thin debris cover, leading to differential ablation across the glacier surface and the generation of an undulating or pitted surface topography (e.g. Mölg et al., 2020; Bartlett et al., 2021). As such, debris-covered glaciers often exhibit ice slopes or cliffs, debris-covered ridges and cones, depressions, and hollows (Iwata et al., 1980). Several studies have shown that enhanced rates of ablation at ice cliffs and supraglacial ponds, which are common features on debris-covered glaciers, act as localised hotspots and may account for the similar overall ablation rates to that of clean-ice glaciers (e.g. Sakai et al., 2000, 2002; Kääb et al., 2012; Buri et al., 2016b; Miles et al., 2016, 2018; Brun et al., 2017). Conversely, multiple studies contest this and state that, despite higher ablation rates often observed at ice cliffs and supraglacial ponds, the insulating effect of a thick debris cover outweighs the ablation at such hotspots (Hambrey et al., 2008; Ragettli et al., 2016; Vincent et al., 2016).

As debris is transferred down-glacier, debris thickness increases towards the glacier terminus resulting in mass loss primarily by surface lowering more than through marginal recession (Hambrey et al., 2008). Mass loss is typically focused on clean-ice areas often located upglacier of the terminus whereas the terminus itself becomes covered in a thick layer of debris (Nakawo et al., 1999; Benn and Lehmkuhl, 2000; Benn et al., 2012; Ragettli et al., 2016; Anderson and Anderson, 2018). This substantially alters the mass balance gradient compared to clean-ice glaciers and promotes reduced driving stress and ice flow (Kääb, 2005; Quincey et al., 2009; Rowan et al., 2015; Dehecq et al., 2019) with a concave surface topography (Anderson and Anderson, 2018) (Figure 2.5). Hence, the presence of debris cover has strong influences on ablation, retreat patterns, and glacier dynamics (Quincey et al., 2009; Scherler et al., 2011; Benn et al., 2012; Deline et al., 2012).

Morphological factors therefore have additional consequences for future glacier response and need to be further constrained.

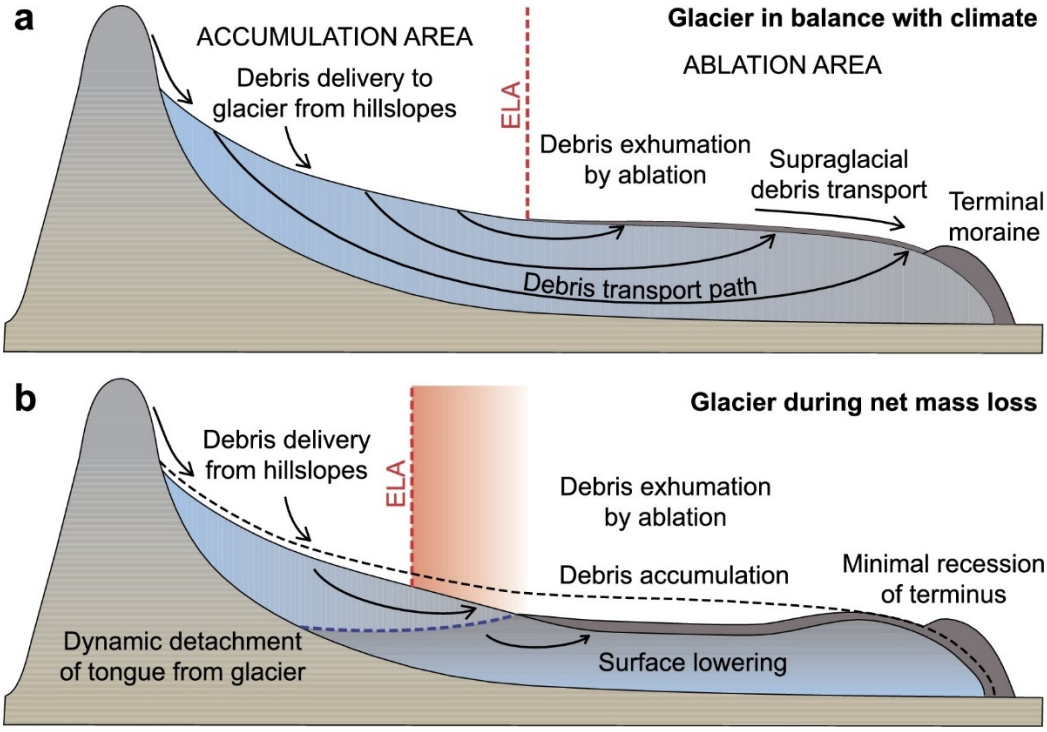


**Figure 2.5:** A conceptual model of the development of a Himalayan debris-covered glacier (a) in balance with climate, and (b) during net mass loss under a warming climate with an upglacier migration of the elevation line altitude (ELA). Reprinted from Rowan et al. (2015) with permission from Elsevier.

Surface lowering on debris-covered glaciers is often associated with a reduction in surface velocity and reduced surface gradients promoting reduced driving stress (Quincey et al., 2009; Benn et al., 2012; Dehecq et al., 2019). As glaciers recede, the snout becomes stagnant or inactive as observed both in the Alps (Capt et al., 2016; Mölg et al., 2019) and across the Himalaya (Quincey et al., 2009; Ragettli et al., 2016; Robson et al., 2018). Salerno et al. (2017) assessed 28 glaciers on the southern slopes of Mount Everest and identified that a reduced downstream surface gradient was the main morphological factor responsible for increased surface lowering and the development of supraglacial ponds in response to climatic change. However, the impact of ice cliffs was not assessed. Furthermore, debris cover and thickness were not significantly responsible for the development of ponds or surface lowering (Salerno et al., 2017). Brun et al. (2019) also observed that the glacier tongue slope and mean glacier elevation were the best predictors of glacier-wide mass balance in most regions across High-Mountain Asia (HMA). Glacier surface morphometry change is required to assess the impact on glacier surface energy balance and therefore important to accurately account for in melt modelling (Rounce et al., 2015).

Benn et al. (2012) summarised three regime stages that debris-covered glaciers progress through. In regime 1, the glacier is dynamically active and ablation predominantly occurs beneath the debris layer. Debris is transported efficiently downglacier, resulting in increased debris cover and thickness towards the terminus. Transition to regime 2 is enhanced by climatic warming, affecting ice influx and ablation rates. High ablation rates in the mid-ablation zone causes surface lowering rather than retreat of the ice margin resulting in a distinctive concave up-glacier profile (Reynolds, 2000; Bolch et al., 2011; Rowan et al., 2015; Anderson and Anderson, 2018). This reduces the driving stresses in the lower ablation zone, creating a positive feedback loop, resulting in lower velocity rates and eventual stagnation (Quincey et al., 2009; Dehecq et al., 2019) enabling meltwater to pond creating perched lakes. Regime 3 is associated with the intersection of supraglacial ponds with the base-level due to surface lowering on areas with reduced surface gradients and low surface velocities (Quincey et al., 2007), which act to further promote ablation.

## 2.4. Surface and structural evolution of debris-covered glaciers

Analysis of debris-covered glacier evolution enables us to constrain timescales and rates of surface feature development aiding our ability to predict future response and implications for water resources or potential hazards. Structural glaciology has aided our knowledge and understanding of sediment distribution (e.g. Bennett et al., 1996), sediment-landforms associations (Roberson, 2008) and glacier flow dynamics (Hambrey and Lawson, 2000; Hambrey et al., 2005; Hambrey and Clarke, 2019). Thus, this technique may provide information on the conditions leading to future glacier disintegration (Azzoni et al., 2017) and yields important details about the evolution of glacier dynamics in response to climatic change.

A number of studies have produced detailed structural maps of both Arctic (Hudleston and Hooke, 1980; Jennings et al., 2016) and alpine glaciers (Hambrey and Milnes, 1977; Glasser et al., 2003; Goodsell et al., 2005b; Herbst et al., 2006), polythermal (Hambrey et al., 2005), surging (Sharp, 1988; Lawson et al., 1994; Woodward et al., 2002) and more recently have highlighted the benefits of multi-temporal analysis (Hambrey et al., 2005; Glasser and Scambos, 2008; Azzoni et al., 2017; Phillips et al., 2017). Few of these studies investigated the structural evolution and surface change of debris-covered glaciers; in part due to the visible reduction of surface features (e.g. Fushimi, 1977; Hambrey et al., 2008; Gibson et al., 2017b). Debris-covered glacier dynamics and response to climate amelioration are therefore limited but are required to aid our understanding of both past and future response, patterns of debris distribution (and therefore ablation patterns) and associated landform assemblages.

Glacier response to changing conditions can be assessed through structural surface expressions of the stress and strain regimes within the glacier system. Stress relates to the amount of compression

and tension upon the ice whereas strain relates to the amount of deformation resulting from the stress. Therefore, glacier structures, which are indicative of the amount of deformation, enable us to assess the stress and strain regimes throughout a glacier system. Through analysis of ice structures over time, an insight into both long- and short-term change can be derived. Ductile structures (e.g. folds and foliation) reveal cumulative strain indicative of the long-term strain history developed from the primary stratification of annual snow layers or crevasse traces under high strain or through rotation by glacier flow (Benn and Evans, 2010). In comparison, brittle structures, including crevasses, typically open due to extensional forces pulling the ice apart once the stress and strain exceeds that of the ice elasticity threshold. Therefore they are often confined to the surface resulting in clearly identifiable fractures (Cuffey and Paterson, 2010).

Hambrey and Lawson (2000) provide a detailed review of the structural styles and deformation in glaciers. A number of features originate from primary stratification derived from the laying of multi-annual snowfall and is generally observed in the accumulation zones. The evolution of glacier structures are typically derived through a series of deformation regimes, which are common to valley glaciers. Figure 2.6 shows the development of a number of commonly identified structural features on valley glaciers which originate as primary stratification in the accumulation zones and get reworked as they progress through the glacier system as identified at the Haut Glacier d'Arolla, Switzerland (Goodsell et al., 2005b). Inhomogeneities within the ice enable easier visual identification of a variety of structures, including foliation and folds as the ice moves through regions of varying stress and strain regimes. The locations and abundance of such features enable us to glean further information regarding historical glacier dynamics and further explore how future response may develop these features. The structures observed at the Haut Glacier d'Arolla also indicated compression at the snout can reactivate crevasse traces as thrust faults (Figure 2.6). Periods of rapid recession are typically associated with less dynamic ice and a reduction in new structures forming, whereas increased ice flux and activity is linked to the generation of new structures (Hambrey and Lawson, 2000).

*This image has been removed by the author for copyright reasons.*

**Figure 2.6:** Schematic diagram of the structural evolution of Haut Glacier d'Arolla, Switzerland. A: Flow-units each with its own pattern of primary stratification, separated by structural discontinuities. B: Primary stratification gradually folded as it flows into the glacier tongue. Cut by open crevasses. C: Continued deformation and formation of longitudinal foliation. Closure and rotation of crevasse traces. D: Reactivation of crevasse traces and opening of splaying crevasses. *Source:* Goodsell et al. (2005b).

Typical glaciological structures observed on valley glaciers are highlighted in Table 2.1 as identified by Goodsell et al. (2005b). One of the most obvious features are crevasses and depending on the direction of fracture and shape, the associated stress regimes can be inferred (Figure 2.7). Observed as surface fractures, crevasses indicate regions where the critical value has exceeded that of the ice.

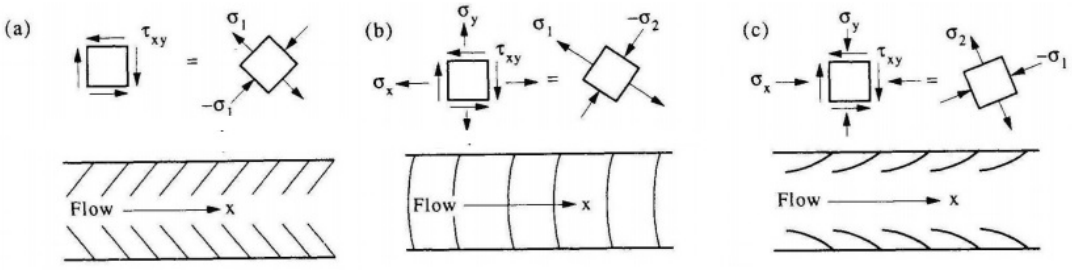


**Figure 2.7:** Crevasse patterns in a valley glacier and associated stress regimes. A: Effect of shear stress exerted by valley walls, B: shear stress and extending flow, C: shear stress and compressive flow. *Source:* Benn and Evans (2010); adapted from Nye (1952). Reproduced with permission of The Licensor through PLSclear.

Ogives are common features on mountainous valley glaciers with icefalls and found on the debris-covered Khumbu glacier, which has an iconic icefall (Hambrey et al., 2008). Two types of ogives have been identified in the literature: wave ogives and Forbes bands. Wave ogives are surface undulations often found at the base of icefalls resulting from a combination of differential ablation and plastic deformation occurring throughout the icefall (Nye, 1958; Goodsell et al., 2002). The wave indicates the passage of thicker ice through an icefall in winter and a trough in summer, representing one year's movement through the ice fall. In comparison, Forbes bands are thought to represent bands of dirty and clean ice each representing a year's flow through the icefall. The colour variations between light and dark bands has been highly debated with theories suggesting that surface debris accumulating in wave troughs (King and Lewis, 1961; Atherton, 1963) or dark bands represent debris-rich englacial ice (Leighton, 1951). Further suggestions included variations in ice type with light bands consisting of bubble-rich white ice and the darker bands of coarse, bubble free ice (Fisher, 1962; Goodsell et al., 2002), or the intensity of foliation within the ogives leading to differential weathering (Goodsell et al., 2002). However, band ogives on the Mer de Glace were found to have similar surface mass balances on both the light and dark bands contrary to the dark bands having ~40% reduced albedo and thus disputes theories of the genesis of band ogives based on the assumption of strong ice ablation contrasts between light and dark bands (Vincent et

al., 2018). Thus, the formation mechanism of ogives is still highly disputed and the potential importance in the development of surface features lower in the glacier systems unknown.

Structural glaciological mapping and surface geomorphological mapping are often based on a combination of high-resolution aerial or satellite imagery and field observations (Goodsell et al., 2005b; Appleby et al., 2010; Azzoni et al., 2017). Aerial and satellite mapping enable glacier-scale mapping to be undertaken across large areas, making it easier for some structures to be observed (e.g. unconformities and flow unit boundaries). However, other features are difficult to identify on images in part due to smaller sizes and fine features (e.g. thrusts) but are much easier to identify in the field. Therefore, where possible, many studies combine both mapping of imagery with field observations to infer past dynamic glacier regimes on decadal to centennial timescales.

**Table 2.1:** Identification of glaciological and surface structures derived from aerial and field observations from Goodsell et al. (2005b).

*This table has been removed by the author for copyright reasons.*

## 2.5. Debris-covered glacier surface features

Debris-covered glaciers in a state of negative mass balance commonly exhibit supraglacial ponds and ice cliffs resulting from variable ablation rates and undulating topography across the glacier surface. Supraglacial ponds are commonly associated with adjacent ice cliffs (Thompson et al., 2016; Watson et al., 2017b). However, ice cliffs are also often observed across debris-covered glaciers without associated ponds and can occur in high numbers on individual glaciers varying in both size and shape (Watson et al., 2016, 2017a). Watson et al. (2017b) observed greater retreat rates of ice cliffs where they were adjacent to supraglacial ponds compared to those that were not. They also highlighted the need to quantify the spatio-temporal dynamics of supraglacial ponds and ice cliffs to fully assess their influence on glacier-scale ablation and thus, glacier dynamics.

Ice cliffs and supraglacial ponds make a disproportionately large contribution to the overall ablation and are an important consideration when assessing the state and future response of debris-covered glaciers (Zhang et al., 2011). The presence and influence of both supraglacial ponds and ice cliffs are therefore important to assess and understand with regard to glacier-scale dynamics. However, when assessing the impact of both ice cliffs and supraglacial ponds on ablation rates, studies are limited in quantity and comparability. A number of studies have assessed the proportion of ablation at ice cliffs to total glacier ablation through a variety of methods including ablation stakes and the development of models (e.g. Sakai et al., 1998; Reid and Brock, 2014), high-resolution DEMs derived from Structure-from-Motion (SfM) and satellite data (Immerzeel et al., 2014; Brun et al., 2016, 2018; Buri et al., 2016a; Thompson et al., 2016; Watson et al., 2017b), and point models (Steiner et al., 2015; Buri et al., 2016a). However, only Miles et al. (2018) have so far quantified ablation rates associated with supraglacial ponds on total glacier ablation rates. Therefore, the effect ice cliffs and supraglacial ponds, and the combined effects, have on both local and glacier-scale ablation rates has yet to be fully investigated.

Studies quantifying ice cliff ablation, summarised in Table 2.2, have shown that ice cliffs contribute to the overall debris-covered ablation rates in varying proportions ranging from ~1.2% (Buri et al., 2016a) to 69% (Sakai et al., 1998). Such variability adds complexity to modelled attempts of debris-covered glacier evolution and to the debate as to whether ice cliffs can account for the debris-covered glacier anomaly. Comparability of melt estimates is not always straightforward as methods vary. For example Vincent et al (2016) used an ice flux method and accounted for glacier emergence whereas Thompson et al. (2016) did not include emergence velocity based on DEM differencing. Furthermore, the quantification of ice cliff area varies considerably and is reported as either a percentage of debris-covered area, the monitored area or glacier area. The variability could also reflect climatic differences between sites and debris properties including thickness (Sakai et al., 1998; Buri et al., 2016b; Watson et al., 2017b). Despite the high variability, previous studies have concluded that ice cliffs drive a disproportionate amount of glacier-wide ablation and further

measurements are required to aid our understanding of their impact on glacier and region wide ablation in addition to the less constrained influence of supraglacial ponds. The quantification of such processes are vital to accurately model glacier-scale ablation patterns and debris-covered glacier evolution (Rounce et al., 2015; Rowan et al., 2015; Shea et al., 2015).

**Table 2.2**: Summary of quantification of ice cliffs to total glacier ablation rates studies highlighting the disproportionate influence on ablation.

| Study | Study site and timing of study | Method | Quantification of ice cliffs to ablation |
|---|---|---|---|
| Sakai et al. (1998) | Lirung Glacier, May – October 1996 | Ablation stakes, point scale | <2% in area, but equates to 69% of total ablation of debris covered area. |
| Sakai et al., (2002) | Lirung Glacier, May – October 1996 | Orientation and radiation model | 1.8% area yet 20% total ablation |
| Han et al. (2010) | Koxkar Glacier, Tuomuer mountain, China, Aug – Sept 2008 | Physically based energy-balance model, point scale | Mean backwasting rate 7.64 m $a^{-1}$, or 7.3% of total melt runoff |
| Juen et al. (2014) | Koxkar Glacier | Distributed ablation model | 1.7% of debris covered area yet 2.5% of total glacier ablation. |
| Reid and Brock, (2014) | Miage Glacier, Italy 2010 – 2011 | Ablation stakes and model, DEM, point scale model | ~7.4% of total ablation but only 1.3 % of the debris covered area |
| Immerzeel et al., (2014) | May – October 2013 | UAV and SfM | 8% in area but equates to 24% total melt |
| Steiner et al. (2015) | Lirung Glacier, Himalaya, May – Oct 2013 | Energy-balance point model | May: 3.25 - 8.6 cm $d^{-1}$<br>Oct: 0.18 - 1.34 cm $d^{-1}$ |
| Thompson et al., (2016) | Ngozumpa Glacier, Himalaya, 2010 – 2012 | DEM Differencing | 5% in area, but equates to 40% volume losses |
| Brun et al. (2016) | Lirung Glacier, Himalaya, May – October 2013 and 2014 | UAV and SfM | Six times higher melt than estimates of glacier-wide melt under debris |
| Buri et al., (2016b) | Hindu-Kush-Karakorum Himalaya, Lirung Glacier, Himalaya | Grid based model | Two ice cliffs equate to 1.23% of the total melt for glacier tongue but only 0.09 % area |
| Watson et al., (2017b) | Khumbu Glacier, Himalaya, Nov 2015 – Oct 2016 | SfM 3D point clouds | Winter: 0.3 – 1.49 cm $d^{-1}$<br>Summer: 0.74 – 5.18 cm $d^{-1}$ |
| Brun et al., (2018) | Changri Nup Glacier, Himalaya; 2015 – 2017 | UAV and SfM, Pléiades DEM | 23-24% ± 5% of total ablation observed on the tongue; 3.1 times higher than average tongue surface |

### 2.5.1. Glacial lakes

In addition to supraglacial ponds and lakes situated on the glacier surface, proglacial and ice-marginal lakes are commonly observed at the margins of receding debris-covered glaciers (Haeberli et al., 2016). Supraglacial ponds are often regarded as the initial phase of glacial lake development and have the potential to coalesce and form large proglacial or moraine-dammed lakes (e.g. Hambrey et al., 2008; Benn et al., 2012). Such lakes are associated with enhanced glacier mass loss (Song et al., 2017; King et al., 2019), accelerated ice flow (King et al., 2018) and potential risk of breaching and causing GLOF events with severe consequences (Haritashya et al., 2018). Global glacial lake volume has dramatically increased by ~48% between 1990 and 2018 and glacial lakes now hold about 0.43 mm of sea level equivalent (Shugar et al., 2020). Understanding supraglacial pond initiation and evolution is therefore important to assess the impacts of mass loss and help mitigate against future hazards associated with the development of large proglacial lakes and contributions to global sea level rise.

Although the number and size of glacial lakes in the European Alps are relatively small (Paul et al., 2007; Shugar et al., 2020), the European Alps are considered to be one of the most susceptible regions to glacier floods based on the number of sites, with 301 recorded glacial floods having occurred in the Alps (Carrivick and Tweed, 2016). As yet, no inventory of glacial lakes for the European Alps as a whole has been undertaken and are limited to individual studies (e.g. Strozzi et al., 2012; Emmer et al., 2015; Buckel et al., 2018) or global studies (Shugar et al., 2020). Thus, a full account of hazards associated with glacial lakes in the European Alps cannot currently be assessed. Comparatively, within the Himalaya, approximately 5000 glacial lakes are present having increased in area by 14% between 1990 – 2015 (Nie et al., 2017) with 6300 glacial flood events having been recorded across central Asia (Carrivick and Tweed, 2016). Due to the recent scientific interest in the Himalaya, numerous glacial lake inventories across the region have been completed (Mool et al., 2001; Zhang et al., 2015; Nie et al., 2017) and highlight the importance of such lakes as both water resources and as potential hazards (Immerzeel et al., 2014; Zhang et al., 2015).

#### 2.5.1.1. Supraglacial pond formation

Supraglacial ponds form on downwasting glaciers with low surface gradients and reduced glacier velocity (Table 2.3) (Luckman et al., 2007; Quincey et al., 2007). These factors have been shown to influence the distribution of ponds, impede drainage and aid the formation of supraglacial ponds (Reynolds, 2000; Quincey et al., 2007; Bolch et al., 2008; Sakai and Fujita, 2010; Salerno et al., 2017). Supraglacial ponds generally form on virtually stagnant glacier tongues with velocities of less than 5 m $a^{-1}$ with low slope gradients (< 2°) (Table 2.3) (Quincey et al., 2007). Reynolds (2000) identified that only small ephemeral ponds were able to form on surface gradients of 6 to 10°, yet were prevalent on gradients of 2 to 6°, and were not able to form on gradients above 10°. It is considered

that surface gradients between 2 and 10° limit drainage conduits and aid coalescence of meltwater and precipitation (Quincey et al., 2007). As the ice melts, supraglacial and englacial drainage systems are fragmented, preventing the meltwater escaping efficiently, and enables it to collect in surface hollows (Benn et al., 2012). Downwasting is further enhanced via the melt ponds transmitting atmospheric energy to the glacier's interior. Where the pond overlies an englacial conduit, surface lowering may intersect them, thereby unroofing them causing them to collapse (Miles et al., 2016). As the surface regularly intersects with englacial conduits, water is transported to regions where it may be impounded enabling ponds to absorb atmospheric energy and transmit it to the underlying glacier ice resulting in further englacial conduit enlargement and collapse supporting additional basin evolution and new pond formation (Miles et al., 2016).

**Table 2.3**: Refined relationship between glacier surface gradients, glacier velocity and supraglacial pond development. Reprinted from Quincey et al. (2007) with permission from Elsevier.

| Surface gradient and velocity characteristics | Interpretation |
|---|---|
| Gradient <2°, stagnant ice | Minimal opportunity for reorganisation of drainage conduits, promoting large scale lake development |
| Gradient <2°, measurable flow | Large lake likely but with a potential for drainage through the reorganisation of drainage conduits through flow |
| Gradient >2°, stagnant ice | No opportunity for reorganisation of drainage conduits through flow, but steeper hydraulic gradient aids drainage and lake development is unlikely |
| Gradient >2°, measurable flow | Opportunity for reorganisation of drainage conduits through flow and steeper hydraulic gradient aids drainage, resulting in most efficient drainage conditions so that lake development is least likely |

Pond formation tends, therefore, to be focussed in regions with low slope gradient, low ice velocity, with negative mass balance, impeded drainage and hollows developed from either differential ablation or englacial conduit collapse. Kirkbride (1993) observed ponds developing upstream of the terminus where roof collapse exposed englacial conduits, thus the location of ponds was linked to the internal drainage system. Ponds have been observed in higher densities near confluences thought to be associated with the closure of conduits and transverse compression (Kraaijenbrink et al., 2016b). Blachut and Ballantyne (1976) suggested that ponds were defined by the underlying subsurface topography. Similar suggestions have been put forward for the formation of supraglacial ponds on the Greenland Ice Sheet (GrIS) resulting in fairly stable locations of such ponds, which repeatedly drain and reform (Yang et al., 2015). The locations of pond formation are still not well constrained and could help predict and mitigate against hazards associated with the development of large proglacial lakes. Thus, the monitoring and identification of additional controls on supraglacial pond formation are required.

#### 2.5.1.2. Supraglacial pond evolution

Supraglacial water bodies typically grow through coalescence of multiple smaller ponds into larger supraglacial lakes via thermo-erosional notching, and calving of associated ice cliffs (Benn et al., 2001). Analysis of four glaciers in the Khumbu region led Hambrey et al. (2008) to identify three key stages of lake evolution starting with: (1) supraglacial pond formation associated with low slope gradients and efficient englacial drainage, (2) lake formation, and (3) expansion including calving at a terminal cliff resulting in final drainage through the breaching of a moraine dam. Measurements of small and growing ponds and lakes are typically lacking and are required to provide a better understanding of which ponds are likely to evolve into potentially dangerous lakes (Cook and Quincey, 2015; Watson et al., 2016).

The evolution of supraglacial ponds differs greatly, even if their starting morphology is the same (Cook and Quincey, 2015). Cook and Quincey (2015) undertook a global analysis of glacial lake area, depth and volume measurements and concluded that the relationships between area and volume are not linearly correlated and there is a need to assess glacial lakes by geomorphological context, including supraglacial ponds, supraglacial lakes, moraine dammed lakes, and ice-damned lakes. However, Cook and Quincey (2015) noted a lack of bathymetric data sets for small supraglacial ponds. Watson et al. (2018b) identified that this lack of data in global assessments disregards the importance of expansion at depth with potential implications for volumetric calculations and water storage budgets. An additional 24 ponds, of which 20 were <5,000 $m^2$ on two glaciers in the Everest region, were incorporated into Cook and Quincey's (2015) area-volume relationship. This additional data supported the relationships previously derived from predominantly proglacial lakes and are also applicable to small ponds. However, this relationship is currently limited to data from the Himalaya and an improved global dataset would help further constrain these relationships.

Supraglacial ponds predominantly expand horizontally in area, which is attributed to the dominant influence of subaerial ice loss via calving, compared to subaqueous processes (Sakai et al., 2003; Röhl, 2008; Vincent et al., 2010; Cook and Quincey, 2015). Yet, subaqueous processes such as thermal undercutting, are thought to be a pivotal component leading to ice cliff calving events (Benn et al., 2001). Sakai et al. (2009) identified fetch (defined as the maximum lake length along the axis of glacier flow, which the wind blows in a given direction) as a primary control on lake evolution through calving due to the effects of the wind driven, warm surface water. Once the fetch exceeds 20 – 30 m with water temperatures of 2 – 3°C, subaqueous thermal undercutting can occur initiating calving (Sakai et al., 2009). Thus, Röhl (2006) concluded that subaqueous melt was also partly controlled by circulation and cliff geometry.

Drainage of the ponded meltwater can occur once a hydrological route is established by overspill resulting in constant drainage maintaining a consistent water level, or through contact with the englacial drainage system. This could result in fairly rapid drainage over a number of hours or days,

or through a dramatic and catastrophic event such as moraine or ice dam breach resulting in a potentially catastrophic GLOF. The probability of drainage through englacial drainage system therefore increases as the lake grows (Benn et al., 2001).

Many of the observations regarding the expansion of ponds have come from a combination of historical maps and satellite imagery along with *in situ* measurements covering multi-decadal time scales. As such, the development of individual small ponds amalgamating and forming one large lake can take several decades to reach full development (Watanabe et al., 1994). For example, the Imja Glacier Lake, Khumbu Himal originated as 5 small lakes in the 1950s and formed a single lake by 1975 (Watanabe et al., 1994). Similarly, glacial lake Tsho Rolpa, located between the Langtang and Everest mountain ranges has now developed into a 1.6 $km^2$ dangerous lake that began as a group of individual supraglacial ponds in the 1950s (Mool et al., 2011). In the Cordillera Blanca, Peru, this process of coalescence was observed over a period of less than 10 years (Reynolds, 2000) and highlights the ability of glacial lakes to undergo substantial expansion over relatively short periods. Watson et al. (2016) and Miles et al. (2017b) also highlight the variability of supraglacial ponds over seasonal and interannual timescales, partially relating to the monsoon in the Himalaya, yet ~40% of ponds exist for multiple years. Therefore, although some lakes may take decades to develop into a large potentially hazardous supraglacial lakes, even relatively short monitoring periods provide essential information regarding locality and persistence to aid our understanding of the processes and influences on glacier behaviour.

### 2.5.2. Ice cliffs

Ice cliffs are areas of exposed ice that serve as a further source of enhanced ablation in addition to supraglacial ponds and, therefore, also require monitoring and further assessment to understand their role in glacier-scale ablation dynamics. Ice cliffs have often been identified in association with ponds and lakes suggesting they play an important role early in the phases of debris-covered glacier evolution (Sakai et al., 1998; Richardson and Reynolds, 2000; Immerzeel et al., 2014; Miles et al., 2016). As supraglacial ponds and lakes evolve, the sides have been observed to steepen, gradually forming ice cliffs surrounding the lake, enhanced by patchy debris cover and differential ablation (Diolaiuti et al., 2005).

#### 2.5.2.1. Ice cliff formation and evolution

Debris slope slumping, sliding of debris from steep slopes, calving and englacial conduit collapse are considered to play important roles in ice cliff formation (Kirkbride, 1993; Benn et al., 2001, 2012; Reid and Brock, 2014), yet ice cliff genesis and understanding of the processes remain limited (Mölg et al., 2020). Mölg et al. (2020) identified that three quarters of all ice cliffs over a period of 140 years on the Zmuttgletscher, Switzerland, were located in a region of erosional features resulting from meltwater stream incision. The remaining cliffs were linked to running water and incision from

supraglacial streams leading to the development of high relief zones (Figure 2.8). Such zones were then enlarged through ice cliff backwasting. Reid and Brock (2014) identified three sets of processes for the formation of bare ice cliffs categorised into M-type, C-type and H-type cliffs. M-type cliffs form with steep slopes at either the glacier margin or sides of medial moraines; C-type cliffs form from the opening of crevasses, and H-type cliffs, or hydrological cliffs, are caused by the thermal erosion and subsequent calving of the side-walls, or roof collapse of englacial conduits. They proposed that the evolution of such ice cliffs are related to the initial slope and aspect of the surrounding topography, ultimately controlling the incoming energy to the ice cliff and surrounding area (Reid and Brock, 2014).

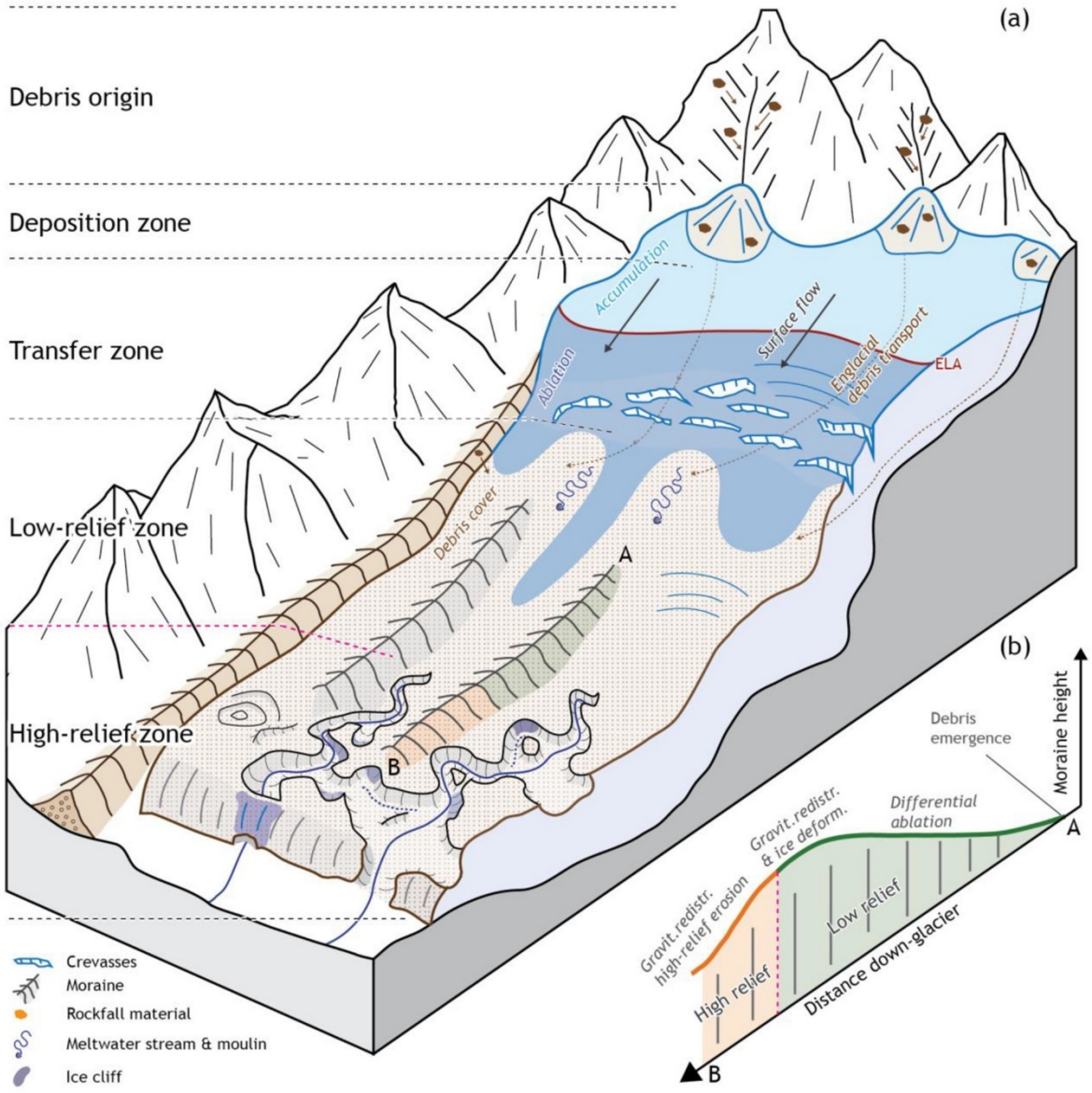


**Figure 2.8:** A**:** Main elements and succession of zones on a debris-covered glacier. B**:** Concept of medial moraine height evolution down-glacier and over time. Reprinted from Mölg et al. (2020) with permission from Elsevier.

Multiple studies conducted in the northern hemisphere have concluded that ice cliffs facing in a predominantly northerly direction persist for longer whereas south facing cliffs melt out much faster (Sakai et al., 2002; Reid and Brock, 2014; Buri et al., 2016b). South facing cliffs receive more shortwave radiation at the top of the cliff as the bottom is typically shaded. North facing cliffs, however, receive less shortwave radiation and more longwave radiation at the base of the cliff resulting in generally larger, steeper and typically debris free north facing cliffs that are generally longer lived (Sakai et al., 2002). Sakai et al. (2002) classified the ice cliffs on the Lirung Glacier into four categories: decayed, temporary, developed, and stable based on their evolution during the observation period. Similarly, they concluded that southeast facing ice cliffs were inherently unstable in comparison to north-facing cliffs. Steiner et al. (2015) further suggested that increased melt observed on sloping cliffs could be a result of a number of factors; the low albedo of the ice cliff with fine debris entrained, exposure to high levels of solar radiation, or high longwave radiation emitted from surrounding debris, including debris cones. As ice cliffs steepen and exceed a slope angle of 38 – 40° debris will no longer be supported and will slide off (Röhl, 2008; Reid and Brock, 2014), exposing bare and dirty ice altering surface albedo further enhancing ablation rates. Han et al. (2010) identified shortwave radiation as the most important heat source resulting in ice cliff ablation. Shortwave radiation accounted for approximately 76% of the total heat available for melt and was found to have stronger influences on the upper portion of the ice cliffs as lower parts were generally shaded, resulting in gently sloping ice cliffs (Sakai et al., 2002). Although individual ice cliffs have been assessed, data regarding the development and evolution of ice cliffs and the roles they have in debris-covered glacier dynamics in combination with that of supraglacial ponds are lacking. Thus, constraint on the formation mechanism and rate of evolution require further quantification to aid models of debris-covered glacier evolution.

## 2.6. Commonly used techniques to assess debris-covered glaciers

Remote sensing has been utilised routinely for glacier change studies (e.g. Nuimura et al., 2012; Berthier et al., 2014) and surface velocity assessment (Scherler et al., 2011). *In situ* data are often lacking for debris-covered glaciers due to inaccessibility and logistical issues (Bolch et al., 2012; Gardelle et al., 2013). Therefore, methods to assess glacier change in remote areas, and over wider temporal and spatial ranges are often utilised. The geodetic method, based on the differencing of multi-temporal DEMs, enables glacier-wide and region-wide data extraction of glacier mass balances in remote areas (e.g. Bamber and Rivera, 2007; Howat et al., 2014; Brun et al., 2017). Glacier change analysis tends to focus on larger areas over multiple decades, e.g. Khumbu region, Nepal (Nuimura et al., 2012); Langtang region, Nepal (Pellicciotti et al., 2015); Mont Blanc, Alps (Berthier et al., 2014). Until now there has been a lack of short-term mass balance studies to assess contemporary change. The recent increase in the number of high-resolution (<2 m) optical satellites,

with far improved repeatability and stereo data collection (e.g. WorldView, GeoEye, IKONOS, SPOT and Pleiades), has facilitated repeat multi-temporal glacier assessments (e.g. Nie et al., 2017). In particular, SPOT6/7 acquire imagery at 1.5 m panchromatic resolution, while Pleiades 1A/B operate at 0.5 m resolution, which aids the extraction of high-resolution topographic data on a repeat basis. Both sets of satellites are phased on the same orbit and are consequently capable of collecting multi-angle imagery in a single pass applicable for accurate 3D reconstructions, compared to satellites with repeat visits with 6 – 7-day gaps, which can result in reduced DEM accuracy due to elevation change occurring between the data acquisition dates.

Analysis of supraglacial ponds and ice cliffs via remote sensing requires high-resolution imagery; Watson et al. (2018a) suggested that medium-resolution data (10 – 30 m) is often still too coarse to accurately detect and map smaller ponds. Mapping is often carried out either manually (e.g. Zhang et al., 2015), through semi-automated approaches utilising multi-spectral imagery and band ratios (e.g. Huggel et al., 2002; Gardelle et al., 2011; Nie et al., 2013), or through the use of object based image analysis (OBIA) (e.g. Robson et al., 2015; Kraaijenbrink et al., 2016b) to aid classification and mapping. Mapping of ice cliffs has recently developed with the use of unmanned aerial vehicles (UAVs) and automated techniques (Immerzeel et al., 2014; Kneib et al., 2021). However, such techniques often limit the ability to assess vertical backwasting of ice cliffs and a move towards 3D mapping of ice cliffs to asses morphology and evolution has developed (e.g. Brun et al., 2016; Watson et al., 2017b).

The combination of *in situ* data to assess localised processes and the ability to assess glacier-scale evolution through field visits and remote sensing enables a holistic approach to assess debris-covered glacier evolution. Furthermore, it enables assessment of both long-term change from historical remotely sensed data, and contemporary processes, which can be empirically detailed.

## 2.7. Research gaps

Debris-covered glacier response to climatic variability remains poorly understood because of the complex feedbacks between climate, mass balance, velocity, change in debris cover and surface features (ice cliffs and ponds) (e.g. Rowan et al., 2015; Dehecq et al., 2019). Studies that integrate observations of these elements over annual, decadal and centennial timescales, and across the full glacier extent can help to unpick some of these complexities and aid our understanding of debris-covered glacier response to climatic change in high-mountain regions.

At present there are few studies that map debris-covered glacier surfaces to assess long-term evolution and use the structural pattern to infer past dynamic behaviour including surface structures, development of debris cover, supraglacial ponds and ice cliffs over temporal scales (Goodsell et al., 2005b; Gibson et al., 2017b; Azzoni et al., 2018). Research is needed to assess

glacier surface change using historical imagery and data that can be difficult to access for remote regions. This will provide identification of long-term evolutionary processes and pre-conditions for the development of surface features.

A second research gap is the dynamics of debris-covered glaciers through assessment of glacier surface elevation change and surface velocity. Despite a wealth of research having been undertaken regarding Himalayan glacier dynamics (e.g. Pellicciotti et al., 2015; Brun et al., 2017), recent change has not been assessed in the Alps to the same extent.

Thirdly, little research has been undertaken to assess simultaneous evolution and implications to glacier-scale ablation of supraglacial ponds and ice cliffs. The majority of studies have focused on either supraglacial ponds or ice cliff contributions to melt rates and only Miles et al.(2018) has previously quantified the contribution of supraglacial ponds to glacier-scale ablation.

Moreover, a large majority of the research regarding debris-covered glaciers has been derived from HMA. Despite the increase of debris cover on alpine glaciers having been documented (e.g. Deline, 2005; Mölg et al., 2019), it has not been adequately assessed in terms of its impact on glacier evolution.

## 2.8. Summary

This review has discussed debris-covered glacier dynamics and evolution as documented in the literature. Climatic warming is expected to continue in the future and thus it is essential to assess and accurately predict glacier evolution and the impacts on runoff and water resources. Despite a recent surge of research quantifying debris-covered glacier response to climate, a number of research gaps remain, which require further constraint for inclusion in global glacier models. Specifically, this research aims to clarify some of these research gaps with respect to investigating the surface evolution, debris-covered glacier dynamics and the combined impacts of supraglacial ponds and ice cliffs at Miage Glacier, European Alps and Hinang Glacier, Nepalese Himalaya.

# Chapter 3 : Study sites

## 3.1. Introduction and rationale for study site selection

This chapter will discuss the regional settings and research that has previously been carried out on the two study glaciers and surrounding areas assessed in this thesis and will outline the rationale behind the selection of these regions. This project initially investigates debris-covered glacier dynamics at Miage Glacier in the European Alps. Miage Glacier was specifically chosen as it is the largest debris-covered glacier in the Alps, and because it exhibits supraglacial ponds, an ice-marginal lake and proglacial lakes, and ice cliffs. Furthermore, Miage Glacier is easily accessible for repeat surveys with road access enabling equipment to be carried to the study sites (Figure 3.1). Thus, a wealth of data was collected at Miage Glacier and enabled testing and improvements to be made to protocols prior to fieldwork being undertaken at the second site, Hinang Glacier.

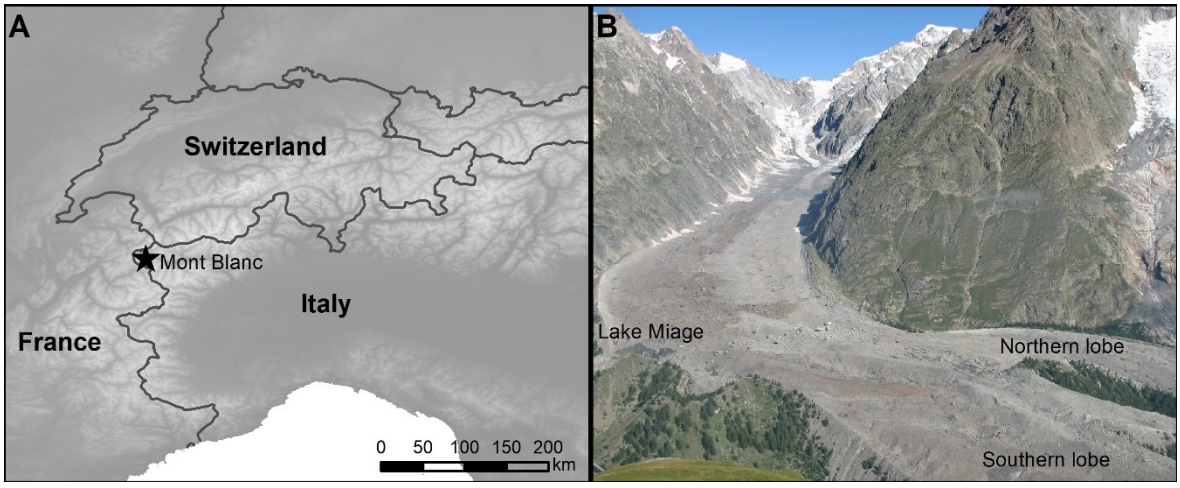


**Figure 3.1:** A: Location of the Mont Blanc massif within the European Alps with Europe DEM for background. B: Miage Glacier looking up the valley towards Bionnassay Glacier at the back, highlighting the northern and southern lobes and Lake Miage. *Photo credit*: S. Nappa, (2009).

Hinang Glacier is located in the Manaslu region of the Himalaya (Figure 3.2), a region with limited previous glaciological research. Hinang Glacier is heavily debris-covered with supraglacial ponds and ice cliffs. The glacier was more difficult to access and took six days of trekking to reach the site; therefore, the opportunity for equipment to be deployed was limited. The general character of glaciers in the European Alps and Himalaya and the specific study glaciers will now be discussed in turn.

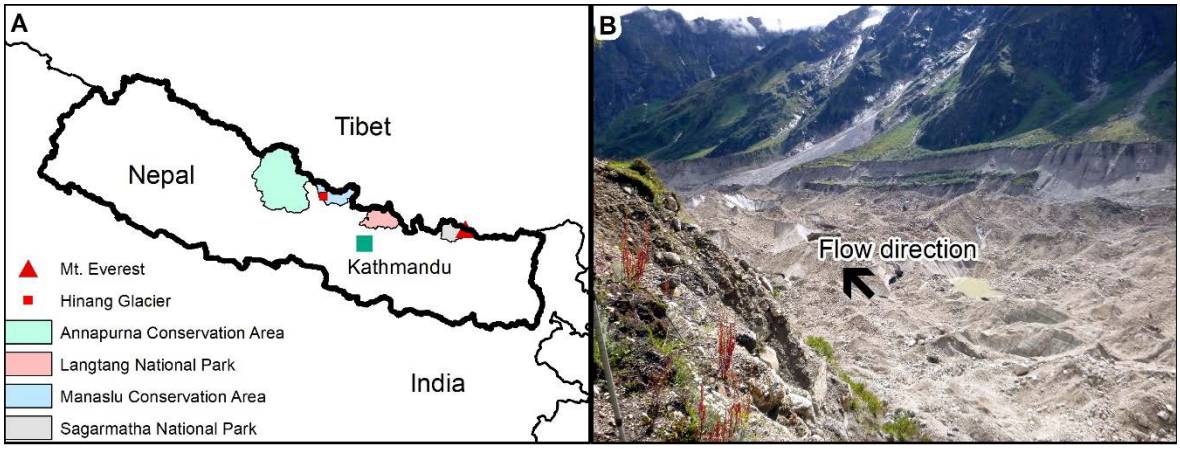


**Figure 3.2:** A: Location of Manaslu conservation area within Nepal situated between the Annapurna conservation area to the west and Langtang national park to the east. B: Hinang Glacier highlighting the undulating surface topography with numerous ice cliffs, taken September 2019.

## 3.2. European Alps

The primary location for data collection and research focus was the European Alps, which forms the focus of three data chapters (Chapters 4 – 6). The accessibility of the region means that Alpine glaciers are well studied, yet there are still numerous research gaps in the literature regarding the evolution of debris-covered glaciers as previously discussed (Section 2.7. Research gaps).

### 3.2.1. Regional and climatic setting

The European Alps mountain range extends 1,200 km from France in the west to Slovenia in the east, across eight countries. The highest peak, Mont Blanc/Monte Bianco, reaches 4809 m on the French–Italian border. The location of the Alps, situated across the centre of the continent with a large range in elevation, means that the climate is highly variable across the range and predominantly influenced by topography. Since the end of the nineteenth century, temperatures in the European Alps have increased by *c.*2°C, more than twice that of the average warming in the northern hemisphere (European Environment Agency, 2009). Temperatures have continued to increase since the 1990s by +1.46°C over the 30–year period, consistent with a negligible increase in snowfall (Figure 3.3). This has driven an increase in the rate of glacier mass loss (Vincent et al., 2017). The European Alps has a total of 2089 $km^2$ of glacierised area (derived from RGI6.0), much of which has been closely monitored by various programmes such as the World Glacier Monitoring Service (WGMS).

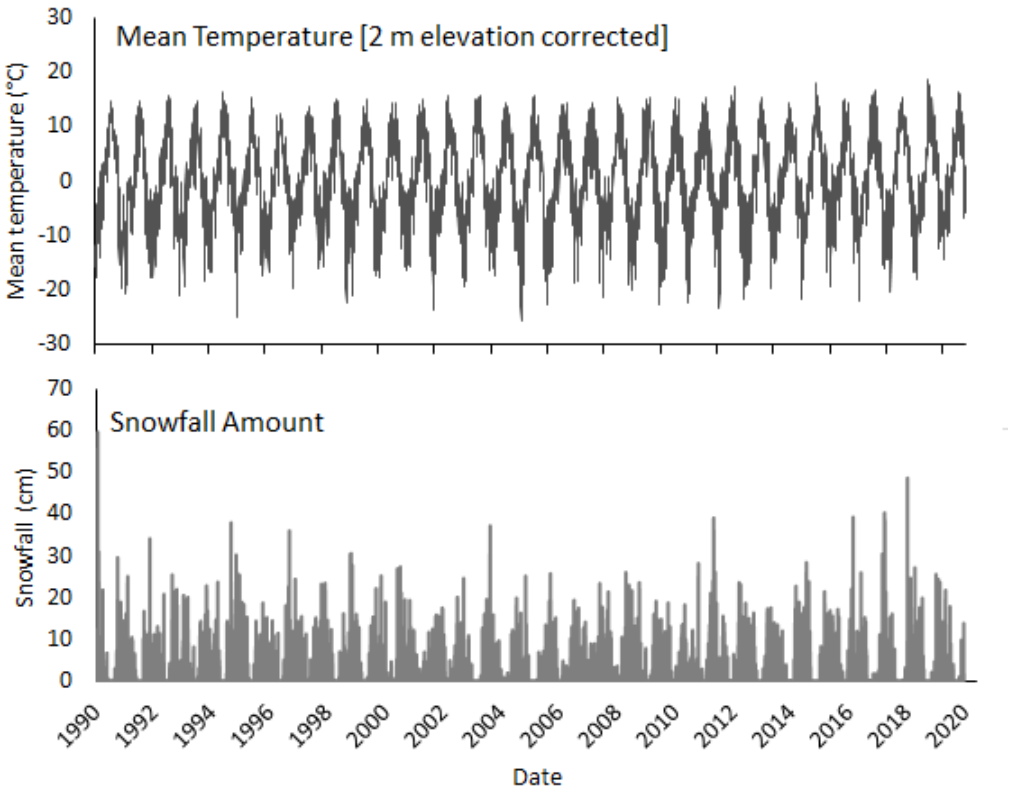


**Figure 3.3:** ERA5 climate data for Miage Glacier from 1990 – 2020 showing daily average temperature (top), and amount of snowfall (bottom). Data from www.meteoblue.com, (Hersbach et al., 2018).

### 3.2.2. Mont Blanc massif

The Mont Blanc massif is one of the most heavily glacierised areas within the European Alps (Deline et al., 2012). Data from the RGI6.0 Sentinel-2 analysis (RGI Consortium, 2017; Scherler et al., 2018) indicates supraglacial debris cover in the European Alps comprises ~28 % of the total glacierised area, of which 28 % is located within the Mont Blanc massif (Figure 3.4). Miage Glacier represents 9.7% of the debris-covered area within the Mont Blanc massif. In comparison to other Alpine massifs, glacier margins in the Mont Blanc region have undergone increased retreat in the last four decades with enhanced retreat during the 2000s coinciding with increased supraglacial debris cover brought about by increased rockfall frequency (Deline et al., 2012). With increasing debris cover (Deline, 2005), glacial lakes including supraglacial ponds are likely to become increasingly important for both ablation and water storage in the Alps (Gobiet et al., 2014). The debris-covered Miage Glacier is unusual in terms of its 'Himalayan-type' development in the Alps and is therefore, a key site to study the evolution of debris-covered glaciers with the presence of glacial lakes in a relatively accessible region in comparison to the Manaslu glaciers.

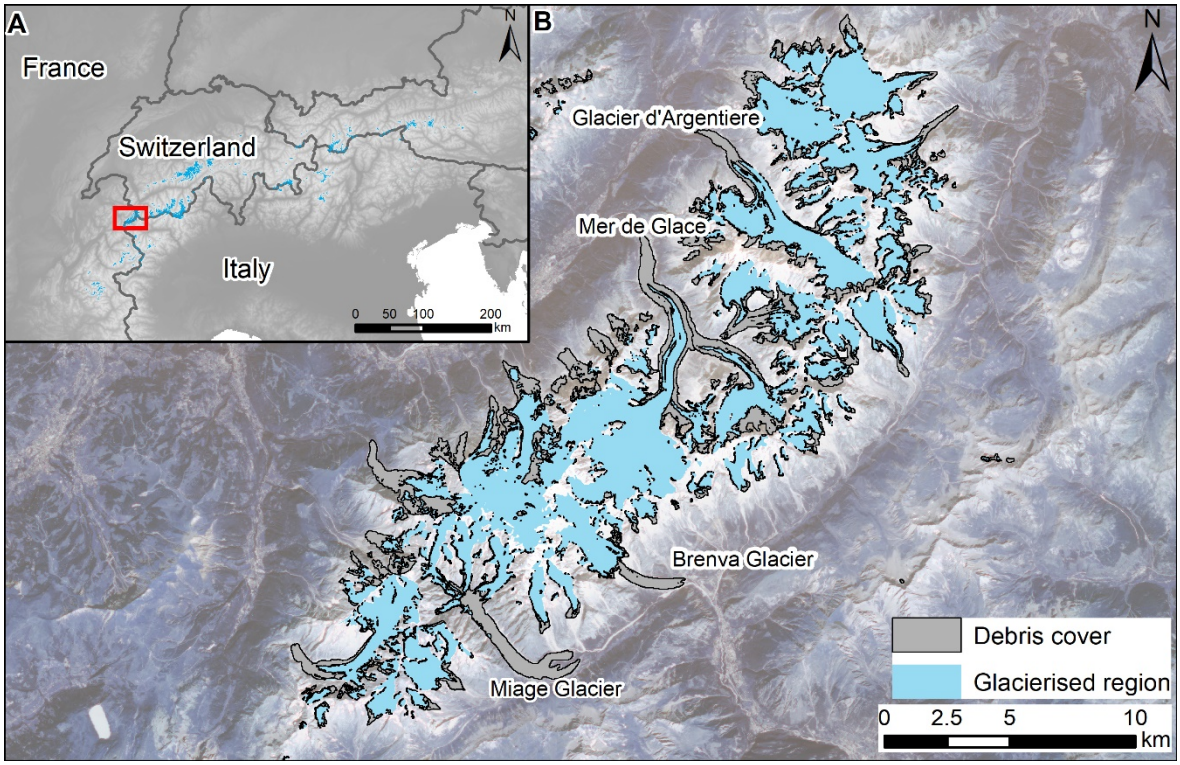


**Figure 3.4:** A: Glacierised regions of the European Alps; red box indicates the Mont Blanc massif as shown in B. Background shows DEM of Europe. B: Glaciers of the Mont Blanc massif showing extent of debris-covered glaciers and main glaciers based on RGI6.0 data with 2018 Planet satellite imagery as background.

### 3.2.3. Miage Glacier

Miage Glacier is the largest debris-covered glaciers in the Alps and lies to the southwest side of Mont Blanc (334170 E, 5077677 N UTM 32N) in the Italian Alps (Figure 3.5) constituting a ~5 km long debris-covered tongue, with an overall area of 11 km$^2$, and debris cover extending from an elevation of ~2400 m down to ~1775 m (Mihalcea et al., 2008; Shaw et al., 2016). The glacier is fed from four steep tributaries including the Mont Blanc Glacier (~2420 – 4100 m), Dome Glacier (~2500 – 3900 m), Bionnassay Glacier (~2800 – 3900 m) and Tête Carrée Glacier (~2500 – 3000 m) (Shaw et al., 2016) in addition to multiple smaller glaciers, including Glacier du Col Infranchissable, Col du Miage, Dômes de Miage and Aiguilles de Tré-la-tête. The glacier flows southeast within the confines of the valley and enters Val Veny where it bends around *c.*90°and flows north-eastwards where it splits into multiple lobes (Shaw et al., 2016). Thomson et al. (2000) noted the gentle slope of the glacier tongue with a gradient of ~5° covering a deeply incised trough. The glacier snout divides into three terminal lobes; the northern, central and southern lobes, covered in debris arising from two medial moraines transporting debris to the snout with a steeper slope (~11°). Ice thickness derived by the RGI6.0 analysis (Farinotti et al., 2019) shows the thickest ice (~193 m) is located in the central valley section of the glacier with thinner ice located in the terminal lobes (Figure 3.6). Runoff from Miage Glacier flows into the Dora di Veny river, which joins the Po river and is the longest river in Italy.

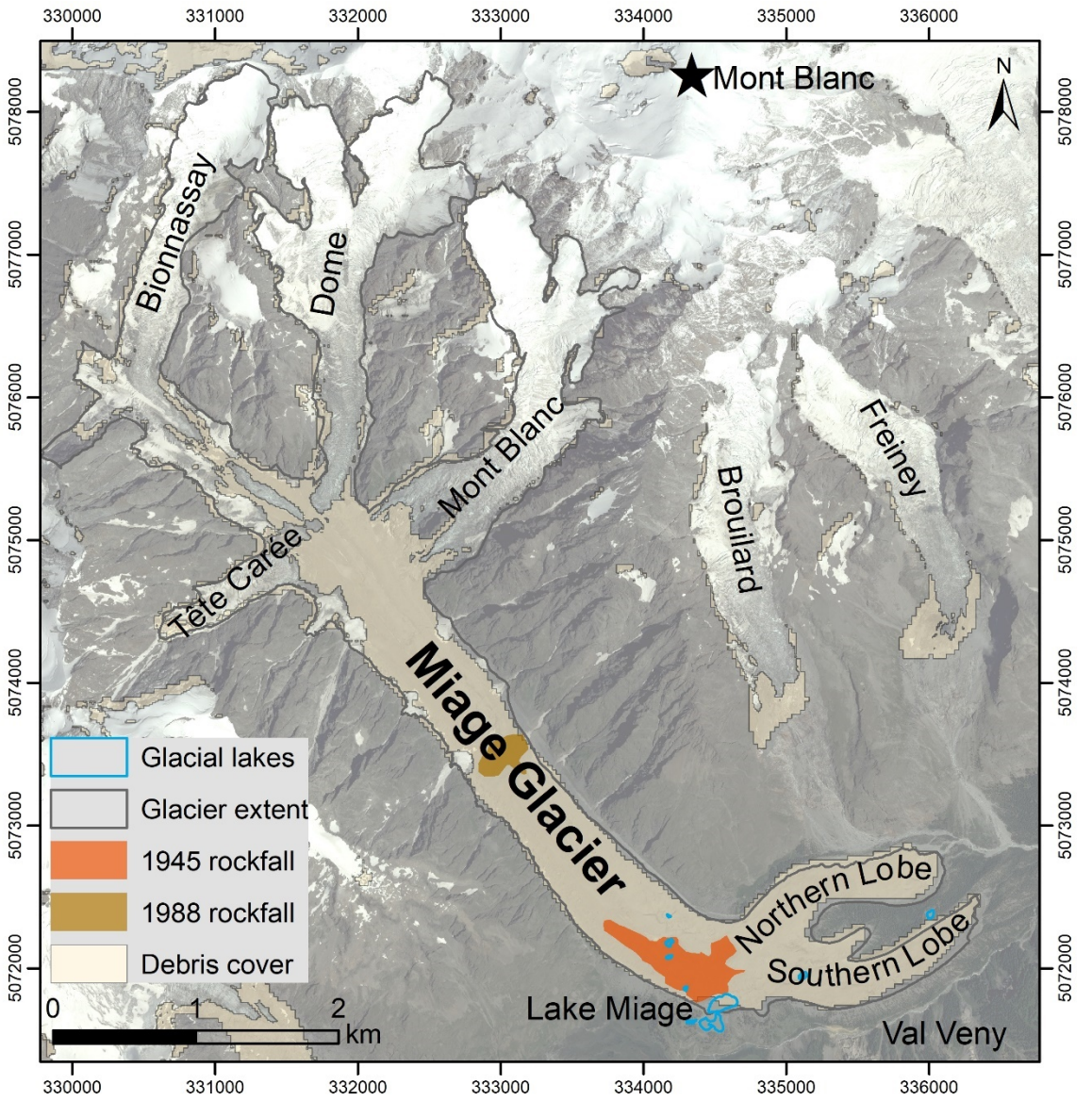


**Figure 3.5:** Location of Miage Glacier and tributary glaciers located on the southwest flank of Mont Blanc in the Italian Alps and debris cover from the RGI6.0 Sentinel analysis (Scherler et al., 2018) with deposits from rockfall events in 1945 and 1988 and the 2015 TerraItaly orthophoto as background. Projection in UTM Zone 32N.

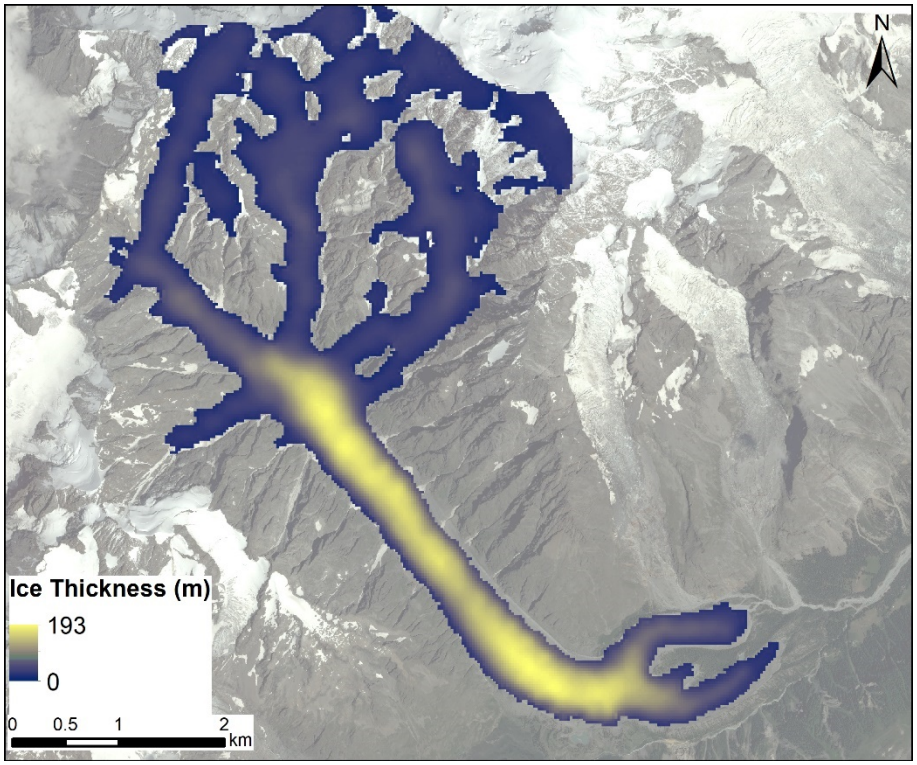


**Figure 3.6:** Ice thickness of Miage Glacier as derived from the RGI6.0 data (Farinotti et al., 2019). Background consists of Planet data, 2018.

The steep mountain sides surrounding Miage Glacier permit frequent rockfall and avalanche events, delivering debris directly to the glacier surface, which over time becomes concentrated on the lower ablation area. Shaw et al. (2016) classified the glacier as having ~4.5 $km^2$ of continuous debris cover with 4.6 $km^2$ of 'clean' ice. The angular, coarse debris varies in thickness from an average of 5 – 20 cm on the glacier tongue to more than 1 m thick ~0.5 km upglacier from the terminal lobes, consisting of gneiss, schist and granite (Thomson et al., 2000; Shaw et al., 2016). Deline (2005) suggests that the presence of the thick debris cover since the Little Ice Age (LIA) termination corresponds with Kirkbride's (2000) model, where periods of positive mass balance and faster ice flow transfer debris to the terminal lobes ('transport-dominant'), whereas negative mass balance and slower flow aid enhanced ablation ('ablation dominant') and promotes the debris cover to extend upglacier. The LIA, therefore, aided debris cover expansion in the Mont Blanc massif with an initial transport-dominant period followed by an ablation-dominant period after 1820. Limited debris cover was noted in the frontal area until the 1840s and developed into a continuous cover during the LIA (Deline, 2005). Deline (2005) identified six stages in which the continuous debris cover seen today developed, starting with discontinuous cover in the frontal region during the last decades of the LIA, 1860 – 1880. Between 1880 and 1930 the debris cover is thought to have developed into the continuous coverage seen today (Figure 3.7).

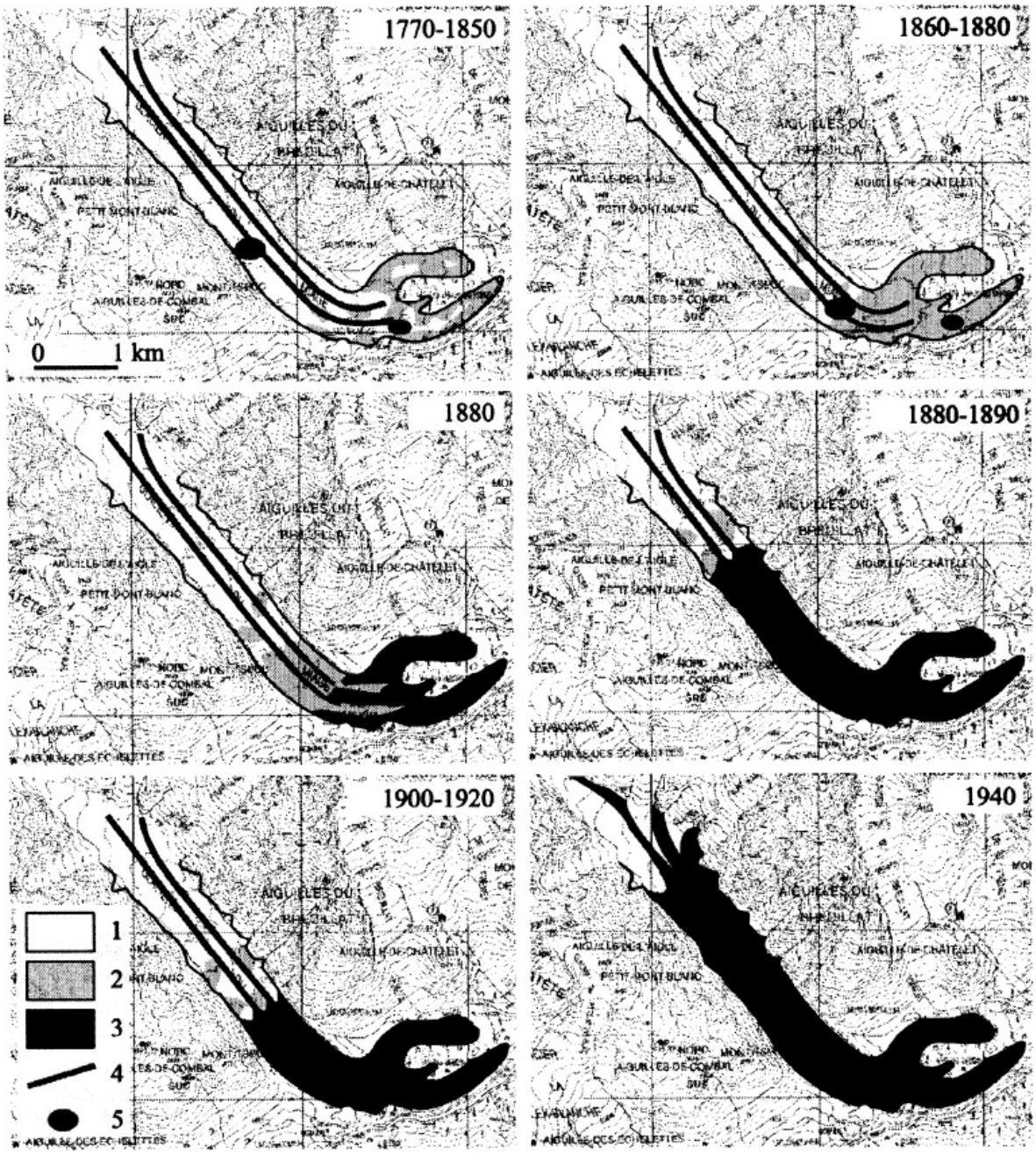


**Figure 3.7:** The six stages of debris cover development since 1770. Key: (1) 'clean' ice, (2) discontinuous debris, (3) continuous debris cover, (4) medial moraine, (5) local rock-avalanche deposit. Reprinted from Deline (2005) with permission from Sage.

The near-continuous debris cover, which developed after the LIA termination, has had a profound impact on glacier evolution (Deline, 2005). Previous mass balance studies of the Mont Blanc region identified a strongly negative trend ($-1.04 \pm 0.23$ m w.e. $a^{-1}$) based on SPOT5 and Pleiades high-resolution DEMs from 2003 to 2012 (Berthier et al., 2014). The rate of mass loss between 2003 – 2012 at Miage Glacier was found to be 19% lower ($-0.84 \pm 0.22$ m w.e. $a^{-1}$.) than the Mont Blanc regional average; this average value includes data from predominantly clean-ice glaciers, such as the Tre-la-téte, which experienced higher rates of mass loss ($-1.34 \pm 0.22$ m w.e. $a^{-1}$; Berthier et al., 2014).

Previous analysis of change by Thomson et al. (2000) based on cartographic and topographic surveys between 1913 and 1999 illustrated a striking complexity of glacier evolution over space and time. Miage Glacier was found to have thickened overall between 1913 and 1957, equivalent to +0.14 m $a^{-1}$ over the 44-year period, with thickening especially evident on the terminal lobes. From 1957 to 1967, the glacier thinned by −0.38 m $a^{-1}$. However, changes across the glacier were heterogeneous with most loss over the valley trunk section of the glacier, but a 20 m elevation increase of the north terminal lobe. From 1967 to 1975, the terminal lobes then lost over 20 m in thickness, but widespread thickening of the valley tongue meant that, overall, the glacier thickened on average by +0.23 m $a^{-1}$. Further overall thickening of 1 m, or +0.04 m $a^{-1}$, occurred between 1975 and 1999, but this time with the thickening focussed on the terminal lobes, whereas decreasing thickness was observed further up-glacier. Diolaiuti et al. (2009) also identified a period of positive mass gain between 1975 and 1991, which was followed by a period of substantial mass loss between 1991 and 2003. However, the presence of glacial lakes or ice cliffs were not reported within either of these previous studies and may have an important, yet under-appreciated, role in influencing the mass balance.

Further studies have investigated meteorological influences with regard to debris cover. Mihalcea et al. (2007) found strong, positive correlation between surface temperature and debris thickness over areas of continuous debris. Weaker correlations were found on partially debris-covered ice, including regions of ice cliffs and crevasses highlighting the influence of varying thicknesses of debris cover on surface temperature. However, Shaw et al. (2016) found that air temperature was also highly dependent on elevation, although local temperature depressions occurred in relation to areas of thin or patchy debris cover. Reid and Brock (2014) found that ice cliffs on Miage Glacier accounted for only 1% of the debris covered area but 7.4% of the total ablation. They concluded that cliff slope and albedo was more important for ablation than enhanced longwave incidence or reduced turbulent fluxes derived from point-based models of five ice cliffs.

A large ice-marginal lake, known as Lake Miage, is located on the south-western margin of the glacier as it bends and flows into Val Veny (Figure 3.5, Figure 3.8). Lake Miage has been the focus of a number of studies at the glacier (e.g. Deline et al., 2004; Conforti et al., 2005; Diolaiuti et al., 2005; Masetti et al., 2010). The lake can be observed in early aerial imagery from 1936. A bathymetric survey of Lake Miage in 2003 observed little change in water depth since 1953 and indicated that the lake had two basins separated by a submerged moraine adjacent to an ice cliff up to 35 m in height above the water surface (Diolaiuti et al., 2005).

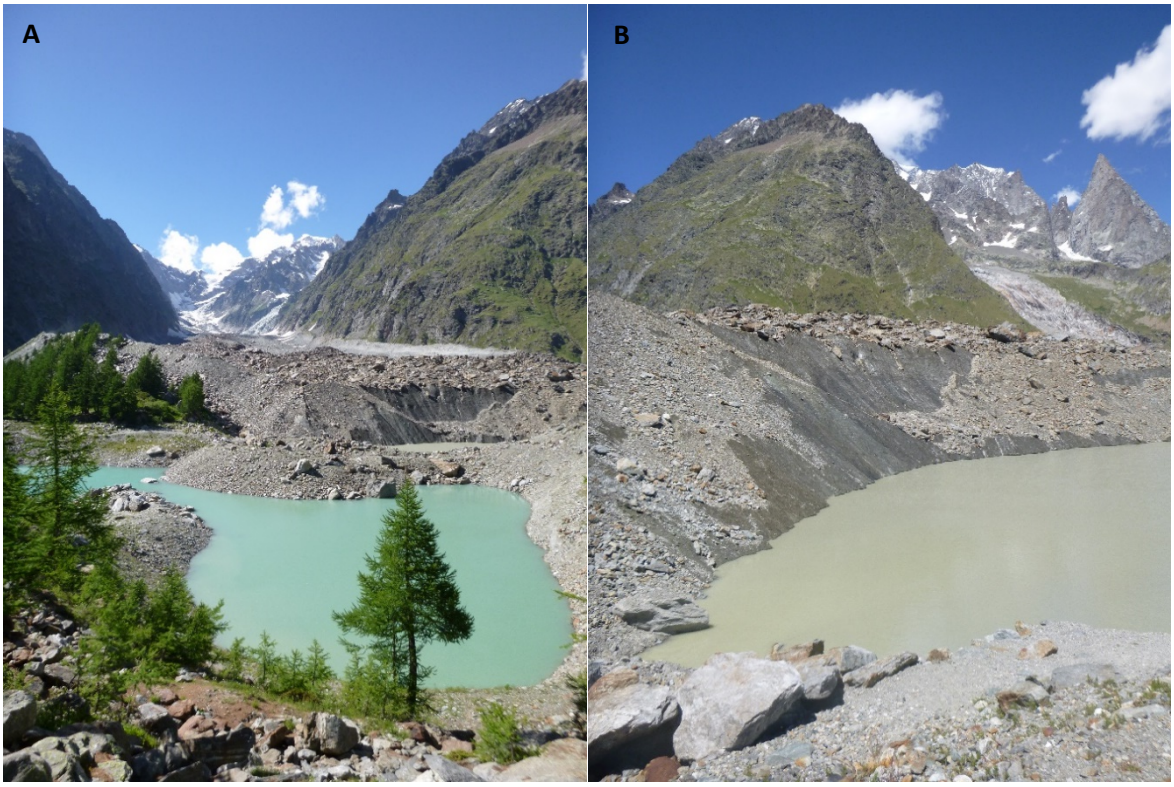


**Figure 3.8:** A: View upglacier with the proglacial lake in the foreground and Lake Miage behind in July 2017. B: View east over Lake Miage.

A lake drainage event in September 2004 demonstrated that the bathymetry of the drained lake bed was different to that previously detected. It had a smoother topography than the undulating and peaky morphology indicated by the earlier bathymetric survey (Masetti et al., 2010). The lake has been recorded to have naturally drained at least 16 times during the twentieth century (Figure 3.9) with the last reported event occurring in 2018 (Stefaniak et al., 2021). However, none of these drainage events were catastrophic flood events, as the lake drained gradually over a period of a few days under the glacier tongue, attributed to the enlargement of crevasses (Deline et al., 2004). Additional analysis of the ice cliffs surrounding Lake Miage by Diolaiuti et al. (2005) identified four distinct zones of calving on the predominantly south-facing cliff. The development of deep melt notches at the waterline at the eastern end were considered the primary cause of calving. However, at the western part, calving events were initiated by the opening of cliff top crevasses, which propagate and result in toppling failure. They suggested differential ablation across the ice cliff surface created an irregular ice cliff geometry resulting in these distinct calving zones.

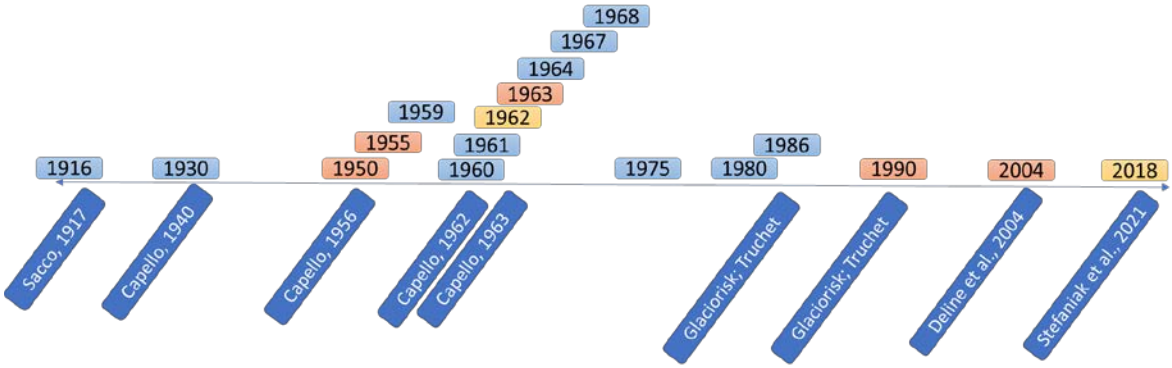


**Figure 3.9:** Timeline of drainage events classified as per information from previous studies. Red – complete drainage, Yellow – partial drainage resulting in multiple basins, Blue – no information on level of drainage provided.

Analysis of the hydrological system by Fyffe et al. (2019) demonstrated that the thick supraglacial debris cover on the lower glacier resulted in smaller supraglacial streams, lower dye trace velocities and lower dye recovery rates compared to those further upglacier where debris cover is thinner. This resulted in a less efficient subglacial drainage network on the lower, continuously debris-covered region. Upglacier, within the confined valley section, fast, efficient moulins and associated drainage networks are present (Fyffe et al., 2019). The formation of one moulin located at ~2340 m elevation was observed to have developed from the drainage of a supraglacial pond, highlighting the influence of pond development and drainage on hydrological networks (Fyffe et al., 2019). It is therefore expected that supraglacial ponds are more likely to develop in the down-glacier reaches of the glacier where thicker debris cover is present, resulting in a less efficient drainage system.

The presence of a continuous debris cover since the LIA has therefore altered the glacier response to ongoing climatic change. The resulting shape and morphology of Miage Glacier has often been compared to the large debris-covered glaciers seen in the Himalaya (Diolaiuti et al., 2009). The selection of Miage Glacier as a study site enabled a multi-annual approach with multiple visits to assess ongoing processes of debris-covered glaciers and supraglacial pond development. Miage Glacier has been the subject of a wide range of glaciological studies including mass balance (Smiraglia et al., 2000; Thomson et al., 2000; Berthier et al., 2014), surface energy balance (Reid and Brock, 2010; Fyffe et al., 2014), near surface meteorology (Brock et al., 2010; Shaw et al., 2016), hydrology (Fyffe et al., 2019), debris evolution (Deline, 2005; Stewart et al., 2021), variable ablation patterns and debris redistribution (Fyffe et al., 2020), geomorphological evolution (Westoby et al., 2020), mass loss processes including ice cliffs (Diolaiuti et al., 2005; Reid and Brock, 2014), and the presence of glacial lakes and associated processes (Tinti et al., 1999; Diolaiuti et al., 2005, 2006). However, comparatively little research has been undertaken on the glacier dynamics at Miage Glacier in the last decade with limited documentation of supraglacial pond and ice cliff presence. The wealth of pre-existing research on Miage Glacier indicates how important this example is for

studying debris-covered glacier dynamics in response to the changing climate and enables a comprehensive understanding of glacier dynamics. To aid this research, field visits were undertaken to Miage Glacier in June – July 2017 and 2018.

## 3.3. Himalaya

The second study site for this project was located in the Manaslu region of the Nepalese Himalaya. The Himalaya represent the largest concentration of glacier ice outside of the poles and has gained the name 'the third pole' (Qiu, 2008; Yao et al., 2012a). Debris-covered glaciers only equate to 17% of the total glacierised region in the Himalaya as derived from the RGI6.0 data (Scherler et al., 2018) (Figure 3.10). However, the increasing abundance of glacial lakes and ice cliffs observed across the range (Nie et al., 2013) highlight the potential impacts on water resources, which >1.9 billion people rely on (Immerzeel et al., 2019).

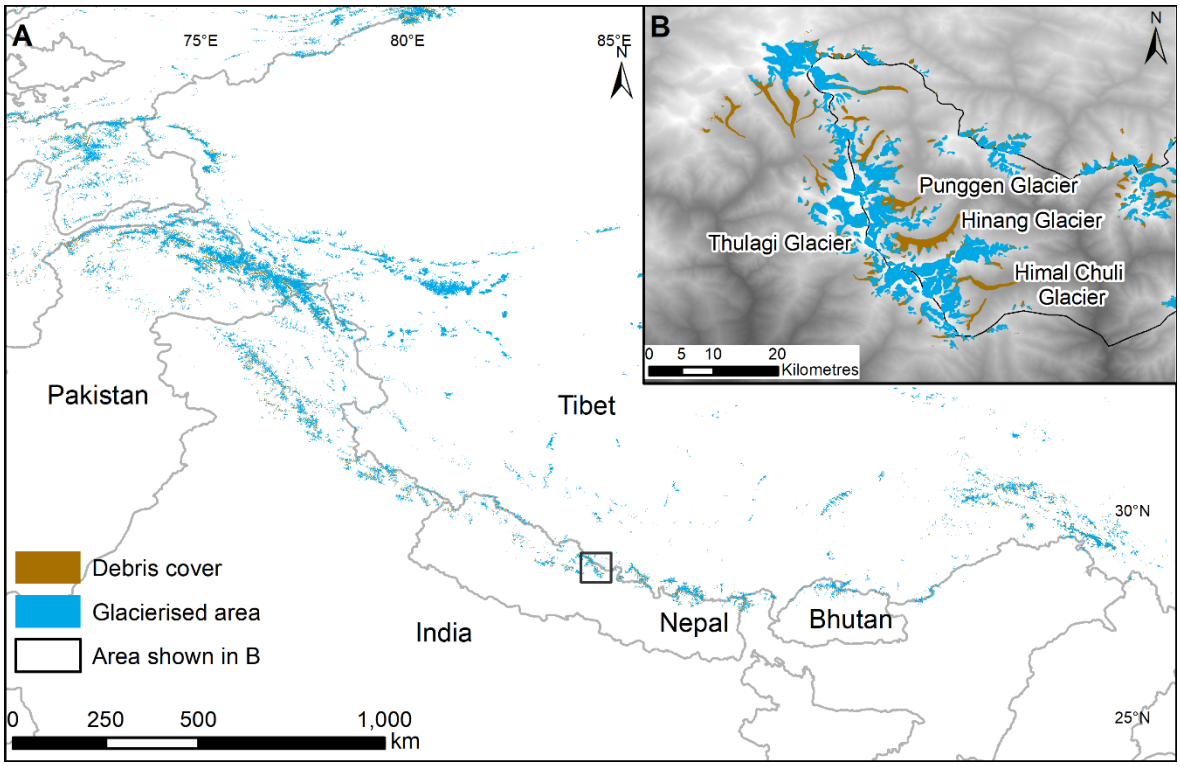


**Figure 3.10:** A: Glaciers and debris cover across the Himalaya based on the RGI6.0 datasets, boxed area refers to the Manaslu conservation area as shown in B**.** B: Glaciers and debris cover in the Manaslu region (shown by black outline) with glaciers of interest noted. Background shows DEM for Manaslu region, Nepal.

### 3.3.1. Regional and climatic setting

The Himalayan range extends for ~2,400 km within the Hindu Kush-Himalayan mountain range. This extends from Afghanistan in the west across 3,500 km to Myanmar in the east and includes the world's highest mountains in excess of 7,000 m (Rana, 2003; Mool et al., 2011). As such, the

mountains act as the headwaters of 10 of the largest rivers in Asia providing >1.9 billion people with water (Immerzeel et al., 2019).

The central and eastern Himalayan climate is dominated by the South Asian summer monsoon and mid-latitude westerlies, which changes to a south-easterly direction during the monsoon (Bookhagen and Burbank, 2010; Immerzeel et al., 2010). Summer monsoon precipitation between June and September results in many glaciers in the region being of 'summer accumulation type' (Bookhagen and Burbank, 2010; Bolch et al., 2012). Despite this, positive temperatures during the summer months result in concurrent mass loss (Bolch et al., 2012). Temperatures in the Manaslu region have increased by +0.45°C since 1990 (Figure 3.11).

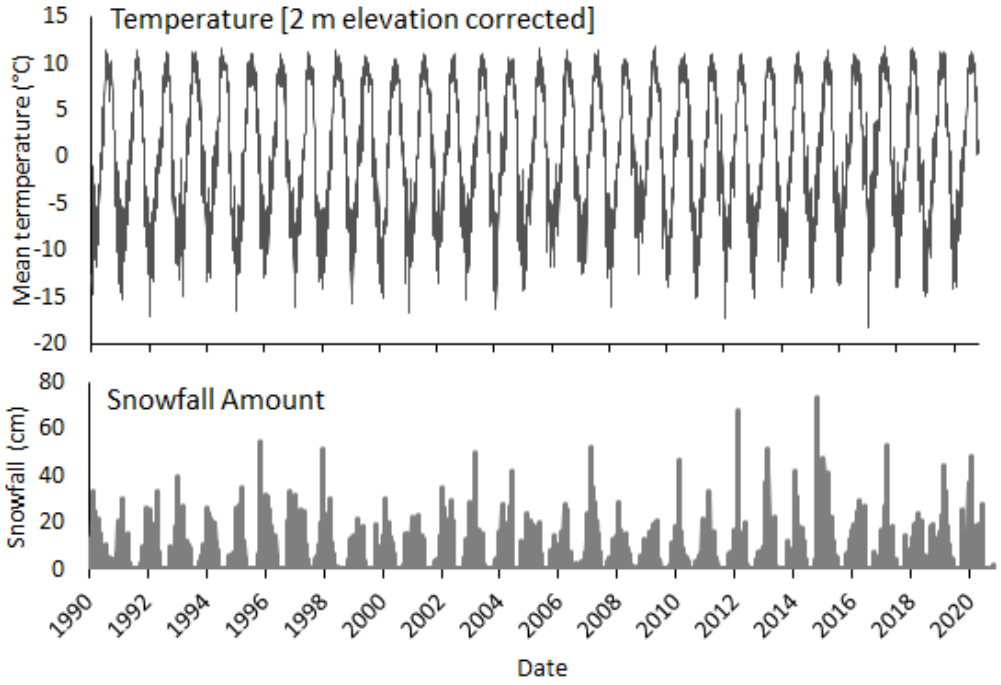


**Figure 3.11:** ERA5 climate data for Hinang Glacier from 1990 – 2020 showing daily average temperature (top), and amount of snowfall (bottom). Note heavy snowfall in 2015. Data from www.meteoblue.com.

The most recent advance in glacier extent across the Himalaya was associated with the LIA (*c.*1300 – 1850) (Rowan, 2017). Since then, glaciers have largely been in a state of retreat with the exception of the Karakoram anomaly and variations between clean-ice glaciers and debris-covered glaciers (Gardelle et al., 2012, 2013; Pellicciotti et al., 2015). The rate of retreat has now exceeded that which can be attributed to the monsoon variability (Mölg et al., 2014). An erroneous report published by the IPCC (2007) reported that Himalayan glaciers could disappear by 2035, rather than the correct date, which should have read as 2350. Although this has since been widely refuted (Cogley et al., 2010; Cogley, 2011), it exposed major gaps in our understanding of glacier dynamics in this region (Bolch et al., 2012). This inaccuracy fuelled a surge in Himalayan glacier research with

a strong focus on debris-covered glaciers and has highlighted a number of gaps in the current research, which have since instigated a wealth of recent studies on the heavily debris-covered glaciers of HMA (e.g. Brun et al., 2017; Dehecq et al., 2019). Despite this, complexities of debris-covered glacier dynamics mean that future glacier response in this region is highly variable with rates of glacier disappearance and volume reduction ranging from 10% of Khumbu Glacier (Rowan et al., 2015), to 75% reduction in Langtang catchment by 2088 (Immerzeel et al., 2012) and up to 83.7% by 2100 in the Dudh Kosi basin depending on various emission scenarios (Shea et al., 2015).

### 3.3.2. Manaslu region

The Manaslu conservation area hosts a number of large, heavily debris-covered glaciers with supraglacial ponds and sits to the west of Kathmandu and both the Khumbu Himal region and Langtang Valley (Figure 3.2) where a wealth of data observing debris-covered glaciers and supraglacial ponds has been obtained in recent years (Benn et al., 2001; Pellicciotti et al., 2015; Rowan et al., 2015; Miles et al., 2016). In comparison, the Manaslu region has been widely neglected in terms of research with the exception of Thulagi Glacier located on the western side of Manaslu, just outside the conservation area, which terminates in the moraine-dammed Thulagi Lake, also known locally as Dona Lake, which has grown to ~0.9 $km^2$. Thulagi Lake is considered to be one of the most potentially dangerous glacial lakes in the Himalaya (Mool et al., 2011; Haritashya et al., 2018).

The Manaslu region holds ~788 $km^2$ glaciers, which are typically between 0.5 – 1 km in width and 5 – 15 km in length, with elevation ranges typically between 3000 to >7000 m a.s.l. (Robson et al., 2015). The glaciers in this region experience the humid, monsoon-driven accumulation predominantly in the summer. Over half (52%) of the glaciers in the Manaslu region experienced an increase in debris cover between 2001 and 2013 (Robson et al., 2018). The eastern side of the Manaslu conservation area is located within the Gorkha district, which was hit by a large earthquake in 2015 (Kargel et al., 2016) and evidence is abundant along the Manaslu trekking circuit, including evidence of landslide activity.

### 3.3.3. Hinang Glacier

Glaciers of the Manaslu region, including Hinang Glacier (Figure 3.12), have only been researched within a study regarding glacier change in the Manaslu region by Robson et al. (Robson et al., 2015, 2018). This glacier will provide a comparison to Miage Glacier to explore local and generic debris-covered glacier dynamics and evolution.

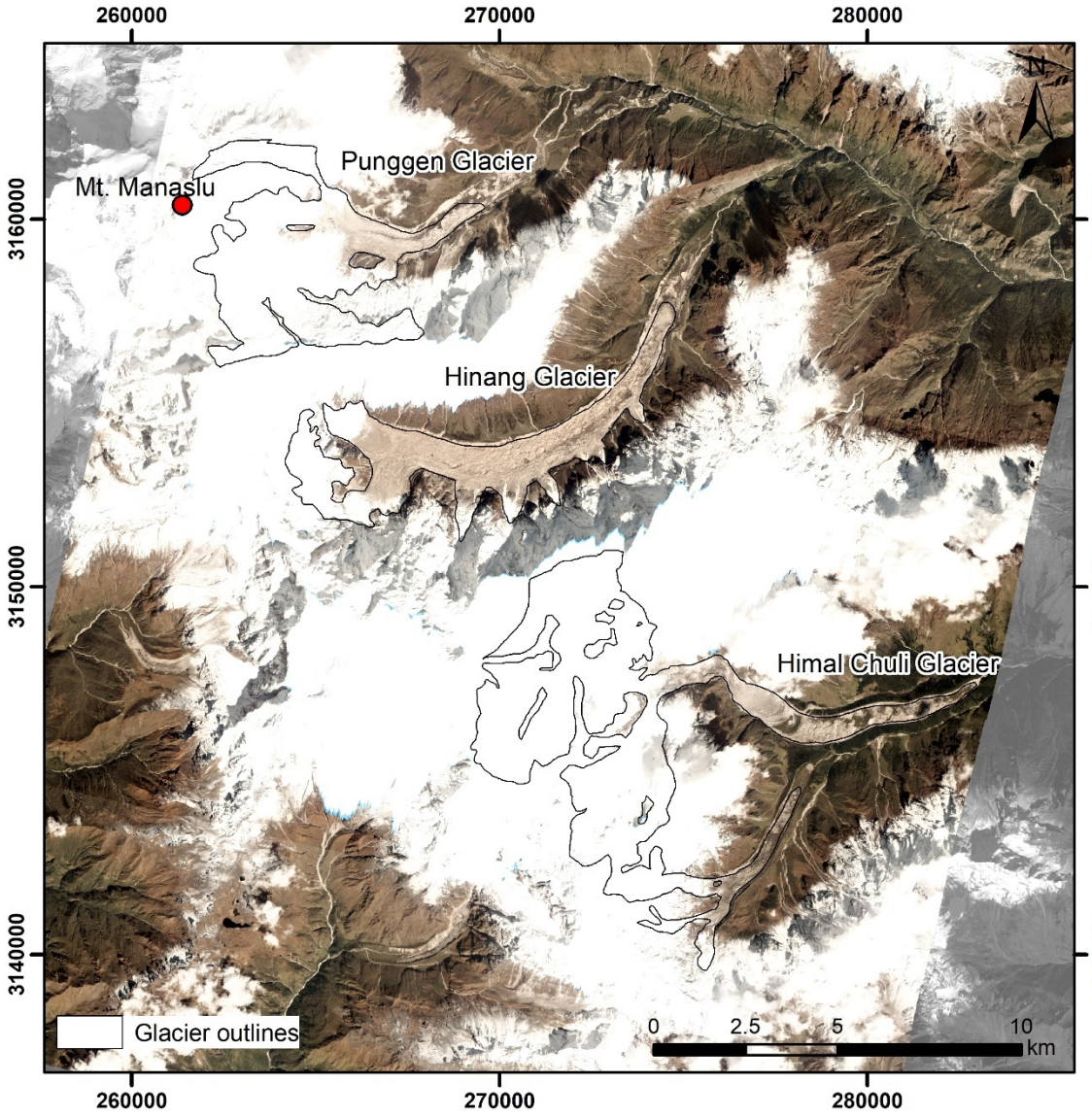


**Figure 3.12:** Glaciers on the eastern side of Manaslu including Punggen Glacier, Hinang Glacier and Himal Chuli Glacier. Background shows Planet data from October 2019.

Hinang Glacier (also referred to as Lanjam Glacier in the RGI/GLIMs inventory) is located to the east of Mount Manaslu, the eighth highest mountain in the Nepalese Himalaya (Figure 3.12) and flows southeast from Manaslu mountain passing through a narrow valley (Robson et al., 2018). Mount Manaslu lies ~230 km west of Mount Everest and exhibits an area with both clean and debris-covered glaciers. Hinang Glacier is located between ~3350 m to 4600 m a.s.l. and is ~12 km long and ~1 km wide, with a maximum ice thickness of ~276 m as derived from the RGI6.0 analysis (Farinotti et al., 2019) (Figure 3.13). Hinang Glacier is a debris-covered glacier with evidence of supraglacial ponds (Figure 3.14 A). Previous research by Robson et al. (2018) on Hinang Glacier showed signs of frontal retreat between 1999 and 2013 along with the northerly lying Punggen Glacier, also referred to Punggeon Glacier by Robson et al. (2018). The spelling used here follows that published on the Himalayan Map House Manaslu and Tsum Valley map. The terminus of Hinang

Glacier underwent substantial stagnation although much of the upper glacier is comparatively active. Runoff from Hinang Glacier flows into the Budhi Gandaki river (Figure 3.14 B), which joins the Trisuli river followed by the Gandak river before becoming a tributary of the river Ganges and is therefore also important to consider for water resource management. The location of Hinang Glacier located in the Manaslu region has therefore been selected to provide significant insight regarding glacier response to climatic change across the Himalaya, impact on potential water resources and future GLOF risk.

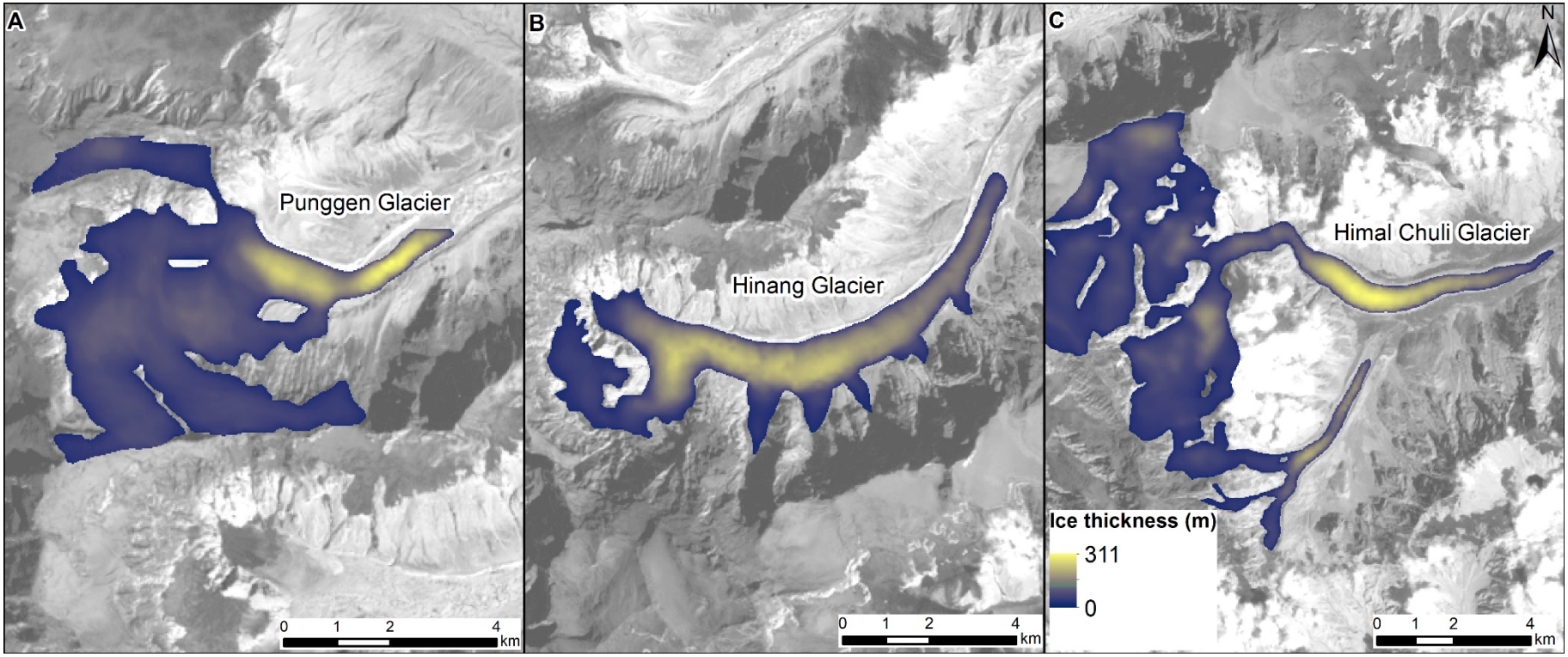


**Figure 3.13:** Ice thickness of the easterly flowing Manaslu glaciers, A: Punggen Glacier; B: Hinang Glacier; C: Himal Chuli Glacier, as derived from the RGI6.0 data. Background shows Landsat satellite data.


**Figure 3.14**: A: Hinang Glacier looking upglacier to the west with a supraglacial pond; B: The Budhi Gandaki river in the lower reaches. Photos taken in September 2019.

# Chapter 4 : Surface evolution of Miage Glacier

## 4.1. Introduction

Glacier response to climatic change is evident through surface structures, which express the stress and strain regimes within the glacier system from which historical flow regimes can be derived. Thus, past glacier dynamics can be derived using high-resolution historical aerial imagery extending our analysis beyond more recent applications using satellite imagery. Understanding the development of surface glacier features and the processes involved is required to improve predictive models of glacier evolution and future response to climatic change, especially our understanding of debris-covered glacier behaviour (Hambrey and Lawson, 2000).

Although Miage Glacier has been assessed in terms of the development of the debris cover since the LIA (Deline, 2005), no structural analysis or assessment of surface evolution has been carried out to identify past glacier dynamics and its evolution towards its current state. This component of the research contributes to the aims and objective 1 as set out in Section 1.3 to complete glacier mapping of surface features on Miage Glacier (1952 – 2018) to assess surface change, structural evolution, and flow regimes. Specifically, the objectives of this chapter are: (i) to assess surface dynamic changes of Miage Glacier over decadal time scales; and (ii) to assess the development of supraglacial ponds and ice cliffs on Miage Glacier. Analysis of surface features utilises historical aerial and satellite imagery covering a period from 1952 to 2018. In addition to the structural analysis, the surface mapping will assess glacier extent, debris extent, and surface features including ice cliff and glacial lake evolution from 1952 – 2018. This chapter will aid understanding the dynamic context of the debris-covered Miage Glacier and will form the basis for the line of questioning identified throughout Chapters 5 and 6.

## 4.2. Methods and data accuracy assessment

### 4.2.1. Data sources

Surface mapping and structural glaciological mapping was undertaken through manual digitisation of surface structures on Miage Glacier utilising satellite and aerial imagery from 1952 to 2018. Historical analysis of Miage Glacier was undertaken using aerial imagery provided by the Institut National de l'Information Géographique et Forestière (IGN) covering 1952 – 2006 and satellite images dating from 2009 to 2018 (Table 4.1). Images were restricted to the summer ablation season (July – September) where clear, 'cloud-free' images were available. Images from the same month were selected where possible to enable comparison of seasonally variable aspects of the glacier geomorphology such as supraglacial ponds and ice cliffs.

The IGN historical aerial images were mosaicked and orthorectified in Agisoft Photoscan Professional Edition with a minimum of six images and six Ground Control Points (GCPs) covering

the glacier for each time period enabling export of high-resolution orthorectified images (Evans et al., 2017; Midgley and Tonkin, 2017). The orthorectified images were exported at a resolution of 1 m for consistency with mapping and later satellite images. All images were compared to the georeferenced 2015 TerraItaly orthophoto (20 cm resolution) prior to analysis to ensure accuracy and consistency. The satellite images from 2009 – 2018 were orthorectified using the RPC models provided with the imagery and pansharpened in Erdas Imagine 2016 to improve the colour resolution to aid identification of surface features. Alignment with the 2015 TerraItaly image was visually assessed to ensure accuracy and consistency.

Structural analysis and surface mapping was undertaken aiming for one image per decade dependent upon the quality and availability of data from 1952 to 2018 (i.e. 1952, 1961, 1979, 1988, 1996, 2009, and 2018) to assess the surface evolution. Digitisation of structures was completed manually in ArcGIS for each of the georeferenced images. For each image, surface features including termini position, debris cover, ogives, crevasses, supraglacial streams, glacial lakes, and ice cliffs were manually digitised by one analyst and edited on multiple days until no further edits were required (e.g. Watson et al., 2017a). Features were identified manually based on colour differences between pixels and structure (e.g. areas of slope and exposed ice). Additional imagery was used having been mosaicked and orthorectified in Agisoft Photoscan to assess the development of glacial lakes only (Table 4.1). For 1993, 2001 and 2004 limited images were available and the overlapping coverage was inadequate for mosaicking, therefore individual images for these years were georeferenced in ArcGIS.

**Table 4.1:** Registration errors and uncertainty derived from data used. Dates in bold are those which the structural evolution and surface change was undertaken. Additional dates were for analysis of glacial lake evolution only. (NB: 1993, 2001 and 2004 georeferenced in ArcMap).

| Data | Acquisition Dates | Resolution (m) | XYZ error Agisoft (m) | Registration error (pixel) | Uncertainty (m) |
|---|---|---|---|---|---|
| IGN Historical images | **27/07/1952** | 1.00 | 1.42 | 5.00 | 2.46 |
| IGN Historical images | 31/07/1958 | 1.00 | 3.88 | 5.00 | 2.46 |
| IGN Historical images | **29/08/1961** | 1.00 | 0.67 | 5.00 | 2.46 |
| IGN Historical images | 12/10/1967 | 1.00 | 0.91 | 5.00 | 2.46 |
| IGN Historical images | **05/09/1979** | 1.00 | 1.46 | 5.00 | 2.46 |
| IGN Historical images | 26/09/1983 | 1.00 | 0.57 | 5.00 | 2.46 |
| IGN Historical images | **26/07/1988** | 1.00 | 0.65 | 5.00 | 2.46 |
| SPOT-1 | 22/07/1990 | 10.0 | - | 20.00 | 10.96 |
| IGN Historical images | 11/08/1993 | 1.32 | - | 6.60 | 2.90 |
| IGN Historical images | **31/07/1996** | 1.00 | 2.60 | 5.00 | 2.46 |
| IGN Historical images | 01/08/2000 | 1.00 | 0.86 | 5.00 | 2.46 |
| IGN Historical images | 13/08/2001 | 1.22 | - | 6.10 | 2.76 |
| IGN Historical images | 30/06/2004 | 0.63 | - | 3.15 | 1.89 |
| IGN Historical images | 01/09/2006 | 1.00 | 0.61 | 5.00 | 2.46 |
| GeoEye | **29/08/2009** | 0.49 | - | 0.98 | 1.12 |
| Planet | 15/07/2010 | 3.00 | - | 6.00 | 3.88 |
| Planet | 06/09/2011 | 3.00 | - | 6.00 | 3.88 |
| Pleiades | 19/08/2012 | 0.50 | - | 1.00 | 1.14 |
| WorldView 2 | 10/08/2013 | 0.50 | - | 1.00 | 1.14 |
| Pleiades | 02/10/2014 | 0.50 | - | 1.00 | 1.14 |
| WorldView 3 | 14/07/2015 | 0.30 | - | 0.60 | 0.85 |
| TerraItaly Orthophoto | **07/07/2015** | 0.20 | - | - | - |
| SPOT orthophoto | 12/10/2016 | 1.50 | - | 3.00 | 2.30 |
| SPOT orthophoto | 13/07/2017 | 1.50 | - | 3.00 | 2.30 |
| SPOT orthophoto | **26/08/2018** | 1.50 | - | 3.00 | 2.30 |

### 4.2.2. Glacier mapping

Structural mapping and identification of structures was based on the criteria defined by Goodsell et al. (2005b) and included identification of primary stratification, flow unit boundaries, crevasses, folds, bedrock outcrops and ogives (Goodsell et al., 2002) (see Table 2.1, Section 2.4.). Additional surface mapping of features was undertaken to include glacier extent, debris cover, supraglacial ponds, ice cliffs and supraglacial streams.

Mapping debris-covered glaciers is challenging due to the presence of debris obscuring sub-debris features, therefore mapping glacier extent and delineating surface features increases potential error (e.g. Paul et al., 2013). Manual mapping is influenced by the image resolution and operator ambiguity in both identification and digitisation of surface features (Watson et al., 2017a). To minimise errors and reduce uncertainty associated with manual digitisation, all mapping was completed by one analyst to ensure consistency. The mapping components were then checked for accuracy by revisiting on independent days until no further edits were required. All images were registered to a common image (2015 orthophoto) allowing termini position, area and surface features to be quantified. The accuracy of mapped components was assessed through repeat digitisation methods. For each of the mapped components the methods for identification, mapping and error and uncertainty analysis will now be discussed in turn.

#### 4.2.2.1. Crevasses

Crevasses appear on the historical imagery as either dark lines on the surface in debris-free areas, or white lines in debris-covered areas where filled with snow (See Table 2.1; (Goodsell et al., 2005b)). Crevasses were typically identified as linear features inclusive of both open fractures and linear imprints indicative of crevasse traces. Crevasses were clearly visible where debris was absent or under a thin layer of debris but were more difficult to visibly identify on the lower glacier under a thicker debris cover. Quantification of the total length of crevasses in addition to direction and location of crevasses were used to interpret the flow regimes.

#### 4.2.2.2. Ogives

Band ogives are classified owing to the repetition of dark and light convex bands in the direction of ice flow at the base of icefalls (Goodsell et al., 2002). Ogives can be identified at the base of the icefalls emerging from the main tributary glaciers and can be traced downglacier where debris is thin enough to observe them. Although the formation mechanism is still not fully understood, the proposed theory by Nye (1958) is generally accepted and assumed to be indicative of the passage through icefalls in a year reflecting the whiter (winter) layers and darker (summer) layers.

#### 4.2.2.3. Glacier extent and termini position

Identification of the debris-covered glacier extent and termini position was aided by indicators of ice presence such as ice cliffs, exposed ice and distinct morphological changes. Glacier extents from the RGI 6.0 (RGI Consortium, 2017) were used to aid initial visual assessment, which can be further complicated by the presence of snow, especially within the high accumulation zones.

For each glacier outline, manual digitisation was carried out three times for comparison and accuracy was assessed via the standard deviation, ranging from 0.05 to 0.34 $km^2$ (Paul et al., 2013). The mean area varied for each year with a maximum of 5% variation. Assessment of the uncertainty for termini position was determined based on the square root of the input imagery resolution and registration error as in Equation 4.1 (Hall et al., 2003; Silverio and Jaquet, 2005). Registration error compared to the 2015 orthophoto was estimated to be <5 pixels for the IGN historical data equating to 5 m, and <2 pixels for satellite imagery based upon improved alignment using RPCs ranging from 1 – 20 m for the 2018 to 1990 data (Table 4.1). This resulted in registration errors ranging from 0.60 to 20 m and uncertainty values therefore ranged from 0.85 – 10.96 m (Equation 4.1).

**Equation 4.1**

$$Uncertainty = \sqrt{[(pixel\ resolution\ image1)^2 + (pixel\ resolution\ image2)^2]} + registration\ error$$

#### 4.2.2.4. Debris cover

For the panchromatic imagery (1952 – 1996) and multispectral satellite imagery (2009 – 2018) debris cover was mapped within the glacier extent aided by a basic supervised maximum likelihood classification in ArcGIS using debris and snow/ice classes based on approximately ten spectral samples for each image, and manually edited. The resulting classification was then manually checked and edited where necessary. For the later images in 2017 and 2018, the debris-cover extent provided by the RGI 6.0 (Scherler et al., 2018) was used as an initial guide. Due to limited ground truth data other than field observations to confirm regions of debris cover, uncertainty was applied at an upper boundary of ±5% in accordance with previous studies (e.g. Paul et al., 2013, 2017; Mölg et al., 2018).

#### 4.2.2.5. Supraglacial ponds and streams

Manual mapping of the waterbodies from the IGN aerial imagery was undertaken. Identification of waterbodies across the glacier surface were aided by the shape, pixel saturation and colour. Supraglacial streams were mapped where traceable based on sinuous surface features cutting through the debris cover.

The presence of water in the satellite imagery between 2009 and 2018 was aided by a Normalized Difference Water Index (NDWI) band ratio utilising the near infrared (NIR) and visible green bands

to identify water on the glacier surface (McFeeters, 1996). The NDWI utilises the visible green and NIR bands of the multispectral satellite imagery based on (Equation 4.2).

NDWI = (Green − NIR) / (Green + NIR) **Equation 4.2**

The NDWI resulted in misclassification of some pixels and manual editing and visual identification was then undertaken. Values closest to 1 indicated the presence of water and was used to aid manual mapping of glacial lakes and streams. Comparisons with the visual RGB imagery enabled operator identification to detect and manually edit any erroneous boundaries. In some cases, areas identified as exposed ice and ice cliffs were highlighted in the NDWI index and were manually edited to delineate pond boundaries and ice cliffs (Figure 4.1).

Operator bias was assessed on five ponds randomly selected from the study area that were digitised independently three times as manual digitisation is likely to be a substantial source of uncertainty. The percentage variability for repeatability was <10% with a standard deviation range of 3 to 78 $m^2$. Total uncertainty for pond delineations was calculated as equal to the coefficient of variation for operator bias as adapted from Steiner et al. (2019) and ranged from 6.5 to 10.4%.

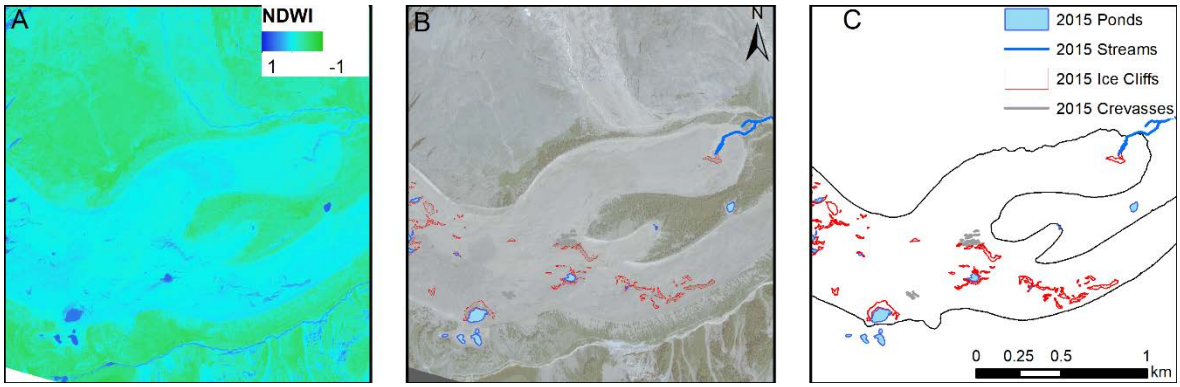


**Figure 4.1:** The use of NDWI to aid mapping of glacial lakes and streams with an example of those mapped in 2015.

#### 4.2.2.6. Ice cliffs

Ice cliffs were manually digitised via visual assessment of exposed ice observed in the debris-covered region. Ice cliffs were defined as exposed ice inclusive of both clean and dirty regions, which were visually assessed. Associations with supraglacial ponds and increased slope angles and aspect derived from SPOT derived DEMs (see Chapter 6) aided identification of ice cliffs to the surrounding terrain. Ice cliffs were classified as a region with a steep slope angle and exposed ice within the debris-covered ablation zone.

Uncertainty was assessed on a random sample of five ice cliffs that were selected from each of the images and digitised three times to assess operator error. The percentage variability for repeatability was <8% with standard deviations ranging from 20.6 to 185 $m^2$; lower variability was observed with the higher resolution data and was highest for the lower resolution data, which indicates a higher degree of uncertainty. The coefficient of variation ranged from 3.13 to 6.5%.

## 4.3. Results

### 4.3.1. Structural evolution 1952 – 2018

Miage Glacier underwent structural change between 1952 and 2018 (Table 4.2) and shows complex glacier dynamics influenced by the four tributary glaciers, which feed the main glacier trunk and determine individual flow unit boundaries. The structural assessment of Miage Glacier from 1952 to 2018 indicate it has undergone a change from one of an active ice flow regime followed by a period of deterioration since 1990s, which has continued until 2018 (Figure 4.2 to Figure 4.3). Mapping individual structures observed on the surface enables further detail of the glacier dynamics to be derived over the 66-year period. A sub-period from 1990 to 2018 is referred to for comparison with Chapter 5 and due to the availability of multi-spectral imagery from this time period enables additional variables to be quantified.

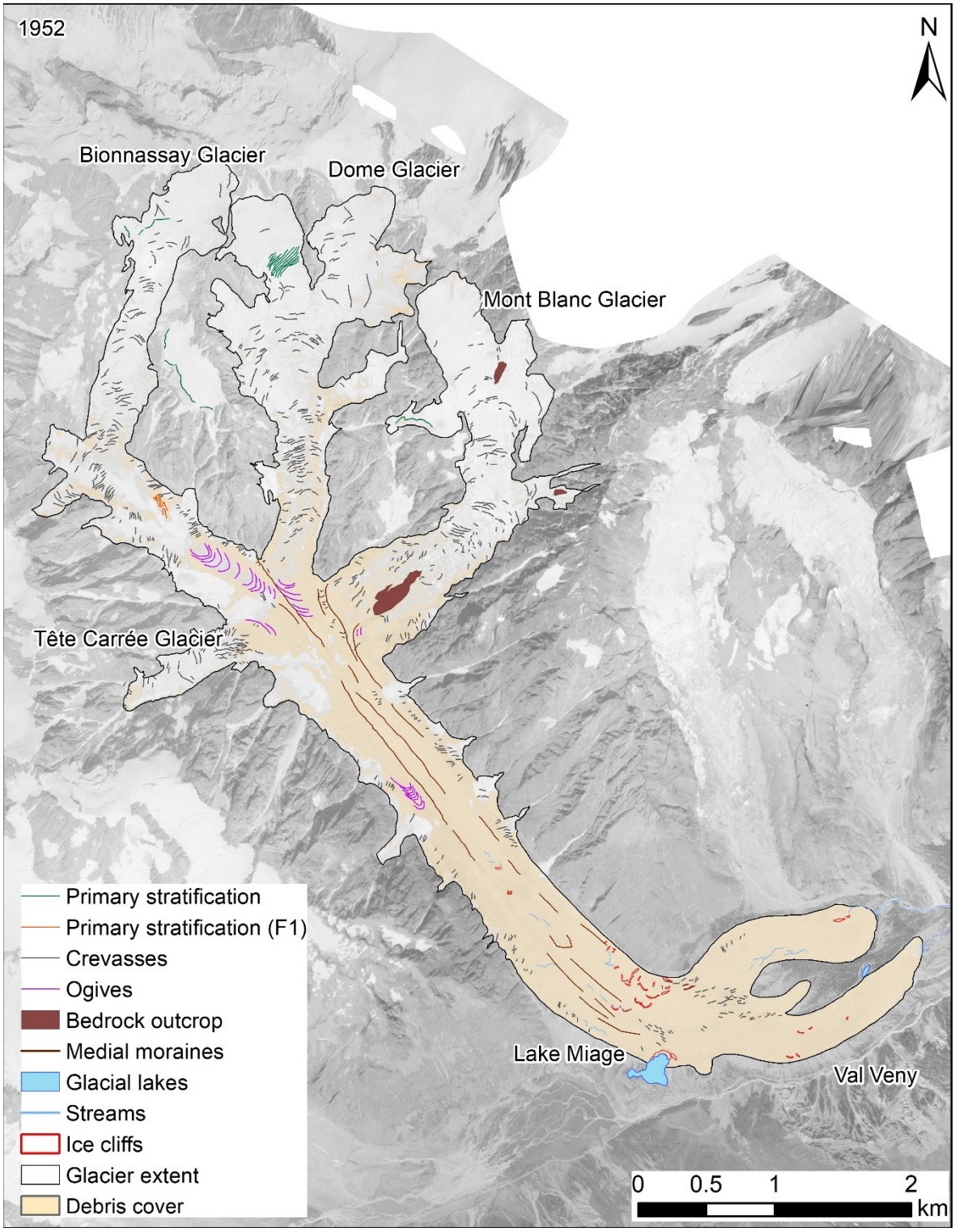


**Figure 4.2:** Mapping of structural and surface features from 1952. Background imagery shows the orthophoto derived from the 1952 aerial images. The 1945 rockfall was not visible in the imagery.

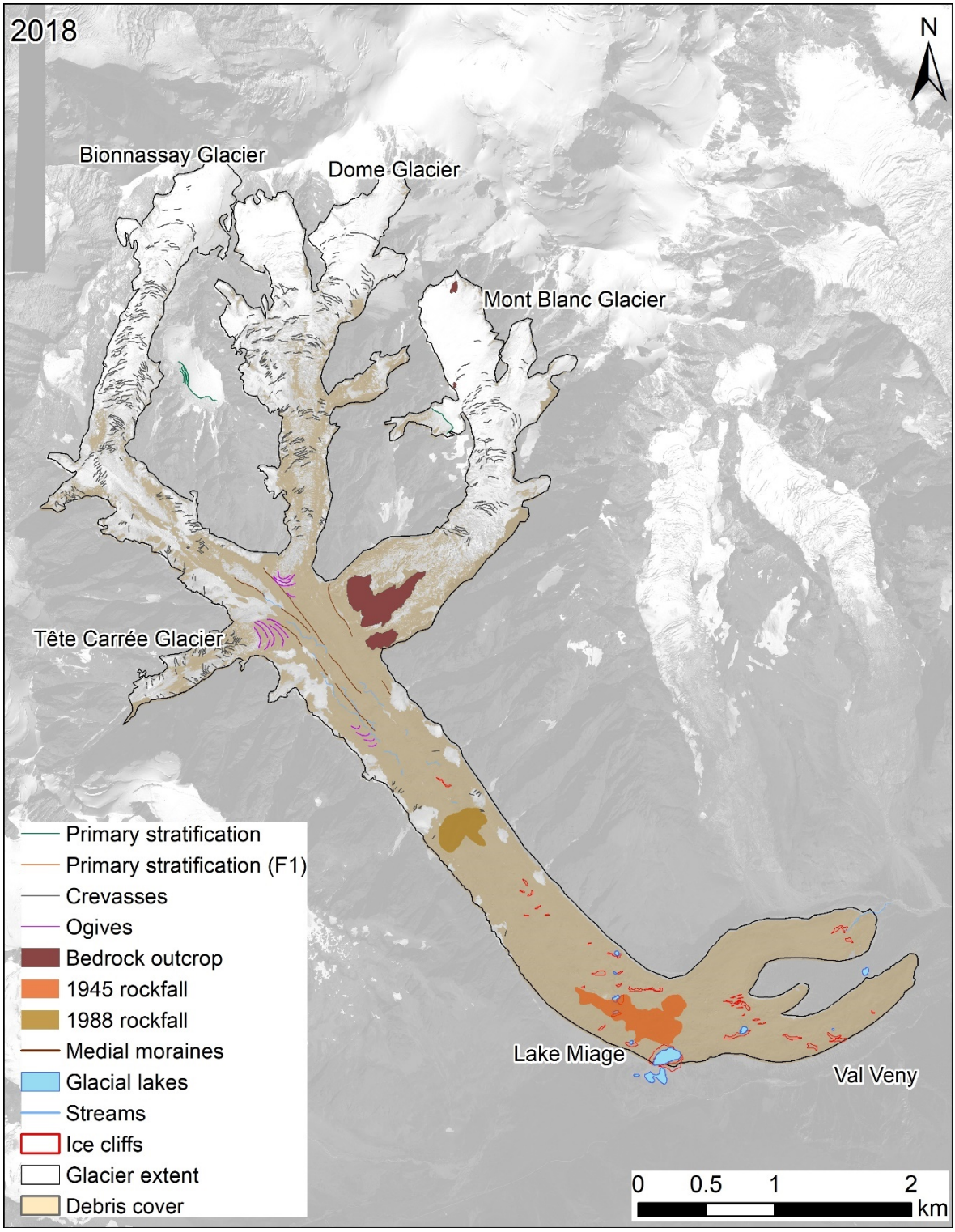


**Figure 4.3:** Mapping of structural and surface features from 2018. Background shows the SPOT 2018 satellite imagery used for digitisation of structures.

At the beginning of the observation period in 1952 systematic layering identified as primary stratification of snow layers is observed in the high accumulation zones of the tributary glaciers, predominantly on Dome Glacier (Figure 4.2). Folding of primary stratification highlighted by incorporated dirt and debris is evident at the top of the main tongue of Miage Glacier, downglacier of Bionnassay Glacier. The presence of the icefalls on all four tributary glaciers results in distinct

ogive bands at the base of the Tête Carrée Glacier, Bionnassay Glacier and Dome Glacier, yet no ogives are visible at the base of Mont Blanc Glacier. The icefalls of Tête Carrée Glacier and Dome Glacier are approximately 90° to the Miage Glacier valley section and the developed ogives become elongated in the direction of flow of the main trunk (SSE). Typical wavelengths of the ogive bands (i.e. the distance between two dark ice bands) vary from ~15 m to 100 m; and are most prominent downglacier of Bionnassay Glacier. The icefalls on all four of the main tributary glaciers indicate intensive multi-directional crevassing including transverse, arcuate and longitudinal overlapping crevasse sets. En-echelon crevasses are observed along the glacier margins of the valley tongue, in addition to a distinct set of longitudinal crevasses observed at the top of the terminal lobes. Medial moraines emanate from the meeting of tributary glaciers, confining ogives and crevasse sets to distinct flow units. Deposits from the 1945 rockfall event were not visibly identifiable in the 1952 imagery and thus are not mapped in Figure 4.2.

In 1961, despite a reduction in the visibility of ogives from Bionnassay Glacier compared to 1952 (Figure 4.4), Dome Glacier and Tête Carrée Glacier exhibit clearly visible ogive bands resulting in an overall increase in cumulative length (Table 4.2). An increase in crevasse density along the margins of the glacier tongue is particularly apparent, consistent with an increase in total crevasse length from 31 km in 1952 to 56 km in 1961 (Table 4.2). Evidence of the 1945 rockfall deposit is observed on the main trunk of Miage Glacier.

By 1979, Tête Carrée Glacier exhibited clearly visible ogive bands, while visibility of ogives on Bionnassay Glacier, Dome Glacier and Mont Blanc Glacier are much clearer. Crevasse density and length also reduced on the glacier surface. Meanwhile, on the high elevations of Mont Blanc Glacier, bedrock outcrops are visible with thin snow cover (Table 4.2).

Additional crevassing on the lower valley section around Lake Miage and above the terminal lobes is evident in 1988 (Figure 4.4). Ogives are present at the base of Tête Carrée Glacier and Dome Glacier, but visibility is limited. The glacier is observed with increased snow cover in the higher elevations potentially accounting for the reduction in ogives, specifically from Bionnassay Glacier.

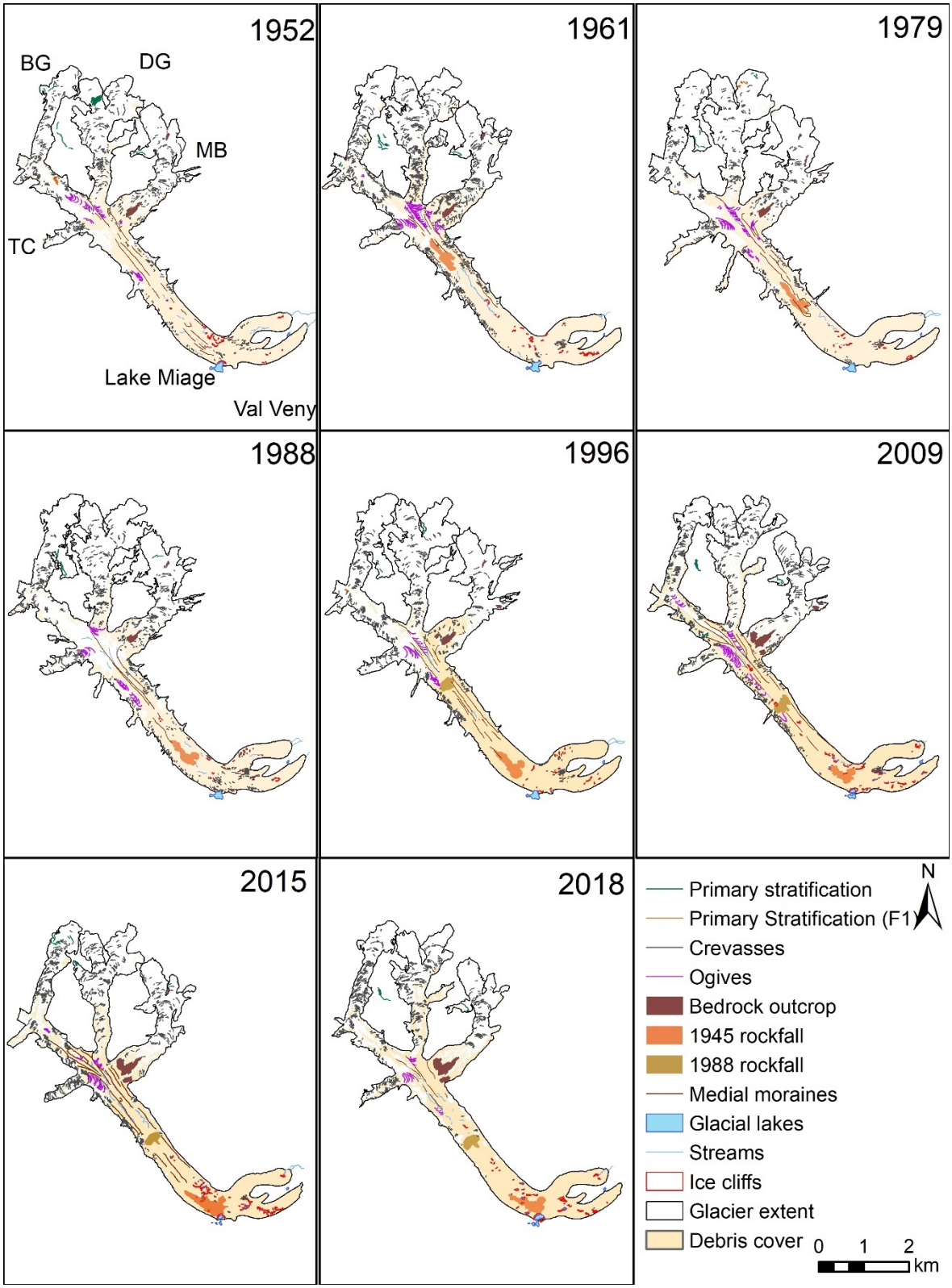


**Figure 4.4:** Structural mapping from 1952 to 2018. TC - Tête Carrée Glacier, BG – Bionnassay Glacier, DG – Dome Glacier, MB – Mont Blanc Glacier.

By 1996 only a limited number of ogives are visible at the base of Tête Carrée Glacier (Figure 4.4). Furthermore, Mont Blanc Glacier shows an increase in the size of the bedrock outcrop (Table 4.2).

In 2009, crevassing is limited to the southern glacier margin and above the terminal lobes and is generally limited to the higher elevations. An increase in the visibility of ogives from Tête Carrée Glacier, Bionnassay Glacier and Dome Glacier are also evident. Two exposed ice cliffs upglacier towards the confluence of the tributary glaciers are evident with a notable circular shape (Figure 4.4).

By 2018, arcuate crevasses on the accumulation zones of the tributary glaciers; Bionnassay Glacier, Dome Glacier and Mont Blanc Glacier, suggest a steep ridge resulting in an extensional regime (Figure 4.3). Limited visibility of ogives at the base of Tête Carrée Glacier and Dome Glacier with typical spacing between the bands reduced since 1952 to ~30 to 55 m. No ogive bands are visible from Bionnassay Glacier or Mont Blanc Glacier. Increasing expanse of rock at the base of the Mont Blanc Glacier icefall indicates further ice thinning and/or loss of ice through avalanching of ice blocks. Limited crevassing is observed on the main valley tongue of Miage Glacier, whilst crevasses at the top of the terminal lobes are now classified as ice cliffs due to the increasing expanse of exposed ice rather than fractures as previously observed.

**Table 4.2:** Summary of structures as derived from the mapping in Figure 4.2 to Figure 4.4.

| Date | Glacier area ($km^2$) | Debris cover (area $km^2$/ % of glacier area) | Crevasses (total length km / density $km/km^2$) | | Ogives (length km / density $km/km^2$) | | Bedrock outcrop area ($km^2$) |
|---|---|---|---|---|---|---|---|
| 1952 | 10.2 ± 0.11 | 4.8 ± 0.24 (47%) | 31.70 | 3.10 | 4.36 | 0.43 | 0.05 |
| 1961 | 10.5 ± 0.13 | 5.4 ± 0.27 (51%) | 56.01 | 5.32 | 7.52 | 0.71 | 0.05 |
| 1979 | 11.1 ± 0.24 | 4.9 ± 0.24 (44%) | 23.37 | 2.11 | 6.08 | 0.55 | 0.06 |
| 1988 | 11.4 ± 0.34 | 4.4 ± 0.22 (40%) | 32.87 | 2.95 | 4.34 | 0.39 | 0.04 |
| 1996 | 10.7 ± 0.11 | 4.5 ± 0.22 (42%) | 28.82 | 2.69 | 3.71 | 0.35 | 0.07 |
| 2009 | 9.6 ± 0.05 | 4.8 ± 0.24 (50%) | 35.35 | 3.67 | 4.16 | 0.43 | 0.11 |
| 2018 | 9.3 ± 0.05 | 4.9 ± 0.25 (52%) | 30.02 | 3.21 | 2.04 | 0.22 | 0.13 |

Quantification of the structures in Table 4.2 indicate an increase in glacier area in the late 1970s and 1980s, followed by continued reduction thereafter (Figure 4.5). Debris cover was typically observed to increase over the study period such that 52% of the total glacier area was covered with supraglacial debris by 2018.

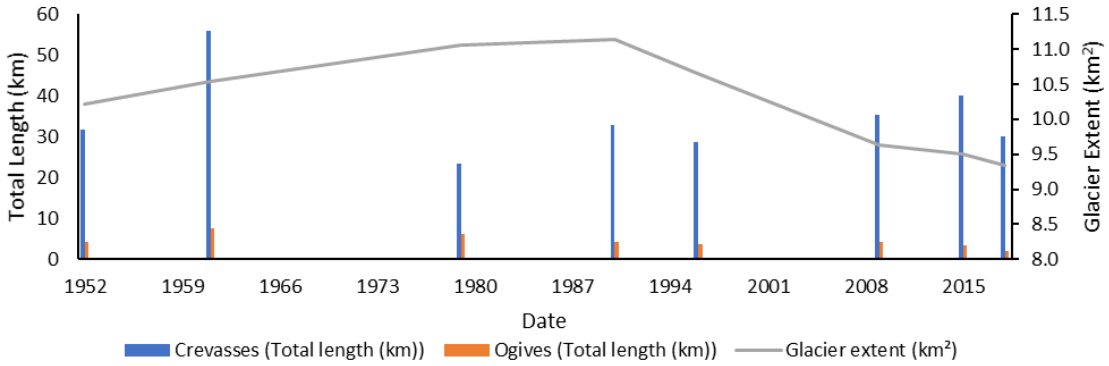


**Figure 4.5:** Glacier extent, crevasse length and ogive length from 1952 – 2018.

### 4.3.2. Surface change 1952 – 2018

Miage Glacier underwent substantial surface change between 1952 and 2018 (Table 4.2). The glacier area decreased by 8 ± 2% between 1952 and 2018 with ~136 ± 4.04 m recession in termini extent along the southern lobe. In comparison, the northern lobe receded very little (~15 ± 4.04 m) between 1952 and 2018. The reduction in glacier area is noted in the higher elevation accumulation zone and where tributary glaciers feed the Miage Glacier valley tongue (Figure 4.2). Debris cover varied between 1952 – 1988 but increased between 1988 and 2018 by ~8.5%, with higher elevations and tributary glaciers becoming noticeably dirtier. Supraglacial ponds substantially increased in number between 1988 to 2018. No supraglacial ponds were observed prior to 1996, with the exception of one small pond in 1961 equating to 95 $m^2$, but ponds covered 6,047 $m^2$ by 2018. The ice-marginal Lake Miage and proglacial Lac Vert are evident since 1952. Because of its large size, trends in glacial lake area were driven largely by changes of Lake Miage. Alongside the development of lakes and ponds was an increase in ice cliff area from 17,326 $m^2$ to 47,616 $m^2$ (+175%) between 1952 and 2018. In accordance with an increase in debris cover and reduction in glacier extent since the 1990s, the surface of the glacier has become increasingly undulating.

**Table 4.3:** Summary of ice cliff and glacial lakes on from 1952 to 2018. Glacial lakes and pond uncertainty is given at the upper value of 10% and uncertainty of ice cliffs at 8%.

| Date | Glacial lake area ($m^2$) Uncertainty at 10%. | Supraglacial pond area ($m^2$) Uncertainty at 10% | Pond density % of glacier area | Ice cliff area ($m^2$) Uncertainty at 8% | Ice cliff density as % of glacier area | % of ponds with ice cliffs |
|---|---|---|---|---|---|---|
| 1952 | 38243 ± 3824 | 0 | 0 | 17326 ± 1386 | 0.17 | 0 |
| 1961 | 39206 ± 3921 | 95 ± 10 | 0.0009 | 19954 ± 1596 | 0.19 | 100 |
| 1979 | 31687 ± 3169 | 0 | 0 | 11403 ± 912 | 0.10 | 0 |
| 1988 | 27897 ± 2790 | 0 | 0 | 11683 ± 935 | 0.10 | 0 |
| 1996 | 32885 ± 3289 | 438 ± 44 | 0.0041 | 10567 ± 845 | 0.10 | 67 |
| 2009 | 27731 ± 2773 | 3407 ± 341 | 0.0355 | 36502 ± 2920 | 0.38 | 77 |
| 2018 | 34468 ± 3447 | 6047 ± 605 | 0.0650 | 47615 ± 3809 | 0.51 | 100 |

Further analysis of the change associated with the glacial lakes with the addition of further data indicates an overall reduction in total area of glacial lakes and of Lake Miage in particular, yet an increase in both the number of glacial lakes, specifically of supraglacial ponds (Figure 4.6). A distinct change in these trends is observed since 2004 presented by an increasing polynomial trend ($R^2$ = 0.69).

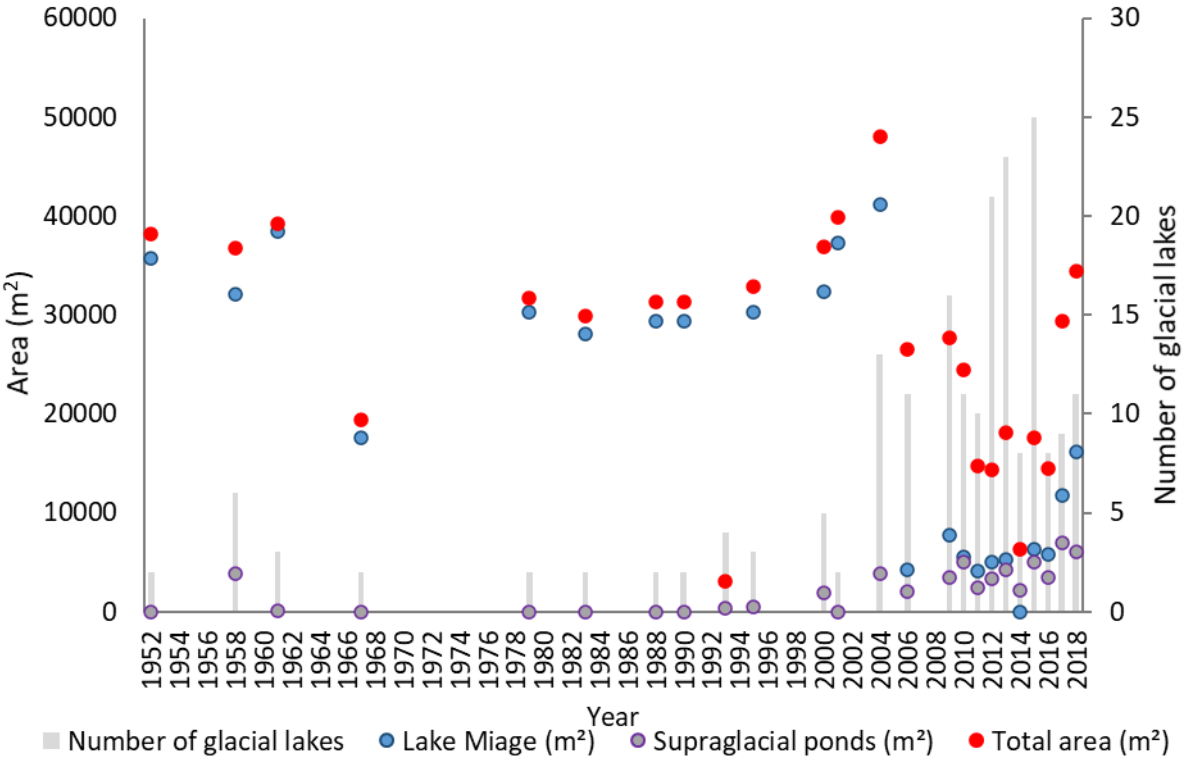


**Figure 4.6:** Variability of glacial lakes at Miage Glacier in area ($m^2$). Data show the overall number of glacial lakes present (grey bar) inclusive of proglacial lakes, ice-marginal lakes and supraglacial ponds, and area of supraglacial ponds (purple dots). *Data covering the area of Lake Miage in 1993 was not available from the imagery.

Historical analysis of the glacial lakes indicates ongoing change since 1952 (Figure 4.7). The most apparent change is of Lake Miage, which shows high levels of water level variability in response to known drainage and refilling events with an overall decline in area. Aerial imagery from 2004 taken prior to a large drainage event documented to have occurred in September 2004 shows one large lake located partly on the glacier and constrained by the lateral moraine on the western side of the glacier. Lake Miage is observed in 2006 with substantially lower water levels and with islands, and in 2009 as 3 separate lakes consisting of a large proglacial lake, a smaller proglacial lake, with substantial reduction in the area of the ice-marginal section. Since 2009, multiple lakes have remained and Lake Miage is limited to the ice-marginal section encompassed by moraine deposits.

Lac Vert, a proglacial lake situated in the northern edge of the southern lobe, has also been a stable feature since 1952. Although some variations in size are evident, the location and presence of the

lake has remained relatively stable with a distinctive tear-drop shape. The area of the lake continued to increase steadily until 2010, at which point it began to decline (Figure 4.6). The lake area is more consistent between 2015 – 2018. Sediment strandlines and reduced vegetation were observed during the field visits around the edge of the lake indicating that water levels were previously higher than at the time of field observation.

Although, the overall number of supraglacial ponds has increased (Table 4.4), the total area of ponded water has reduced (Figure 4.6). The presence of supraglacial ponds on Miage Glacier has been observed across the glacier surface; Figure 4.7 shows the distribution of supraglacial ponds mapped from the available imagery between 1952 and 2018. Two regions can be highlighted as key areas for supraglacial pond presence; Zone 1 (Figure 4.7a) indicating a band of ponds across the glacier surface, is located from the southern margin to the northern margin prior to the eastwards bend into Val Veny. Zone 2 (Figure 4.7) is located at the top of the southern lobe. In comparison to the northern lobe, the southern lobe has a higher frequency of supraglacial ponds. Zone 1 appears in the region of thickest ice as determined from the RGI6.0 ice thickness data (Farinotti et al., 2019) whereas Zone 2 appears in an area of comparatively thinner ice (Figure 4.7c). Very few ponds have been observed between 1952 and 2018 on the upper valley tongue.

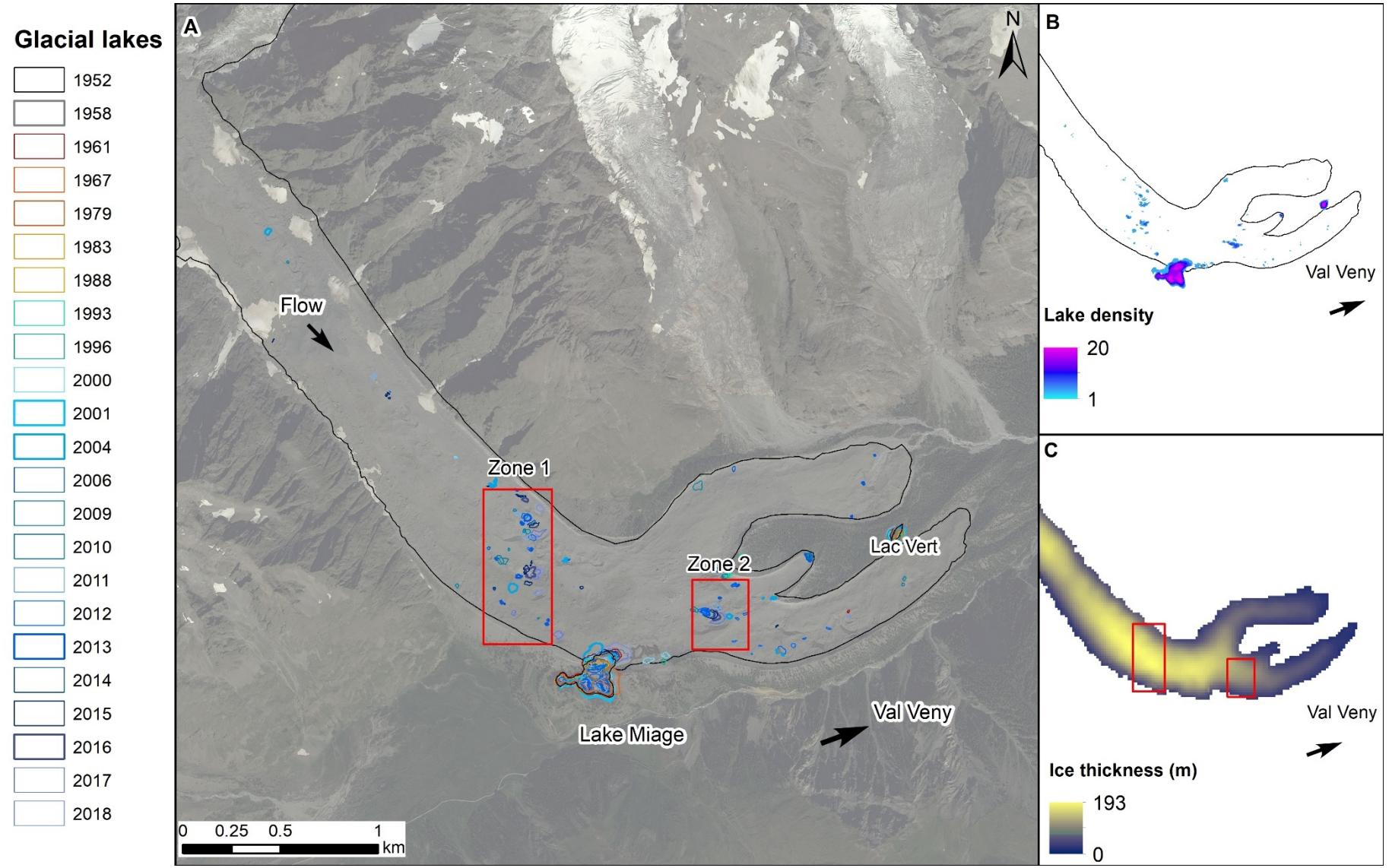


**Figure 4.7:** A: Glacial lake change from 1952 – 2018, manually digitised from aerial and satellite imagery. B: Glacial lake density derived from the number of years water has been present. C: Ice thickness derived from the RGI6.0 (Farinotti et al., 2019).

Four supraglacial ponds of interest (see Chapter 6) are discussed in turn to assess the evolutionary characteristics. Supraglacial pond 1 (S1) was located just above the southern terminal lobes in zone 2 where supraglacial ponds have been observed in years prior to 2017 and 2018 (Figure 4.8). A pond has been present here with a large ice cliff since 2012. Prior to 2012, a pond was identified in 2004 without ice cliffs, although longitudinal crevasses were apparent nearby in a topographically undulating area.

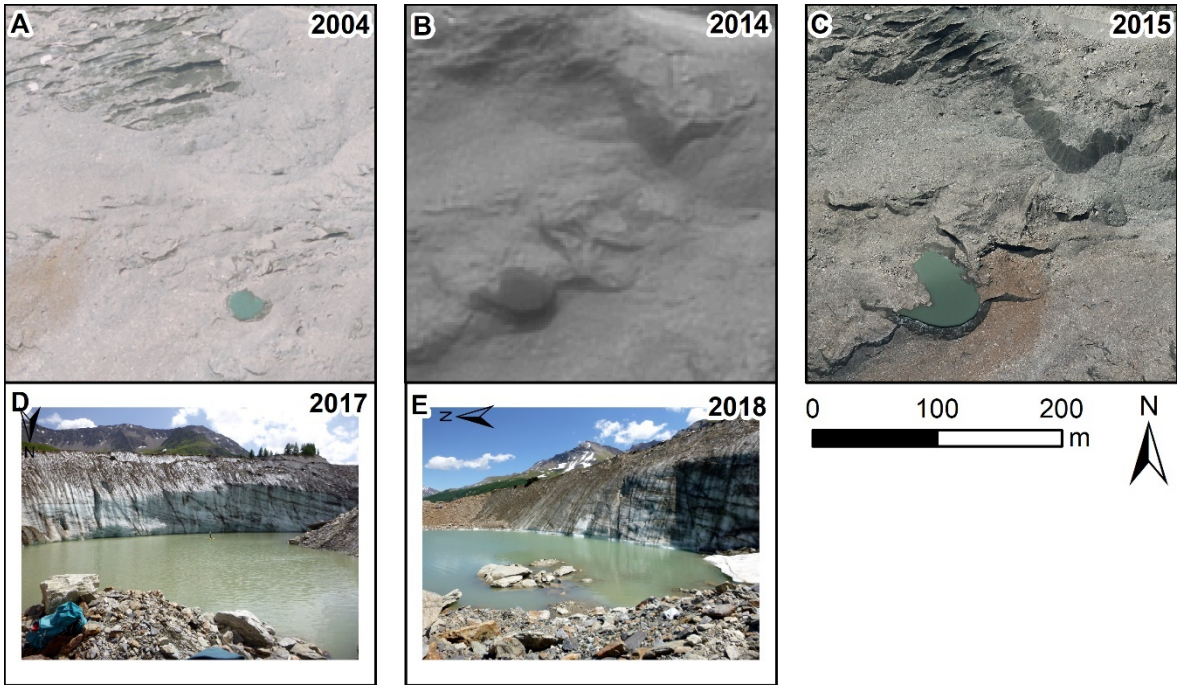


**Figure 4.8:** Development of S1 located at the top of the northern terminal lobe.

Supraglacial ponds S2 – S5 were located in Zone 1 across the width of the glacier. Supraglacial pond 2 (S2) appears in the imagery in 2015 with ice cliffs and dirty ice present in the current location of the pond. Prior to 2015, the location appears to be relatively smooth with homogenous debris cover. Images from 2015 and 2016 show a slight depression but there was no clear evidence of water indicating that the pond likely formed during the 2017 melt season.

Supraglacial pond 3 (S3) was not observed prior to 2004. Pooling of water slightly upglacier was observed with ice cliffs present in 2015. The pond was surveyed in 2017 and was the smallest of the supraglacial ponds surveyed. The region along the southern margin is topographically undulating and ponds were typically observed to be located between the higher elevations of the central medial moraine and the southern lateral moraine in a region of lower elevation (Figure 4.9).

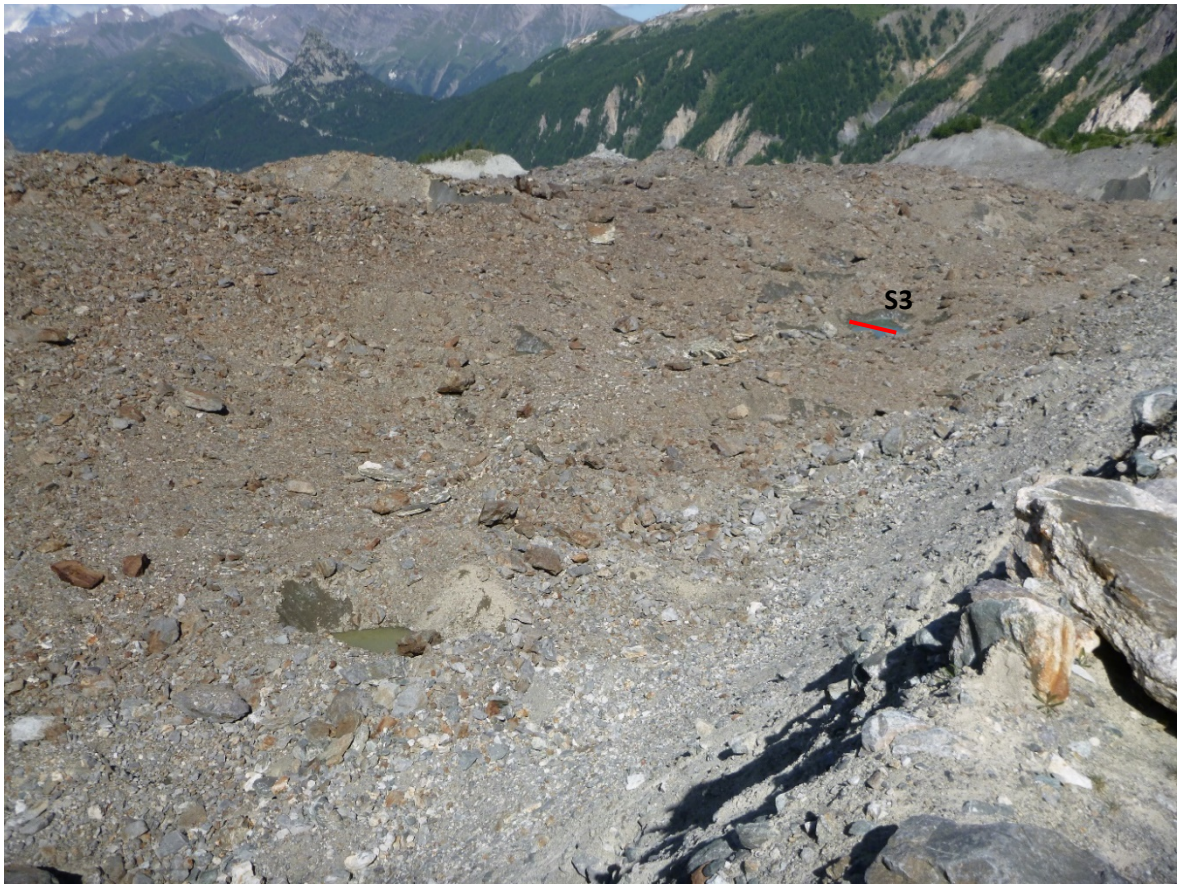


**Figure 4.9:** The debris-covered Miage Glacier in 2017 looking southeast from the southern lateral moraine. S3 (~22 m across, along red line) and a smaller melt pond can be observed in the photo.

Supraglacial pond 4 (S4) is located along the true left margin, just above where the valley glacier of the glacier turns to the east into Val Veny. This is an area characterised by exposed ice cliffs and ponds and supraglacial streams. In 2004, small supraglacial channels cut through the debris evolving into 2 small ponds present by 2009. Two ponds remained present in 2012 nearby the location of the current pond. By 2015, the topography in the vicinity of the lower pond was exploited by a supraglacial stream. The 2017 location of the pond was located nearby supraglacial channels having reformed between 2016 and 2017. This resulted in an area of collapsing cliffs and undulating debris-covered topography resulting in partial drainage and cliff collapse between visits in 2017 and 2018 (Figure 4.10).

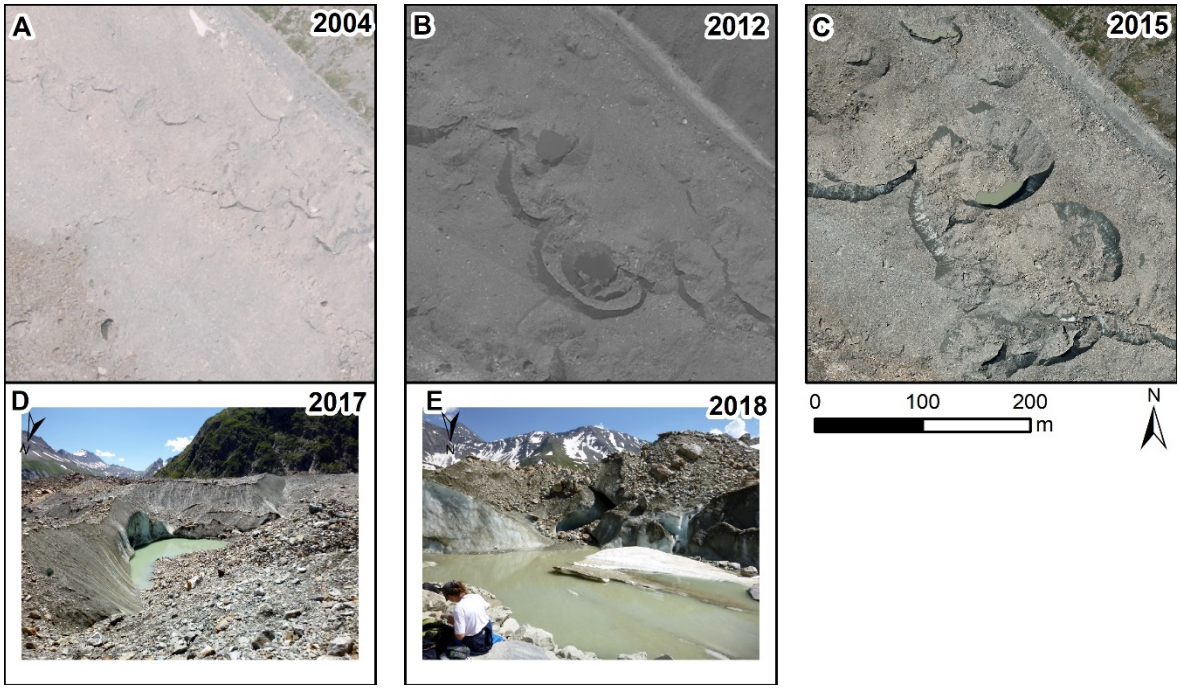


**Figure 4.10:** Development of S4 along the northern margin of the valley tongue.

Supraglacial pond 5 (S5) has only been present since 2013 when there was one small pond (Figure 4.11). Subsequently, two small ponds developed by 2015, and had coalesced by 2017. Another pond was present to the southwest of S5 in 2004, with a relatively smooth surface. Ice cliffs pre-existed the pond in 2012 and by 2014 a much rougher surface topography can be observed and was evident in both the 2017 and 2018 visits.

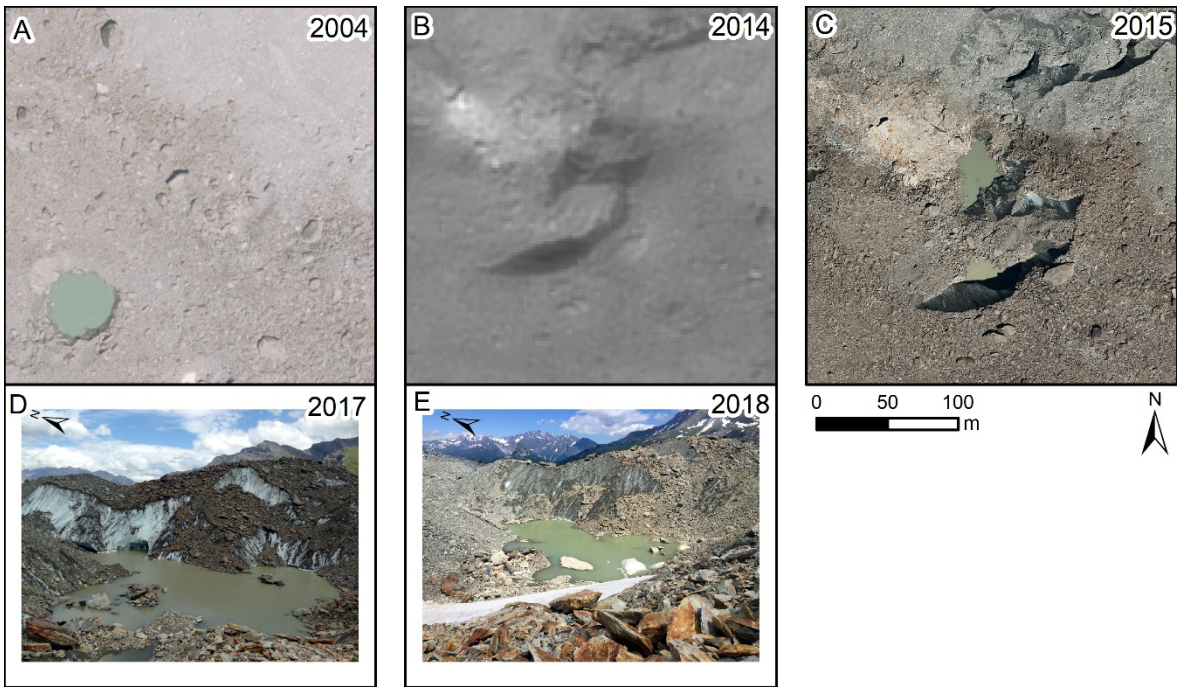


**Figure 4.11:** Development of S5 from 2004 – 2018.

## 4.4. Discussion

### 4.4.1. The evolution of Miage Glacier

Previous studies have detailed how Miage Glacier has evolved over the period 1913 to 1999 (Smiraglia et al., 2000; Thomson et al., 2000). The data sets presented here are in agreement from 1952 and provide an update to those observations through a period of continued climate warming since the 1990s to 2018. The combined results represent a rare opportunity to examine debris-covered glacier dynamics across decadal and centennial timescales. Thomson et al. (2000) and Smiraglia et al. (2000) described spatially and temporally complex patterns of change through the twentieth century; modest terminal recession since the LIA maximum were punctuated by a small advance during the late twentieth century in response to positive mass balances between the 1960s to 1980s, as observed elsewhere in the Alps (Diolaiuti et al., 2003; Huss, 2012). With reference to the 3-stage debris-covered glacier evolution model of Benn et al. (2012), Miage Glacier was consistent with 'Regime 1' during the twentieth century (Thomson et al., 2000) in that it experienced limited water storage on the glacier surface. Over the period 1988 to 2018, these data reveal that Miage Glacier has transitioned into 'Regime 2', characterised by increased surface water storage and expanding debris cover (Table 4.2 and Table 4.3).

In terms of surface changes, there has been only modest overall area loss (−8%) (Table 4.2) and a small amount of recession of the terminal lobes (of ~135 ± 4.04 m) over the full observation period from 1952 to 2018, but there are notably more substantial local area reductions in the tributary glaciers that feed Miage's main trunk. Debris cover has expanded by ~0.4 $km^2$ up-glacier from 1988 to 2018, increasing from 40% to 52% of the total glacier surface area (Figure 4.4, Table 4.2). Likewise, the increasing debris cover at Miage Glacier is similar to that seen since the 1990s on Zmuttgletscher (Mölg et al., 2019) and on the glaciers of the Ortles-Cevedale Group, Italy (Azzoni et al., 2018). Multiple flow units identified by the incorporation of debris, are derived from the numerous icefalls and confluence of tributary glaciers as flow is divided around the bedrock outcrops on Mont Blanc Glacier. The debris forms lateral and medial moraines, fed from the bedrock outcrops, glacially eroded valley sides, and small but frequent landslide, rockfall and avalanche events (Deline, 2009; Rowan et al., 2015). Over the study period, identification of these flow units becomes limited and the merging and thickening of debris has resulted in a massive, non-distinct unit as the surface topography becomes increasingly undulating, enhanced by the availability of debris to the glacier surface from the intensification of rockfall events and resulting differential ablation (Reynolds, 2000). Identification of two rockfall events in *c.*1945 and 1988 through distinct lithological variations to the surrounding debris (Figure 4.4) can be traced downglacier and generally maintain their shape (Deline, 2009) indicating relatively stable ice flow velocity across the glacier width of the multiple flow units. However, the *c.*1945 rockfall deposits (Deline, 2009) were not visibly identified in the 1952 imagery but is observed by 1961 and could

indicate some discrepancy over the exact date of the event. As debris is transported down-glacier (Goodsell et al., 2005a), the terminal lobes are considered to have undergone longitudinal compression and debris accumulation resulting in increased debris thickness (Mihalcea et al., 2008; Foster et al., 2012).

Notably, supraglacial ponds have begun to emerge on the surface of Miage Glacier since 1990s with a noticeable increase in number since 2004 indicating a potential tipping point or threshold has been reached (Table 4.4 and Figure 4.6) and now cover >6000 $m^2$, whilst ice cliffs have increased in area by 308% since 1988 (Table 4.3). The recent emergence and growth of supraglacial ponds and ice cliffs on Miage Glacier is a particularly striking surface expression of the transition to 'Regime 2' of the debris-covered glacier evolution model (Benn et al., 2012). These observations are broadly consistent with the evolution of debris-covered glaciers elsewhere that are experiencing negative mass balances in response to climate change (e.g. Benn and Lehmkuhl, 2000; Scherler et al., 2011; Benn et al., 2012; Bolch et al., 2012; Rowan et al., 2015).

### 4.4.2. Decay of Miage Glacier since 1990s

Miage Glacier shows complex glacier dynamics largely influenced by the four large tributary glaciers, which feed the main glacier trunk. The structural evolution of Miage Glacier from 1952 to 2018 indicates it has undergone a change from one of an active ice flow regime followed by a period of substantial deterioration since the 1990s, which has continued until 2018. The initial state of the glacier in 1952 indicates an active ice flow regime with production of primary stratification in the accumulation zones and formation of new, multi-directional crevasses through the icefall indicating intense strain regimes, and ogives forming in the compressional zones at the base of the icefalls (Figure 4.2). Previous studies observed a period of thickening between 1975 and 1999 (Thomson et al., 2000) attributed to a wave of ice, which migrated downglacier (Smiraglia et al., 2000). This was observed during the 1980s with an increase in the abundance of crevasses compared to previous years, especially in the lower valley tongue with a convex surface in relation to the valley sides suggestive of comparatively increased ice mass, but structural evidence (as discussed below) suggests a persistent state of deterioration and ice loss since this period.

The spacing between ogives on Miage Glacier reduced over the observation period and is considered to represent a reduction in annual velocity (e.g. King and Lewis, 1961; Goodsell et al., 2002; Vincent et al., 2018). Assuming the ogives represent annual passage of winter and summer bands (Nye, 1958), a reduced distance between the spacing of the bands could indicate reduced passage of ice through the icefalls. Tête Carrée Glacier has continued to produce new ogives, albeit closer spaced throughout the observation period as has Dome Glacier, but to a lesser extent indicating continued ice flux and reduced ice flow velocities.(Figure 4.3). The visibility of ogives is

dependent upon on a number of factors including ice flux through the ice fall (e.g. Azzoni et al., 2017), obscuration by debris or snow cover, quality of the imagery and presence of shadowing. The expansion of the bedrock outcrop at the base of Mont Blanc Glacier icefall since 1996, reduction of ogive spacing and reduction of Mont Blanc Glacier accumulation area supports a reduction in ice flux through the icefall and progression towards a state of deterioration. It is therefore likely that Mont Blanc Glacier will become detached from Miage Glacier if further ice collapse around the bedrock outcrop continues resulting in reduced ice flux to the valley section.

Collapse features near to the confluence of the tributary glaciers with Miage Glacier, identified as two circular sections of exposed ice were observed in 2009 (Figure 4.4). These were classified as ice cliffs in the imagery due to the exposure of ice and are considered to be linked to the positions of previous supraglacial ponds and moulins, as identified in 2010 by Fyffe et al. (2012). Previous studies on the Forni Glacier, Switzerland (Azzoni et al., 2017) and the Pasterze Glacier, Austria (Kellerer-Pirklbauer and Kulmer, 2019) observed similar circular structures associated with faults, although these features were observed lower on the ablation zone in comparison to those observed at Miage Glacier. Due to the debris cover it is not possible to ascertain whether faults existed prior to the collapse of these features. Further evidence of collapse is the disintegration of the northern lobe outlet stream, which appears after 1988 with no prior visible observation.

The combination of reduced crevassing, visibility of ogive bands, ice flux via Mont Blanc Glacier, and the presence of collapse structures since the 1990s suggest reduced glacier dynamics and progression to an enhanced state of deterioration. Thus, resulting in a more undulating surface promoting debris redistribution (Zhang et al., 2011; Gibson et al., 2017a) and enabling coalescence of meltwater and ablation to occur on exposed ice surfaces.

### 4.4.3. The development of surface features

Over the full observation period from 1952 to 2018, Miage Glacier has seen an increase in ice cliff area from 17,326 $m^2$ to 47,615 $m^2$ and the presence of supraglacial ponds has grown from zero to 6,047 $m^2$ indicating a further state of the deterioration scenario and evolution into 'Regime 2' (Benn et al., 2012) (Table 4.3). Furthermore, a distinct increase in supraglacial pond area and ice cliff density since the 1990s could represent a response to an increase in temperature and precipitation in the early 1990s (Salerno et al., 2014). Such an increase in surface features is likely to have future implications for the evolution and mass balance of Miage Glacier (e.g. Benn et al., 2012; Pellicciotti et al., 2015; Thompson et al., 2016; Watson et al., 2017b). Furthermore, ponded area is often used as a proxy for water storage and glacier ablation (Gardelle et al., 2011; Liu et al., 2015; Watson et al., 2016), yet small ponds are often overlooked and not included in such assessments.

The development of ice cliffs in a region where longitudinal crevasses previously dominated, emphasises the importance of pre-existing structures, which have become exposed and are subjected to enhanced ablation further promoting regions of high-relief and undulating topography (e.g. Mölg et al., 2020). The region of crevassing above the terminal lobes (Figure 4.2 and Figure 4.3) indicated a region of extensional strain normal to the direction of the crevasse as the ice flows into the separate terminal lobes has been observed since 1952 and has become more undulating over time. Thus, such regions are important to monitor and assess in terms of ablation patterns and evolution of debris-covered glaciers.

Locations of supraglacial pond formation are observed above the terminal lobes along the main valley trunk with repeated pond presence at similar locations. Concurrently, increased debris cover and reduced ice flow along the northern margin resulting from reduced mass transfer from Mont Blanc Glacier was observed. This represents a reduction of the driving stress and hence promotes glacier stagnation and reduces the likelihood of intercepting englacial conduits (Quincey et al., 2007; Watson et al., 2016; Dehecq et al., 2019). Thus, many of the supraglacial ponds were observed to form in two zones; one covering a band from the southern to the northern margin located above Lake Miage (Zone 1) and the second on the southern terminal lobe (Zone 2) (Figure 4.7), with limited up-glacier ponds where glacier flow is considered to be more active. The steeper terminal lobes further add to inhibit pond development. The distribution of supraglacial ponds are further attributed to topographic controls of the valley and ice thickness due to overdeepenings at the bed and may have influenced the presence of a persistent pond at S1 since 2012 as in Figure 4.8 (Farinotti et al., 2019; Magnin et al., 2020; Viani et al., 2020). The rotation of the glacier into the valley, Val Veny, is likely to cause intense lateral drag and extensional stress previously observed on the Forni Glacier (Azzoni et al., 2017). Such a regime is considered to have promoted the formation and of ice cliffs and supraglacial ponding on Miage Glacier similar to those observed on Langtang Glacier, Nepal by Kraaijenbrink et al. (2016b), which formed near confluences from tributary glaciers in regions of transverse compression and associated increased strain acting to close englacial conduits, limiting drainage and promote ponding.

In addition to the glacier flow regimes and topographic controls, which are likely to exert controls on the locations where supraglacial ponds tend to form, it is considered that ponds are likely to occur in locations associated with pre-existing ice weaknesses. Supraglacial ponds form where regions of structural weakness can be exploited, such as crevasse traces and englacial conduits, and thus often coincide with drainage and expansion processes as observed at Spillway Lake (Benn et al., 2017). It is presumed that the presence of pre-existing structural weaknesses are also play a role in determining the location of pond formation. Many debris-covered glaciers are located in high-mountain regions, which commonly have large icefalls such as the Khumbu Glacier, Nepal (Fushimi, 1977). Icefalls often dominate the glacier dynamics resulting in a complex structure and

inherent structural weaknesses. Examples in the Alps identified a ring fault observed on the Forni Glacier tongue, Switzerland, which was later replaced by an ice-contact lake (Azzoni et al., 2017). The locations of supraglacial ponds at Miage Glacier are typically observed close to regions of crevassing upglacier and in areas of ice cliffs and crevasses as evident with S5, which formed in a region previously dominated by undulating surface topography and ice cliffs (Figure 4.11). It is therefore considered that pre-existing structural weakness in the ice once intersected with meltwater, have the potential to be exploited and form sections of exposed ice initiating the formation of ice cliffs or supraglacial ponds and thus ponds and cliffs are often identified in regions of high relief and supraglacial streams (Mölg et al., 2020). Furthermore, Zone 2 represents the higher positions of ponds on the glacier surface with limited ponding up-glacier attributed to an extensive supraglacial drainage system upglacier where debris is comparatively thinner and reduced efficiency of the lower glacier hydrological system (Fyffe et al., 2012). Thus, the combination of debris cover, glacier flow, valley and bed topography, and the hydrological system exploiting pre-existing ice weaknesses are important factors in controlling the distribution of ponding on the surface of Miage Glacier.

## 4.5. Summary

Structural mapping and analysis of surface features at Miage Glacier from 1952 to 2018 has enabled assessment of the evolution of the glacier dynamics. Miage Glacier represents a compound and complex glacier consisting of four main tributary glaciers with icefalls joining at the confluence with the valley tongue thus resulting in multiple flow units with heavily crevassed and faulted glacier ice. The overall glacier dynamics appear to have gone from one of an active ice flow regime with increased glacier activity in the 1980s, to one of deterioration since the 1990s. The changes are largely evident on the glacier valley tongue with increasing debris cover (+10% from 1996 – 2018) and increasing total area of supraglacial ponds (>6000 $m^2$ by 2018) and ice cliffs on the lower section (+308% since 1988). Collapse features are evident around the base of Mont Blanc Glacier icefall, an ice cliff structure, and at the northern lobe terminus. It is expected that if climatic change progresses as predicted, Miage Glacier will continue to deteriorate with an increase in the number and extent of ponds, ice cliffs and collapse features.

This study has shown that repeat structural analysis is able to provide important insights into both long- and short-term glacier evolution to better understand the response to current and future conditions. Furthermore, analysis has highlighted the time period since the 1990s as key in terms of its deterioration and the importance of supraglacial ponds and ice cliffs on future glacier evolution, and the potential implications of debris cover, glacier flow, valley and bed topography, and the hydrological system exploiting pre-existing ice weaknesses in the development and

distribution of ice cliffs and supraglacial ponds. Further analysis of the glacier dynamics over this period of sustained decay (1990 – 2018) is required to further assess and understand the processes of the evolution of Miage Glacier. Quantifying changes in mass balance and surface velocity over this time period, and exploring contemporary interactions between glacial lakes and ice cliffs may provide further insight into debris-covered glacier evolution. These will be examined in Chapters 5 and 6.

# Chapter 5 : Mass balance and surface velocity of Miage Glacier

## 5.1. Introduction

The previous chapter highlighted the development of surface features and an undulating surface topography since the 1990s. As previously recognised (see Chapter 2), such surface features are important for altering glacier mass balance and ice dynamics. Thus, this chapter is concerned with the mass balance and surface velocity of the debris-covered Miage Glacier in the Mont Blanc massif, European Alps, over nearly three decades from 1990 to 2018. The relatively recent development of supraglacial ponds and ice cliffs on Miage Glacier (Figure 4.4) may have an important, yet under-appreciated, role in influencing the mass balance. The presence of glacial lakes at Miage Glacier has been documented (Tinti et al., 1999; Diolaiuti et al., 2005), but supraglacial ponds have received little detailed attention, with most studies focussing on the ice-marginal lake, Lake Miage, located on the southern margin as the glacier turns eastwards into Val Veny (Figure 3.5).

Debris-covered glacier response to climatic variability remains poorly understood because of the complex feedbacks between climate, mass balance, velocity, change in debris cover and surface features (ice cliffs and ponds). Studies that integrate observations of these elements over annual, decadal and centennial timescales, and across the full glacier extent can help to unpick some of these complexities. This chapter provides a detailed appraisal of the dynamics of the debris-covered Miage Glacier over a 28-year time period from 1990 to 2018. This study overlaps with previous census periods for this glacier covering 1913 to 2012 (Thomson et al., 2000; Diolaiuti et al., 2009; Berthier et al., 2014), enabling long-term evolution and dynamics to be assessed. Specifically, the objectives of this study are: (i) to assess topographic changes of Miage Glacier over multi-decadal and multi-annual time scales; (ii) to assess the role of supraglacial ponds and ice cliffs on Miage Glacier dynamics; and (iii) to place the findings within the broader context of long-term observations at this glacier. Overall, this work provides an integrated assessment of the long-term evolution and feedbacks between mass balance, velocity, and surface features, which aids our understanding of debris-covered glacier response to climatic change in the world's high mountain regions.

## 5.2. Methods

A range of data sources were utilised for this study including satellite imagery for DEM production, surface velocity and surface gradient analysis (Table 5.1). Satellite data ranged from coarse resolution 30 m Landsat-derived surface displacements from 1990/91 to 2017/18, to high-resolution SPOT (1990, 2016 and 2018 data supplied by European Space Agency (ESA)), LiDAR Digital Terrain Model (DTM; 2 m) (2008 supplied by Valle d'Aosta; http://metadati.partout.it/metadata_documents/ Specifiche_LIDAR.pdf), and Pleiades (2012 – 2014) (data supplied by ESA) DEMs (Table 5.1). All analyses were carried out in PCI Geomatica

Orthoengine, open-source image correlation software CIAS (Kääb and Vollmer, 2000; Heid and Kääb, 2012) and ArcGIS.

**Table 5.1:** Data sets used within this study (SPOT and Pleiades data provided by ESA, 2008 LiDAR DEM from Valle d'Aosta). All datasets used the panchromatic band for DEM extraction and SWIR for surface velocity analysis.

| Date of acquisition (dd/mm/yr) | Sensor | Image Resolution (m) | Image Pairs | Data extracted |
|---|---|---|---|---|
| 26/08/2018 | SPOT-7 | 1.5 | Stereo | DEM/ Surface gradient |
| 12/10/2016 | SPOT-7 | 1.5 | Stereo | DEM/ Surface gradient |
| 26/08/2015 | TerraItaly Orthophoto | 0.2 | - | Aid GCP collection |
| 02/10/2014 | Pleiades 1B | 0.5 | Stereo | DEM/ Surface gradient |
| 19/08/2012 | Pleiades 1A | 0.5 | Stereo | DEM/ Surface gradient |
| 20/08/2008 | LiDAR – Valle d'Aosta | 2.0 | - | DEM/ Surface gradient |
| 19/08/1990 | SPOT-1 | 10.0 | 2 overlapping images | DEM/ Surface gradient |
| 22/07/1990 | SPOT-1 | 10.0 | | |
| 20/09/1989 | SPOT Ortho | 10.0 | - | Aid GCP collection |
| 16/08/1990 | Landsat5 TM | 30.0 | | Surface velocity |
| 19/08/1991 | Landsat5 TM | 30.0 | | |
| 16/07/2008 | Landsat5 TM | 30.0 | | Surface velocity |
| 05/09/2009 | Landsat5 TM | 30.0 | | |
| 19/08/2017 | Landsat8 OLI | 30.0 | | Surface velocity |
| 23/09/2018 | Landsat8 OLI | 30.0 | | |

### 5.2.1. Digital Elevation Models (DEM) extraction

The data sets used for DEM production were acquired during the ablation season to provide input images with little or no snow cover at similar dates for each year (ideally July to September). The number of useable data sets was limited by cloud cover and appropriate viewing-angles required for elevation extraction. Where possible, contemporaneous tri-stereo Pleiades data were used for higher accuracy DEMs to be produced due to the inclusion of nadir imagery.

All DEMs (1990 – 2018) were produced based on automatic stereo-correlation using the normalised cross correlation (NCC) algorithm within PCI Geomatica Orthoengine. The images were aligned based on the Rational Polynomial Coefficient (RPC) models and geolocation was improved by use of additional Ground Control Points (GCPs) from high-resolution 2015 orthoimagery (0.2 m). Tie-points were then identified in each image pair (Table 5.2). GCPs based on ortho-corrected imagery from 1989 with the same resolution were used to improve the georeferencing. Tie-points were then automatically selected in corresponding image pairs. GCPs and tie-points maintained low residuals, <5.5 pixels equating to <16 m for the 1990 DEM, and <3 m for all other DEMs. All automatically

assigned GCPs and tie-points were manually checked to remove any erroneous points. The number of GCPs varied depending on the ability to accurately identify matching locations (Table 5.2). As such, increased numbers of tie-points were used to aid point matching for elevation extraction.

**Table 5.2:** Summary of the GCPs and tie-points used to enhance the alignment of the imagery prior to DEM extraction.

| DEM | Number of GCPs | Residuals X, Y (Pixels) | Number of tie-points | Residuals X, Y (Pixels) |
|---|---|---|---|---|
| 1990 | 90 | 0.79, 0.34 | 150 | 1.56, 0.23 |
| 2012 | 2 | 1.53, 2.10 | 96 | 0.12, 0.03 |
| 2014 | 2 | 2.18, 5.41 | 64 | 0.22, 0.06 |
| 2016 | 36 | 0.39, 0.64 | 48 | 0.14, 0.04 |
| 2018 | 16 | 0.54, 1.51 | 40 | 0.10, 0.03 |

During the DEM production, smoothing was set to medium with a Wallis filter in PCI Geomatica Orthoengine to improve image contrast in areas of shadow and reduce noise in the resulting models (Baltsavias et al., 2007). DEMs were produced at extra high detail within mountainous terrain to enable extraction of finer details including ice cliffs to produce a geocoded DEM output at twice the resolution of the input data and range from a 20 m 1990 DEM, to two 1 m resolution Pleiades datasets from 2012 and 2014. SPOT6 and 7 are now available in 12-bit encoding and are therefore comparable to Pleiades data providing higher radiometric resolution and improved contrast over snow/ice, which reduces the signal saturation (e.g. Berthier et al., 2014). However, as Miage Glacier is mainly debris covered, this improvement for mapping is less important in this study with the exception of the higher accumulation zones and tributary glaciers.

The DEMs were cleaned, edited and assessed based on the correlation scores. Correlation coefficient scores range from 0 indicating a total mismatch, to 1 indicating a perfect match for each image pixel (Cheng, 2015). Pixels with poor correlation resulting from poor matches (<0.5) and identifiable interpolation errors outside of the glacier extent were removed to aid co-registration. A total of five DEMs were generated from satellite images to determine temporal change in surface elevation and geodetic mass balance.

#### 5.2.1.1. DEM differencing

In order to assess change over time, DEM differencing was carried out based on the co-registration method developed by Nuth and Kääb (2011). This method provides a workflow for DEM co-registration and bias correction via minimising root mean square residuals of the elevation biases over stable terrain as previously detailed in Robson et al. (2018). Unstable areas within the imagery including all glaciated areas, were masked out to aid co-registration on stable terrain. Each pair of

DEMs (e.g. 1990 and 2008) were co-registered separately. Elevation bias is stronger on steeper terrain and was therefore normalised for slope and plotted against aspect. This process is reiterated until the improvement of the standard deviation of the residual over stable terrain was less than 2% (Figure 5.1). DEM co-registration shifts of each pair were less than 5.1 m (Table 5.3).

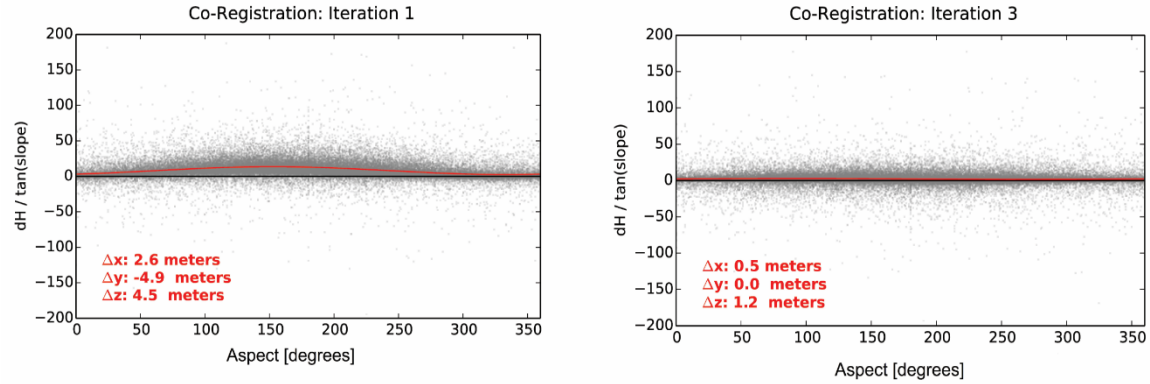


**Figure 5.1:** Example plots of the coregistration method showing slope normalised terrain elevation differences between two DEMs over stable (non-glacier) terrain A: before co-registration, and B: after 3 iterations. The co-registration shifts that were applied during the processing are shown in red text.

Filtering and editing was undertaken with pixels with surface changes exceeding three times the standard deviation of the stable terrain elevation bias removed and spline (area <10 pixels) and polynomial (areas >10 pixels) interpolations used to fill the gaps following the approaches by Bolch et al. (2011) and Gardelle et al. (2013).

**Table 5.3:** DEM co-registration shifts and DEM differencing uncertainty. The mean deviation, standard deviation and uncertainty are based on the co-registered DEM pairs. Statistics are based on stable (non-glacier) terrain. DEM differencing uncertainty represents the sum of standard errors for each 100 m elevation band.

| DEMs | X (m) | Y (m) | Z (m) | Mean deviation (m) | Standard deviation (m) | DEM differencing uncertainty (m) |
|---|---|---|---|---|---|---|
| 1990-2018 | -5.1 | 0.7 | -2.1 | -0.2 | 24.6 | 0.22 |
| 1990-2008 | -2.8 | -3.8 | -2.6 | 1.0 | 13.5 | 0.27 |
| 2008-2018 | 1.0 | 3.7 | -0.6 | -0.7 | 6.4 | 0.12 |
| 2012-2018 | 1.8 | 2.5 | 0.5 | 0.6 | 5.4 | 0.10 |
| 2012-2014 | 1.6 | -4.4 | -0.2 | 0.7 | 4.3 | 0.10 |
| 2014-2016 | -3.2 | 1.9 | -0.4 | -1.0 | 4.8 | 0.09 |
| 2016-2018 | 3.2 | 2.9 | 0.5 | 0.5 | 5.9 | 0.20 |

#### 5.2.1.2. Geodetic mass balance and surface elevation change

Surface elevation change was calculated based on the mean change over each time period of DEM differencing for areas delineated by glacier extents relevant to that time period. The geodetic mass balance was determined based on an assumed ice density of 850 ± 60 kg $m^{-3}$ (Huss, 2013). Emergence velocity was not calculated for this study following commonly used methods for glacier-wide geodetic mass balance calculations (e.g. Thomson et al., 2000; Paul et al., 2007; Gardelle et al., 2013; Pellicciotti et al., 2015; Berthier et al., 2016; Thompson et al., 2016), but this is consistent with previous studies of glacier thickness change (e.g. Thomson et al., 2000; Diolaiuti et al., 2009). However, it is acknowledged that by not considering emergence velocity a source of uncertainty is introduced.

In order to determine the uncertainty for glacier surface elevation change and geodetic mass balance, the approach outlined by Gardelle et al. (2013) as described by Falaschi et al. (2019) was used. This method accounts for the uncertainties relating to (i) the volume to mass conversion ($Ep$), (ii) the uncertainty related to glacier area digitisation ($Ea$), and (iii) the glacier volume change uncertainty ($E\Delta v$). A density of 850 ± 60 kg $m^{-3}$ was used to convert the ice volume to a mass ($Ep$), following Huss (2013) and a glacier area uncertainty of 5% based on the value from repeat digitisations ($Ea$). The total volume change uncertainty ($E\Delta v$) was determined over 50 m elevation bands ($E\Delta vi$) based on the standard error (SE). The standard error (SET) considers the standard deviation of elevation changes over stable terrain (Equation 5.1), the number of pixels in the DEM difference in that elevation band (Equation 5.2), and the degree of spatial autocorrelation, which, based on Bolch et al. (2011), was taken to be 20 times the pixel size (King et al., 2017). The volume change uncertainty per elevation band ($E\Delta vi$) was then summed-up over the entire glacier (Equation 5.3). Finally, *Ep*, *Ea* and $E\Delta v$ were combined in a root mean square sum (Equation 5.4). The surface elevation change uncertainty ranged from ±0.01 to ±0.13 m, and the geodetic mass balance uncertainties ranged from ±0.09 to ±0.27 m w.e. $a^{-1}$ (Table 5.3).

$$E\Delta h = \frac{\sigma stable}{\sqrt{N}} \quad \textbf{Equation 5.1}$$

$$N = \frac{Ntot \times PS}{2d} \quad \textbf{Equation 5.2}$$

$$E\Delta vi = \sum_i^n E\Delta hi * Ai \quad \textbf{Equation 5.3}$$

$$E\Delta tot = \sqrt{E^2\Delta v + E^2 p + E^2 a} \quad \textbf{Equation 5.4}$$

### 5.2.2. Surface velocity

Surface velocity was measured using a feature-tracking approach. Pairs of Short Wave Infrared (SWIR) band Landsat5 Thematic Mapper (TM) and Landsat8 Operational Land Imager (OLI) imagery from 1990/1991, 2008/2009 and 2017/2018 were used to determine annual glacier surface velocities (Table 5.1) from the same orbit (row/path) to aid velocity tracking (Sam et al., 2016).

Features on the surface were matched using a normalised cross-correlation of orientation (NCC-O) images using open-source software, CIAS (Kääb and Vollmer, 2000). Orientation images were used to reduce the influence of scene illumination by using gradients between neighbouring pixel values instead of raw digital numbers where variations in scene illumination and presence/absence of shadow varied (Robson et al., 2018). Surface features were tracked in CIAS providing displacement vectors. Reference block size and search size were set in relation to the input image resolution while the search size was set to twice the expected surface velocity. As the input images all had the same resolution, the block, search and output resolution values were set to 15, 20 and 30 respectively.

Displacement vectors were filtered by initially removing those with a signal to noise ratio (SnR) <0.5. They were then filtered by direction and magnitude, removing any apparent erroneous points. A 3x3 focal statistics filter was used to remove displacement vectors, which varied more than 20% in direction or magnitude to the surrounding mean values (Robson et al., 2018). Manual filtering was required including removal of points associated with cloud or shadow. Displacement vectors were then converted into surface velocity per year.

GNSS positions of 6 boulders were recorded during field visits in 2017 and 2018 using a Trimble Geo7x GNSS and post-processed using RINEX data from the Morgex base station <15 km from Miage Glacier. The mean accuracy of position data was ±0.03 m, enabling comparison of surface velocity rates around Lake Miage. Analysis of boulder movement shows a mean of 12 m $a^{-1}$ in the vicinity of Lake Miage complementing the results from the 2017 – 2018 surface velocity data.

Surface velocity accuracy was determined by measuring displacements over stable terrain based on 87 random points <500 m from Miage Glacier termini. The points were situated along stable terrain with a gentle slope, free from shadow and snow/cloud were identified from satellite imagery and fieldwork. The accuracy associated with the surface velocity feature tracking is stated in Table 5.4.

**Table 5.4:** Accuracy assessment of the surface velocity feature tracking (m $a^{-1}$).

| **Velocity data set** | **Standard Deviation (over date time)** | **Mean (m $a^{-1}$)** |
|---|---|---|
| 1990 – 1991 Landsat 5 | 5.29 | 9.18 |
| 2008 – 2009 Landsat 5 | 2.25 | 5.71 |
| 2017 – 2018 Landsat 8 | 4.82 | 6.58 |

### 5.2.3. Longitudinal profile and surface gradient

The longitudinal profile of Miage Glacier was assessed based on the output DEMs. The longitudinal profile of the centreline was extracted in ArcGIS and plotted to enable the overall gradient in the profile to be calculated and provides an update to that presented by Smiraglia et al. (2000). The gradient was calculated for the total distance from the glacier southern lobe termini to the base of Bionnassay Glacier where the tributary glaciers join. The profile gradient was then also calculated for the debris-covered extent as derived from Chapter 5 and the region where supraglacial ponds were present.

## 5.3. Results

### 5.3.1 Surface elevation change and geodetic mass balance 1990 – 2018

The overall trend in elevation change across the 1990 to 2018 study period is one of downwasting (Figure 5.2). Between 1990 and 2018, Miage Glacier experienced substantial downwasting of $-1.01 \pm 0.09$ m $a^{-1}$ on average; however, thinning rates have slowed from $-1.07 \pm 0.16$ m $a^{-1}$ between 1990 and 2008, to $-0.85 \pm 0.06$ m $a^{-1}$ between 2008 and 2018 (Table 5.5).

**Table 5.5:** Vertical surface elevation change and geodetic mass balance of Miage Glacier from 1990 to 2018 based on DEM differencing. Standard errors for elevation change and uncertainty values for geodetic mass balance provided.

| Date | Surface elevation change (m $a^{-1}$) | Mean geodetic mass balance (m w.e. $a^{-1}$) | Debris-covered region surface elevation change (m $a^{-1}$) |
|---|---|---|---|
| 1990 – 2018 | −1.01 ± 0.09 | −0.86 ± 0.27 | −1.25 ± 0.09 |
| 1990 – 2008 | −1.07 ± 0.13 | −0.88 ± 0.22 | −1.17 ± 0.13 |
| 2008 – 2018 | −0.85 ± 0.01 | −0.67 ± 0.12 | −1.30 ± 0.01 |
| 2012 – 2018 | −0.62 ± 0.02 | −0.53 ±0.10 | −1.82 ± 0.02 |
| 2012 – 2014 | −0.51 ± 0.10 | −0.35 ± 0.17 | −1.36 ± 0.10 |
| 2014 – 2016 | −0.45 ± 0.03 | −0.30 ± 0.09 | −0.92 ± 0.03 |
| 2016 – 2018 | −0.85 ± 0.10 | −0.64 ± 0.20 | −1.21 ± 0.10 |

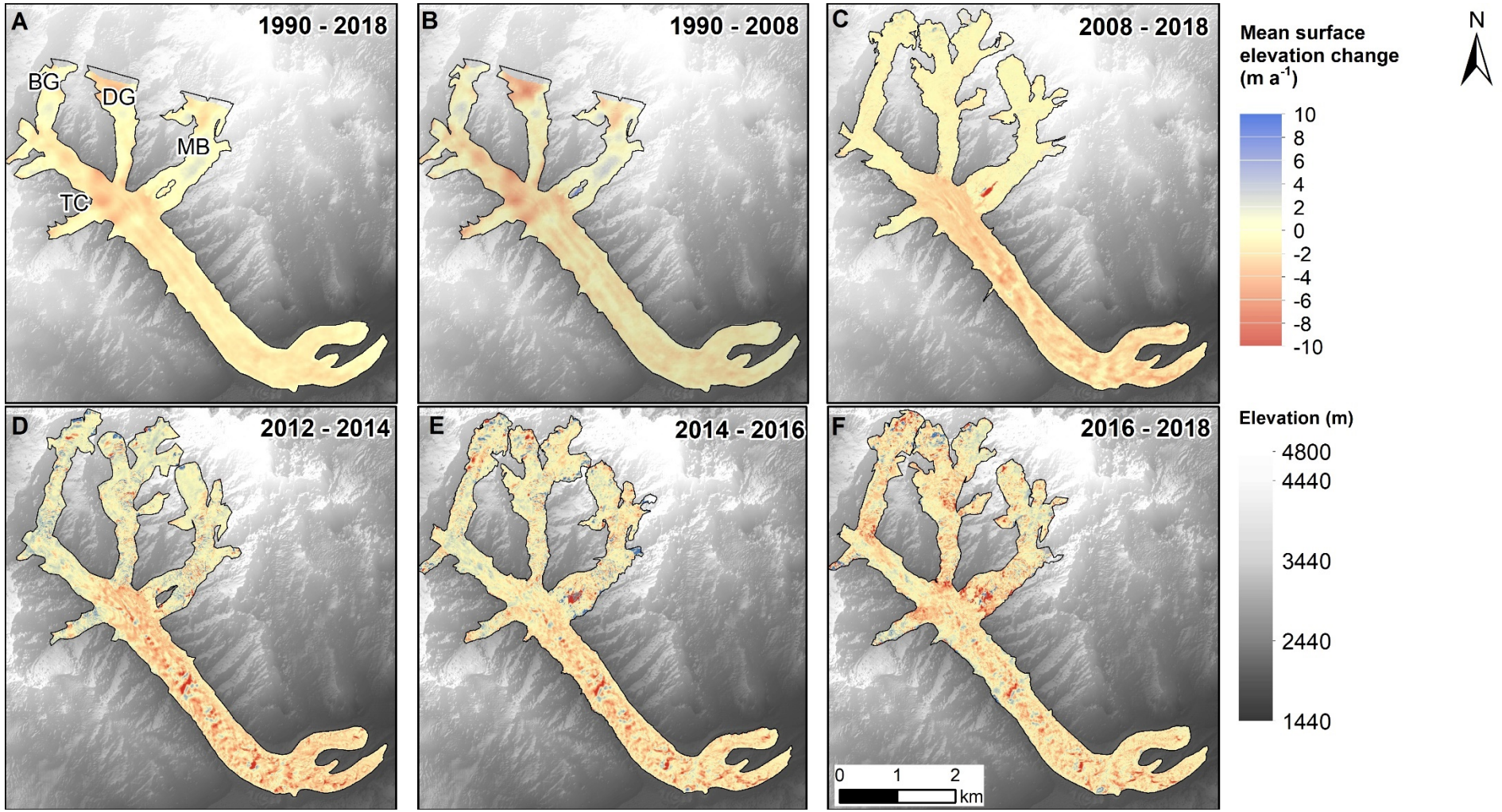


**Figure 5.2:** Mean annual surface elevation change in metres with a hillshaded elevation model as background. A: 1990 – 2018, B: 1990 – 2008, C: 2008 – 2018, D: 2012 – 2014, E: 2014 – 2016, F: 2016 – 2018. Note uncertainty associated with the nunatak at the base of Mont Blanc Glacier due to shadow in input data.

High thinning rates were evident at the base of Tête Carrée Glacier (TC) and Bionnassay Glacier (BG) where debris cover has expanded over the period (Figure 5.2). In comparison, the debris-covered valley tongue has undergone sustained downwasting over the full period, but thinning rates are reduced on the terminal lobes. From 1990 – 2018, the debris-covered region experienced mean annual downwasting of −1.25 ± 0.09 m $a^{-1}$; in comparison, the terminal lobes underwent thinning rates of −0.94 ± 0.09 m $a^{-1}$. The tributary glaciers present the largest increases in surface elevation associated with snow accumulation and ice dynamics at higher elevations (Figure 5.2).

Pleiades and SPOT6/7 DEM differencing from 2012 to 2018 enables recent change to be explored at higher spatial and temporal resolutions (Figure 5.2). Table 5.5 indicates that the rate of thinning has increased over the period 2012 to 2018 from −0.51 ± 0.04 m $a^{-1}$ between 2012 to 2014, to −0.85 ± 0.10 m $a^{-1}$ from 2016 to 2018, with a mean surface elevation change of −0.62 ± 0.02 m $a^{-1}$ over the period 2012 – 2018, yet these rates are lower than the 2008 – 2018 period indicating reduced mass loss in the last decade.

Heterogeneous elevation change is evident across the glacier surface with enhanced thinning at the base of Mont Blanc Glacier (MB) associated with a physical detachment and icefall events resulting in a visibly larger nunatak area. The nunatak at the base of Mont Blanc Glacier was often in shadow in the input data and likely to be responsible for the uncertainty associated with opposing trends in Figure 5.2. Collapse features at the base of Dome Glacier were also evident between 2012 and 2014 depositing an area of rock and ice of ~9343 $m^2$ to the glacier surface (Figure 5.3). Once deposited on the surface, debris will become entrained and increase debris to both the surface of the glacier and englacially.

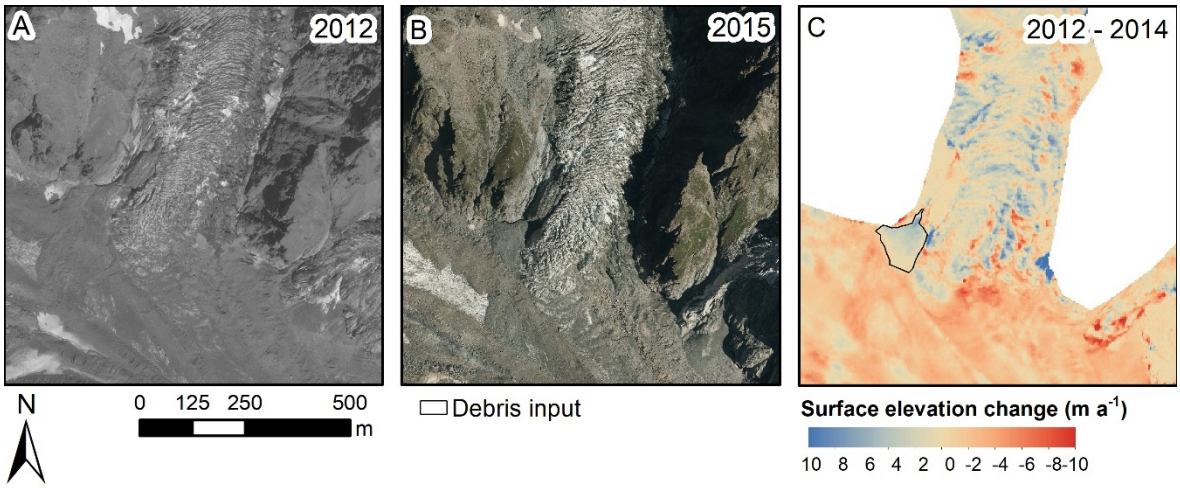


**Figure 5.3:** Debris inputs onto Miage Glacier from Dome Glacier. A: Image of the area before deposition. B: Area of deposition after the event. C: Amount of surface change between 2012 and 2014.

### 5.3.2. Surface velocity change 1990 – 2018

Over the observation period, the mean surface velocity of the glacier decreased by 46% from 35 ± 0.05 m $a^{-1}$ in 1990/91 to 16 ± 0.05 m $a^{-1}$ in 2017/18, (Figure 5.4). The ice in the terminal lobes has undergone a strong reduction in mean velocity over the same period from 20 ± 0.23 m $a^{-1}$ to 6 ± 0.11 m $a^{-1}$, a velocity reduction of 70%. Central parts of the northern and southern lobes are near stagnant at <3 m $a^{-1}$. The tributary glaciers and central valley section show the most vigorous flow rates but have also seen an overall decrease in velocity over the study period.

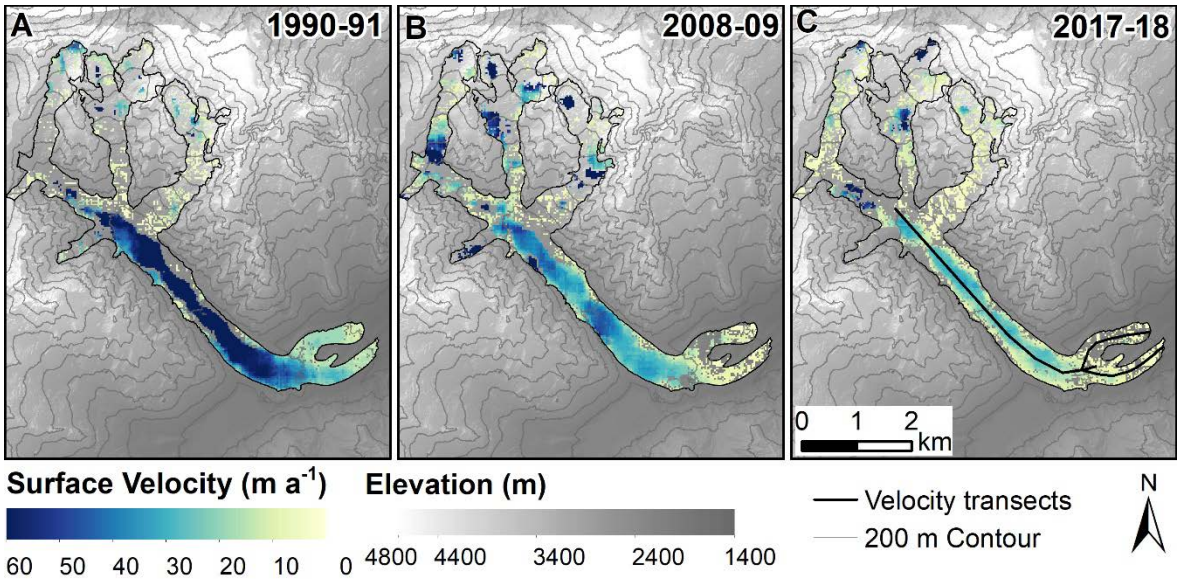


**Figure 5.4:** Landsat derived surface velocity displacements. A: 1990 – 1991, B: 2008 – 2009, , C: 2017 – 2018 with velocity transects used in Figure 5.5 and Figure 5.6. Contours at 200 m intervals.

The central valley section indicates active flowing ice. Surface velocity reduces once the ice flows eastwards into Val Veny and splits into the terminal lobes (Figure 5.5). The northern and southern lobes experienced a decrease in velocity within these areas.

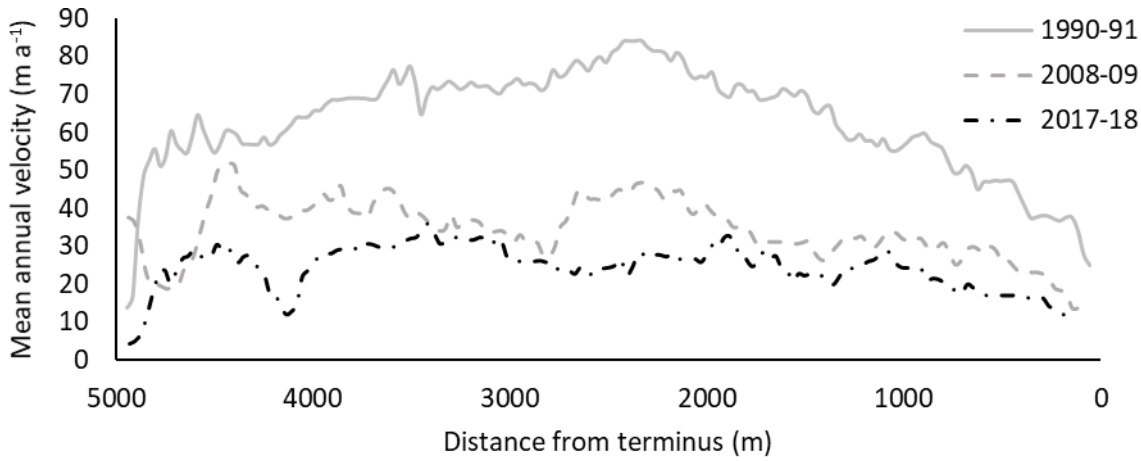


**Figure 5.5:** Landsat derived ice flow velocity fields with longitudinal profiles along the centreline to the top of the terminal lobes.

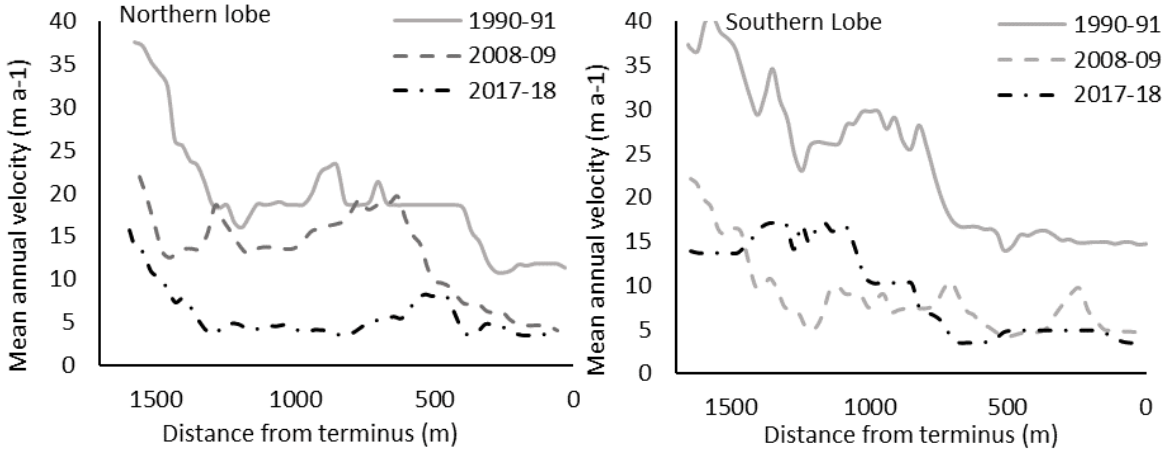


**Figure 5.6:** Downstream surface velocities along the northern lobe (left) and southern lobe (right) as shown in Figure 5.4C.

Faster ice flow is apparent on the central section flowing in a straight line down valley before the glacier splits into the terminal lobes and turns into Val Veny (Figure 5.5). Variations in ice flow are evident in transects along the terminal lobes with an overall decrease at the ice margins to rates of <5 m $a^{-1}$ (Figure 5.6).

### 5.3.3. Longitudinal profiles and surface gradients

The longitudinal gradient of the centreline has reduced modestly over the study period from 6.63 to 5.91° (Figure 5.7). Furthermore, the valley section from the base of Bionnassay Glacier to the top of the terminal lobes has changed very little from 5.21 to 5.15°. Supraglacial ponds are present on the section of the glacier with overall lowest and thus 'flattest' section, which has undergone very slight increase in gradient from 4.10° in 1990 to 4.82° by 2018.

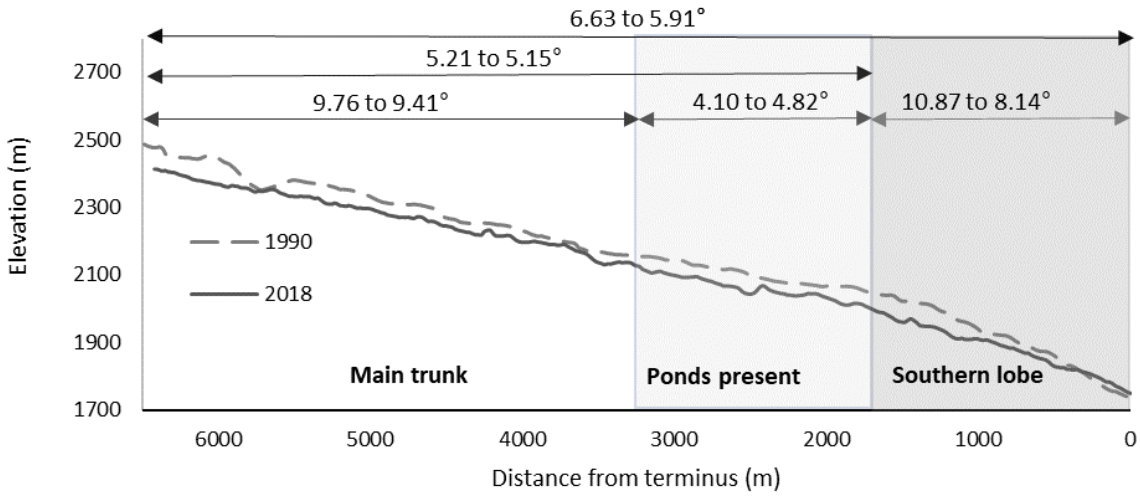


**Figure 5.7:** Longitudinal profile of the glacier centreline in 1990 and 2018.

### 5.3.4. Analysis of supraglacial ponds and ice cliffs

Surface elevation change patterns from 2012 to 2018 show specific regions with higher thinning rates (Figure 5.2) that are coincident with the locations of supraglacial ponds and ice cliffs (Figure 5.8). Areas of positive elevation change are evident attributed to advection of hummocky topography, pond water level change or debris redistribution. For each DEM, the associated surface lowering in areas with mapped supraglacial ponds and ice cliffs was extracted (Table 5.6). All ponds and ice cliffs present in the satellite imagery from 2012, 2013 and 2014 were merged and extracted from the 2012 – 2014 DEM differencing, and repeated for the 2014 – 2016 and 2016 – 2018 periods.

For the periods 2012 – 2014 and 2014 – 2016 comparable rates of surface lowering (−3.77 ± 0.10 m $a^{-1}$ and −3.79 ± 0.20 m $a^{-1}$ respectively) were determined at ice cliff locations. However, in the latter period of assessment (2016 – 2018) surface lowering had reduced to −3.48 ± 0.25 m $a^{-1}$ when ice cliffs presented a lower percentage of the debris-covered area during this time (Table 5.6).

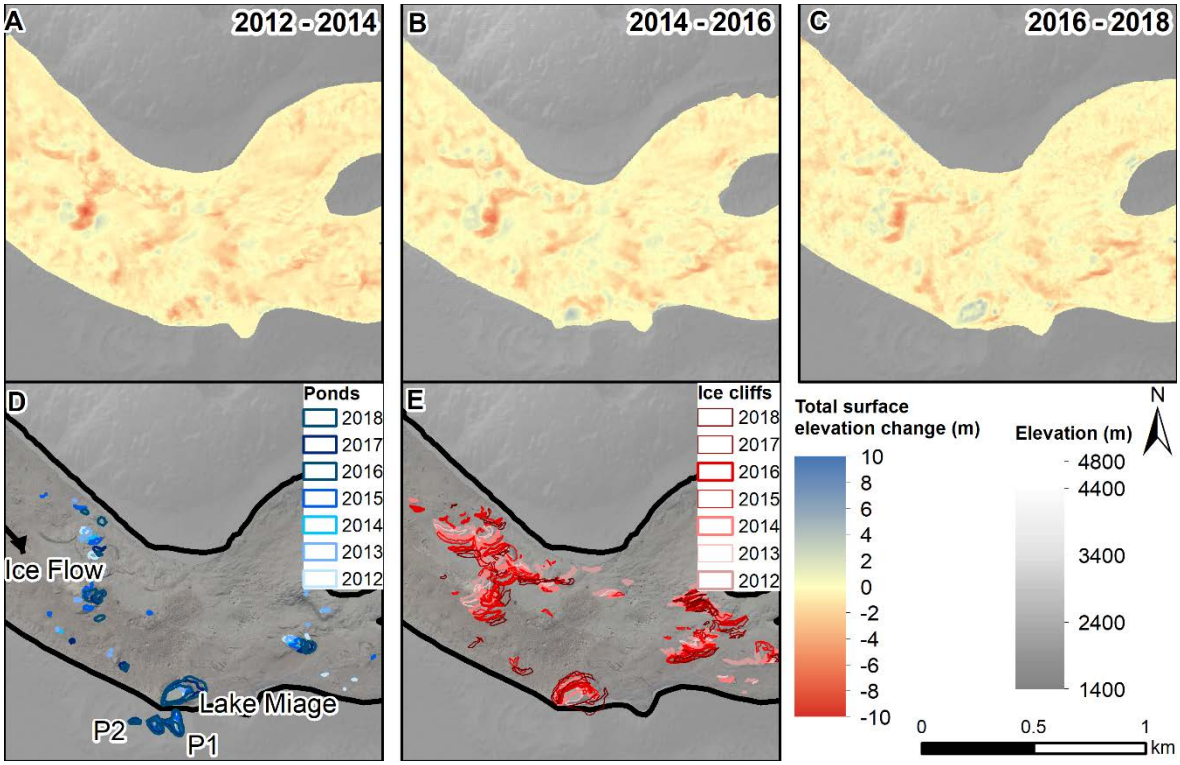


**Figure 5.8:** A: Total surface change from 2012 – 2014, B: Surface change from 2014 – 2016, and C: Surface change from 2016 – 2018, and D: Locations of supraglacial ponds from 2012 – 2018 and E: Locations of ice cliffs from 2012 – 2018.

**Table 5.6:** Variations in ablation rates associated with supraglacial ponds and ice cliffs, and density as a percentage of the debris-covered area from RGI6.0 analysis. Proportions of pond and ice cliff contributions to the total ablation rates are also calculated. Uncertainty was calculated at 5% for ice cliffs and 7% for supraglacial ponds.

| Year | 2012 – 2014 | 2014 – 2016 | 2016 – 2018 |
|---|---|---|---|
| Ice cliff elevation change (m $a^{-1}$) | −3.77 | −3.79 | −3.48 |
| Ice cliff density as % of glacier area | 1.07 | 1.32 | 0.99 |
| Ice cliff factor of mean surface lowering | 7.39 | 8.42 | 4.09 |
| Ice cliff % of total ablation | 7.64 | 9.1 | 4.0 |
| Pond elevation change (m $a^{-1}$) | −4.11 | −1.78 | −4.55 |
| Pond density as % of glacier area | 0.15 | 0.21 | 0.27 |
| Pond factor of mean surface lowering | 8.05 | 3.96 | 5.35 |
| Pond % of total ablation | 1.19 | 0.69 | 0.58 |

Although supraglacial ponds and ice cliffs account for up to 8 times the mean glacier surface lowering, the quantification is complex since ice cliffs also backwaste and energy dissipates beyond the pond outlines which is not accounted for, thus the figures in Table 5.6 represent minimum contributions.

## 5.4. Discussion

### 5.4.1. Recent and long-term evolution of Miage Glacier

As previously identified in Chapter 4, these data provide additional detail regarding glacier dynamics to assess the evolution of Miage Glacier through a period of continued climate warming since 1990 (+1.46°C over the 30–year period, Figure 3.3). Further to the data presented in Chapter 4, this chapter supports a state of downwasting and reduced velocity since 1990 following the small advance during the late twentieth century in response to positive mass balances between the 1960s to 1980s as discussed by Thomson et al. (2000) and Smiraglia et al. (2000) and observed elsewhere in the Alps (Diolaiuti et al., 2003; Huss, 2012). Over the period 1990 to 2018, these data reveal that Miage Glacier has transitioned into 'Regime 2', characterised by downwasting ice and glacier slowdown, in addition to surface water storage, and expanding debris cover as identified in Chapter 4.

In terms of volumetric changes, there has been only modest overall area loss from 1990 to 2018 (−11%) (Table 4.2), yet there has been continued and pervasive thinning, although the rate of thinning appears to have slowed overall (Table 5.5), possibly as a consequence of the expanding and suspected thickening debris cover that has the effect of slowing ablation rates. However, the most recent results show that the trend of thinning is non-linear, with mass loss of −0.35 ± 0.10 m w.e. $a^{-1}$ between 2012 and 2014, and a higher rate of −0.64 ± 0.20 m w.e. $a^{-1}$ between 2016 and

2018 (Table 5.5). In response to this continued thinning across the glacier, the longitudinal gradient of the centreline has reduced modestly over the study period from 6.63 to 5.91° (Figure 5.7). Furthermore, the valley section from the base of Bionnassay Glacier to the top of the terminal lobes has changed very little from 5.21 to 5.15°. Concurrently, Miage Glacier has slowed substantially (by ~46% on average) from 34 ± 0.05 m $a^{-1}$ in 1990 to 16 ± 0.05 m $a^{-1}$ in 2018, with near-stagnant flow rates on the terminal lobes (<3 m $a^{-1}$) (Figure 5.4).

These observations are broadly consistent with the evolution of debris-covered glaciers elsewhere that are experiencing negative mass balances in response to climate change, although with some key differences and complexities (e.g. Benn and Lehmkuhl, 2000; Scherler et al., 2011; Benn et al., 2012; Bolch et al., 2012; Rowan et al., 2015). Reduced flow rates and progressive stagnation are being driven by reduced inputs and progressive disconnection from tributary glaciers (exemplified by the rapid thinning of Mont Blanc Glacier base where it connects to Miage Glacier; Table 5.5), as well as thinning and flattening on the main tongue, which has the effect of reducing shear stress and internal deformation rates (e.g. Quincey et al., 2009; Dehecq et al., 2019). Less vigorous flow and sustained negative mass balance means that Miage Glacier struggles to evacuate debris that is sourced from valley slopes and that melts-out from englacial septa (e.g. Kirkbride and Deline, 2013). Consequently, the supraglacial debris cover has progressively thickened and extended further upglacier. Progressive thinning, flattening, slowing, and a reduction in the efficiency of meltwater evacuation has led to the development of supraglacial ponds and associated ice cliffs in recent years, representing localised hotspots of ablation (Figure 5.8 and Table 5.6; (Benn et al., 2012)).

### 5.4.2. Regional and global comparisons

The mass balance results presented here highlight the importance of a surface debris cover in moderating glacier response to climatic change, but also that debris-covered glacier responses can themselves be highly variable. Broadly, the negative mass balance of Miage Glacier is consistent with results from other studies in the Mont Blanc massif and the Alps more generally (Paul et al., 2007; Huss, 2012; Berthier et al., 2014; Rabatel et al., 2016; Vincent et al., 2017; Mölg et al., 2019; Zekollari et al., 2020). Between 2003 and 2012, mass loss from Miage Glacier was 19% lower (−0.84 ± 0.22 m w.e. $a^{-1}$) than the Mont Blanc regional average, which includes a number of clean-ice glaciers where rates of mass loss have been higher (Berthier et al., 2014). Across the European Alps more broadly, the 1990-2008 mean geodetic mass balance (−0.88 m w.e. $a^{-1}$; Table 5.5) is similar to the mean annual mass balance of −0.83 m w.e. $a^{-1}$ between 1990 – 2010 calculated from decadal means for the Swiss Alps (Huss et al., 2015).

The presence of a continuous, thick debris cover at Miage Glacier appears to retard mass loss compared to nearby clean-ice glaciers, and the most rapid thinning rates are currently focussed

around supraglacial ponds and ice cliffs (Sakai et al., 2000; Reid and Brock, 2014; Thompson et al., 2016; Mölg et al., 2019). Similar to the 1990 – 2018 trend at Miage Glacier, the debris-covered Glacier de Tsarmine also exhibited a deceleration of lowering rates since 1999 despite increasing air temperatures (Capt et al., 2016). By contrast, Zmuttgletscher in Switzerland, has a thinner and less extensive debris cover, and was found to exhibit similar mass loss to clean-ice glaciers; although supraglacial ponds were few and their influence on ablation not analysed (Mölg et al., 2019). These seemingly contradictory results highlight the complexity of responses to climate change, not just when comparing ablation rates of debris-covered glaciers with clean-ice glaciers, but also when comparing the responses of different debris-covered glaciers to one another (e.g. Pellicciotti et al., 2015; Vincent et al., 2016; Salerno et al., 2017).

The reasons behind the most recent 2016 – 2018 intensification in thinning rates at Miage Glacier compared to 2012 – 2014 (from 1990 – 2008 to 2008 – 2018) are unclear (Table 5.5), but the results highlight the non-linear nature of ablation of debris-covered glaciers. One possibility is a lagged response to temperature and precipitation changes and associated changes in ice flux, as seen elsewhere (e.g. Kääb et al., 2012; Senese et al., 2012). Continued monitoring will be required to assess to what extent this represents a longer-term trend of enhanced thinning rates, or merely a brief deviation.

The observation that Miage Glacier has slowed over the course of the 1990 – 2018 monitoring period is consistent with similar findings from across the European Alps, including Switzerland (Capt et al., 2016; Mölg et al., 2019), Austria (Kellerer-Pirklbauer and Kulmer, 2019), and France (Vincent et al., 2009). Likewise, the increasing debris cover at Miage Glacier is similar to that seen since the 1990s on Zmuttgletscher (Mölg et al., 2019) and on the glaciers of the Ortles-Cevedale Group, Italy (Azzoni et al., 2018).

The recent emergence and growth of supraglacial ponds and ice cliffs on Miage Glacier is a particularly striking surface expression of the transition to 'Regime 2' of the debris-covered glacier evolution model (Benn et al., 2012). These features have played an important role in the glacier's mass balance, and may continue to do so in the future. Specifically, there is a spatial coincidence between areas of rapid thinning, reduced velocity at the valley margins, and the locations of ice cliffs and ponds (Figure 5.8). These surface features contribute disproportionately to ablation, as has been reported for other sites globally (Sakai et al., 2002; Nicholson and Benn, 2006; Immerzeel et al., 2014; Pellicciotti et al., 2015; Ragettli et al., 2015; Brun et al., 2016; Thompson et al., 2016; Miles et al., 2017a). Mapped ice cliffs between 2016 and 2018 account for up to 8 times the mean surface lowering equating to ~4% of total geodetic mass loss yet only account for ~1% of the total glacier area, although there has been a reduction in cliff density and contribution to negative mass balance since 2012 – 2014 (Table 5.6). Nonetheless, these results are comparable to those of Reid

and Brock (2014) who found that ice cliff ablation on Miage Glacier during 2010 – 2011 accounted for ~7.4% of total ablation, despite only covering 1.3% of the glacier area. Likewise, at Zmuttgletscher, Switzerland, ice cliffs were found to cover up to 1.8% of the debris-covered area, yet drove 5% of glacier-wide volume loss (Mölg et al., 2019). However, these figures for glaciers in the European Alps are substantially lower than those found on Lirung Glacier, Ngozumpa Glacier and Changri Nup Glacier in the Himalaya where ice cliff backwasting accounted for 69%, 40% and 23% of the total mass loss respectively despite a comparatively small area coverage (2%, 5% and 7% respectively) (Sakai et al., 1998; Thompson et al., 2016; Brun et al., 2018). Such disparity between the Alpine and Himalayan examples suggest substantial regional variations of contributions of ice cliffs to mass loss.

Supraglacial ponds at Miage Glacier accounted for up to 8 times the glacier-wide mean surface lowering and contributed between 0.58 and 1.19% of the geodetic mass loss in the 2012-2018 study period, despite only covering between 0.27 and 0.15% of glacier area respectively. These values are lower than that contributed by ice cliffs, explained in part by the lower density of ponds across the glacier surface (Table 5.6). Although, there are no comparable data on supraglacial pond-related glacier ablation in the Alps, by comparison, in the Langtang region of Nepal, up to 12.5% of glacier ablation is driven by supraglacial ponds, despite ponds only covering 1.69% of the debris-covered area (Miles et al., 2018). This disproportionate ablation rate per unit area coverage is similar in magnitude to the 2012 – 2014 values at Miage (Table 5.6; i.e. ablation percentage is around 7.4 to 7.9 times the percentage of glacier area cover). However, at Miage Glacier, there is an apparent slowdown in the contribution of supraglacial ponds to surface lowering and geodetic mass balance loss from 2012 – 2014 to 2016 – 2018 (Table 5.6).

Many ponds on Miage Glacier, and other debris-covered glaciers, are coeval with adjacent ice cliffs (e.g. Thompson et al., 2016; Watson et al., 2017a). Together, supraglacial ponds and ice cliffs covered between 1.2 to 1.5% of the total glacier area but were typically responsible for a disproportionately large amount of the net annual mass loss, ranging from 5 to 10% of the overall ablation between 2012 and 2018 (Table 5.6). However, the contribution of supraglacial ponds and ice cliffs to the geodetic mass balance is likely to be underrepresented in this study because ablation rates distal to these focal points are not quantified.

## 5.5. Summary

This study provides an integrated assessment of multi-decadal (1990 – 2018) changes in geodetic mass balance, surface velocity, and the roles of supraglacial pond and ice cliff development on Miage Glacier, Mont Blanc Massif, Italy. Miage Glacier has transitioned from a period of active flow and limited surface water storage during the twentieth century to one of downwasting ice with

continued thinning since 1990 (−0.86 ± 0.27 m w.e. $a^{-1}$) and a dramatic reduction in glacier surface velocity from a mean of 34 ± 0.05 m $a^{-1}$ in 1990 to 16 ± 0.05 m $a^{-1}$ in 2018. During the observation period, Miage Glacier has undergone significant widespread downwasting although surface lowering has slowed from −1.07 ± 0.13 m $a^{-1}$ between 1990 and 2008, to −0.85 ± 0.01 m $a^{-1}$ between 2008 and 2018, which is attributed to an expanding debris cover. Despite the long-term negative mass balance, recent surface lowering results show a deceleration in thinning indicating complex, non-linear changes over time. The presence of supraglacial ponds and ice cliffs serve to enhance mass loss locally and were responsible for ~5% of the total mass loss between 2016 and 2018, despite only covering 1.3% of the total glacier area. Further exploration and quantification of melt rates associated with supraglacial ponds and ice cliffs will provide additional constraint of the processes associated. This will be examined in Chapter 6.

With reference to other studies in the Alps and other high-mountain regions, this study illustrates the varied and complex response of debris-covered glaciers to climatic change. In general, Miage Glacier is entering a more advanced state of deterioration, although the contributions of ponds and ice cliffs to total mass loss are comparably lower than for Himalayan glaciers; Miage Glacier remains relatively steep limiting future expansion of supraglacial ponds and their associated ice cliffs. Comparisons with debris-covered glaciers in other regions will be examined in Chapters 7 and 8.

# Chapter 6 : Morphological analysis of glacial lakes and ice cliffs

## 6.1. Introduction

Glacial lakes have been identified as loci of enhanced glacier ablation and have been highlighted in Chapter 5 as an important component of the mass balance of Miage Glacier (e.g. Sakai et al., 2002; Nicholson and Benn, 2006; Immerzeel et al., 2014; Pellicciotti et al., 2015; Ragettli et al., 2015; Thompson et al., 2016; Miles et al., 2017a). Thus, monitoring glacial lake development, and the contribution to glacier mass loss is important to assess future impacts and contributions to debris-covered glacier dynamics and evolution.

Although supraglacial ponds and ice cliffs exhibited up to 8 times the mean glacier surface lowering, the quantification of this value is complex. Ice cliffs also backwaste in addition to surface lowering and energy dissipates beyond the pond outlines, which was not previously accounted for, thus the figures in Chapter 5 are considered to represent minimum contributions. Therefore, to further explore the influence and dynamics of supraglacial ponds and ice cliffs at Miage Glacier, bathymetric and photogrammetry surveys undertaken in 2017 and 2018 examined the evolution of five supraglacial ponds and Lake Miage, and their associated ice cliffs to reveal additional details of how important these features might be for the evolution of Miage Glacier. This chapter utilises photogrammetry surveys and Structure from Motion (SfM) workflows to determine ice cliff evolution alongside bathymetric surveys of adjacent ponds at Miage Glacier in 2017 and 2018. Specifically, this chapter (i) quantifies water storage change at the glacier surface and margins between 2017 and 2018; (ii) quantifies ice loss associated with the presence of supraglacial ponds and ice cliffs; and (iii) considers the development and evolution of surface features at Miage Glacier.

## 6.2. Methods

Bathymetric and photogrammetry surveys were undertaken in June/July 2017 that included four supraglacial ponds (S1 – S4), Lake Miage and three proglacial lakes (P1 – P3) with repeat surveys carried out June/July 2018 on three of the same supraglacial ponds (S1 – S2 and S4) and one additional pond (S5), and Lake Miage and proglacial lakes (Figure 6.1). The methods utilised for the bathymetric surveys, and photogrammetry surveys and quantification of change will be discussed in turn.

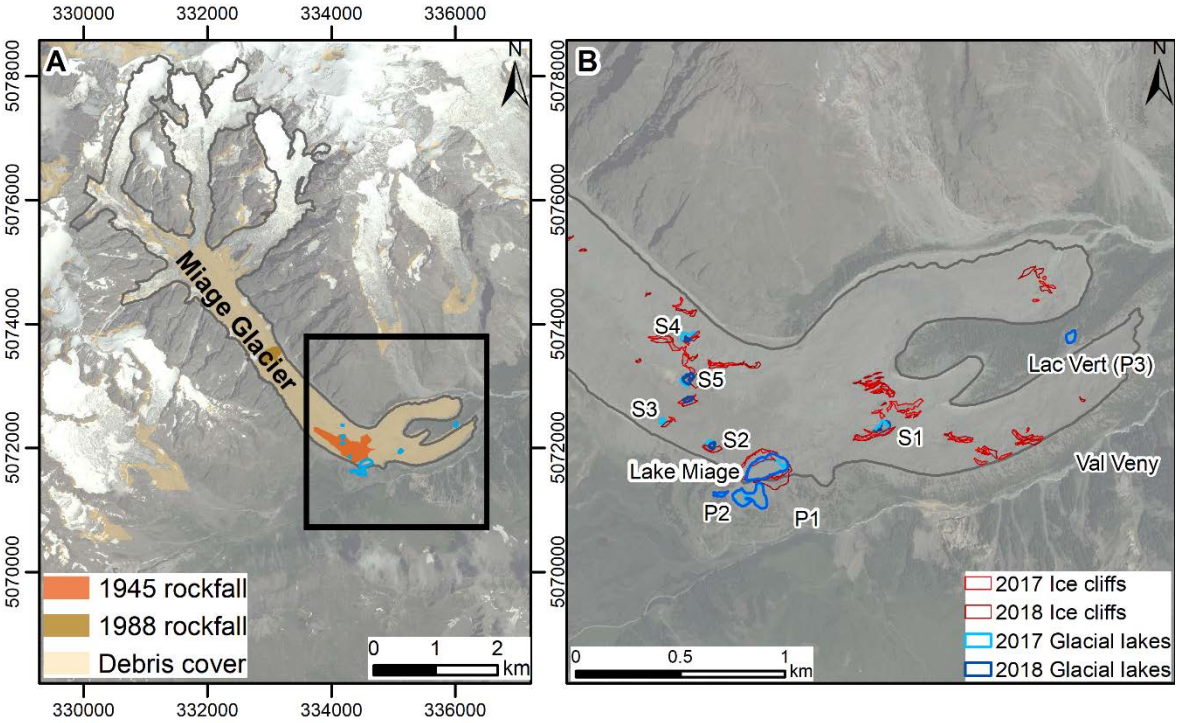


**Figure 6.1:** A: Location of Miage Glacier and the glacial lakes surveyed. Black box represents area in B: glacial lakes and ice cliffs present in 2017 and 2018.

### 6.2.1. Bathymetric surveys

Bathymetric surveys of the ice-marginal lake (Lake Miage), three proglacial lakes (P1 – P3) and five supraglacial ponds (S1 – S5, Figure 6.1) were undertaken in July 2017 and July 2018. A Seafloor Systems Hydrone remote control bathymetric survey boat with an Ohmex SonarMite BTX v4/5 echo sounder, with a reported accuracy of ±0.0025 m, was used wherever ponds with depths were sufficient to accommodate the survey boat. Although smaller ponds were present (<10 observed), they were too shallow to survey with the boat.

The level of the water edge, where accessible, was surveyed with a Trimble Geo7x GNSS and post-processed. RINEX data were collected from the base station in Morgex (<25 km from the glacier) to post-process the datasets. All GNSS data were post-processed to improve the accuracy. Lake and pond extents were accurate to a mean XYZ positional accuracy of ±0.06 m; however, due to the obscured view of the sky by the ice cliffs, some points during the bathymetric survey recorded a lower accuracy, but were not excluded from the datasets to ensure a complete coverage. All points recorded an accuracy of <1.5 m with the exception of the S4 2017 survey which recorded some points with a maximum accuracy of 4.8 m.

The GNSS unit and echo sounder were attached to the bathymetric survey boat enabling morphometric analysis of the lake and pond beds. The Ohmex SonarMite and Airmar P66 transducer are able to detect depths ranging from 0.3 – 75 m. The transducer operates at an output

range of 2 Hz with an ultrasonic ping rate of 3 – 5 Hz dependent on water depth. The biggest source of measurement error is attributed to the sound velocity setting. The sound velocity can be set from 1400 to 1600 $ms^{-1}$. Cold, fresh water, typically found in glacial lakes, ranges between ~1403 to 1427 $ms^{-1}$ (Purdie et al., 2016). Sound velocity was set according to the temperature of the surface water taken with a temperature probe and based on the UNESCO equation provided by the National Physical Laboratory to set the appropriate value (Chen et al., 1977). Temperature profiles taken in 2018 indicated variations of supraglacial pond surface and depth temperatures at the lake bed varied by less than 1.2°C, whereas proglacial lakes indicated substantially higher variability (0.3 – 11.7°C). This equates to a change in sound velocity of between 1.9 to 2.5 $ms^{-1}$ and is considered to have a negligible affect on the depth measurements for this study. The effect to which turbidity, salinity and sediment concentration have on the sound velocity are again assumed to be negligible (Chikita et al., 2000). Comparison with a measured point over a static location, with a known depth to a flat, firm base at the edge of the water was used to check the sound velocity settings and adjust accordingly for each survey. Verification points were limited to shallow areas (<1 m depth) where access was possible and indicated readings were within ±5 cm of the measured sonar depth.

The bathymetric survey boat collected two to three depth measurements per second, travelling at an average speed of 1.5 $ms^{-1}$. Survey point summary and errors are provided in Table 6.1. For each survey, water level points were taken with the Trimble GNSS and included in the bathymetric interpolation to improve area and volume calculations. It was not possible to collect water level/edge points where ice cliffs were present, so SPOT imagery and the photogrammetric models (see Section 6.2.2) were used to delineate the extent of ponds along the ice cliffs. Although previous studies have adopted a natural neighbour approach (e.g. Thompson et al., 2016; Watson et al., 2018b), three interpolation methods were tested and the accuracy of predictions assessed using a root mean square error (RMSE) between the raw sonar depths and the interpolated depths. Out of the natural neighbour, IDW and spline algorithms tested, IDW produced the lowest estimates whilst enabling preservation of data measurements and was therefore adopted in this study. A suitable output resolution was assessed in ArcGIS based on the mean distance between points and resulted in maps ranging in resolutions from 0.05 m to 0.4 m.

**Table 6.1:** Number of depth measurements, mean XY GNSS accuracy and RMSE for the IDW interpolations for the bathymetric maps.

| Lake | | Number of depth measurements | Mean XY GNSS Accuracy (m) | Mean interpolation standard error (RMSE) |
|---|---|---|---|---|
| Lake Miage – Ice-marginal lake | 2017 | 8149 | 0.022 | 0.390 |
| | 2018 | 4007 | 0.367 | 0.344 |
| Proglacial lake 1 – P1 | 2017 | 5783 | 0.024 | 0.108 |
| | 2018 | 6052 | 0.191 | 0.113 |
| Proglacial lake 2 – P2 | 2017 | 1224 | 0.040 | 0.046 |
| | 2018 | 1723 | 0.024 | 0.101 |
| Lac Vert – P3 | 2017 | 4025 | 0.461 | 0.065 |
| | 2018 | 1986 | 0.364 | 0.069 |
| Supraglacial pond 1 – S1 | 2017 | 5059 | 0.026 | 0.438 |
| | 2018 | 1735 | 0.048 | 0.134 |
| Supraglacial pond 2 – S2 | 2017 | 3256 | 0.023 | 0.764 |
| | 2018 | 1217 | 0.027 | 0.853 |
| Supraglacial pond 3 – S3 | 2017 | 2032 | 0.020 | 0.129 |
| | 2018 | - | - | - |
| Supraglacial pond 4 – S4 | 2017 | 2420 | 0.280 | 0.030 |
| | 2018 | 850 | 0.019 | 0.076 |
| Supraglacial pond 5 – S5 | 2017 | - | - | - |
| | 2018 | 1879 | 0.021 | 0.488 |

### 6.2.2. Photogrammetry surveys

Ground based photogrammetry surveys were limited to supraglacial ponds with adjacent ice cliffs and undertaken in clear weather conditions. Ice cliffs were also observed elsewhere on the glacier but did not have associated supraglacial ponds and were not surveyed.

Each ice cliff survey typically took <2 hours, with between 126 to 415 images dependant on cliff size and extent of undulating topography. Images were taken with a Sony Alpha 7R camera, with a fixed focal length lens (35 mm) and 42-megapixel sensor. A range of ground-based camera locations with oblique angles were used to provide good coverage of the ice cliff, water edge and surrounding areas. The required image overlap for SfM with multi view stereopsis (SfM-MVS) image processing was visually assessed. Identifiable A3 paper sized fluorescent yellow and orange ground control points (GCPs) with a central black marker were distributed at various heights and locations to encompass the survey area. Positions of the GCP targets were recorded with the Trimble Geo7x GNSS and post-processed with a mean accuracy of ±0.03 m.

Photos of the ice cliffs were processed using SfM-MVS workflows in Agisoft Photoscan to create 3D representations of the ice cliffs as point clouds (e.g. Westoby et al., 2012). Processing followed the in-built workflows in Agisoft prior to export. Photos were aligned and those with a low-quality value (<0.7) were removed from the model based on quality estimations and visual checks. Once a sparse

point cloud was processed, outliers from the area of interest were removed, retaining the maximum number of points with an acceptable error (<1 pixel). A dense point cloud was processed with 'high quality' settings. Georeferencing accuracy was <0.08 m and 3D GCP placement uncertainty was typically <0.04 m (Table 6.2). The resultant models showed some areas that could not be resolved due to sparse imagery coverage or unfavourable slope angles including channels transporting meltwater to the supraglacial pond from adjacent ice cliffs. Regions within gullies did not receive high camera coverage and are therefore not well defined in the resulting models. A total of six GCPs were used for each model to reduce vertical errors (Tonkin and Midgley, 2016). Control and check points were used to assess the resulting models and are reported in Table 6.2.

The models were exported as 3D point clouds along with orthophotos and DEMs for further analysis in ArcGIS and CloudCompare. The models were analysed to calculate ice cliff area (calculated as the exposed surface), maximum ice cliff height, slope and aspect. Surface area of the ice cliff was calculated as the exposed surface. Slope and aspect were calculated using the dip direction and angle tools within CloudCompare.

**Table 6.2:** Errors of the photogrammetry SfM ice cliff models during processing and summary of GCPs, check points and accuracy.

| Lake or pond | | Resolution mm/pix | Georeferencing XYZ uncertainty (m) | Mean point density (per $m^2$) | No. control GCPs | RMSE – control (m) | No. check points | Accuracy – check (m) |
|---|---|---|---|---|---|---|---|---|
| S1 | 2017 | 3.58 | 0.028 | $5.9 \times 10^4$ | 6 | 0.04 | 3 | 0.05 |
| | 2018 | 2.09 | 0.028 | $4.0 \times 10^4$ | 6 | 0.06 | 7 | 0.06 |
| S2 | 2017 | 5.28 | 0.026 | $2.2 \times 10^4$ | 6 | 0.02 | 13 | 0.05 |
| | 2018 | 3.69 | 0.034 | $3.7 \times 10^4$ | 6 | 0.03 | 11 | 0.06 |
| S3 | 2017 | 1.84 | 0.026 | $1.7 \times 10^5$ | 6 | 0.02 | 12 | 0.05 |
| | 2018 | 1.47 | 0.032 | $1.5 \times 10^4$ | 6 | 0.03 | 8 | 0.06 |
| S4 | 2017 | 3.31 | 0.027 | $6.6 \times 10^4$ | 6 | 0.02 | 3 | 0.08 |
| | 2018 | 2.59 | 0.026 | $1.1 \times 10^5$ | 6 | 0.07 | 7 | 0.07 |
| S5 | 2017 | - | - | - | - | - | - | - |
| | 2018 | 3.50 | 0.032 | $4.5 \times 10^4$ | 6 | 0.07 | 7 | 0.08 |
| Miage | 2017 | 12.1 | 0.030 | $3.4 \times 10^3$ | 6 | 0.02 | 17 | 0.05 |
| | 2018 | 8.90 | 0.028 | $6.6 \times 10^3$ | 6 | 0.03 | 20 | 0.06 |

## 6.2.3. Quantification of change

### 6.2.3.1. Photogrammetric ice cliff models

The SfM model point clouds were aligned based on identifiable boulders to account for displacements between the two surveys in 2017 and 2018 except for Lake Miage which originates on stable ground at the western margin. Once co-registered, ice cliff change was quantified using the Multiscale Model to Model Cloud Comparison (M3C2) cloud-to-cloud differencing method in

CloudCompare as this method has been shown to be effective for determining change in river canyon and glacial environments based on the methods described by Lague et al. (2013), Westoby et al. (2016), Midgley and Tonkin (2017), Watson et al. (2017b) and Bash et al. (2018). This method enables quantification of the 3D distance of two point clouds along the normal surface direction, by calculating distances from a reference point cloud (cloud 1) to a target point cloud (cloud 2) (Lague et al., 2013).

The M3C2 method requires suitable selection of two user-defined parameters (the normal scale and projection scale) dependent upon the point clouds. The normal scale (*D*) is used to calculate surface normals dependent upon surface roughness and point cloud geometry. The projection scale (*d*), refers to the cloud-to-cloud distance the calculation is averaged across. It should be large enough to include an average of ~30 points (Lague et al., 2013; Watson et al., 2017b). Following approaches from Westoby et al. (2016), Midgley and Tonkin (2017), Watson et al. (2017b) and Bash et al. (2018), the normal scales (*D*) were estimated based upon a trial and error approach (Equation 6.1) through refinement of a rescaled measure of the normal scale *n(i):*

$$n(i) = \frac{D}{\sigma i(D)} \qquad \textbf{Equation 6.1}$$

Where *n(i)* is the normal scale (*D*) divided by the roughness (σ) measured at the same scale around *i.* The roughness scale was reiterated until *n(i)* was between 20 -25 to ensure the calculation is not influenced by local surface roughness and thereby the estimated normal error ($E_{norm}$) was <2% (Lague et al., 2013). For this study, the normal scales (*D*) ranged between 0.6 m and 1.0 m and the projection scale (*d*) was set at 0.3 m to ensure a minimum of 30 points were sampled in each cloud as suggested by Lague et al., (2013).

The Level of Detection (LoD) threshold for a 95% confidence level indicates whether the calculated change is significant based on local roughness, the number of points within the cylinder, and the registration error. The registration error was set to the point cloud errors inclusive of SfM reconstruction and GNSS errors and previously assessed in Agisoft. Significance values equal to 1 indicate areas where the confidence interval exceeds 95% and was satisfied for the ice cliff faces.

Distance calculations were clipped to the ice cliff faces. Retreat rates were calculated for the survey period between 2017 and 2018. Ice cliffs at Lake Miage were separated into the north and south-facing sections to improve point detection with the M3C2 algorithm. Total errors were calculated for each ice cliff model using the georeferencing errors and displacement error between the two corresponding surveys.

#### 6.2.3.2. Bathymetric surveys

Once the photogrammetry SfM models were co-registered based on identifiable boulders and features, the bathymetric lake surveys were also aligned enabling regions of morphological bed change to be assessed. Raster differencing indicates the regions of depth increase and decrease.

## 6.3. Results

### 6.3.1. Glacial lakes bathymetry

Of the water bodies surveyed in both 2017 and 2018 (all except S5), volume increased from 174,047 $m^3$ to 248,951 $m^3$ (Table 6.3, Table 6.4). Supraglacial ponds increased in volume by +46% (inclusive of S5), proglacial lakes by +59% and the ice-marginal Lake Miage by +42% between 2017 and 2018.

The supraglacial ponds and Lake Miage show fluctuations in volume and area between the two surveys with the Lake Miage, S1, and S5 experiencing volume increases, whilst S2, S3 and S4 underwent volume decreases (Table 6.3). S3 drained completely between 2017 and 2018, which appears to be associated with a crevasse observed in this location in 2018 that the pond previously occupied in 2017. The supraglacial ponds and Lake Miage surveyed in 2017 and 2018 represent a pond density of 0.3 and 0.4% respectively of the debris-covered area, and although they experienced variations in volume, their total water volume increased by 50,924 $m^3$.

**Table 6.3:** Area, depth, lake levels and volume of lakes surveyed July 2017 and 2018. *S5 area in 2017 estimated from satellite imagery rather than bathymetric survey.

| | Year | Area ($m^2$) | Max. depth (m) | Lake level elevation (m) | Volume ($m^3$) |
|---|---|---|---|---|---|
| Lake Miage – Ice-marginal | 2017 | 11931 | 36.94 | 2007.60 | 119968 |
| | 2018 | 16028 | 30.56 | 2009.81 | 170354 |
| Proglacial lake 1 (P1) | 2017 | 8535 | 12.86 | 2007.60 | 36976 |
| | 2018 | 10757 | 16.12 | 2009.80 | 58409 |
| Proglacial lake 1 (P2) | 2017 | 412 | 1.29 | 2012.60 | 297 |
| | 2018 | 880 | 2.27 | 2013.50 | 736 |
| Lac Vert (P3) | 2017 | 1516 | 6.02 | 1815.90 | 3213 |
| | 2018 | 1904 | 4.67 | 1816.38 | 5318 |
| Supraglacial pond 1 (S1) | 2017 | 1495 | 13.30 | 1964.30 | 7600 |
| | 2018 | 1989 | 16.68 | 1962.50 | 11426 |
| Supraglacial pond 2 (S2) | 2017 | 569 | 26.73 | 2030.20 | 3112 |
| | 2018 | 500 | 16.80 | 2026.65 | 2384 |
| Supraglacial pond 3 (S3) | 2017 | 232 | 4.18 | 2049.20 | 298 |
| | 2018 | - | - | - | - |
| Supraglacial pond 4 (S4) | 2017 | 698 | 14.05 | 2054.60 | 2585 |
| | 2018 | 207 | 5.27 | 2048.40 | 323 |
| Supraglacial pond 5 (S5) | 2017 | 1464* | - | - | - |
| | 2018 | 1488 | 21.61 | 2044.48 | 5781 |

Lake Miage increased in both area and volume from 2017 to 2018, expanding from 11,931 $m^2$ to 16,028 $m^2$, equating to ~68% of the surface water storage at Miage Glacier despite a reduction in maximum depth of 6.38 m. The deepest section was located in the centre of the lake, however a deep section evident in 2017 further developed by 2018 close to the north-facing ice cliffs. The east end of the lake shows the greatest deepening close to the ice cliffs in comparison to the western end, which shows comparatively little change proximal to the lateral moraines (Figure 6.2).

Lake Miage neighbours two proglacial lakes situated to the south and southwest (Figure 6.2). The larger of the proglacial lakes (P1) has a submerged ridge, which separates the two basins when water levels are lower than during the field visits. Water levels, taken with the GNSS, were the same for both Lake Miage and P1 in 2017 and 2018. The smaller proglacial lake located close by (P2), however, did not show the same water level increase between 2017 and 2018. The total volume for these three lakes combined was 157,240 $m^3$ in 2017 and 229,500 $m^3$ in 2018 equating to 90% of the total surface water storage, in accordance with higher water levels for all three lakes and areal expansion of Lake Miage.

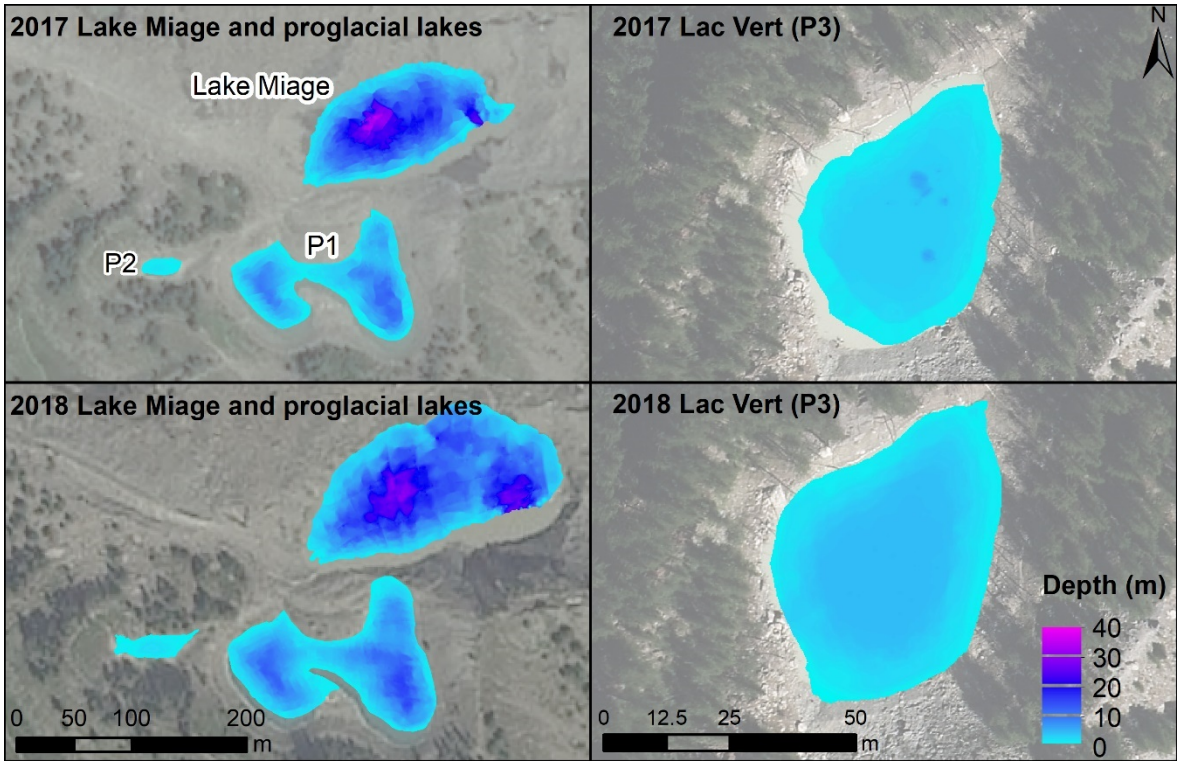


**Figure 6.2:** Bathymetric maps of Lake Miage, P1, P2 and Lac Vert (P3) in 2017 and 2018. Background images are SPOT satellite images from 2017 and 2018, and TerraItaly OrthoPhoto from 2015 (P3).

A drainage event of Lake Miage occurred in September 2018 with photographic evidence showing substantial volume loss (Figure 6.3). It is understood that the drainage occurred over the course of a few days between approximately 25/09/2018 and 29/09/2018 resulting in the reduction of the water level from the notch line, identifiable in the image via a conduit at the eastern end of the lake. The lake drained an estimated ~102,000 $m^3$ based on the assumption the bathymetry remained stable since the survey in the previous July.


**Figure 6.3:** Lake Miage taken on 29/09/2018 facing east looking towards Val Veny. Blue line refers to the previous water line. *Photo credit:* Connor Downes (2018).

The supraglacial ponds (S1 – S5) held a volume in excess of 13,595 $m^3$ in 2017 and ~20,000 $m^3$ by 2018 accounting for 8% of the total volume stored at Miage Glacier surface (Table 6.3). All supraglacial ponds showed a decrease in water levels between the two surveys. S1 had the largest area and experienced an increase in both area and volume over the survey period (Figure 6.4). S2 possesses a very deep section of 26.73 m, which happens to be the greatest depth of all supraglacial ponds surveyed in 2017, albeit with a comparatively small area. S2 underwent a reduction in both area and volume by 2018 consistent with a reduction in maximum depth of ~10 m. S3 experienced a reduction in area and volume due to its complete drainage by 2018. S4 also showed signs of drainage resulting in a substantial depth decrease of ~9 m, and area reduction. By 2018, S4 was approximately a third of the area it was in 2017 indicating substantial drainage. S5 surveyed in 2018 showed a deep channel along the centreline of the pond with the deepest section measuring >21 m. S5 showed limited area change based on satellite imagery from the study period in 2017, but is thought to have increased in depth enabling bathymetric surveys to be undertaken in 2018.

**Table 6.4:** Changes in lake properties from 2017 to 2018. Values for Lake Miage post drainage are estimated assuming the bathymetry has not changed since the 2018 survey.

| | Area ($m^2$) | Max. depth (m) | Lake level (m) | Volume ($m^3$) |
|---|---|---|---|---|
| Lake Miage – Ice-marginal lake | +4097 | −6.38 | +2.21 | +50387 |
| Lake Miage – Post drainage (estimated) | −8421 | | | −101843 |
| Proglacial lake 1 (P1) | +2222 | +3.25 | +0.90 | +21434 |
| Proglacial lake 2 (P2) | +468 | +0.98 | +2.20 | +440 |
| Lac Vert (P3) | +388 | −1.34 | +0.48 | +2106 |
| Supraglacial pond 1 (S1) | +493 | +3.38 | −1.80 | +3826 |
| Supraglacial pond 2 (S2) | −69 | −9.93 | −3.55 | −728 |
| Supraglacial pond 3 (S3) | - | - | - | - |
| Supraglacial pond 4 (S4) | −491 | −8.78 | −6.20 | −2262 |
| Supraglacial pond 5 (S5) | - | - | - | - |

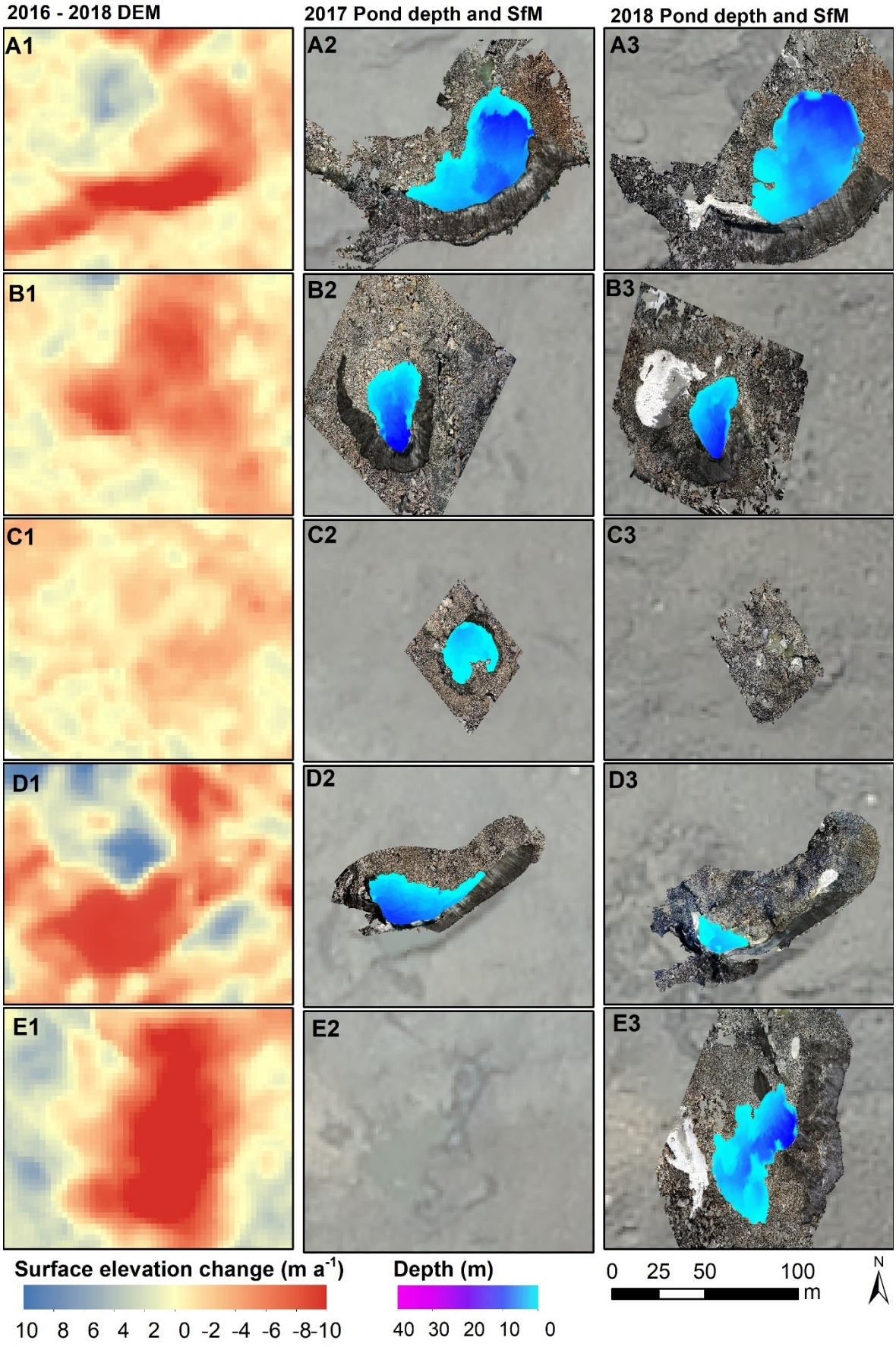


**Figure 6.4:** Left column A1-E1: Mean annual elevation change from 2016 – 2018 derived in Chapter 5. Central column A2-E2: Bathymetry and photogrammetry surveys in 2017 with SPOT7 orthophoto background. Right column A3-E3: Bathymetry and photogrammetry surveys in 2018 with SPOT7 orthophoto background.

### 6.3.2. Ice cliff characteristics

All ponds were surrounded partly by north-facing cliffs (Figure 6.4). Part of the ice cliff surrounding Lake Miage, also faced a southerly direction, which was observed with a lower slope gradient (8 – 10°) in comparison to the north-facing slope (26 – 29°) in both the 2017 and 2018 surveys (Table 6.5).

**Table 6.5:** Summary of 2017 and 2018 ice cliff geometry results.

| Model | | Max. height of ice cliff (m) | Surface Area ($m^2$) | Aspect (°) | Mean (max) slope (°) |
|---|---|---|---|---|---|
| Lake Miage (N/S) | 2017 | 32.29 | 10406 | 336/162 | 26/8 |
| | 2018 | 42.22 | 11615 | 338/154 | 29/10 |
| S1 | 2017 | 26.64 | 2346 | 358 | 23 |
| | 2018 | 29.6 | 1692 | 356 | 29 |
| S2 | 2017 | 13.24 | 943 | 35 | 10 |
| | 2018 | 18.29 | 1807 | 57 | 16 |
| S3 | 2017 | 4.79 | 165 | 22 | 2 |
| | 2018 | - | - | - | - |
| S4 | 2017 | 15.76 | 1055 | 325 | 12 |
| | 2018 | 15.40 | 864 | 277 | 6 |
| S5 | 2017 | - | - | - | - |
| | 2018 | 24.8 | 1728 | 283 | 18 |

Ice cliff heights ranged from ~5 m (S3) to ~42 m (Miage) over the two surveys. Between 2017 and 2018, the Lake Miage ice cliff exhibited an increase in surface area from 10,406 $m^2$ to 11,615 $m^2$ (Table 6.5). The Lake Miage ice cliff showed a strong increase in surface area of the north-facing section. The ice cliff at S1 shows a reduction in surface area (2346 – 1,692 $m^2$) despite an increase in height (26.6 – 29.6 m). S2 ice cliff increased in surface area (943 – 1,807 $m^2$) but maintained a relatively stable aspect and slope angle. S3 ice cliff had disappeared with no sign of exposed ice in 2018. Ice cliff S4 maintained a stable height although the eastern-facing side of the S4 ice cliff was observed to have partially collapsed, consistent with a reduction in mean slope angle (12 to 6°). S5 showed a relatively large ice cliff in excess of 24 m in height.

### 6.3.3. Supraglacial pond morphology and cliff interactions

Displacements of identifiable rocks indicate the glacier velocity is approximately 10 – 15 $ma^{-1}$ in the regions surrounding the supraglacial ponds. As the S1 ice cliff retreated, the pond expanded upglacier (Figure 6.4A). The deepest section of the pond is located to the north edge below the ice cliff. S2 pond has undergone a decrease in area attributed to undercutting to the east of the ice cliff. The deepest section of the pond has remained beneath the north-facing section of ice cliff (Figure 6.4B). S3 showed significant drainage but a small amount of water is located where it is thought the deepest section of the pond was previously. Presence of a crevasse can be traced through the area

in 2018 where S3 was previously located (Figure 6.4C). S4 also reduced in size and is confined to the base of ice cliff by 2018. It is likely that the reduction in pond area and volume has reduced in association with the partial collapse of the ice cliff (Figure 6.4D). S5 pond increased in area and depth and was, therefore, suitable for surveying in 2018. Again, the deepest section of the pond was observed under the large exposed ice cliff (Figure 6.4E).

### 6.3.4. Quantification of ice cliff change

The ice cliffs retreated substantially ranging from −0.93 $ma^{-1}$ to −8.15 $ma^{-1}$ (Table 6.6), equating to a total volumetric ice loss of 39,569 $m^3$ between 2017 and 2018. The highest ice cliff retreat rates occurred around the margins of S4 (−8.15 $ma^{-1}$) and S1 (−5.24 $ma^{-1}$) respectively (Table 6.6, Figure 6.5), particularly around north-facing slopes. The northern-facing Lake Miage ice cliffs experienced higher melt rates in comparison to the southern-facing cliff and was observed to have migrated further onto the glacier.

**Table 6.6:** Mean ice cliff retreat rates between 2017 and 2018 assessed through the M3C2 algorithm.

| Lake | Mean M3C2 distance (m) | St Deviation (m) | Mean annual retreat rate (m) | Volume ice lost ($m^3$) | Mean daily retreat rates (cm $d^{-1}$) | Total Error ($E_T$) (m) |
|---|---|---|---|---|---|---|
| Miage N | −2.70 | 2.62 | −2.79 | 14048 | −0.76 | 0.26 |
| Miage S | −0.91 | 2.35 | −0.93 | 1067 | −0.26 | 0.26 |
| S1 | −5.12 | 3.72 | −5.24 | 12011 | −1.44 | 0.83 |
| S2 | −2.41 | 2.44 | −2.47 | 4077 | −0.68 | 1.00 |
| S3 | - | - | - | - | - | 1.05 |
| S4 | −7.93 | 1.69 | −8.15 | 8366 | −2.23 | 1.01 |

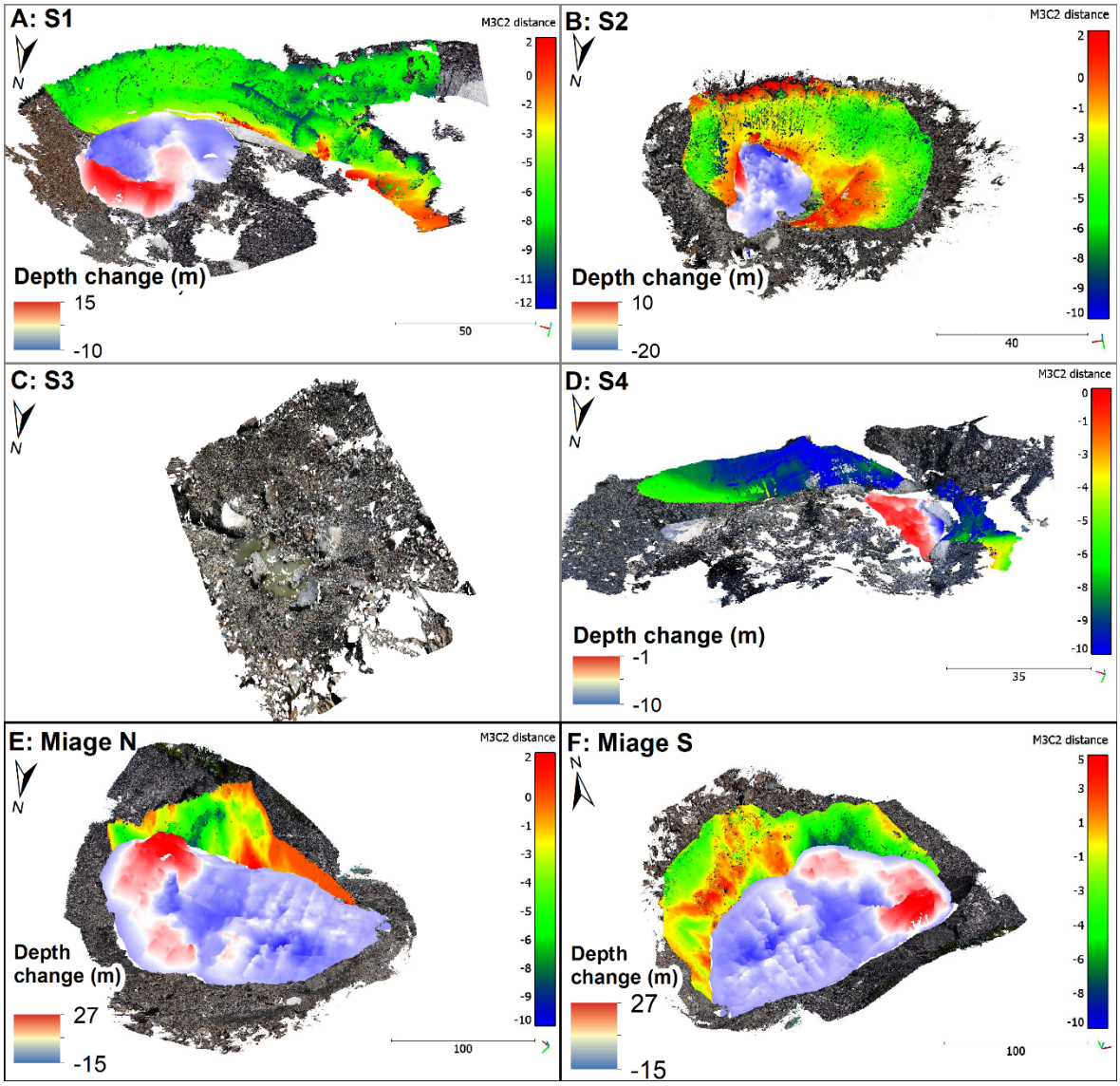


**Figure 6.5:** A-F: Ice cliff and bathymetric change between the two survey periods in 2017 and 2018. Units in m. Photogrammetry models displayed for context.

### 6.3.5. Ablation season pond dynamics

Ablation season pond dynamics show increased pond numbers at the beginning of the season, which then reduce, as such the total ponded area reduced from 25,556 $m^2$ to 6,069 $m^2$ in 2017 with similar levels in 2018 (Figure 6.6 and Table 6.7). In both years, an increase of pond number and area/volume was calculated in August, which then decreased in the following September and October.

The estimated volumes in Table 6.7 were calculated from the Watson et al. (2018b) updated area-volume relationship with additional small supraglacial ponds from Cook and Quincey's (2015) relationship as in Equation 6.2.

$$V = 0.1535A^{1.39} \qquad \textbf{Equation 6.2}$$

**Table 6.7:** Summary of ponds mapped throughout the ablation season from 2017 – 2018.

| Date | Number of ponds | Area ($m^2$) | Estimated volume ($m^3$) |
|---|---|---|---|
| June 2017 | 11 | 26556 | 216618 |
| July 2017 | 9 | 28514 | 239133 |
| August 2017 | 9 | 34285 | 308961 |
| September 2017 | 5 | 8519 | 44601 |
| October 2017 | 7 | 6069 | 27838 |
| June 2018 | 11 | 39399 | 374829 |
| July 2018 | 9 | 36944 | 342763 |
| August 2018 | 11 | 38574 | 363964 |
| September 2018 | 11 | 32208 | 283255 |
| October 2018 | 8 | 6958 | 33664 |

Lake Miage drained at the end of the ablation seasons in both 2017 and 2018 in September/October. The months preceding the drainage show signs of increasing area and growth.

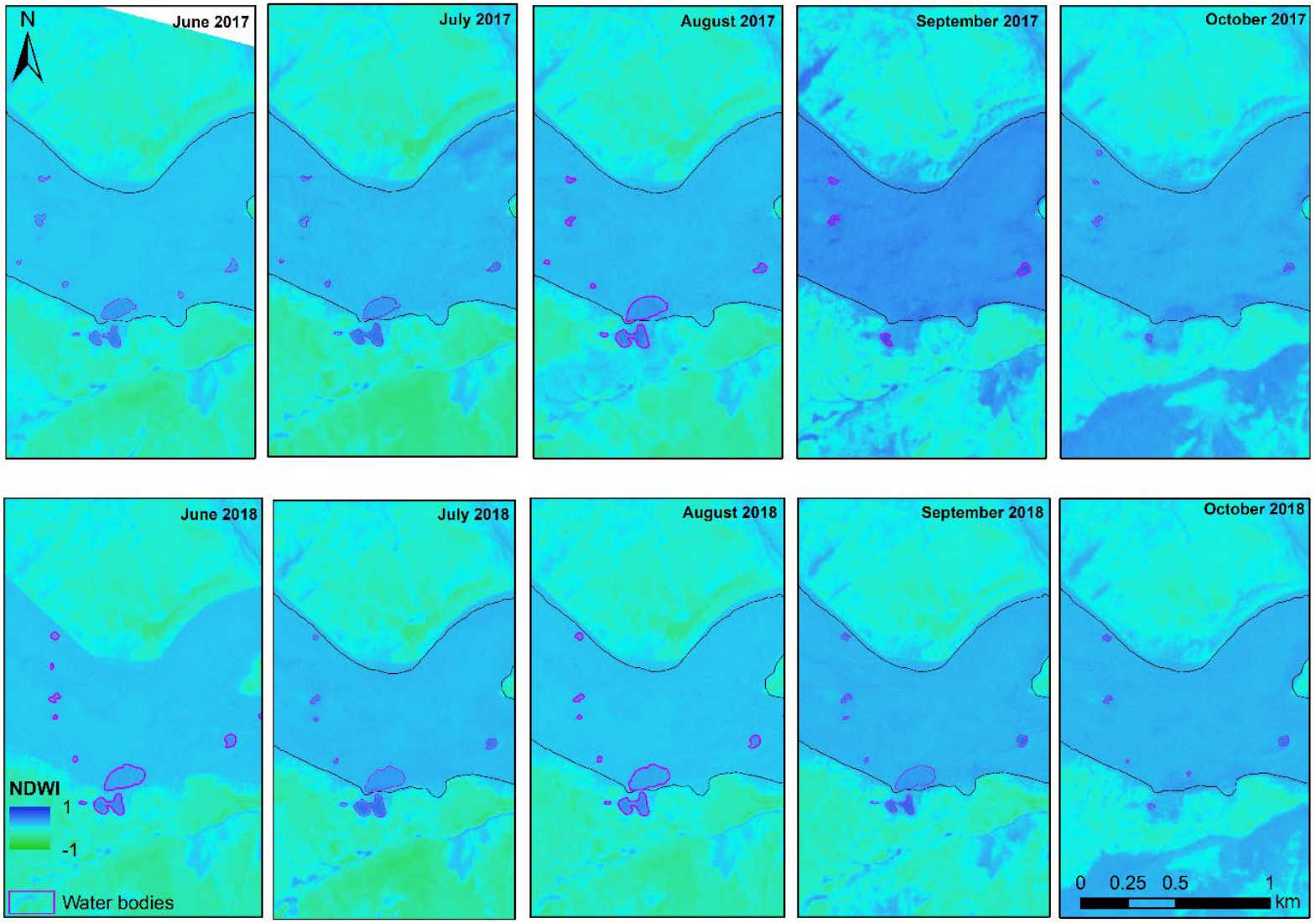


**Figure 6.6:** Water bodies at Miage Glacier from June – October 2017 (top row) and June – October 2018 (bottom row).

## 6.4. Discussion

### 6.4.1. The evolution of Miage Glacier

The first-order DEM-differencing technique as discussed in Chapter 5 provides an indication of contribution to mass balance but cannot capture the full range of ice cliff and pond dynamics. The field-based photogrammetry and bathymetric surveys presented in this chapter, reveal a detailed understanding of Miage Glacier evolution. The data presented in Chapters 4 and 5 reveal that Miage Glacier has transitioned into 'Regime 2', characterised by expanding debris cover, downwasting ice and glacier slowdown, in addition to perched ponds and associated enhanced ablation around the ponds (Benn et al., 2012). The transition to 'Regime 3' requires the development of base-level lake often in combination with an elevated hydrological base associated with large terminal moraines, which is not evident at Miage Glacier (Quincey et al., 2007). Thus, it is unlikely for the glacial lakes at Miage Glacier to develop a hazardous GLOF risk (Benn et al., 2012) and is likely to remain in 'Regime 2' for the foreseeable future. However, the presence of supraglacial ponds and ice cliffs provide evidence of rapid mass loss and are important contributors to the glacier dynamics and the overall melt budget.

Furthermore, this study contributes to the global bathymetry dataset of small supraglacial ponds, which have been seldom analysed, especially in alpine regions (Cook and Quincey, 2015). GNSS accuracy has been reported for the bathymetry data for the first time providing assessment of the spatial accuracy of the bathymetric surveys along with analysis of interpolation methods used. Although there is potential for additional water storage in undercut cliff sections, these were not accessible with the survey boat and interpolated data is considered to provide a conservative estimate.

### 6.4.2. Glacial lake variability and pond dynamics

Glacial lakes have increased in number worldwide since 1990 in response to climatic change and glacier retreat and is evident in the Alps (Shugar et al., 2020). Glacial lakes, including supraglacial ponds, are likely to become increasingly important for both ablation and water storage in the Alps (Gobiet et al., 2014). The supraglacial ponds comprise a relatively small (~8%), yet important, component of the total water storage at Miage Glacier (Table 6.4), and play an important role in glacier-scale ablation. In one year, the total volume of surface water storage at Miage Glacier has increased by 50,924 $m^3$ (46%) (Table 6.3 and Table 6.4) despite evidence of drainage events, highlighting the potential for rapid increase but also high intra and inter-annual variability (e.g. Miles et al., 2017b). High rates of variability likely represent a combination of snowmelt and meltwater generation (Gardelle et al., 2011), interactions with englacial conduits and drainage events (Gulley and Benn, 2007), and precipitation inputs (Liu et al., 2015).

Long-term trends indicate an overall increase in the number of small ponds (Figure 4.6), yet seasonal variations reveal summer growth and maximum ponded area likely in response to seasonal controls on temperature, precipitation and surface hydrology and thus also often coincides with sporadic drainage events (Watson et al., 2016). During the ablation season, higher numbers of small ponds account for increasing area with a maximum size in the middle of summer storing increased thermal energy (Miles et al., 2018), which often promotes further meltwater production and pond expansion prior to drainage, once it encounters an englacial conduit or drainage route. A reduction in ponded area and number was observed prior to winter in a similar cyclical pattern previously observed by Miles et al. (2017b), Narama et al. (2017) and Watson et al. (2016). Despite these examples being influenced by the Himalayan monsoon, similar trends are observed with the seasonal ablation season at Miage Glacier highlighting the importance of summer temperatures as the predominant factor in meltwater generation and potential for englacial ablation and interception with englacial conduits resulting in drainage events (Gulley and Benn, 2007; Miles et al., 2016).

Despite increased supraglacial pond volume (S1 – S5), which held a volume in excess of 13,595 $m^3$ in 2017 and ~20,000 $m^3$ by 2018, only one pond observed a clear increase in pond depth (Table 6.4). Cook and Quincey (2015) hypothesised that supraglacial ponds initially grow by area at a faster rate than by depth via subaqueous melt. Supraglacial ponds are typically short-lived once a link to the englacial perennial system has formed allowing them to drain, as seen with S3 through interception with a crevasse (Figure 6.4), and later refill. If no connection to the englacial drainage system is made, rapid growth has been attributed to subaerial and water-line melting (Benn et al., 2001) enabling areal growth as seen with S1 and S5. Thus, volume increase for supraglacial ponds at Miage Glacier is primarily attributed to areal expansion rather than subaqueous bed melt, supporting Cook and Quincey (2015).

The surveyed supraglacial ponds and Lake Miage all had adjacent ice cliffs and reached a maximum depth of 37 m at Lake Miage in a region where ice thickness ranges from 0 to >95 m. The supraglacial ponds were present in regions with ice thickness >100 m (Farinotti et al., 2019). It is considered that Lake Miage has a relatively thick sediment layer on its bed as partially evident in Figure 6.3. Thus, enhanced ablation and expansion is promoted around the ice cliffs and regions of thinner debris. Similar expansion processes were observed at Spillway Lake (Thompson et al., 2012) and supports drainage via an englacial conduit located at the eastern end of the Lake Miage.

### 6.4.3. V-A scaling relationships

This study has shown the development of small supraglacial ponds, which have become established on Miage Glacier are important for glacier dynamics and glacier-scale ablation. Yet, the inclusion of

small supraglacial ponds (<10,000 $m^2$) is limited in global bathymetric datasets (Watson et al., 2016), which glacier melt models require for accurate inclusion of glacier evolution. Area-depth relationships of the ponds and lakes at Miage Glacier indicate a power law relationship based on coefficient of determination ($R^2$) values between supraglacial ponds and proglacial lakes at Miage Glacier (Table 6.8). In comparison, area-volume relationships are best represented by a linear relationship between supraglacial ponds at Miage Glacier (Table 6.8). When combining these data points with those of Cook and Quincey's (2015) and Watson et al.'s (2018b) area-volume assessments, the pond area-volume power law and exponential relationships as previously stated are supported.

**Table 6.8:** Regression values ($R^2$) relationships for supraglacial ponds and proglacial lake area-volume and comparisons with data from Cook and Quincey (2015) and Watson et al. (2018b).

| | **Linear $R^2$** | **Exponential $R^2$** | **Power law $R^2$** |
|---|---|---|---|
| Supraglacial ponds – area-depth (2017 and 2018) | 0.43 | 0.42 | 0.64 |
| Proglacial lakes – area-depth (2017 and 2018) | 0.90 | 0.72 | 0.90 |
| Supraglacial ponds – area-volume (2017 and 2018) | 0.99 | 0.75 | 0.94 |
| Proglacial lakes – area-volume (2017 and 2018) | 0.00 | 0.07 | 0.13 |
| Supraglacial ponds area-volume (incl. Cook and Quincey, 2015; and Watson et al., 2018 data). | - | - | 0.99 |
| Proglacial/moraine dammed area-volume (incl. Cook and Quincey, 2015 data). | - | 0.96 | - |
| All glacial lakes area-volume (incl. Cook and Quincey, 2015; and Watson et al., 2018) | - | - | 0.98 |

In addition, Cook and Quincey (2015) found that supraglacial ponds formed a distinct population when comparing their mean depth and area with other, larger glacial lakes. However, at Miage Glacier, supraglacial ponds were much deeper in relation to their area compared to the proglacial and ice-marginal lakes (Figure 6.7). It was suggested that supraglacial pond volume increases at a slow rate with increased area due to being relatively shallow; however, this appears not to be the case at Miage Glacier. This is consistent with higher rates of expansion and drainage of these lakes and compares to Cook and Quincey's (2015) description of more mature supraglacial ponds where lake volume increases more rapidly, with increased calving rates associated with deeper water as the lake-bottom ice melts out. However, the ponds on Miage Glacier are considered to represent comparatively immature ponds and therefore lake development may not be consistent with other studies and could take on any of the trajectories suggested in Cook and Quincey's (2015) analysis.

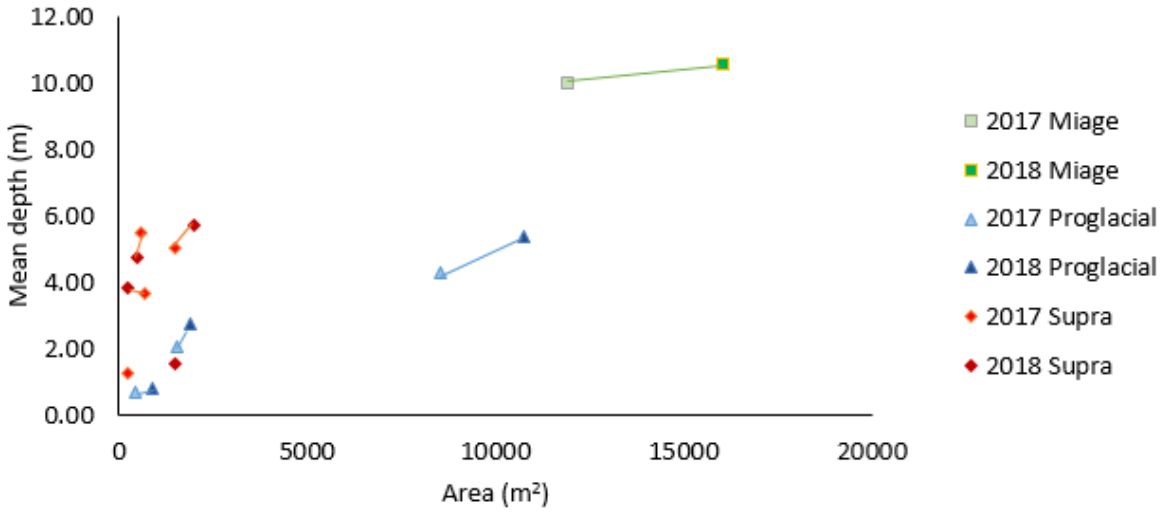


**Figure 6.7:** Lake and pond area plotted against mean depths for 2017 and 2018 surveys.

### 6.4.4. Ice cliff dynamics

Photogrammetric surveys undertaken in 2017 and 2018 show that ice cliff backwastage resulted in an annual ice loss of 39,569 $m^3$ for the five ice cliffs surveyed, which accounted for 0.3 – 0.4% of the debris-covered area with ice cliff retreat rates up to −8.15 m $a^{-1}$ (Table 6.6). However, considerable variations in ice cliff retreat was observed (Figure 6.5) and often associated with vertical runnels (e.g. S1, S2), or cliff degradation (e.g. S4).

Analysis of the ice cliffs associated with supraglacial ponds supports earlier work of Reid and Brock (2014) whereby higher melt rates were observed at the top of ice cliffs compared to the lower slopes which are sheltered from wind-induced turbulent heat fluxes (Figure 6.5). They found that as the cliff tops melt quicker, the development of a shallower slope profile accumulates debris and led to lowered albedo further enhancing cliff decay. For example, S4 appears to be have disintegrated having retreated by a mean of −8.15 m $a^{-1}$ consistent with a reduction in slope (12 - 6°) (Table 6.6). Additionally, the S1 ice cliff indicates a central band associated with a change in slope, which underwent retreat rates in excess of −9 m $a^{-1}$ compared to the mean rate of −5.24 m $a^{-1}$ (Table 6.6) via subaerial melt. Higher rates of retreat at the top of the ice cliff are consistent with slope lowering compared to lower rates observed below the ridge.

Ice cliffs have been observed to preserve for a number of years on Miage Glacier including one observed for 8 years by Reid and Brock (2014). S1 has been present in satellite imagery for 6 years, in association with a supraglacial pond, indicating that these processes may not result in complete decay or disintegration in all situations. Therefore, ice cliffs potentially undergo cycles of retreat and slope lowering until calving events are initiated often as a result of water-level undercutting, which reinstates the higher slope angles. Diolaiuti et al. (2006) suggested thermal undercut notches

at Lake Miage with growth rates of ~30 – 35 m $a^{-1}$ were important for the initiation of such calving events and maintaining steep slope angles at the base of ice cliffs (Brun et al., 2016). Observed calving events at Lake Miage have previously been observed at the south-facing ice cliff, including a large event in 1996 in which the resultant displacement wave engulfed 11 tourists (Diolaiuti et al., 2005, 2006). Diolaiuti et al. (2005) suggested differential ablation at the cliff face creates irregular geometry, forming distinctive calving zones as previously discussed. This is supported by differential ice cliff retreat rates shown in the M3C2 analysis across the southern facing cliff (Figure 6.5).

Calving at Lake Miage is considered a primary control on ice cliff persistence. The increase in lake volume between 2017 and 2018 (Table 6.4) is attributed to rapid calving and waterline notching of the northern facing cliff at the eastern end of the lake resulting in the observed area increase and extension onto the glacier. In comparison, the south facing cliff saw less retreat attributed to subaerial melt (Table 6.6) and was observed during the survey period with relatively thick debris cover and lower slope values. It is considered that the southern-facing ice cliff at Lake Miage undergoes a cyclical regime of lowered slope angle, build-up of thicker debris in response to lower slope angles and therefore reduced ablation rates with predominance of subaqueous melt and thermal notch undercutting, which encourages calving to occur. This promotes increased slope angles where ice once again becomes exposed, increasing ablation. Once ice of the calving face is exposed it will undergo backwasting from long- and short-wave radiation (e.g. Steiner et al., 2015), gradually reducing slope angle. Kirkbride and Warren (1997) also observed cyclical calving stages over several weeks controlled by the rate of water line melting at the Maud Glacier, New Zealand. A longer-term cycle was identified where calving of the submerged ice foot occurred.

Between 2017 and 2018, the ice cliffs surveyed at Miage Glacier accounted for 0.3 – 0.4% of the debris-covered area, although additional ice cliffs were present without associated ponds and likely account for additional ice loss but are considered to be more transient. Ice cliffs on Miage Glacier had a varied aspect with predominantly north-facing slopes, often observed to persist attributed to lower incoming solar radiation (Sakai et al., 2002; Kraaijenbrink et al., 2016a; Thompson et al., 2016; Watson et al., 2017a) and is likely responsible for the south-facing ice cliff surrounding Lake Miage having a lower mean slope in comparison to the north-facing slope (Table 6.5).

### 6.4.5. Morphological relationships between ponds and adjacent ice cliffs

Although the importance of supraglacial ponds and ice cliffs have previously been highlighted in terms of surface processes and contribution to glacier-scale ablation (e.g. Reid and Brock, 2014; Brun et al., 2016; Watson et al., 2017b, 2018b; Miles et al., 2018), the co-evolution of ponds and cliffs have seldom been assessed together despite important feedback processes, including the importance of calving and undercut notches for ice cliff persistence and calving (Watson et al.,

2018b), having been identified. Analysis of supraglacial ponds and ice cliffs at Miage Glacier show they progressively grow together and often decay simultaneously. Although Lake Miage's volume and cliff area increased simultaneously between 2017 and 2018, S1 and S2 experienced inverse relationships as pond volume of S1 increased, ice cliff area decreased and S2 pond volume decreased but saw an increase in ice cliff area. S3 and S4 saw a simultaneous decrease in both pond volume and ice cliff area consistent with drainage and ice cliff collapse over the annual study period (Table 6.4). By contrast, S1 has been observed over a number of years, and S2 appear to be more stable. One explanation for the inconsistent evolutionary patterns could be that pond volume and cliff area dynamics vary in response to cyclical processes and are able to regain a state of equilibrium unless either the pond or ice cliff exceeds the tipping point resulting in rapid drainage and collapse. Persistence is therefore considered to be dependent upon the balance between subaqueous melt, subaerial melt and calving events (Benn et al., 2001; Sakai et al., 2009).

Morphological analysis aids understanding of pond expansion processes. Watson et al. (2018b) concluded that the bathymetry of ponds with ice cliffs can indicate whether pond expansion is likely based on pond deepening approaching the ice cliff. The deepest sections of S2, S4 and S5 ponds are located below the steepest sections of north-facing ice cliffs attributed to the thermodynamics of supraglacial ponds with ice cliffs despite pond reductions for S2 and S4. Warmer water is transferred to the bed close to the ice cliff encouraging subaqueous melt of the bed (Chikita et al., 2001). Miles et al. (2016) identified water temperature and pond geometry to be important for transferring atmospheric energy to a glacier's interior and promoting ablation. Watson et al. (2018b), Thompson et al. (2016), and Miles et al. (2016) also observed ponds with maximum depths adjacent to ice cliffs. It is therefore likely that signs of expansion processes including maximum depth close to ice cliffs are observed until englacial conduits are encountered initiating rapid drainage and decay. Once drainage has occurred, the buttressing effect provided by the water is removed, promoting collapse of the ice cliff. Conversely, with regard to S1, the deepest section was located away from the ice cliffs and surrounded by shallower water but underwent expansion during the survey period. The location of the deepest section in S1 is close to an inflow to the lake from a supraglacial stream indicating that pond inflow locations also influence the thermal regime and morphology of the bed despite expansion processes occurring.

Expansion processes including calving, water-line notching and subaqueous melt are important for the co-existence and development of ponds and ice cliffs and will be discussed in turn. Although calving appears to be the main mechanism for growth of Lake Miage, the small supraglacial ponds appear to be dominantly melt-driven, forming small incised runnels on the cliff surface (Figure 6.5). Zhang et al. (2019) also found that ice melting and calving processes played dominant roles in driving lake enlargement in the central Himalaya. Larger ice cliffs are more likely to undergo calving due to a larger fetch, influencing pond circulation resulting in thermal notching and encouraging

melt at the bed approaching the cliff face (e.g. S4). However, this is limited with the smaller ponds and ice cliffs due to reduced fetch (e.g. S3). Mertes et al. (2017) attributed shallow pond depths near small ice cliffs to signify newly exposed ice or thick subaqueous debris restricting basal melt. The heavily debris-covered area of S3 in 2018 supports that the pond base was likely to have been heavily debris-covered during the 2017 survey. The disappearance of the ice cliffs or exposed ice at the site of S3 in 2018 supports the concept that the presence of ponds is important for the existence of ice cliffs (Watson et al., 2017b).

Water line melting has been shown to be an important factor in supraglacial pond growth and for the onset of calving for cliffs >15 m in height (Benn et al., 2001). S1, S2 (in 2018), S4, S5 and the Lake Miage ice cliffs exceeded 15 m in height and evidence of water line notches were observed (Figure 6.4). No calving events were observed at any of the supraglacial ice cliffs during the survey period attributed to the ponds being smaller than the ~80 m fetch threshold for calving initiation (Sakai et al., 2009). Röhl (2008) also observed ice loss predominantly through subaerial melt in horizontal dimensions during early stages of development, while later stages were dominated by subaqueous calving.

Lake floor deepening has been attributed to subaqueous calving or melt by heat conduction through sediments (Chikita et al., 1999). However, at Lake Miage it is highly likely that the presence of glacial debris on the bed and sloped sides (Masetti et al., 2010) (Figure 6.3) will reduce melt and hinder subaqueous calving (Benn et al., 2001) resulting in a central deep section away from the ice cliffs with reduced sediment, which underwent little change between the two surveys in comparison to the expansion in area. A bathymetric study of Lake Miage in 2003 by Diolaiuti et al. (2005), based on 556 points collected prior to the 2004 drainage event, showed a maximum depth of ~25 m. In this study, we have shown Lake Miage to reach a maximum depth of 37 m in 2017 (Figure 6.2), indicating the lake has deepened substantially through subaqueous melt based on comparisons of surface lake levels resulting in increased water storage.

## 6.5. Summary

Analysis of pond-ice cliff interactions at Miage Glacier was assessed over the 2017 – 2018 survey period. The total volume of water storage at Miage Glacier increased by 46% from 174,047 $m^3$ in 2017 to 254,732 $m^3$ in 2018; however, intermittent drainage events suggest this is highly variable over both seasonal and annual timescales. Although supraglacial ponds only equate to 8% of the water storage, they are important to consider as they are expected to increase in number over the coming decades with increasing debris cover and, along with ice cliffs, are important for understanding glacier scale ablation.

All ice cliffs underwent substantial vertical retreat ranging from −0.93 m $a^{-1}$ to −8.15 m $a^{-1}$ resulting in a loss of 39,569 $m^3$ of ice. The highest retreat rates are attributed to an ice cliff in a state of decay. Ablation at the ice-marginal Lake Miage is primarily by calving, which exhibits a cyclical pattern of slope lowering by subaerial melt, burial by debris, thermal notch undercutting and subsequent increase via calving. In comparison, the smaller supraglacial ponds appear to be melt-driven, forming surface runnels in response to a smaller fetch. Supraglacial pond volume was driven by areal expansion with limited subaqueous basal melt or depth increase. Ice cliff and pond persistence are reliant upon a state of balance between subaqueous melt, subaerial melt and calving events.

Supraglacial ponds and ice cliff co-existence are important in determining expansion processes through calving, water-line notching and subaqueous melt. As such, deep sections of supraglacial ponds are typically observed close to the associated ice cliff apart from where meltwater inflows interrupt the thermodynamics of the pond. European alpine ponds and ice cliffs have a substantial combined impact on glacier ablation rates and are therefore important to monitor to assess future glacier evolution and glacier scale ablation rates, which are expected to increase in response to warming temperatures. This study provides further understanding of simultaneous ice cliff and pond dynamics and contributes to the global dataset of small supraglacial pond bathymetric studies. Such data are required for future debris-covered glacier evolution assessments and refining pond-cliff relationships to accurately model debris-covered glacier evolution. Expansion of the results will be examined in Chapter 8.

# Chapter 7 : Debris-covered glacier dynamics in Manaslu, Nepal 1970 – 2019

## 7.1. Introduction

Following the identification of an increase in supraglacial ponding and ice cliff development at Miage Glacier, which represented regions of enhanced ablation and contributed up to eight times the mean mass loss rates (Chapters 4 – 6), a comparison with heavily debris-covered Himalayan glaciers was undertaken. This enabled the assessment of environmental settings to further understand the evolution of debris-covered glaciers in Alpine and Himalayan environments.

This chapter aims to assess debris-covered glacier dynamics in the Manaslu region focusing on Hinang Glacier and the neighbouring easterly flowing glaciers, specifically Punggen Glacier to the north and Himal Chuli Glacier to the south with similar environmental influences associated with the proximity of the glaciers to each other and their orientations (Figure 3.12, Table 7.1). Only limited research has been carried out in this region with the exception of studying the patterns of spatial variability of glacier change, and mapping of debris cover across the Manaslu region (Robson et al., 2015, 2018). Robson et al. (2018) observed reduced surface velocity across the debris-covered tongues over time and variable, yet increasing, rates of mass loss over the 1970 to 2013 period. Debris-free glaciers in the Manaslu region with lower elevations and bottom heavy hypsometries were observed to be losing the most mass. However, the evolution of surface features including supraglacial ponds and ice cliffs has not yet been explored.

The objectives of this chapter are to (i) conduct high-resolution mapping of glacier surface features, (ii) assess the glacier dynamics of the easterly flowing Manaslu glaciers, and (iii) examine the impact of supraglacial ponds and ice cliffs on the evolution of Himalayan debris-covered glaciers. By comparing and contrasting the evolution of debris-covered glaciers in different regions a greater understanding of the climatic response of debris-covered glaciers and individual controls influencing glacier evolution can be appreciated.

**Table 7.1:** Characteristics of the easterly flowing Manaslu glaciers. Data collated from GLIMs and Robson et al. (2018).

| | **Punggen Glacier** | **Hinang Glacier** | **Himal Chuli Glacier** |
|---|---|---|---|
| Glacier number (GLIMs ID) | G084584E28535N | G084577E28496N<br>G084689E285011N | G084759E28427N |
| Orientation (°) | 67.5 | 67.5 | 67.5 |
| Minimum elevation (m) | 3843 | 3498 | 3268 |
| Maximum elevation (m) | 7606 | 7597 | 7165 |
| Hypsometric index | 1.81 | Not calculated | |

## 7.2. Methods

A range of data sources were used in this study, including satellite imagery from 1970 to 2019. The 1970 Corona satellite imagery was processed by Robson et al. (2018) to produce a DEM and orthophoto. The 2013 SETSM DEM was also previously downloaded by Robson et al. (2018) and is derived from WorldView satellite imagery. Although no longer available for download, it has since been replaced by the 8 m resolution High-Mountain Asia (HMA) DEM (available via NSIDC). However, the HMA was not used for this study as coverage in this region is limited with gaps across the study sites for specified years. Furthermore, the mosaic product is derived from imagery collected over 2002 to 2016 and does not represent the glacier surface during a specific time period. Additional DEMs were extracted from stereo SPOT imagery from 2016 and 2019 in PCI Geomatica following the methods previously detailed in Section 5.2. The derived orthophotos were then used to aid glacier mapping. Due to limited coverage and cloud free imagery covering these glaciers in the Manaslu region, the only suitable, available stereo satellite data between 2013 and 2019 were from March and April 2016, which include some snow cover. Thus, care must be taken when interpreting the results using the 2016 DEM. However, it represents the best available data and the lower debris-covered sections of the glaciers have little snow cover and were therefore included to provide additional details of glacier evolution.

Landsat imagery was used to assess surface velocity change from 1991/1992, 2013/2014 and 2018/2019 using a normalised cross-correlation of orientation images (NCC-O) method implemented through the CIAS software (Kääb and Vollmer, 2000; Heid and Kääb, 2012). Post-processing methods are detailed in Section 5.2. All data used within this study are detailed in Table 7.2 including the data sources and derived information used within this study.

**Table 7.2:** Data sets used within this study (SPOT and Pleiades data provided by ESA). Some snow cover exists in the 2016 data and must be interpreted with caution. All datasets used the panchromatic band for DEM extraction and SWIR for surface velocity analysis.

| Date of acquisition (dd/mm/yr) | Sensor | Image Resolution (m) | Image Pairs | Data extracted |
|---|---|---|---|---|
| 19/11/1970 | Corona | 1.8 | Stereo | DEM /Glacier mapping |
| 16/11/2013 | WorldView 1/2 | 8.0 | Stereo | DEM |
| 17/11/2013 | SETSM | | | |
| 25/11/2013 | | | | |
| 19/01/2014 | | | | |
| 16/11/2013 | SPOT6 | 1.5 | | Glacier mapping |
| 25/04/2016 | SPOT6 | 1.5 | Stereo | DEM |
| 23/03/2016 | | | | |
| 27/10/2019 | SPOT7 | 1.5 | Tri-stereo | DEM/ Glacier mapping |
| 13/10/2019 | Pleiades 1A | 0.5 | Tri-stereo | DEM/ Glacier mapping |
| 26/09/1991 | Landsat5 TM | 30.0 | | Surface velocity |
| 14/10/1992 | Landsat5 TM | 30.0 | | |
| 08/10/2013 | Landsat8 OLI | 30.0 | | Surface velocity |
| 11/10/2014 | Landsat8 OLI | 30.0 | | |
| 22/10/2018 | Landsat8 OLI | 30.0 | | Surface velocity |
| 25/10/2019 | Landsat8 OLI | 30.0 | | |
| 2019 May to November | Planetscope | 3.0 | Individual scenes | NDWI<br>Pond mapping |

### 7.2.1. Glacier mapping

Glacier surfaces were mapped from orthophotos derived from the 1970 Corona imagery, 2013 SPOT orthophoto and 2019 SPOT/Pleiades orthophotos and glacier change assessed. Methods were used as detailed in Sections 4.2. and 5.2. including mapping of the glacier extent, debris cover, crevassing, ogive bands, and surface features (including supraglacial ponds and ice cliffs). Uncertainty and accuracy estimates were calculated as previously documented via repeat mapping and are presented in Table 7.3 and with the results. Supraglacial ponds were mapped with a maximum percentage variation of 8% and standard deviations ranging from 21 to 450 $m^2$. Repeat mapping of ice cliff standard deviations ranged from 20 to 337 $m^2$ with maximum percentage variations of 6%.

**Table 7.3:** Accuracy and uncertainty estimates associated with the mapped components. Ranges show the maximum and minimum values for Punggen Glacier, Hinang Glacier and Himal Chuli Glacier.

| Date | Glacier extent/ termini position ($km^2$/m) | Debris cover at ±5% ($km^2$) | Supraglacial ponds at ±10% ($m^2$) | Ice cliffs at ±8% ($m^2$) |
|---|---|---|---|---|
| 1970 | ±0.26 / 9.09 | 0.14 – 0.63 | 1204 | 960 – 5040 |
| 2013 | ±0.25 / 7.5 | 0.19 – 0.44 | 305 – 1140 | 180 – 2700 |
| 2019 | ±0.13 / 7.5 | 0.20 – 0.57 | 326 – 3459 | 240 – 1500 |

### 7.2.2. Digital Elevation Model (DEM) analysis

Details for DEM extraction, analysis and uncertainty assessment are the same as used for Miage Glacier in Section 5.2.1. Digital Elevation Models (DEM) extraction. Table 7.4 details the GCPs and tie-points used in the DEM extraction within PCI Geomatica.

**Table 7.4:** Summary of the GCPs and tie-points used to enhance the alignment of the imagery prior to DEM extraction.

| DEM | Number of GCPs | Residuals X, Y (Pixels) | Number of tie-points | Residuals X, Y (Pixels) |
|---|---|---|---|---|
| 2016 | 16 | 1.12, 2.74 | 256 | 0.90, 0.60 |
| 2019 | 97 | 0.87, 2.23 | 32 | 0.16, 0.19 |

DEM co-registration was carried out as previously detailed in Section 5.2.1. following the methods by Nuth and Kääb (2011); however, once the co-registered surface elevation had been filtered to remove errors, which exceeded three times the standard deviation of stable terrain (Gardelle et al., 2013), gaps were then filled with a trend interpolation as recommended by McNabb et al. (2019).

Glacier hypsometry was calculated based on the glacier extents and the extracted 2019 DEM based on the methods by Robson et al. (2018) and King et al. (2017) using Equation 7.1.

$$\boldsymbol{HI} = \frac{\boldsymbol{Hmax - Hmed}}{\boldsymbol{Hmed - Hmin}} \text{ if } 0 < HI < 1 \text{ then } \boldsymbol{HI} = \frac{\boldsymbol{-1}}{\boldsymbol{HI}} \qquad \textbf{Equation 7.1}$$

### 7.2.3. Surface velocity

Analysis was carried out using the CIAS software and processing steps were followed as detailed in Section 5.2.2., including a comprehensive assessment of the uncertainties related to the surface velocity calculation. Table 7.5 presents the accuracy assessment for the derived surface velocity datasets.

**Table 7.5:** Accuracy assessment of the surface velocity feature tracking calculated for each glacier based on stable ground.

| | Punggen Glacier | | Hinang Glacier | | Himal Chuli Glacier | |
|---|---|---|---|---|---|---|
| **Velocity data set** | **Standard Deviation (m $a^{-1}$)** | **Mean error (m $a^{-1}$)** | **Standard Deviation (m $a^{-1}$)** | **Mean error (m $a^{-1}$)** | **Standard Deviation (m $a^{-1}$)** | **Mean error (m $a^{-1}$)** |
| 1991 / | | | | | | |
| 1992 | 45.03 | 31.98 | 53.53 | 38.80 | 43.23 | 27.70 |
| 2013 / | | | | | | |
| 2014 | 33.33 | 15.57 | 32.36 | 16.64 | 21.85 | 6.73 |
| 2018 / | | | | | | |
| 2019 | 38.24 | 20.96 | 30.69 | 11.13 | 25.31 | 7.88 |

### 7.2.4. Bathymetric surveys

A field visit to Hinang Glacier was undertaken in September 2019, and four accessible supraglacial ponds were surveyed with the Seafloor Systems Hydrone remote control bathymetric survey as detailed in Section 6.2.1. For each of the four ponds surveyed, a photogrammetry survey was also carried out and a SfM derived model created to assess ice cliff – pond relationships. Due to time and equipment limitations in addition to difficulty accessing the highly undulating glacier and supraglacial ponds, only four ponds and associated ice cliffs were surveyed. Additional supraglacial ponds were observed both from the higher lateral moraines and satellite imagery but were deemed either unsafe or not accessible to cross the glacier due to the terrain and ability to transfer the equipment to the locations of the ponds. Details of the four bathymetric surveys completed in September 2019 including the number of depth measurements, GNSS accuracy of the depth points, and the mean interpolation error (RMSE) are detailed in Table 7.6. Locations of the surveyed supraglacial ponds on Hinang Glacier are shown in Figure 7.1.

**Table 7.6:** Number of depth measurements, mean XY GPS accuracy and RMSE for the IDW interpolations for the bathymetric maps.

| Pond | Number of depth measurements | Mean XY GPS accuracy (m) | Mean interpolation standard error (RMSE) |
|---|---|---|---|
| Supraglacial pond 1 – H1 | 1713 | 0.08 | 0.168 |
| Supraglacial pond 2 – H2 | 5846 | 0.47 | 0.476 |
| Supraglacial pond 3 – H3 | 2577 | 0.11 | 0.600 |
| Supraglacial pond 4 – H4 | 2416 | 0.07 | 0.297 |

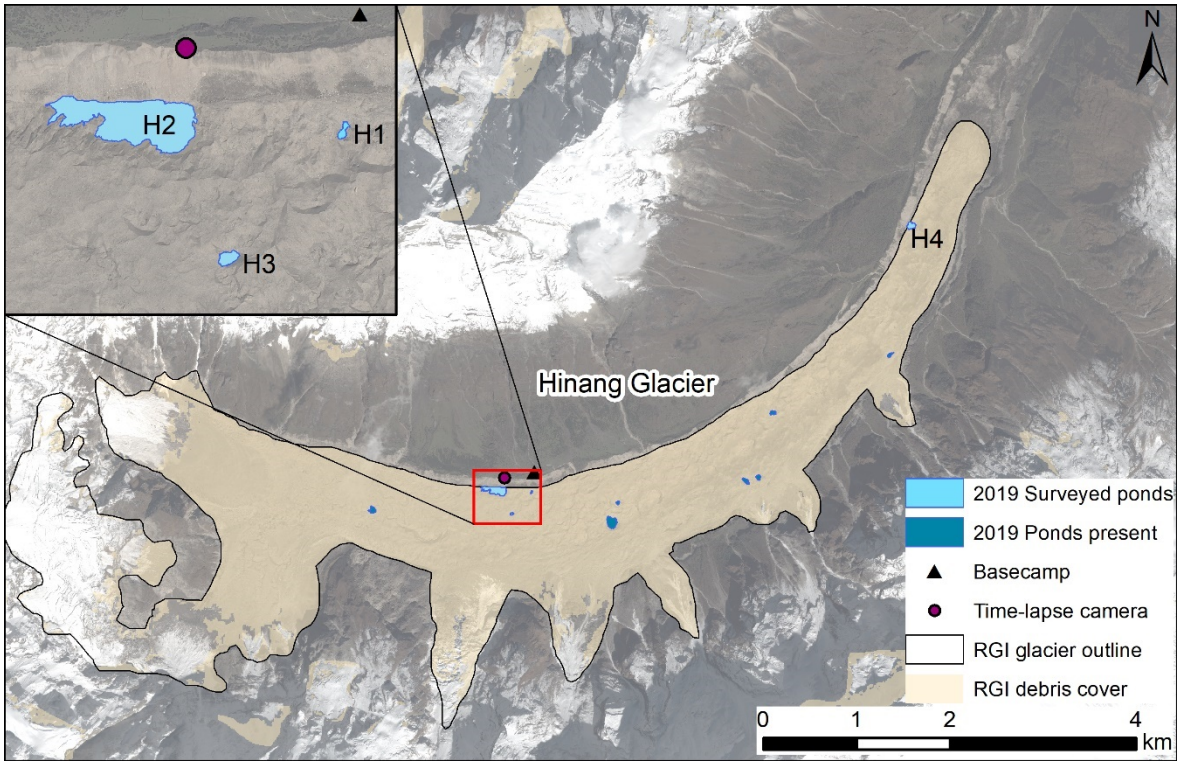


**Figure 7.1:** Locations of the ponds that were surveyed on Hinang Glacier in September 2019 and additional ponds that were identified using Planet satellite imagery. Purple dot indicates the location where the time-lapse camera was installed in 2019.

### 7.2.5. Photogrammetry surveys

All photogrammetric surveys were undertaken in September 2019 in clear weather conditions. Surveys were generally carried out in the mornings when the weather was clearer and drier as afternoon monsoon rain and cloud often came up the valley obscuring views. The photogrammetry surveys were limited to the adjacent ice cliffs that surrounded the bathymetrically surveyed supraglacial ponds. Large ice cliffs were observed across the glacier due to the undulating surface topography. Each ice cliff survey typically took <2 hours, with between 126 to 415 images dependant on cliff size and extent of undulating topography. The spread of GCPs was limited to more stable areas, which were accessible as the large cliff faces and unstable debris was difficult to manoeuvre upon. Therefore, the GCPs were not always ideally spatially placed around the ice cliff but were located to get the best spatial coverage possible (Table 7.7).

**Table 7.7:** Errors of the photogrammetry SfM ice cliff models during processing and summary of GCPs, check points and accuracy.

| Pond | Resolution mm/pix | Georeferencing XYZ uncertainty (m) | Mean point density (per $m^2$) | No. control GCPs | RMSE - control (m) | No. check points | Accuracy – check (cm) |
|---|---|---|---|---|---|---|---|
| H1 | 2.22 | 0.08 | $5.6 \times 10^4$ | 4 | 0.02 | 4 | 0.06 |
| H2 | 137 | 0.40 | $1.3 \times 10^3$ | 5 | 0.25 | 5 | 0.41 |
| H3 | 2.40 | 0.11 | $4.1 \times 10^4$ | 5 | 0.10 | 4 | 0.16 |
| H4 | 6.41 | 0.07 | $6.8 \times 10^3$ | 4 | 0.03 | 3 | 0.12 |

Quantification of change or ice loss associated with the supraglacial ponds or ice cliffs was not possible due to only having surveyed them during one field season. During the fieldwork, an enlaps Tikee time-lapse camera was placed high up on the northern lateral moraine (Figure 7.1) to capture glacier change including those of the largest pond surveyed (H2). It is hoped that future work will enable more detailed analysis of glacier and pond/cliff evolution at this location.

## 7.3. Results

### 7.3.1. Surface mapping

Glacier surface change was mapped from orthophotos derived from the imagery obtained in 1970, 2013 and 2019 (Figure 7.2 to Figure 7.4). Glacier extent reduced for all three easterly flowing glaciers in the Manaslu region, with a maximum reduction of 16% for Punggen Glacier, and a minimum of 4.5% for Hinang Glacier between 1970 and 2019 (Table 7.8). During this period, debris-cover expanded upglacier by between 2 – 9% of the glacier area with the largest increase observed on Punggen Glacier having expanded upglacier by ~1.5 km. The presence of supraglacial ponds increased on all three glaciers over the 1970 to 2019 period with the largest ponded area increase observed on Hinang Glacier from 0 to 43,235 $km^2$. Conversely, despite the increase in supraglacial ponds, ice cliffs have existed across the glacier surfaces of all three glaciers since the start of the study period in 1970 and maintained a relatively stable extent throughout the observation period (Table 7.8).

Icefalls are present on all three glaciers and transfer ice mass between the higher accumulation zones to the lower debris-covered regions confined within the valleys. Ogives are visible on all three glaciers at the base of the icefalls associated with ice flux across the steep topography from the higher accumulation zones. Crevasses were limited to the upper and lateral regions and decreased over the observation period, in part due to the increase in debris cover limiting their visibility in the imagery.

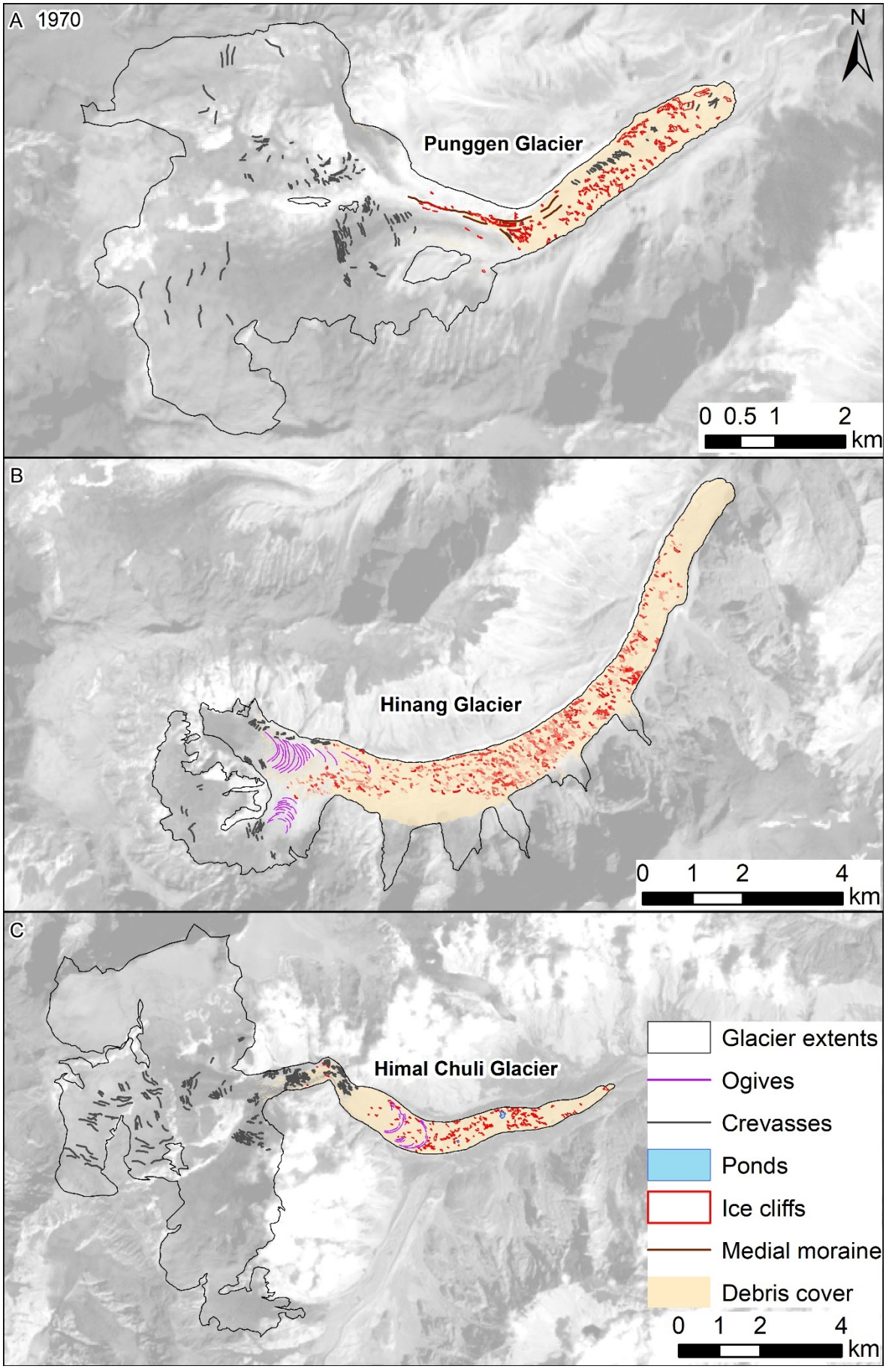


**Figure 7.2:** Surface mapping in 1970 of A: Punggen Glacier, B: Hinang Glacier and C: Himal Chuli Glacier. Background images show Landsat imagery.

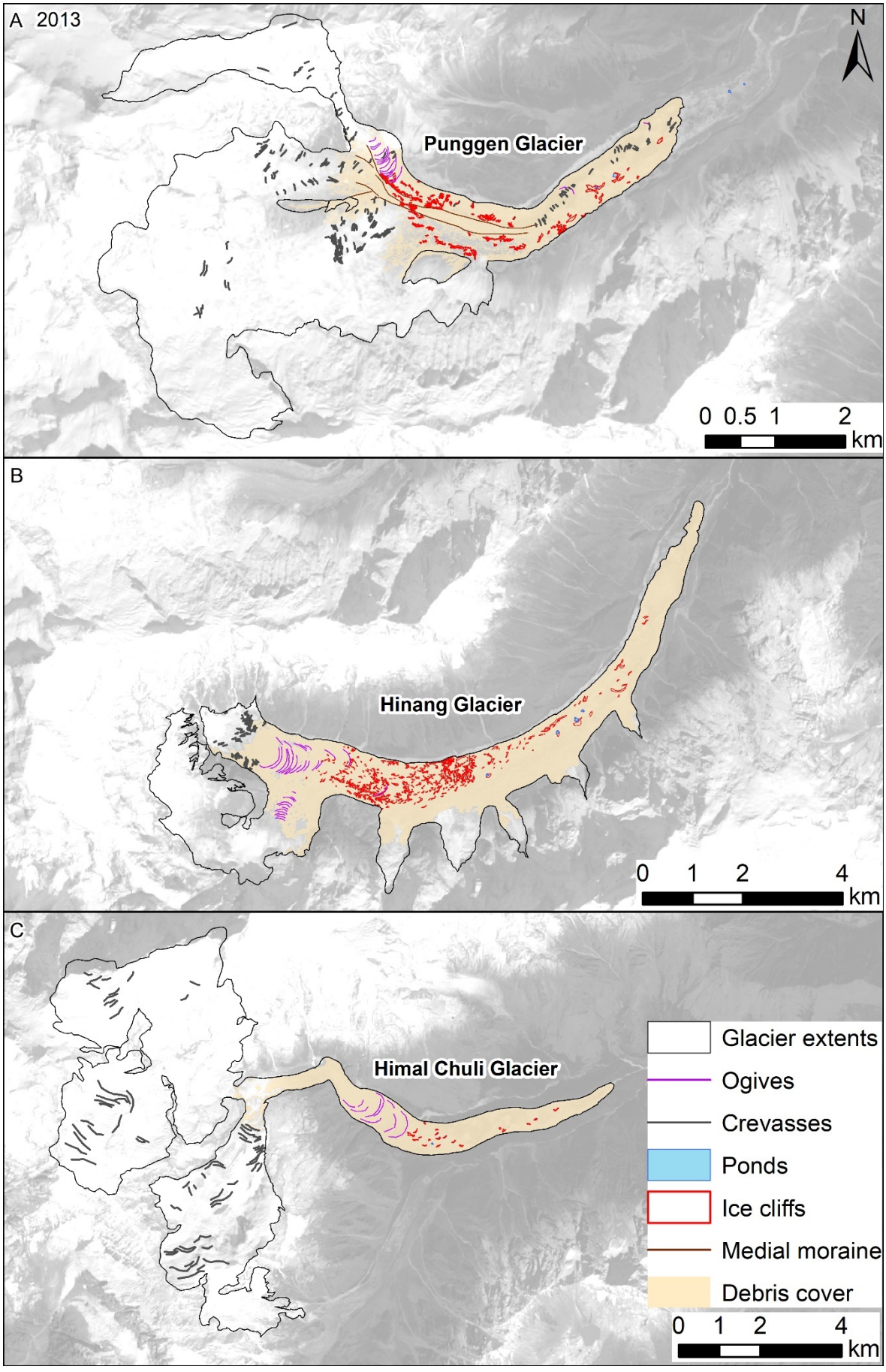


**Figure 7.3:** Surface mapping in 2013 of A: Punggen Glacier, B: Hinang Glacier and C: Himal Chuli Glacier. Background images show Landsat imagery from the corresponding year.

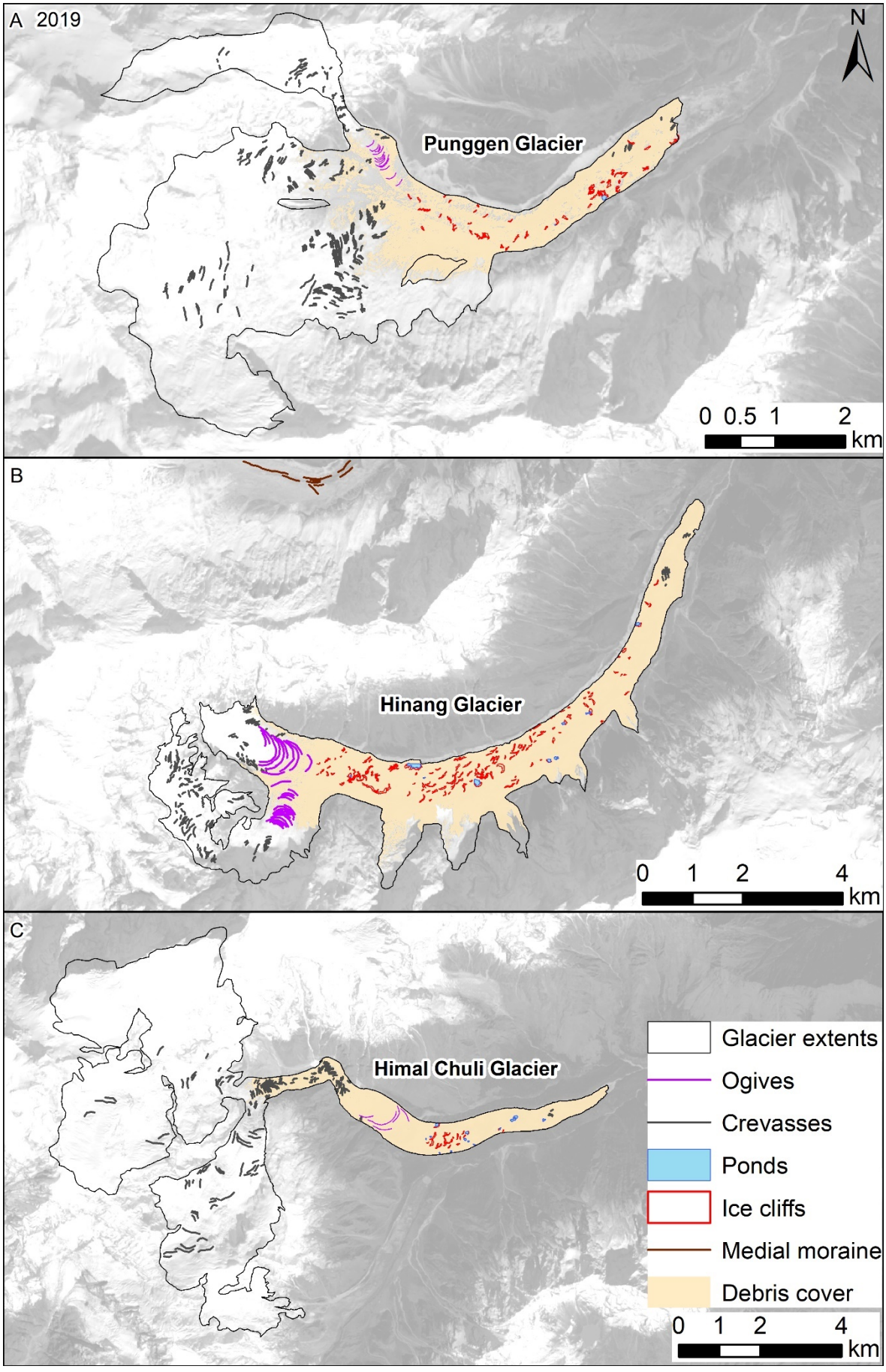


**Figure 7.4:** Surface mapping in 2019 of A: Punggen Glacier, B: Hinang Glacier and C: Himal Chuli Glacier Background images show Landsat imagery from the corresponding year.

**Table 7.8:** Glacier surface change derived from mapping of the orthophotos in 1970, 2013 and 2019 as shown in Figure 7.2 to Figure 7.4.

| | **1970** | | | **2013** | | | **2019** | | |
|---|---|---|---|---|---|---|---|---|---|
| **Surface feature** | Punggen | Hinang | Himal Chuli | Punggen | Hinang | Himal Chuli | Punggen | Hinang | Himal Chuli |
| Glacier extent ($km^2$) | 22.1 | 19.9 | 39.7 | 18.7 | 19.0 | 37.9 | 18.6 | 18.6 | 36.9 |
| Debris extent ($km^2$) | 2.7 | 10.4 | 5.3 | 3.9 | 11.8 | 5.8 | 3.9 | 11.3 | 5.5 |
| Debris extent as % of total glacier area | 12 | 52 | 13 | 21 | 62 | 15 | 21 | 61 | 15 |
| Supraglacial ponds ($m^2$) | 0 | 0 | 15047 | 14252 | 9738 | 3807 | 4076 | 43235 | 28456 |
| Percentage cover of supraglacial ponds of the total glacier area | 0 | 0 | 0.04 | 0.08 | 0.05 | 0.01 | 0.02 | 0.23 | 0.08 |
| Ice cliffs ($km^2$) | 0.19 | 0.84 | 0.16 | 0.14 | 0.45 | 0.03 | 0.05 | 0.25 | 0.04 |
| Percentage cover of ice cliffs of total glacier area | 0.86 | 4.22 | 0.40 | 0.75 | 2.37 | 0.08 | 0.27 | 1.34 | 0.11 |
| Ogives (km) | - | 11.30 | 4.82 | 3.92 | 9.20 | 4.76 | 2.34 | 12.20 | 2.56 |
| Crevasses (km) | 17.30 | 5.30 | 30.40 | 13.27 | 4.90 | 22.84 | 23.70 | 13.06 | 22.50 |

### 7.3.2. Surface elevation change 1970 – 2019

The overall trend in surface elevation change over the 1970 to 2019 study period is of sustained surface lowering for all three of the easterly flowing Manaslu glaciers (Figure 7.5). Hinang Glacier experienced the highest rates of surface lowering (−0.47 ± 0.05 m $a^{-1}$), while Punggen Glacier underwent the least surface lowering (−0.27 ± 0.03 m $a^{-1}$). Himal Chuli Glacier experienced −0.33 ± 0.03 m $a^{-1}$ surface lowering over the full study period from 1970 to 2019 (Table 7.9).

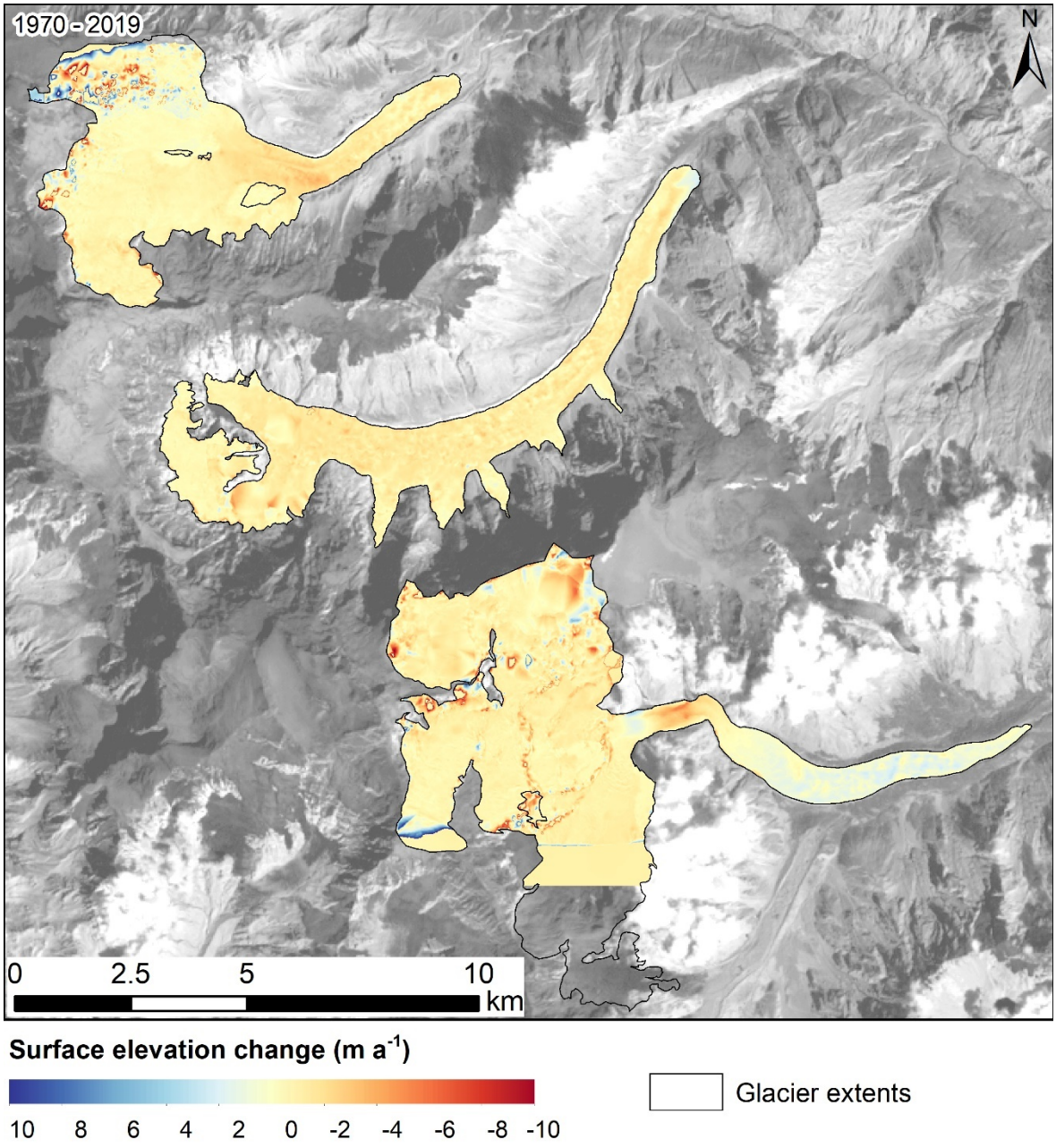


**Figure 7.5:** Surface elevation change in 1970 – 2019 covering Punggen Glacier, Hinang Glacier and Himal Chuli Glacier.

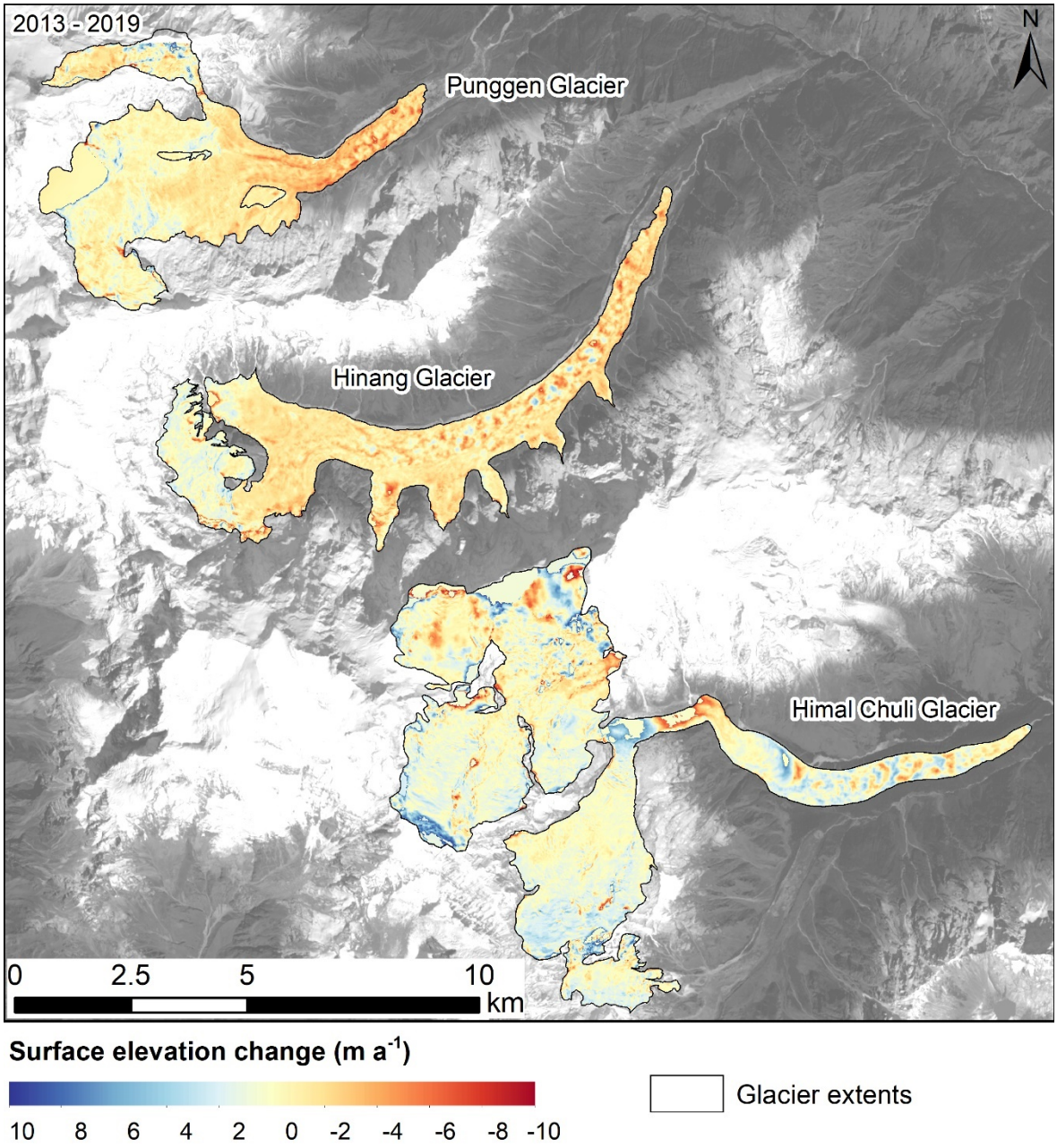


**Figure 7.6:** Surface elevation change in 2013 – 2019 covering Punggen Glacier, Hinang Glacier and Himal Chuli Glacier.

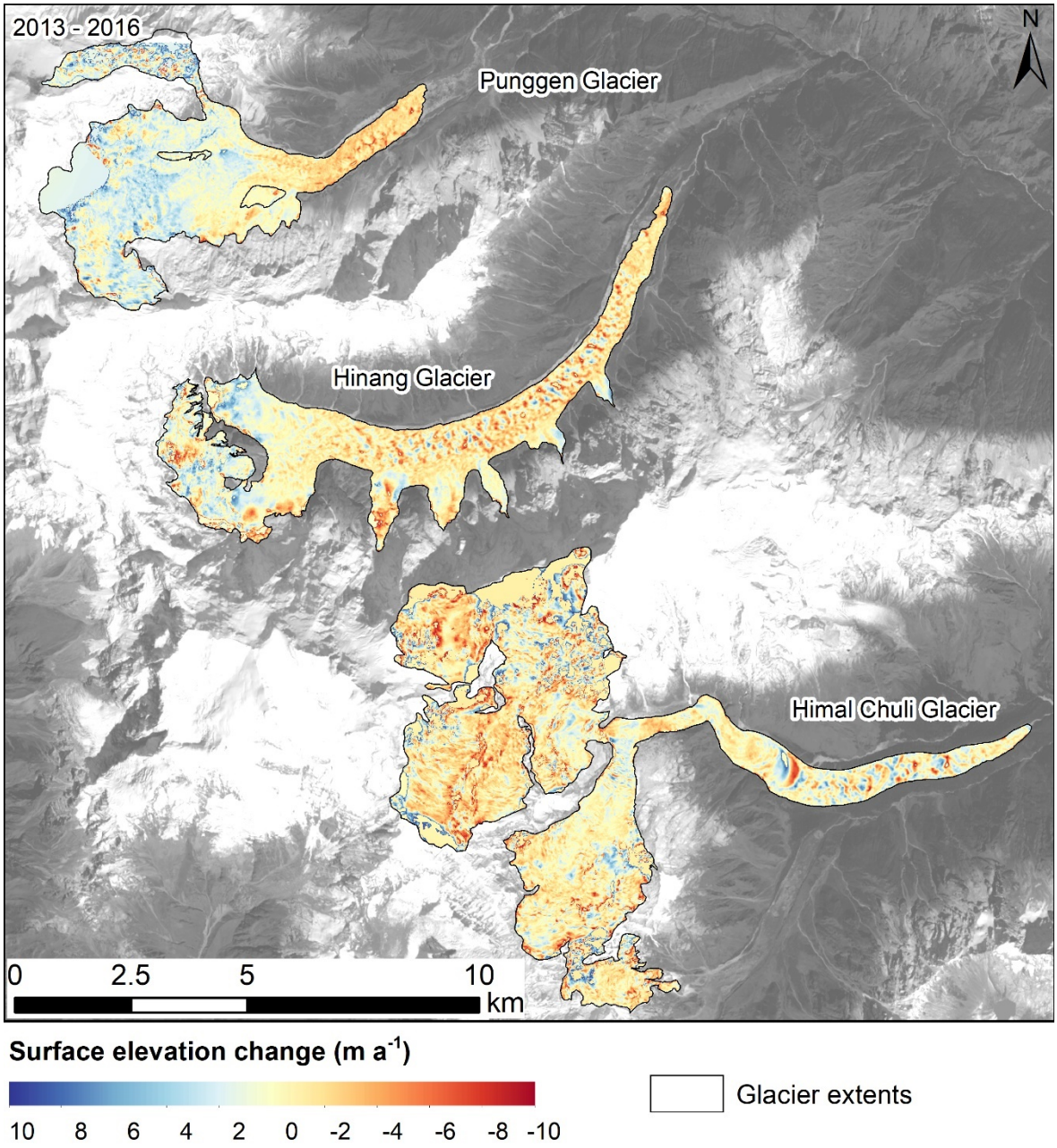


**Figure 7.7:** Surface elevation change in 2013 – 2016 covering Punggen Glacier, Hinang Glacier and Himal Chuli Glacier.

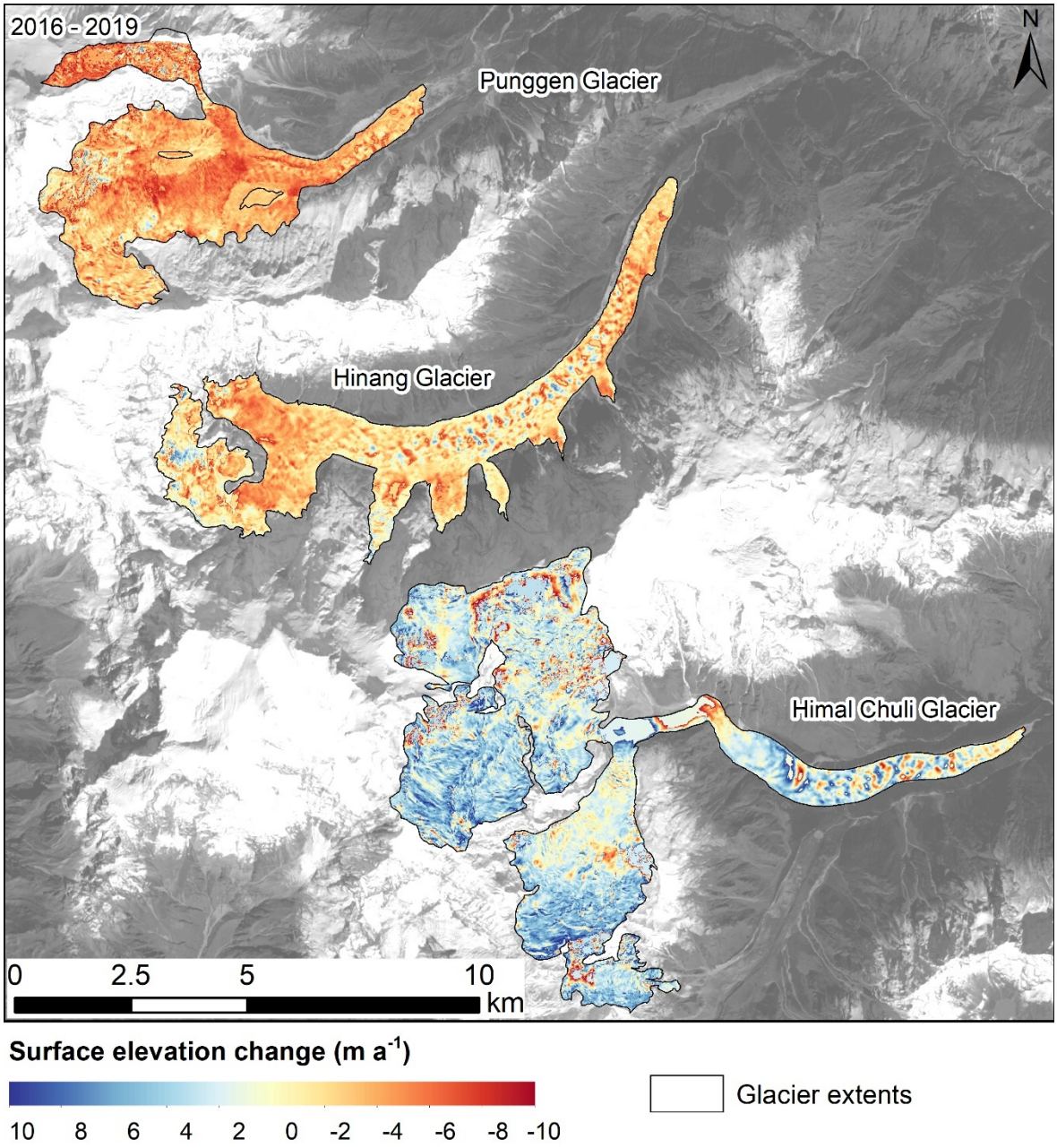


**Figure 7.8:** Surface elevation change in 2016 – 2019 covering Punggen Glacier, Hinang Glacier and Himal Chuli Glacier.

**Table 7.9:** Glacier surface elevation change per year and calculated geodetic mass balance of Punggen Glacier, Hinang Glacier and Himal Chuli Glacier from 1970 to 2019. *Care should be taken when interpreting the results associated with the 2016 DEM data as snow cover in the upper reaches incorporates mass loss from seasonal snow cover.

| | Surface elevation change (m $a^{-1}$) | | | Geodetic mass balance (m w.e.$a^{-1}$) | | |
|---|---|---|---|---|---|---|
| | **Punggen** | **Hinang** | **Himal Chuli** | **Punggen** | **Hinang** | **Himal Chuli** |
| 1970 – 2019 | −0.27 ± 0.03 | −0.47 ± 0.05 | −0.33 ± 0.03 | −0.23 ± 0.04 | −0.40 ± 0.07 | −0.24 ± 0.04 |
| 1970 – 2013 | −0.38 ± 0.04 | −0.40 ± 0.04 | −0.67 ± 0.06 | −0.32 ± 0.06 | −0.34 ± 0.06 | −0.49 ± 0.09 |
| 2013 – 2019 | −0.93 ± 0.11 | −1.23 ± 0.14 | +0.58 ± 0.07 | −0.79 ± 0.15 | −1.05 ± 0.19 | +0.49 ± 0.10 |
| 2013 – 2016 | +0.82 ± 0.10 | −0.49 ± 0.09 | −0.42 ± 0.11 | +0.70 ± 0.13 | −0.41 ± 0.10 | −0.55 ± 0.11 |
| 2016 – 2019 | −3.81 ± 0.34 | −2.13 ± 0.20 | +0.53 ± 0.06 | −3.24 ± 0.56 | −1.81 ± 0.32 | +0.45 ± 0.08 |

Over the 1970 – 2019 study period, high thinning rates were generally observed on the lower debris-covered valley sections of the glaciers, with limited surface lowering in the higher accumulation zones (Figure 7.5). These areas in the upper reaches also exhibit regions of positive surface elevation change associated with snow accumulation, including along ridges, and ice dynamics at higher elevations.

Variable surface lowering rates were observed on all three glaciers from 1970 – 2019, but indicate substantially increased rates of surface lowering between 2013 and 2019 on Punggen Glacier and Hinang Glacier with up to $-1.23 \pm 0.16$ m $a^{-1}$ surface lowering on Hinang Glacier (Table 7.9, Figure 7.6). In contrast, during this period Himal Chuli Glacier experienced an overall positive mass balance of $+0.58 \pm 0.07$ m $a^{-1}$ indicating strong individual glacier variability.

Heterogenous elevation change is evident across the glacier surfaces and between the three glaciers. Punggen Glacier shows a region of high thinning rates on the southern side at the base of steep section as ice flows into the valley section where debris cover has increased (Figure 7.2, Figure 7.5 to Figure 7.8). Hinang Glacier shows fairly homogenous surface lowering across the glacier surface over the full study period, with a zone of positive surface elevation change at the glacier terminus suspected to result from debris accumulation. Himal Chuli Glacier shows high rates of surface lowering on the narrow icefall, which transfers ice from the accumulation zone to the main trunk, yet highly variable surface elevation change on the trunk glacier. Overall, the trunk section was dominated by slightly positive surface elevation change over the full observation period from 1970 to 2019 (Figure 7.5). Despite overall long-term surface lowering, regions on the valley glacier including a rockfall deposit as identified by Robson et al. (2018)and presence of a large supraglacial pond are evident with surface lowering between 2013 and 2016 (Figure 7.7) and surface increase between 2016 – 2019 (Figure 7.8) showing high levels of variability and heterogenous change. Variability in elevation change can be observed on all three glaciers with high levels of heterogenous surface lowering associated with the debris-covered regions, supraglacial ponds and ice cliffs (Figure 7.9, Table 7.10). Punggen Glacier and Hinang Glacier show high rates of surface lowering under the mapped debris-covered regions between 2013 to 2019 compared to Himal Chuli Glacier, which shows positive surface elevation change, yet regions of ice cliffs are strongly associated with ice loss (Table 7.10).

**Table 7.10:** Summary of surface elevation change on regions associated with debris cover, supraglacial ponds and ice cliffs. Uncertainty of supraglacial ponds and ice cliffs was estimated <8%.

| | | Surface elevation change (m $a^{-1}$) | | |
|---|---|---|---|---|
| | | **Debris cover** | **Supraglacial ponds** | **Ice cliffs** |
| Punggen Glacier | 1970 – 2013 | −0.42 ± 0.03 | | |
| | 2013 – 2019 | −2.29 ± 0.12 | | |
| | 2013 – 2016 | −1.02 ± 0.10 | −2.47 | −4.57 |
| | 2016 – 2019 | −4.21 ± 0.34 | −4.46 | −4.35 |
| Hinang Glacier | 1970 – 2013 | −0.46 ± 0.05 | | |
| | 2013 – 2019 | −1.62 ± 0.15 | | |
| | 2013 – 2016 | −0.92 ± 0.09 | −1.30 | −1.19 |
| | 2016 – 2019 | −2.33 ± 0.20 | −2.42 | −2.30 |
| Himal Chuli Glacier | 1970 – 2013 | +0.09 ± 0.05 | | |
| | 2013 – 2019 | +0.39 ± 0.08 | | |
| | 2013 – 2016 | −0.16 ± 0.11 | −2.16 | −0.65 |
| | 2016 – 2019 | +0.06 ± 0.06 | +0.68 | −0.35 |

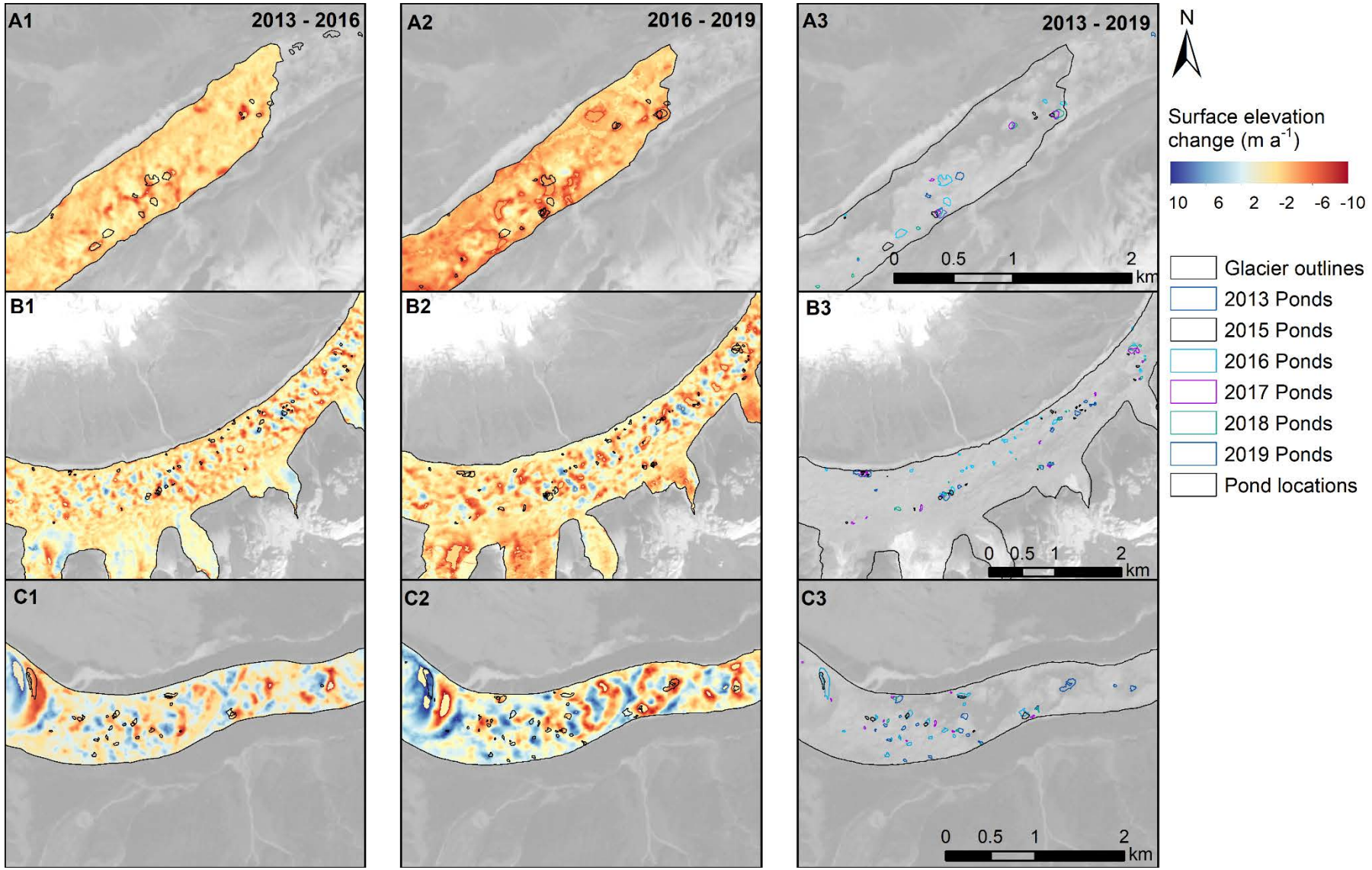


**Figure 7.9:** Surface elevation change m $a^{-1}$ and supraglacial pond locations 2013 – 2016 for Punggen Glacier (A1), Hinang Glacier (B1) and Himal Chuli Glacier (C1). Elevation change and pond locations between 2016 – 2019 for Punggen Glacier (A2), Hinang Glacier (B2) and Himal Chuli Glacier (C2). Supraglacial pond distribution between 2013 and 2019 for Punggen Glacier (A3), Hinang Glacier (B3) and Himal Chuli Glacier (C3).

Longitudinal profiles show a highly undulating glacier surface on Punggen Glacier, which has increased in the lower section and lowered in the upper region associated with the steeper topography (Figure 7.10). Hinang Glacier shows very little change and a comparatively smooth surface topography with a low overall surface gradient <5°, and Himal Chuli Glacier shows a similar profile inversion to that of Punggen Glacier and highest surface gradient of the three glaciers (>5°). Furthermore, all three glaciers indicate very little change in surface gradient from 1970 to 2019 with the highest change detected on regions where supraglacial ponding was observed on Punggen Glacier (reduction of 0.73°).

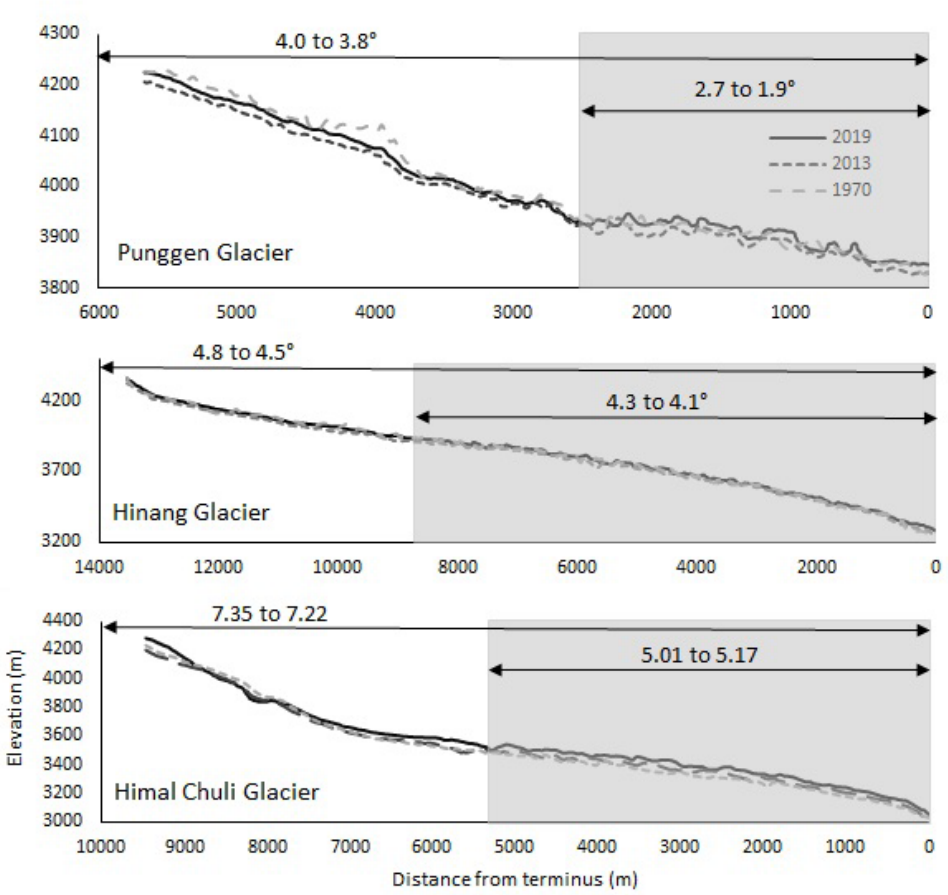


**Figure 7.10:** Longitudinal profiles of Punggen Glacier, Hinang Glacier and Himal Chuli Glacier with the overall change in surface gradient and change over the regions associated with supraglacial ponding. Greyed out section indicates the regions where supraglacial ponding was observed.

Hypsometric indexes were calculated for the three glaciers based on the 2019 DEM and showed that Punngen Glacier and Hinang Glacier exhibited equidimensional hypsometries with values of −0.46 and −0.54 respectively. In comparison, Himal Chuli Glacier exhibited a very top heavy hypsometry with an index of −1.67, relating to the large accumulation zones in comparison to the debris-covered ablation zone.

### 7.3.3. Surface velocity change 1991 – 2019

The surface velocity of Punggen Glacier and Hinang Glacier reduced over the 1991 to 2019 period with an overall reduction of 36 and 19% respectively (Figure 7.11, Table 7.11). Yet, Himal Chuli Glacier underwent a reduction between 1991/1992 and 2013/2014 followed by an increase in mean surface velocity and exhibited the largest overall reduction between 1991 to 2019 of 45%. The most prominent reduction in surface velocity was observed in the lower 500 m terminus region of all three glaciers where rates <5 m $a^{-1}$ indicate stagnation. The stagnating zone is also progressively migrating upglacier from the terminus.

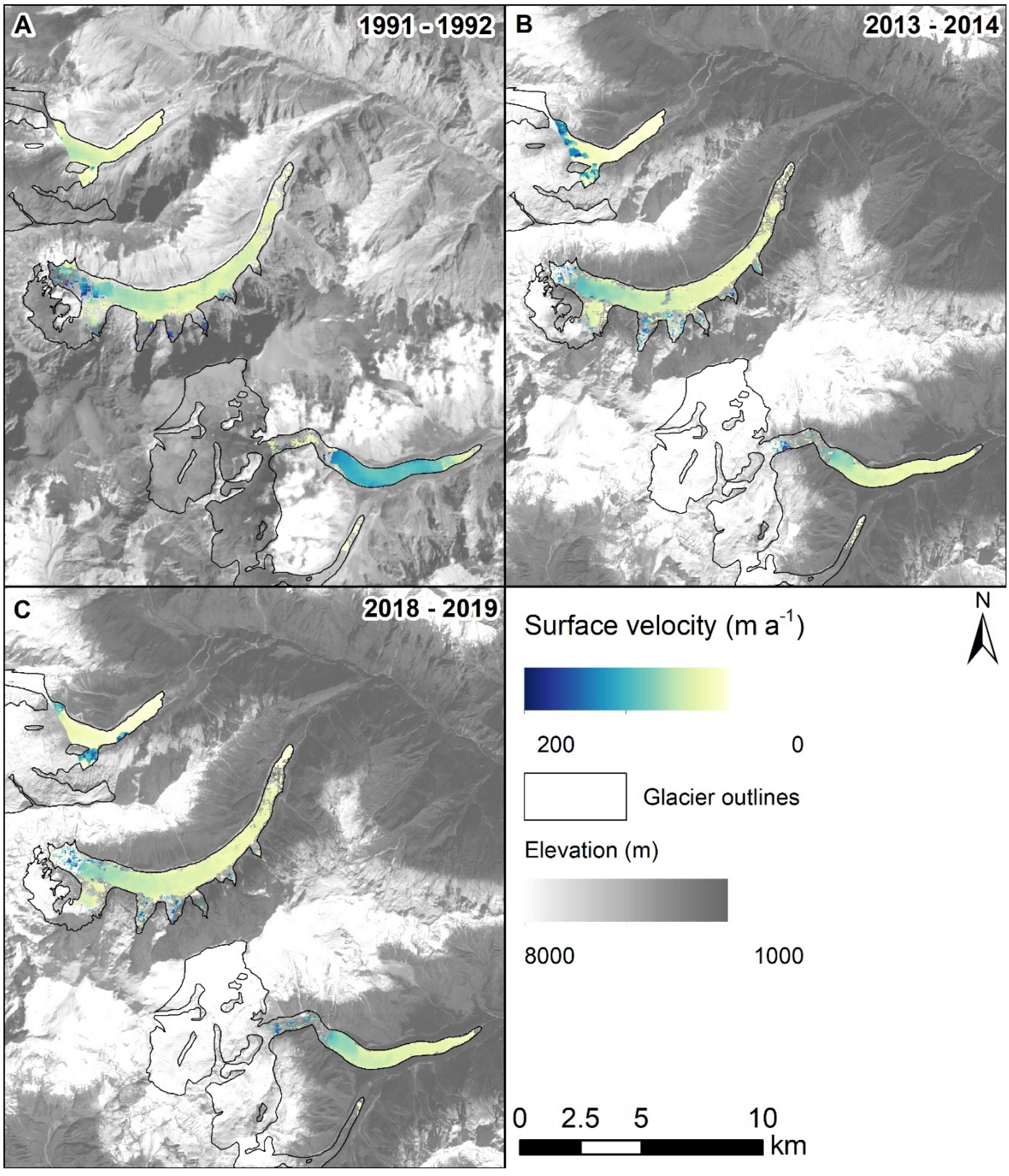


**Figure 7.11:** Surface velocity in A: 1991/1992, B: 2013/2014, and C: 2018/2019.

**Table 7.11:** Mean surface velocity change from 1991 to 2019 for Punggen Glacier, Hinang Glacier and Himal Chuli Glacier calculated from regions shown in Figure 7.11.

| Time period | Punggen Glacier surface velocity (m $a^{-1}$) | Hinang Glacier surface velocity (m $a^{-1}$) | Himal Chuli Glacier surface velocity (m $a^{-1}$) |
|---|---|---|---|
| 1991 / 1992 | 27.86 | 46.61 | 78.55 |
| 2013 / 2014 | 25.88 | 40.24 | 35.18 |
| 2018 / 2019 | 17.91 | 37.77 | 43.55 |

Punggen Glacier exhibited an increase in surface velocity in the upper reaches in 2013/2014 where steeper topography transfers ice via the icefall, but by 2018/2019 this was limited to the tributary glacier around a nunatak (Figure 7.11c, Figure 7.2). By 2018/2019 the most active ice flow was restricted to the higher elevations, tributary glaciers and narrow icefalls, which confine the transfer of ice from the accumulation zones.

### 7.3.4. Photogrammetry and bathymetry analysis

The four surveyed supraglacial ponds and ice cliffs surveyed on Hinang Glacier in September 2019 are shown in Figure 7.12. Pond depths varied from 5.42 m to 25.7 m (Table 7.12). The largest of the ponds surveyed was also the largest pond present on the glacier during the survey period and held a volume of 107,246 $m^3$, whilst the smallest pond only held 280 $m^3$. The four supraglacial ponds combined held a volume of 142,958 $m^3$. The four surveyed ponds are representative of 53% of the total ponded area and H2 represents 39% of the total ponded area alone.

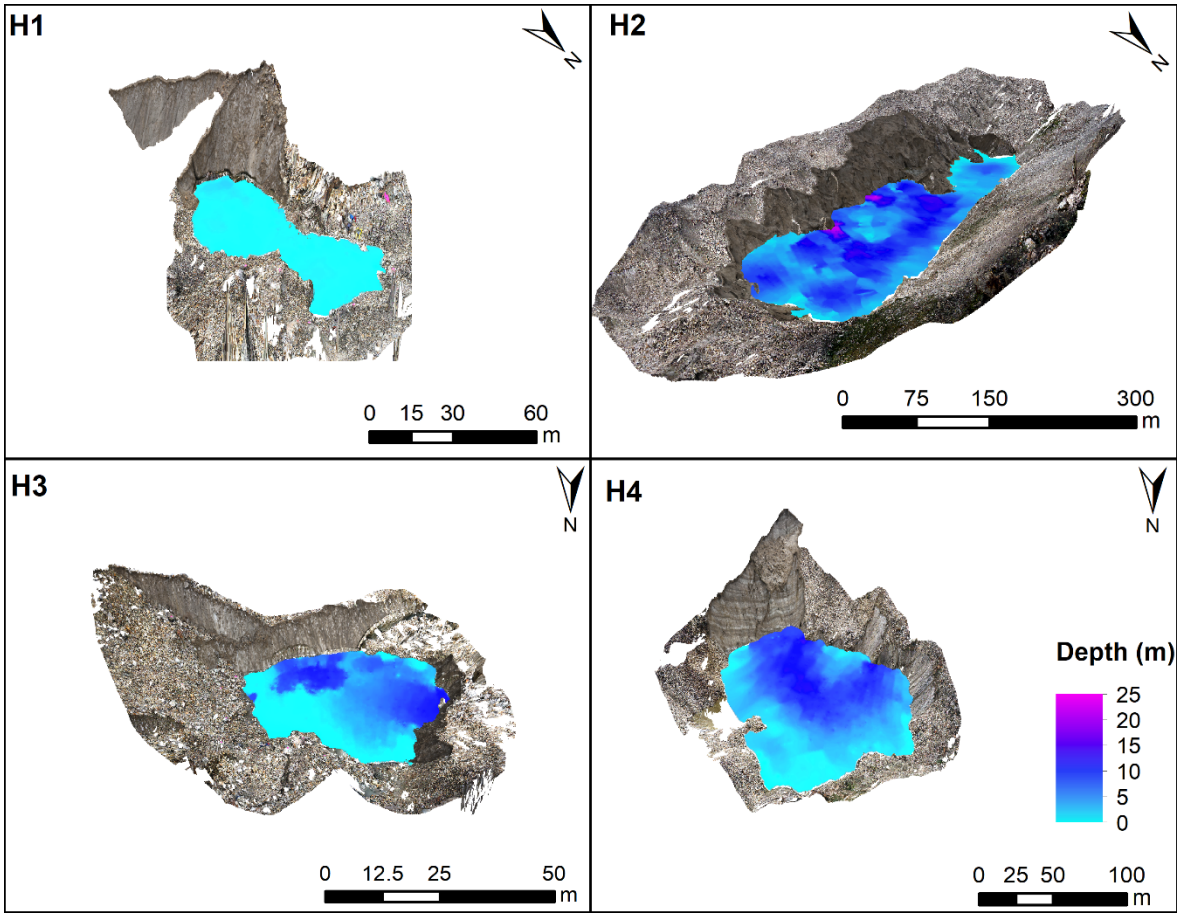


**Figure 7.12:** Bathymetric surveys of the supraglacial ponds and SfM photogrammetry models of the adjacent ice cliffs.

**Table 7.12:** Area, depth, lake levels and volume of supraglacial ponds surveyed in September 2019. Uncertainties were calculated from RMSE.

| | Area ($m^2$) | Max. depth (m) | Lake level (m) | Volume ($m^3$) |
|---|---|---|---|---|
| Supraglacial pond 1 (H1) | 329 | 5.42 ± 0.01 | 3948.08 | 280 ± 0.17 |
| Supraglacial pond 2 (H2) | 16791 | 25.7 ± 0.06 | 3962.19 | 107246 ± 0.48 |
| Supraglacial pond 3 (H3) | 714 | 14.12 ± 0.04 | 3966.40 | 3198 ± 0.60 |
| Supraglacial pond 4 (H4) | 5290 | 14.43 ± 0.04 | 3616.10 | 32234 ± 0.30 |

The maximum height of the ice cliffs varied from 8.69 m to 31.64 m and the surface area ranges from 425 to 18,199 $m^2$. The ice cliffs were predominantly north facing with mean slopes ranging from 5 to 24° (Table 7.13). The ice cliff with the highest surface area and maximum height, was adjacent to the largest supraglacial pond surveyed (H2).

**Table 7.13:** Summary of 2019 ice cliff geometry results.

| Model | Max. height of ice cliff (m) | Surface Area ($m^2$) | Aspect (°) | Mean slope (°) |
|---|---|---|---|---|
| H1 | 8.69 | 425 | 083 | 24 |
| H2 | 29.23 | 18199 | 013 | 10 |
| H3 | 15.25 | 784 | 256 | 6 |
| H4 | 31.64 | 3439 | 313 | 5 |

### 7.3.5. Monsoon season pond variability

To further explore the seasonal variability of supraglacial ponds throughout the 2019 monsoon season, ponds were mapped from PlanetScope 3 m resolution optical satellite imagery once per month from May to November (Figure 7.13). Furthermore, the four supraglacial ponds surveyed on Hinang Glacier in September were identified individually to determine whether they were transient or more persistent features. H1, the smallest of the surveyed ponds, appeared to be a highly transient and short-lived feature, while H2 and H3 persisted throughout the monsoon season. H4 formed in July and persisted throughout the rest of the monsoon season (Table 7.14).

Seasonal variability at Hinang Glacier was observed with the highest number of ponds present at the beginning of the monsoon season in May to June after which the number declined towards winter. Despite a reduction in the number of ponds from May to August, the total ponded area varied and declined after August towards the winter season with a lowest ponded area and pond number in November indicating a number of drainage events.

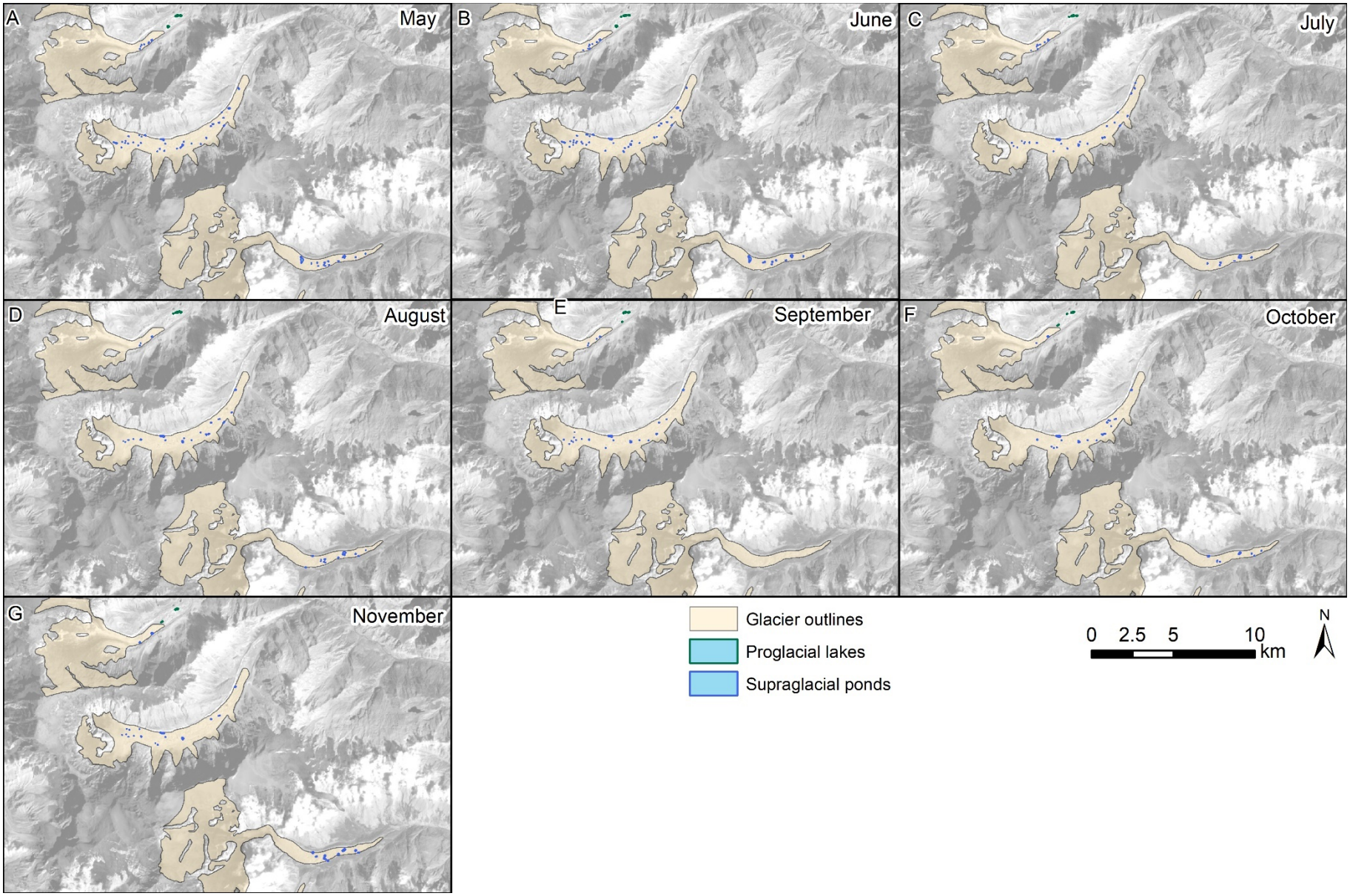


**Figure 7.13:** Seasonal variability of supraglacial ponds over Punggen Glacier, Hinang Glacier and Himal Chuli Glacier.

Estimated pond volumes were calculated based on the updated power law relationship defined by Watson et al. (2018b) and Cook and Quincey (2015) (Equation 6.2).

**Table 7.14:** Changes in supraglacial pond number, area and volumes over the monsoon season from May to November 2019 at Hinang Glacier.

| | Number of ponds | Area ($m^2$) | Estimated Volume ($m^3$) | H1 area ($m^2$) | H2 area ($m^2$) | H3 area ($m^2$) | H4 area ($m^2$) |
|---|---|---|---|---|---|---|---|
| 29 May 2019 | 37 | 54436 | 587476 | 0 | 6326 | 503 | 0 |
| 10 June 2019 | 43 | 58890 | 655339 | 0 | 7275 | 509 | 0 |
| 18 July 2019 | 25 | 47026 | 479356 | 0 | 15560 | 518 | 2061 |
| 28 August 2019 | 19 | 55906 | 609643 | 0 | 18685 | 674 | 4405 |
| 20 September 2019 | 19 | 45450 | 457173 | 343 | 18199 | 690 | 4066 |
| 27 October 2019 | 18 | 53872 | 579033 | 0 | 19249 | 573 | 3930 |
| 21 November 2019 | 17 | 39445 | 375437 | 0 | 13816 | 701 | 3933 |

Comparatively, the ponds on Punggen Glacier (Table 7.15) show a similar seasonal trend to that of Hinang Glacier (Table 7.14) with an overall reduction in ponded area over the monsoon season, yet Himal Chuli Glacier underwent substantially higher variability with a decrease in ponded area until August followed by a slight increase with an overall reduction in pond area and volume by November (Table 7.15). The variability in pond area and volume at Himal Chuli Glacier is largely dominated by a large pond located on the rockfall deposit.

**Table 7.15:** Changes in supraglacial pond properties over the monsoon season from May 2019 to November 2019 for Punggen Glacier and Himal Chuli Glacier. Imagery was not available covering Himal Chuli Glacier in September 2019.

| | Punggen Glacier | | | Himal Chuli Glacier | | |
|---|---|---|---|---|---|---|
| | Number of ponds | Area ($m^2$) | Estimated volume ($m^3$) | Number of ponds | Area ($m^2$) | Estimated volume ($m^3$) |
| 29 May 2019 | 7 | 7250 | 35643 | 13 | 72399 | 873246 |
| 10 June 2019 | 8 | 9279 | 50227 | 9 | 75258 | 921545 |
| 18 July 2019 | 8 | 7557 | 37758 | 6 | 33585 | 300227 |
| 28 August 2019 | 3 | 4619 | 19047 | 11 | 45033 | 451353 |
| 20 September 2019 | 4 | 4607 | 18978 | - | - | - |
| 27 October 2019 | 2 | 4696 | 19490 | 7 | 27583 | 228349 |
| 21 November 2019 | 2 | 5679 | 25383 | 12 | 26960 | 221212 |

## 7.4. Discussion

### 7.4.1. Glacier evolution and variability of the eastern Manaslu glaciers

The easterly flowing glaciers of the Manaslu conservation area present spatial and temporal variability over the study period from 1970 to 2019. Despite the similarities of location, flow direction, relative altitude (~3050 – 6800 m asl), and assumed monsoonal weather patterns, these three glaciers show substantial inter glacier variation. Some of these variations are considered to be influenced by dynamic flow behaviour relating to glacier hypsometry in addition to individual glacier dependent debris-covered glacier dynamics.

Over the study period, between 1970 and 2019, all three glaciers exhibited overall negative mass balances consistent with rates of mass loss elsewhere across the Himalaya, which have persisted for several decades (Azam et al., 2018; Bolch et al., 2019; King et al., 2019; Shean et al., 2020). Furthermore, accelerating rates of mass loss were observed on Punngen Glacier and Hinang Glacier with geodetic mass loss rates having increased fourfold (Table 7.9). This trend of accelerating rates of mass loss has been observed across the Himalaya (e.g. Kääb et al., 2012; Gardelle et al., 2013; Brun et al., 2017; King et al., 2020a) including in the Everest region (King et al., 2020a), yet the rates observed here are higher than those previously observed. Rates between 2009 and 2018 in the Everest region equated to −0.38 ± 0.11 m w.e. $a^{-1}$, and are similar to the global mean rate of glacier mass loss of −0.47 m w.e. $a^{-1}$ (Zemp et al., 2019). However, between 2013 and 2019 rates of in excess of −0.93 m w.e. $a^{-1}$ were observed on Punggen Glacier and Hinang Glacier and suggest much higher rates of mass loss in the Manaslu region in comparison to the Everest region during the past decade. Previous mass loss rates in Manaslu of −0.21 to −0.16 m w.e. $a^{-1}$ between 2000 and 2013 (Robson et al., 2018) were broadly consistent with the regional east (−0.22 to −0.33 m w.e. $a^{-1}$) to west (−0.45 to −0.55 m w.e $a^{-1}$) gradient of mass loss across the Himalaya (Kääb et al., 2012; Gardelle et al., 2013; Brun et al., 2017; Lovell et al., 2019). However, many of these studies have not investigated more recent trends beyond the mid-2010s, which have indicated higher rates of mass loss in the past few years (Bolch et al., 2011; King et al., 2017, 2020a). Rates in excess of those observed here have been observed on the Panchi Nala Glacier in the Himal Pradesh region of western Himalaya, which underwent extensive lowering of −1.62 m between 2000 and 2013 (Shukla and Garg, 2019). They surmised that increases in the mean winter minimum temperature and decreases in winter snowfall are likely to be the main drivers of such high rates of depletion consistent with increasing temperatures and reduced precipitation identified in Manaslu as in Figure 3.11 (Kattel and Yao, 2013; Panthi et al., 2015). Thus, there are high levels of variability within the broad east to west gradient attributed to the strong influence of the Indian and East Asian monsoon (Yao et al., 2012b; Lovell et al., 2018). Although this trend appears to be variable, these data support previous studies, which also observed increasing mass loss trends on the Manaslu glaciers in recent periods (Robson et al., 2018), with the exception of Himal Chuli Glacier.

In comparison to Punggen Glacier and Hinang Glacier, Himal Chuli Glacier shows far more complex dynamics and variability over the study period. The overall mass balance was similar to the neighbouring glaciers showing a negative mass balance, yet further analysis showed a higher rate of mass loss between 1970 to 2013 and a positive mass balance of +0.58 ± 0.07 m $a^{-1}$ between 2013 and 2019 despite the neighbouring glaciers continuing to exhibit enhanced negative mass loss during this period (Table 7.9 and Figure 7.5 to Figure 7.8). During this period of mass gain (2013 – 2019), Himal Chuli Glacier also exhibited surface velocity variability and shows a decrease in surface velocity between 1991 – 1992 and 2013 – 2014 followed by an increase in surface velocity in 2018 – 2019 with a noticeable increase below the icefall (Figure 7.11). Despite this slight increase in surface velocity in 2013 – 2014, the glacier slowed overall by 45%. Comparatively, Punggen Glacier slowed by 35% and Hinang Glacier by 21% in response to sustained mass loss and reduced transfer of ice from the higher accumulation zones over the survey period resulting in reduced driving stress (Quincey et al., 2009; Dehecq et al., 2019). All three glaciers were observed with near stagnant surface velocities in the lower glacier termini.

Although the 2016 SPOT imagery included snow cover in the higher accumulation areas, the lower debris-covered regions were relatively clear of snow. Therefore, care must be taken when interpreting the 2016 extracted DEMs and derived rates of change due to the snow artificially amplifying the rates of mass loss and mass gain as presented in Table 7.9. However, these data present the only available imagery or elevation data in this region during this time period. Regardless of this artificial enhancement, DEM differencing analysis indicates a substantial increase in mass loss from 2016 – 2019 on the lower, snow-free sections compared to the previous time periods.

During the study period (1970 – 2019), glacier extent only reduced slightly with a maximum of 16% for Punggen Glacier despite being at the highest elevation of the three study glaciers. Concurrently, the three glaciers underwent increased debris-cover extent that expanded up to the icefalls on each glacier. Furthermore, the icefalls appeared to be darkening over the survey period associated with the incorporation of finer wind-blown surface debris trapped within faulted ice (e.g. Goodsell et al., 2002). The presence of the icefall, indicative of steeper topography, is considered to act as a topographic barrier to continued debris expansion due to the steepness and inability of debris to withstand angles in excess of 28 – 40° (Röhl, 2008; Reid and Brock, 2014). Thus, only the finer surface debris and possible uplifted basal debris (Goodsell et al., 2002) are likely to be responsible for this darkening trend and larger debris particles from rock falls and melt-out will accumulate at the base of the icefalls and increase debris thickness before being redistributed (Gibson et al., 2017a).

These evolutionary traits are broadly consistent with debris-covered glaciers elsewhere in the Himalaya and worldwide including those previously observed at Miage Glacier (Chapters 4 – 6), which also exhibit sustained negative mass balance, reduced flow rates and stagnation, low surface gradient and increasing surface debris cover and development of surface features with an increasingly undulating surface topography (Quincey et al., 2009; Benn et al., 2012; Bolch et al., 2012; Rowan et al., 2015; Anderson and Anderson, 2018; Dehecq et al., 2019). However, additional complexities observed at Himal Chuli Glacier and contributions of surface features in terms of glacier evolution require further consideration.

### 7.4.2. Himal Chuli Glacier flow behaviour

Himal Chuli Glacier has exhibited variability in surface velocity and periods of both positive and negative mass balance over the full observation period from 1970 to 2019 compared to Punggen Glacier and Hinang Glacier. Despite the three glaciers being in the same region with the same broad climate conditions (Table 7.1), site specific factors must explain differences in glacier behaviour.

The hypsometric index for Himal Chuli Glacier support a very top heavy glacier, with large accumulation zones capable of capturing extensive winter accumulation. In comparison, Punggen Glacier and Hinang Glacier have small accumulation zones and are indicative of equidimensional hypsometries. Robson et al. (2018) previously calculated a hypsometric index of 1.81 indicating a very bottom heavy hypsometry; however, the reduction in glacier extent by 2019 is considered to have resulted in a substantial change in glacier hypsometry and is consistent with previous studies, which identified bottom heavy glaciers are losing the most mass (King et al., 2017; Lovell et al., 2019). Furthermore, ERA5 climate data provided by MeteoBlue (Figure 3.11), at Hinang Glacier show high levels of snowfall in excess of 73 cm in October 2014, yet this snowfall was not measured at Himal Chuli Glacier and appears to be limited to the higher elevations (Appendix 1). It is considered that the large accumulation zone of Himal Chuli Glacier is able to transfer ice via the central tributary pumping ice into the icefall promoting unstable flow to the lower ablation zones. Thus, accounting for the variability of surface elevation trends and representing a redistribution of ice mass downglacier in response to precipitation at higher elevations and glacier hypsometry controlled by the icefall through the narrow valley.

Robson et al. (2018) observed increased velocities on Himal Chuli Glacier in the same region where surface elevation gain was observed in Figure 7.9,C2. Previous reports of increased surface velocities in regions of surface elevation gain with surface lowering upglacier have been associated with surge-type behaviour observed in the Everest and Annapurna regions (Lovell et al., 2018; King et al., 2020a). The Sabche Glacier on the southwest flank of nearby Annapurna, has surged at least four times over the last 50 years and it was assumed to be partially controlled by the subglacial

topography associated with an overdeepening, and a topographical constriction upglacier acting to moderate the timing and duration of the surges (Lovell et al., 2018). It is therefore possible that the same mechanisms could be true of Himal Chuli Glacier, with a topographical constriction presented by the flow around a bend above the icefall moderating the downglacier ice flux from the large accumulation zone. It is considered that the region of elevation gain identified in Figure 7.9,C2. could therefore represent a mini-surge front as ice is transferred from the large accumulation zone to the ablation zone. It is unlikely that a full surge event has occurred as despite a surface velocity increase, the recorded surface velocities do not support a full active phase with velocities of at least one magnitude higher than the quiescent phase (Murray et al., 2003). Although no previous surge events have been recorded in the Manaslu region, Sevestre and Benn (2015) highlighted the central Himalaya as a potential location where surge-type behaviour is likely to occur on larger, longer and shallower glaciers. However, without further examination on a near-annual analysis, it is not possible to assess the potential development of a surge front or confine the timings of the transfer of ice through the icefall resulting in unstable flow.

### 7.4.3. Importance of surface features

Surface features including supraglacial ponds and ice cliffs have been shown to be important components of a glacier system and play an important role in the rates of mass loss of debris-covered glaciers (e.g. Benn et al., 2001, 2012; Reid and Brock, 2014; Pellicciotti et al., 2015; Thompson et al., 2016; Watson et al., 2017a, 2018b; Miles et al., 2018) and contribute disproportionately to glacier-scale ablation. Regions of high relief associated with ice cliffs and supraglacial ponds are contemporary drivers of glacier topographic change in the Himalaya (King et al., 2020b; Mölg et al., 2020). In this respect, the glaciers of the Manaslu region have followed a similar trajectory in terms of evolution (Benn et al., 2012) with the development of proglacial lakes identified at Punggen Glacier over the study period consistent with terminus stagnation and a slight reduction in glacier extent, indicative of future progression and development of glacial lakes in this region. All of the study glaciers experienced increases in supraglacial pond number and area over the survey period covering between 0.02 to 0.23% of the total glacier area (or maximum 0.52% of the debris-covered area) by 2019 and accounted for up to five times the mean surface lowering (Figure 7.2 and Table 7.8). In the Langtang region of Nepal, up to 12.5% of glacier ablation is driven by supraglacial ponds, despite ponds only covering 1.69% of the debris-covered area (Miles et al., 2018). However, this was inclusive of modelled subaqueous melt rates based on an energy balance model. Thus, the approach utilising DEM analysis cannot replicate subaqueous ablation or thermal energy transported englacially and thus represents a conservative estimation of ablation associated with supraglacial ponds.

Regional variations in contributions of ice cliffs to total glacier ablation have been suggested (Chapter 6). Mapped ice cliffs between 2013 and 2019 on Punggen Glacier act as hotspots with rates of up to 6 times the mean surface lowering yet only cover ~0.75% of the total glacier area and account for <1% of the total mass loss (Table 7.8). Comparatively, ice cliffs exhibited a larger expanse covering up to 4% total area of Hinang Glacier, but accounted for <1% total mass loss. These rates are substantially lower than those found on Lirung Glacier, Ngozumpa Glacier and Changri Nup Glacier where ice cliff backwasting accounted for 69%, 40% and 23% of the total mass loss respectively despite a comparatively small area coverage (2%, 5% and 7% respectively) (Sakai et al., 1998; Thompson et al., 2016; Brun et al., 2018). Variability between Himalayan examples suggest considerable regional variations of contributions of ice cliffs to mass loss and are likely to represent differences in the state of evolution and localised influence of the monsoon (Benn et al., 2012; Yao et al., 2012a). Thus, it is considered that Lirung Glacier, Ngozumpa Glacier and Changri Nup Glacier are indicative of glaciers with well-established high relief zones and represent a potential future evolutionary state for the Manaslu glaciers.

The location of such high relief zones, and the associated ablative processes, may in part be influenced by the glacier debris thickness, which can vary from glacier to glacier and may account for some of the variability when compared to Punggen Glacier and Himal Chuli Glacier (Rounce et al. 2018). Hinang Glacier underwent a substantial increase in supraglacial ponding (from 0 to >43,000 $m^2$) since 1970 and has been observed to have a highly undulating surface topography since the 1970s. The undulating topography and low longitudinal gradient of Hinang Glacier enables meltwater ponding to migrate across the surface (Figure 7.10). Thus, the dominant presence of ice cliffs across the surface in the 1970s is likely to have promoted accommodation space for meltwater coalescence further promoting enhanced ablation associated with undulating surface topography and evolution of such surface features (Pellicciotti et al., 2015; King et al., 2020b; Mölg et al., 2020).

The pattern of supraglacial ponding over the monsoon season (Figure 7.13) show a maximum number and areal extent in the summer when meltwater generation is high and thus, pond expansion occurs, with a reduction towards winter despite seasonal and inter-annual variability (Sakai et al., 2000; Watson et al., 2016; Miles et al., 2017b). Punggen Glacier exhibited the lowest number and area of ponds throughout the monsoon season. Although Himal Chuli Glacier has higher pond volumes in May and June 2019, this is dominated by the large pond formed on the rockfall deposits and once it has the total ponded volume drops dramatically. The higher surface velocity, and dynamic flow behaviour observed at Himal Chuli Glacier, is suspected to play a dominant role in the drainage and refilling regime of a large pond (Figure 7.13), via the opening and closing of englacial drainage pathways, upon the rockfall deposits and other supraglacial ponds upon this glacier (Benn et al., 2001; Miles et al., 2017b; Robson et al., 2018). Thus, ponding on Himal Chuli Glacier is likely to be more variable with fewer persistent ponds in comparison to the

neighbouring glaciers. The ponded area and volume on Hinang Glacier is comparatively more stable throughout the monsoon season. Of the four surveyed ponds in September 2019 (Figure 7.13, Table 7.14), H1 had only recently formed and then drained and was the smallest of the sampled ponds. H2, H3 and H4 persisted through the remaining monsoon season considered to represent more persistent ponds located on Hinang Glacier compared to higher rates of transient ponding on Himal Chuli Glacier in response to the variable flow acting to open and enable meltwater drainage and redistribute debris (Benn et al., 2001, 2012; Shukla et al., 2018). It is suspected that persistent ponds are typically larger and have a higher contribution to glacier-scale ablation compared to transient ponds (Shukla et al., 2018). Thus, as supraglacial ponds are likely to become more established and present more persistent features, the contributions to overall ablation may also continue to increase. Continued supraglacial pond monitoring could provide additional details and identification of dynamic flow behaviour and ablation rates associated with debris-covered glacier surface hydrology at glacier and regional scale.

### 7.4.4. Regional comparisons

Glacier mass loss has been consistent since the 1970s across the Himalaya (Bolch et al., 2019) and is true of the glaciers within the Manaslu region. The mean loss over the 1970 – 2019 survey period of the three glaciers equates to −0.29 ± 0.05 m w.e. $a^{-1}$ and is slightly lower than the global mean of −0.47 ± 0.20 m w.e. $a^{-1}$ (Zemp et al., 2019) attributed to the high elevations and insulating effect of an assumed thick debris cover. The results are consistent with findings from other regions across the Himalaya experiencing a substantial increase in rates of mass loss over the survey period from 1970 – 2019, yet the values of −0.93 ± 0.12 and −1.23 ± 0.15 m w.e. $a^{-1}$ for Punggen Glacier and Hinang Glacier between 2013 and 2019, are within ranges also observed in South-eastern Tibet and the western Himalaya (Neckel et al., 2017; Shukla and Garg, 2019). King et al. (2020a) also observed higher rates of mass loss over contemporary time periods (2009 to 2018) in comparison to longer term mean ice loss in the Everest region. Despite, the heterogenous trends of accelerating mass loss across the Himalaya, Himal Chuli Glacier deviates from this trend in the latter time period exhibiting positive mass balances attributed to the complexities associated with top heavy hypsometry, highly dynamic flow behaviour and transferal of ice mass through confines within the glacier system (Lovell et al., 2018; King et al., 2020a).

Structural mapping identifies the presence of both steep icefalls and ogives at all three glaciers (Figure 7.2) and are a relatively common feature on many debris-covered glaciers owing to their prevalence in tectonically active, high-mountain regions with steep topography (e.g. Khumbu Glacier, Miage Glacier, Lirung Glacier). The presence of the steep icefall acts as a topographic barrier for the debris to expand (Röhl, 2008) and thus promotes debris thickening on the glacier trunk

rather than continued expansion upglacier. By 2019, all three glaciers had increased in debris-cover extent up to the base of the icefalls. Yet, the icefalls appeared to be darkening over the survey period associated with finer wind-blown surface debris (Goodsell et al., 2002). With further expansion of debris cover expected across Himalayan glaciers in the coming decades (Herreid and Pellicciotti, 2020), it is expected that the icefalls will get darker still and the debris will continue to thicken on the lower ablation zones.

The continued development of surface features, especially of supraglacial ponds and glacial lakes, since 1970s has been observed across the Himalaya (Gardelle et al., 2011; Nie et al., 2013; Liu et al., 2015; Zhang et al., 2015; Watson et al., 2016) as has the development of high relief regions (Benn et al., 2017). The Manaslu glaciers also exhibit increasing net supraglacial pond area, yet the area of ice cliff and exposed ice has reduced and is potentially related to a reduction in crevassing, which can pose as a feature for initiation (Mölg et al., 2020). Furthermore, a reduction in crevassing can result in limited rerouting or drainage of ponded supraglacial meltwater and influence the hydrology of debris-covered glaciers (Quincey et al., 2009; Fyffe et al., 2019; Miles et al., 2020).

Despite heterogenous negative mass balance recorded across the Himalaya in response to increasing temperatures (Bolch et al., 2019; Zemp et al., 2019), it is well established that individual glacier responses are highly variable (Fujita and Nuimura, 2011). Previous studies have shown spatial variability in the rates of mass loss of Himalayan glaciers associated with local temperature and precipitation trends (Mukherjee et al., 2018), glacier terminus type (Brun et al., 2019; King et al., 2019) and glacier surface debris cover (Brun et al., 2019; King et al., 2019). The variability between the three-easterly flowing Manalsu glaciers suggest that despite similar environmental conditions and assumed debris cover properties (e.g. lithology and thickness), individual glacier dynamics including glacier hypsometry, play a key role in the evolution and patterns of mass loss. This study highlights the importance for understanding glacier dependant flow dynamics and supraglacial pond development over short, contemporary assessments, as shown here to exhibit substantial variability, which would not be detected over comparatively long-term assessments.

## 7.5. Summary

The easterly flowing glaciers of the Manaslu region in the Nepalese Himalaya are exhibiting long-term mass loss since the 1970s with a mean rate of −0.29 ± 0.05 m w.e.$a^{-1}$. Accelerating rates of mass loss have been observed on Punggen Glacier and Hinang Glacier between 2013 – 2019 in addition to a reduction in surface velocity and terminal stagnation. Both glaciers have increased presence of supraglacial ponds and high relief zones on the low gradient ablation zones, consistent with increasing debris-cover extent and limited glacier length reduction. In comparison, Himal Chuli Glacier exhibits contrasting trends, with variable surface velocity and a period of positive surface

elevation change between 2013 and 2019 (+0.58 ± 0.07 m $a^{-1}$). Furthermore, surface ponds were more variable and dominated by one large pond situated on rockfall debris, which appears to drain and refill. These variations are attributed to dynamic flow behaviour associated with a top heavy glacier hypsometry transferring ice through the icefall to the ablation zone resulting in unstable flow and highlights the importance for high temporal assessment of glaciers in this region.

The glaciers in this study are expected to undergo future downwasting and stagnation, with the eventual development of supraglacial pond networks although no indication of this has been observed here. Development of the proglacial ponds at Punggen Glacier should also be monitored and indicate this glacier is already transitioning to an advanced state of regime 2 (Benn et al., 2012). Glaciers of the Manaslu regions thus show similar stages of evolution as previously seen at Miage Glacier in Chapters 4 to 6 and will be explored further in Chapter 8.

# Chapter 8 : Debris-covered glacier evolution in the European Alps and Nepalese Himalaya: Overall discussion

## 8.1. Overview of thesis

This chapter will highlight the relevance of the findings in relation to the aims and objectives detailed in Section 1.3 and provide future prognoses for the glaciers investigated. Furthermore, a conceptual model of debris-covered glaciers has been developed in combination with previous studies and the findings from this thesis. Detailed discussions relating to the individual chapters are found within the respective chapters. Methodological considerations are then considered and suggestions for future work provided.

This thesis has covered many of the complexities associated with debris-covered glacier evolution in two differing regions; the Alps and Himalaya. The thesis has evolved from having a strong focus on glaciers in the Manaslu region and assessing proposed methods at Miage Glacier to one where several research questions have focused on Miage Glacier. Furthermore, it has highlighted the importance of surface features, which impact glacier scale ablation rates and thus, the rate and trajectory of debris-covered glacier evolution. Glacier evolution has been assessed through identification of reduced glacier activity and establishment of surface features including small supraglacial ponds and ice cliffs at Miage Glacier (Chapter 4), attributed to a sustained period of negative mass balance and reduced ice mass transfer from the accumulation zones resulting in a substantial velocity reduction and a lowering of the longitudinal profile (Chapter 5). The contributions of supraglacial ponds and ice cliffs to ablation rates are important for glacier-scale ablation and Chapter 6 highlights the key processes associated with simultaneous mass loss of supraglacial ponds and adjacent ice cliffs. Debris-covered glacier evolution of Punggen Glacier, Hinang Glacier and Himal Chuli Glacier in the Manaslu region of the Nepalese Himalaya highlight key inter-glacier variability in relation to glacier hypsometry despite similar environmental conditions (Chapter 7) and emphasise the complexities associated with modelling debris-covered glacier evolution highlighting future avenues of research in this region. These observations have been used to predict future evolution of the studied debris-covered glaciers assuming a continued global climatic warming scenario (Sherwood et al., 2020). The findings from this thesis suggest that the prevalence of supraglacial ponds and ice cliffs have increased over the past decade and enhance the rate of ablation despite expanding debris layers. The datasets generated and analysed in this thesis highlight both spatial and temporal variability across debris-covered glaciers and add to the limited number of bathymetric surveys of small supraglacial ponds.

## 8.2. Discussion of study objectives

### 8.2.1. Debris-covered glacier surface evolution

Glacier surface evolution of four debris-covered glaciers mapped over temporal scales on the Alpine Miage Glacier (1952 – 2018) and Himalayan Punggen Glacier, Hinang Glacier, and Himal Chuli Glacier (1970 – 2019) were addressed in Chapters 4 and 7. In all cases, the glaciers showed an increase in debris-cover extent consistent with the development of surface features including supraglacial ponds and ice cliffs, yet limited terminal retreat broadly consistent with debris-covered glaciers in a state of negative mass balance (Benn and Lehmkuhl, 2000; Scherler et al., 2011; Benn et al., 2012; Rowan et al., 2015). Furthermore, surface and structural mapping of Miage Glacier indicated a reduction in ice mass evident by the partial collapse of Mont Blanc Glacier and reduction in accumulation area. Reduced glacier activity was observed over the survey periods with collapse features and a reduction in ice transfer from the higher accumulation zones to the lower ablation zones.

Miage Glacier represents a compound and complex glacier consisting of four tributary glaciers with icefalls joining at the confluence with the valley tongue resulting in heavily crevassed and faulted glacier ice (Goodsell et al., 2002). The overall glacier dynamics appear to have gone from an active ice flow regime to one of reduced activity. Furthermore, the development of surface features has dramatically increased since the 1990s with an increasingly undulating surface topography indicative of a development from regime 1 with limited water storage throughout the twentieth century, towards regime 2 with increasing water storage by 2018 (Benn et al., 2012). Similarly, glaciers in Manaslu exhibited ice cliffs and an undulating surface topography prior to the 1970s yet limited supraglacial ponding. An increase in supraglacial ponds and the development of proglacial lakes at Punggen Glacier since 2013 marks a similar evolution towards regime 2. These trends in the development of surface features on debris-covered glaciers have previously been acknowledged (e.g. Sakai et al., 2002; Benn et al., 2012; King et al., 2020b), yet few studies have previously assessed this on glaciers in different regions to assess regional and environmental factors in debris-covered glacier evolution. Comparison of the evolution of surface features at Miage Glacier and the Manaslu glaciers, appear to be broadly consistent.

Mapping of the glaciers highlighted similar topographical features at each of the investigated glaciers, including icefalls and production of ogives. All four glaciers exhibited at least one icefall, which act to transfer and regulate ice mass between the upper accumulation zones and lower ablation zones via the icefalls. The presence of the icefalls symbolises a topographic constraint to further up-glacier debris expansion and is therefore likely to result in debris thickening on the lower ablation area in the future. Ogives were observed at the base of all icefalls and reduced spacing of bands on Miage Glacier suggest decreased ice flux over the survey period (Nye, 1958; Goodsell et al., 2002). Ogives on the Manaslu glaciers did not show a distinct reduction in spacing, partly

considered to be linked to increased ice flux from comparatively larger accumulation areas through the icefall. However, increased debris cover over the survey period in these regions are likely to have to have limited visibility and thus analysis.

Supraglacial ponds developed either before or after a bend in the valley topography at both Miage Glacier and Himal Chuli Glacier, which altered the direction of glacier flow and likely represents a compressional regime in this region (e.g. Kraaijenbrink et al., 2016b). This region of compression is likely to be important for regulating or limiting surface water movement and thus affecting the hydrological drainage system (Fyffe et al., 2019). Valley topography is therefore an important consideration when assessing and predicting the distribution of supraglacial pond development. Previous studies have also highlighted the relevance of valley topography on pond development including basal topography and the presence of overdeepenings associated with regions of thicker ice (e.g. Figure 3.6 and Figure 3.13) for potential pond formation (Linsbauer et al., 2016; Magnin et al., 2020). These features are likely to be common across debris-covered glaciers due to the development of a thick debris cover in highly tectonically active regions with steep topography. Therefore, valley and bed topography should be accounted for when predicting the distribution of ponds and where locations of large, potentially hazardous, lakes are likely to form consistent for both Miage Glacier and the Manaslu glaciers.

### 8.2.2. Temporal analysis of debris-covered glacier dynamics

The evolution of glacier dynamics through assessment of glacier surface elevation change and ice velocity at Miage Glacier (1990 – 2018) and the Manaslu glaciers (1970 – 2019) were assessed through remote sensing approaches as discussed in Chapters 5 and 7. All glaciers are in a state of sustained negative mass balance over the full observation periods, consistent with reduced surface velocity rates and up-glacier migration of stagnating ice, low surface gradients, migrating up-glacier surface debris cover and the development of surface features with an increasingly undulating surface topography (Quincey et al., 2009; Benn et al., 2012; Bolch et al., 2012; Rowan et al., 2015; Dehecq et al., 2019). Despite these comparative similarities between Miage Glacier and the Manaslu glaciers, inter-glacier variability over spatial and temporal scales exist.

All of the study glaciers exhibited long-term negative mass balance; however, rates observed at Miage Glacier were much higher between 1990 – 2018 (−0.86 ± 0.27 m w.e. $a^{-1}$) compared to those observed in Manaslu between 1970 – 2019 (mean of −0.29 ± 0.05 m w.e. $a^{-1}$). This could reflect increasing surface lowering trends in recent decades and the longer observation period for Manaslu. However, surface elevation change slowed from −1.07 ± 0.13 m $a^{-1}$ between 1990 and 2008, to −0.85 ± 0.01 m $a^{-1}$ between 2008 and 2018 at Miage Glacier indicating complex, nonlinear changes over time. Furthermore, mass balance of the Manaslu glaciers showed highly variable rates with

periods of positive mass balance over the 2013 – 2019 period. This is attributed to the effect of local precipitation and increased snowfall at higher elevations (Figure 3.11 and Appendix 1) influenced by monsoon climates, in addition to dynamic flow behaviour (Kääb et al., 2012; Yao et al., 2012a; Gardelle et al., 2013). The inconsistency of the glacier dynamics indicates individual glacier controls relating to glacier hypsometry whereby the equidimensional glaciers including Miage Glacier, Punggen Glacier and Hinang Glacier underwent limited variability in comparison to the very top heavy Himal Chuli Glacier. The complex, nonlinear changes of debris-covered glaciers over differing spatial and temporal scales are therefore considered to be associated with local temperature and precipitation trends (Mukherjee et al., 2018), and glacier surface debris cover (Brun et al., 2019; King et al., 2019), including differences in spatial debris cover thickness and local properties are likely to affect the temperature profile and energy available for melt at the ice surface (Gibson et al., 2017a; Rowan et al., 2021). Local controls therefore have a substantial impact on the energy budget and mass loss rates of individual debris-covered glaciers.

Glaciers in Manaslu exhibited low surface gradients (<5°) whereas Miage Glacier had comparatively higher gradients (>6°) and higher rates of surface gradient change over the study period. Punggen Glacier and Himal Chuli Glacier began to develop an inversion in surface gradient over the observation period consistent with previous studies of debris-covered glaciers in combination with reductions in surface velocity (Anderson and Anderson, 2018; Dehecq et al., 2019). Reductions in surface velocity between 1991 – 1992 and 2018 – 2019 were observed on all three Manaslu glaciers by 19 – 45%, yet Hinang Glacier showed very little change in surface gradient and also the smallest percentage decrease in surface velocity (Table 7.11). Miage Glacier also showed a dramatic reduction in glacier surface velocity (46%) between 1990 and 2018 attributed to a reduction in ice flux from the higher elevation accumulation zones. Surface velocity of Miage Glacier and Punggen Glacier were similar in the most recent observation periods (16 and 18 m $a^{-1}$ respectively), while Hinang Glacier and Himal Chuli Glacier exhibited rates in excess of 37 and 43 m $a^{-1}$ respectively. Results were comparable to other debris-covered glaciers across the Himalaya and indicative of surface velocity reductions in recent periods (e.g. Kääb, 2005; Quincey et al., 2009; Heid and Kääb, 2012; Haritashya et al., 2015).

The establishment of surface features are important for assessing glacier-wide mass balance as they represent regions of enhanced ablation (e.g. Sakai et al., 2000; Buri et al., 2016b; Miles et al., 2016; Thompson et al., 2016), but the variability in rates of enhanced loss over spatial and temporal scales is significant. The presence of supraglacial ponds and ice cliffs at Miage Glacier serve to enhance mass loss locally and were responsible for ~5% of the total mass loss between 2016 and 2018, despite only covering 1.3% of the total glacier area. In comparison, ice cliffs have shown a sustained presence since the 1970s on the Manaslu glaciers, promoting a highly undulating surface topography and accounted for up to 4.6% of the glacier area on Hinang Glacier, yet only 2.4 times

the mean surface lowering. Ice cliffs appear to have a stronger influence in mass loss at Miage Glacier compared to Manaslu glaciers despite accounting for a lower density. Thus, such discrepancies in regional comparisons (e.g. Sakai et al., 1998; Reid and Brock, 2014; Thompson et al., 2016; Brun et al., 2018; Mölg et al., 2019) are considered to represent differences in the state of evolution and localised influence of the monsoon (Benn et al., 2012; Yao et al., 2012a) in addition to mapping and methodological differences. Attempts to standardise a method for ice cliff detection and quantification of total ablation should therefore be considered (e.g. Kneib et al., 2021).

Supraglacial ponds have become more pronounced although high levels of seasonal and annual variability were observed (Miles et al., 2017b). Nevertheless, such surface features promoted additional mass loss and accounted for up to six times the mean surface lowering rates (Table 7.10). Thus, supraglacial ponds and ice cliffs do not appear to outweigh sub-debris melt at the glaciers in this study and may relate to the relatively small pond sizes and highly transient features over the monsoon and ablation seasons (Hambrey et al., 2008; Shukla et al., 2018).

### 8.2.3. The importance of surface features on topographic evolution

Supraglacial ponds, ice-marginal lakes and their associated ice cliffs were observed to have significantly higher ablation rates than the surrounding debris-covered terrain on Miage Glacier and the Manaslu glaciers. Supraglacial ponds and ice cliffs at Miage Glacier increased ablation rates by a factor of eight exhibiting their importance in both overall ablation and the evolution of debris-covered glaciers. Furthermore, ice cliffs with mean annual retreat rates of −8 m $a^{-1}$ were observed. Analysis of supraglacial ponds and ice cliffs support previous studies, which indicate they play an important role in the rates of mass loss of debris-covered glaciers (e.g. Benn et al., 2001, 2012; Reid and Brock, 2014; Pellicciotti et al., 2015; Thompson et al., 2016; Watson et al., 2017a, 2018b; Miles et al., 2018). Although a thicker and more extensive debris cover has the potential to reduce ablation, some debris-covered glaciers in the Himalaya have experienced similar rates of mass loss to clean-ice glaciers; a phenomenon referred to as the 'debris-cover anomaly' (Pellicciotti et al., 2015; Vincent et al., 2016). This behaviour results from high rates of enhanced localised ablation in the vicinity of supraglacial ponds and ice cliffs (e.g. Buri et al., 2015; Miles et al., 2016). However, these effects do not seem to be prevalent at either Miage Glacier or the Manaslu glaciers where the development of supraglacial ponds are currently limited with no indication of pond networks forming. Thus, the insulating effect of debris cover appears to have had an overall more important effect on the mass balance than the mass loss associated with ice cliffs and supraglacial ponds (e.g. Hambrey et al., 2008).

Pond morphology suggests that the maximum depths are often found approaching the highest section of ice cliffs and it is considered that the positioning of the ice cliffs, drive the water circulation and heat transfer within the pond. Thompson et al. (2016), Miles et al. (2016) and Watson et al. (2018b) observed similar trends on the Ngozumpa Glacier, Lirung Glacier and Khumbu Glacier respectively. However, it is observed on both Miage Glacier and Hinang Glacier that where large ice cliffs exist on multiple sides of the ponds, either a central deep section forms, or multiple deep basins form. Watson et al. (2018b) suggested that this trend did not extend to smaller ponds and central basins were likely to represent newly exposed ice cliffs or regions of thick basal debris restricting subaqueous melt (Mertes et al., 2017).

This study has shown the development of small supraglacial ponds (<10,000 $m^2$), which have become established on Miage Glacier and Hinang Glacier, are important for glacier-scale ablation. Yet, the inclusion of small supraglacial ponds in global bathymetric datasets remain limited (Watson et al., 2016). When combining the data points from Miage Glacier and Hinang Glacier with those of Cook and Quincey (2015) and Watson et al. (2018b) area-volume assessments, the pond area-volume power law relationships are supported (Table 8.1).

**Table 8.1:** Volume-area relationships for supraglacial ponds and glacial lakes represented by regression values ($R^2$) when combined with data from Cook and Quincey (2015) and Watson et al. (2018b).

| | **V-A relationship** | **Power law $R^2$** |
|---|---|---|
| All glacial lakes area-volume (incl. Cook and Quincey, 2015; and Watson et al., 2018). | $V=0.178A^{1.38}$ | 0.99 |
| Supraglacial ponds area-volume (incl. Cook and Quincey, 2015; and Watson et al., 2018 data). | $V=0.487A^{1.34}$ | 0.99 |
| Supraglacial ponds <10,000 $m^2$ (incl. Miage Glacier, Hinang Glacier and Watson et al. 2018 data). | $V=0.196A^{1.37}$ | 0.93 |

Figure 8.1 shows that the ponds at Miage Glacier and Hinang Glacier fit with the relationships previously identified by Cook and Quincey (2015). As the ponds are comparatively small, and exhibit highly transient features, the future trajectory is likely to follow that of growing supraglacial ponds but may change if supraglacial ponds coalesce and networks begin to form.

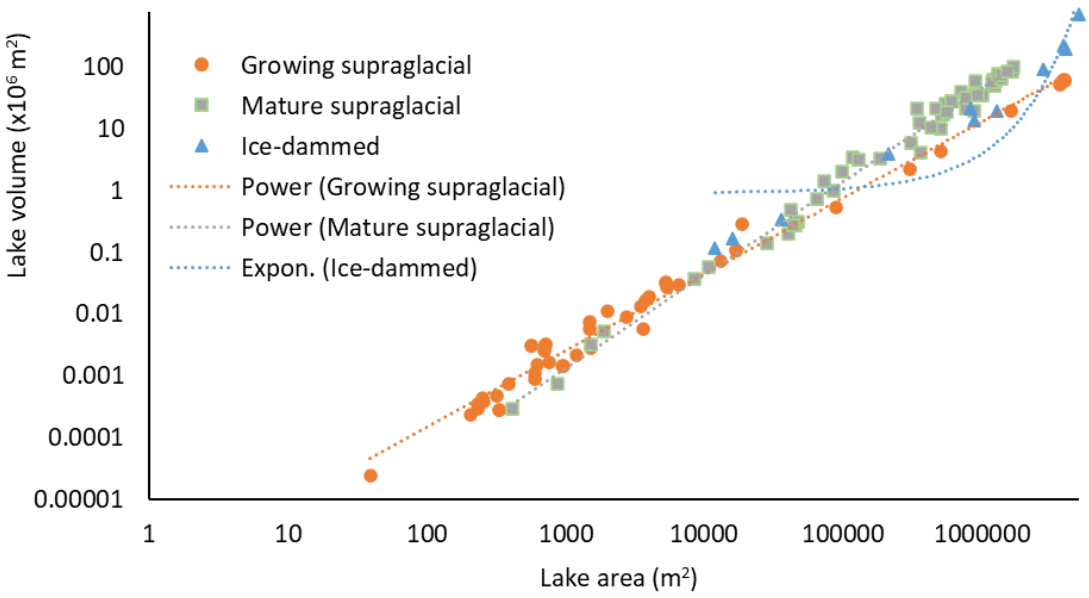


**Figure 8.1:** Supraglacial ponds at Miage Glacier and Hinang Glacier plotted alongside results from Cook and Quincey (2015) on logarithmic scales. Ponds gathered within this study are consistent with growing supraglacial ponds.

Assessment of the timings of development, expansion, and drainage show high levels of variability associated with both the Alpine ablation season and the Himalayan Monsoon with a strong decline in supraglacial ponding area towards winter (Watson et al., 2018b). At both Miage Glacier and the Manaslu glaciers, although some supraglacial ponds persisted throughout the season there was a high rate of drainage events supporting previous studies, which associate increased meltwater generation with the opening of englacial conduits (Gulley and Benn, 2007). However, in this study winter drainage was not assessed and may account for additional pond variability. Furthermore, the ice-marginal Lake Miage was noted to have drained at the end of the ablation season multiple times and could be draining on an annual timescale despite it not always being recorded. Thus, its size and expansion is considered to be predominantly driven by the early season snow melt.

To determine whether there were any common controls on pond development on both Miage Glacier and the Manaslu glaciers, a basic analysis using correlation and generalised linear models (GLMs) were used to compare pond area (from which pond depth and volume have a previously assessed relationship (see Cook and Quincey, 2015; Watson et al., 2018b) against pond altitude, glacier ice thickness, surface velocity, distance from the terminus and glacier width. For the analysis 5 ponds at Miage Glacier, 2 ponds at Punggen Glacier, 8 ponds at Hinang Glacier and 11 ponds at Himal Chuli Glacier were included (Table 8.2).

**Table 8.2:** Correlation and GLM analysis of pond area and glacier dependant variables.

| Pond area vs. | $R^2$ value | GLM p-value |
|---|---|---|
| Altitude | 0.0552 | 0.204 |
| Ice thickness | 0.0041 | 0.762 |
| Velocity | 0.0908 | 0.345 |
| Distance from the terminus | 0.0004 | 0.683 |
| Glacier width | 0.0869 | 0.458 |

Analysis shows that there is no correlation or statistical significance in the assessed glacier variables on pond area. However, when using GLMs, altitude and velocity indicate there might be a relationship despite not being statistically significant in this case. Further assessment should be carried out using a global database of supraglacial ponds (e.g. Cook and Quincey, 2015; Watson et al., 2018b), which could be further developed to determine pond specific details and assess whether there are generic glacier controls, which could aid identification of regions prone to supraglacial pond development and aid modelled predictions of debris-covered glacier evolution.

## 8.3. Implications and importance of study

### 8.3.1. Future prognosis of Miage Glacier

Given that climate predictions suggest temperatures will increase (Sherwood et al., 2020), it is anticipated that Miage Glacier will continue to experience negative mass balance in the future. Based on extrapolation of dynamic trends outlined in this study since 1990, we suggest that Miage Glacier will continue to thin, that the glacier will continue to slow, and that debris cover will continue to expand upglacier, as well as thicken. It is also possible that the overall glacier profile will become shallower although changes in the gradient have been relatively modest since 1975 (Smiraglia et al., 2000). Ablation is likely to be enhanced at the base of the tributary glaciers resulting in thinning and eventual decoupling and recession from the main stem of Miage Glacier. Reduced inputs of ice will likely lead to further reductions in surface velocity and stagnation, which will promote flattening and the inability of the main glacier trunk to evacuate englacial and supraglacial sediment. Indeed, it is also likely that sediment inputs from valley sides will be enhanced with continued climate warming (Deline, 2009; Ravanel et al., 2017), further promoting expansion and thickening of the debris cover (Stewart et al., 2021).

Extrapolation of other trends and elements of the dataset become far more speculative because of the non-linear changes evident in some of our datasets. Perhaps most notable among these uncertainties is the future role that supraglacial ponds and adjacent ice cliffs might play in glacier mass balance. It is evident from the dataset that ponds and ice cliffs represent ablation hotspots. However, their current distribution is limited to a relatively small zone upglacier from the terminal lobes where the main trunk turns into Val Veny (Figure 4.7). Even within this zone, ponds and ice

cliffs are highly focussed and are not pervasive features at present. A key limitation on their future development will be that the glacier remains, overall, relatively steep (~5° on the valley tongue and >8° on the terminal lobes (Figure 5.7) (e.g. Reynolds, 2000; Quincey et al., 2007). In accordance with observations on other debris-covered glaciers (e.g. Benn et al., 2012; Rowan et al., 2015), there is evidence that thinning of the terminal lobes is reducing under a thickening debris cover, and that ablation is focused in the cleaner ice zone at the base of the tributary glaciers, with the overall effect of flattening the glacier profile (Smiraglia et al., 2000). Further slowdown of the glacier may also be conducive to pond development (Quincey et al., 2007). The data show that changes in ice cliffs and ponds, and their contributions to mass balance, are very complex and will require continued monitoring to unravel their overall significance for the future of the glacier. On the one hand, water storage in supraglacial ponds has increased, as has pond density; on the other hand, pond contribution to ablation has slowed. Likewise, ice cliff backwasting can be substantial (up to −8.15 m $a^{-1}$), but ice cliff density and contribution to ablation have both reduced recently.

The development of surface ponds and ice cliffs has been shown to be very important for the evolution and down-wasting of debris-covered glaciers in other locations (e.g. Benn et al., 2012; Pellicciotti et al., 2015; Thompson et al., 2016; Watson et al., 2017b). In the Himalaya, the development and coalescence of ponds, and the ultimate development of a moraine-dammed proglacial or supraglacial lake characterises 'Regime 3' in the model of Benn et al. (2012). It is also notable that ablation rates associated with ice cliffs are much lower for Miage Glacier than for Himalayan glaciers (e.g. Thompson et al., 2016; Watson et al., 2017b). Ultimately, it is unclear whether Miage Glacier will develop toward this phase, but it does not appear to be transitioning to Regime 3 currently or in the near future and may remain in Regime 2 for the foreseeable future.

### 8.3.2. Future prognosis of the Manaslu glaciers

With reference to the 3-stage model of debris-covered glacier evolution (Benn et al., 2012), glaciers of the Manaslu region appear to be in a more advanced phase of decay ('Regime 2') since the 1970s. This is exhibited by overall negative mass balances and downwasting ice, increased surface water storage, expanding debris cover and glacier slowdown, despite Himal Chuli Glacier undergoing periods of comparative positive mass balance and variable surface velocity. Thus, it is likely that as climate is expected to continue to warm, these glaciers will continue to thin, stagnate, and undergo additional debris-cover development with comparatively little terminus reduction (Rowan et al., 2015; Herreid and Pellicciotti, 2020). Furthermore, due to the already low surface gradient, it is likely that surface ponding will increase and further inversion of the longitudinal profiles will develop (Rowan et al., 2015; Anderson and Anderson, 2016).

Although, supraglacial ponds have increased during this time and ice cliffs have been present since the 1970s, they do not appear to be expanding dramatically and there is no evidence of coalescing ponds or development of pond networks (Figure 7.2 to Figure 7.4). Thus, it is considered that these ponds are currently unlikely to reach the hydrological base indicative of a transition towards regime 3 in the near future (Benn et al., 2012). There is currently a lack of evidence to support the development of a supraglacial pond network on the lower sections of the glaciers despite them showing a reduction in surface velocity and low surface gradients. Thus, in the long-term continued development of ponding may increase and result in a network and the potential for ponds to coalesce and form larger ponds. Furthermore, many of the ponds assessed here are highly transient features, although often appear to refill in similar locations and thus increasing numbers of persistent ponds may start to be observed. If this scenario occurs, it is likely that rates of loss associated with these features will then increase and be comparative to those observed elsewhere in the Himalaya (Sakai et al., 1998; Thompson et al., 2016; Brun et al., 2018; Miles et al., 2018). Punggen Glacier has existing proglacial lakes, which have developed close to the glacier terminus, yet have shown little change over the survey period and have not undergone rapid expansion. Thus, it would appear that the easterly flowing glaciers in Manaslu are in an advanced state of regime 2, but do not yet indicate a transition to regime 3 (Quincey et al., 2009; Benn et al., 2012; King et al., 2018). In the long-term future with enhanced climatic change, the glaciers may continue to develop on this trajectory towards regime 3 and continued monitoring should be undertaken.

### 8.3.3. Conceptual model of debris-covered glacier evolution

Alpine and Himalayan debris-covered glacier evolution, as derived from the four glaciers studied in this thesis, indicate largely similar trajectories of debris-covered glacier evolution despite individual trends and complexities. Thus, it supports previous studies which have referred to Miage Glacier as a 'Himalayan type glacier' (Deline and Ravanel, 2014). Here, a conceptual model of debris-covered evolution is presented with regard to the data collected here and with reference to existing literature.

As summarised from Chapters 6 and 7, Miage Glacier has transitioned to a phase dominated by 'Regime 2', yet the Manaslu glaciers with the development of proglacial lakes (Punggen Glacier) and increased presence of supraglacial ponds and comparatively greater undulating topography with large ice cliffs, characterise a transition towards an advanced stage of 'Regime 2' in the model of Benn et al. (2012). It is also notable that ablation rates associated with ice cliffs, and overall density, are much lower for Miage Glacier than for the Himalayan glaciers (e.g. Thompson et al., 2016; Watson et al., 2017b). Thus, it would indicate that Miage Glacier is limited by a comparatively steep surface gradient and is therefore in an earlier phase of debris-covered glacier evolution in

comparison to the Manaslu glaciers. As such, the Manaslu glaciers may start to form a network of coalescing ponds and hydrological base level lakes earlier than would be expected for Miage Glacier.

The stages of debris-covered glacier evolution include a build-up of debris and increasing debris thickness across the glacier surfaces in response to a nearly global glacier recession observed since the LIA (Deline, 2005; Rowan, 2017; Shukla and Garg, 2019) (Figure 8.2). The LIA was a relatively short period of widespread cooling in the northern hemisphere, which occurred between 1400 and 1700 in the common era (CE) and resulted in a LIA advance around 1300-1600 CE. However, studies identified variable timing of the LIA across the Central Himalaya in response to the influence of the Westerlies and the monsoon (Rowan, 2017). Since the LIA, climate has been warming and resulted in global negative mass balance and destabilisation of valley walls, which develops a debris cover on the glaciers below. Once a thick debris cover has established over the majority of the glacier surface, surface ablation is likely to reduce with variable enhanced melt due to differential debris thickness (Østrem, 1959) coinciding with surface velocity reduction. Thus, an undulating surface topography (e.g. Bartlett et al., 2021) develops with the ability for meltwater to pond in surface hollows and steep sections where debris cannot stabilise expose ice and begin to form ice cliffs (Röhl, 2008). These features develop enhanced hotspots for ablation and if conditions for continued develop allow, will develop to form hydrological base level lakes with coalescing ponds and the development of pond networks. Thus, the development of regime 3 depends greatly on the ability of coalescing ponds and networks to form promoting a state of advanced decay and disintegration with a decoupled margin (Benn et al., 2012).

The proposed conceptual model advances our existing understanding of debris-covered glacier evolution by integrating glacier specific and regional considerations (Figure 8.2). The inclusion of glacier hypsometry, topographical constraints and local meteorological variability have been incorporated into the framework of the 3-stage model as proposed by Benn et al. (2012).

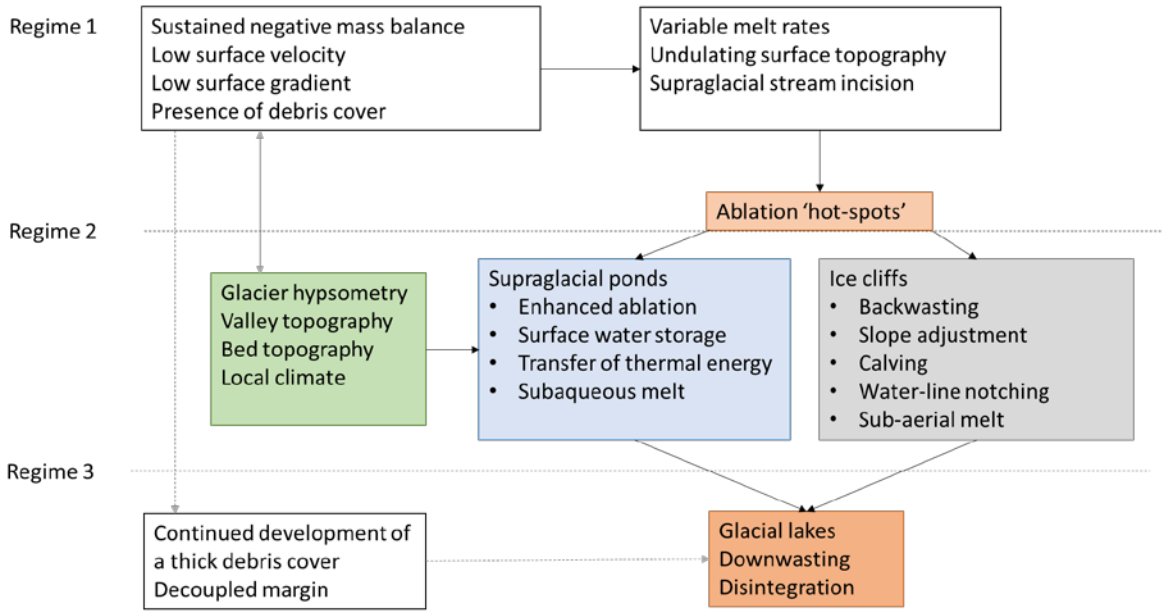


**Figure 8.2:** Revised conceptual model of debris-covered glacier evolution developed from the Benn et al. (2012) model.

### 8.3.4. Importance of this research

Although a thicker and more extensive debris cover has the potential to reduce ablation, some debris-covered glaciers in the Himalaya have experienced similar rates of mass loss to clean-ice glaciers; a phenomenon referred to as the 'debris-cover anomaly' (Pellicciotti et al., 2015; Vincent et al., 2016). This behaviour results from high rates of enhanced localised ablation in the vicinity of supraglacial ponds and ice cliffs (e.g. Buri et al., 2015; Miles et al., 2016). However, these effects do not seem to be prevalent at Miage Glacier or the Manaslu glaciers where the development of ice cliffs and supraglacial ponds is limited. Thus, the insulating effect of debris cover appears to have had an overall more important effect on the mass balance than the mass loss associated with ice cliffs and supraglacial ponds (e.g. Hambrey et al., 2008).

Recent studies of glacier mass balance in Annapurna located to the west of Manaslu showed no significant difference between debris-covered and clean-ice glaciers (Lovell et al., 2019). Furthermore, glacier mass loss of the Manaslu glaciers show comparative rates of mass loss to those previously observed in across the eastern and central Himalaya (−0.22 to −0.33 m w.e. $a^{-1}$) (Kääb et al., 2012; Gardelle et al., 2013) from 1970 to 2019 but substantial increase since 2013. Robson et al. (2018) previously discussed the complexity of mass loss on clean-ice glaciers and debris-covered glaciers in the Manaslu region depending on debris thickness. Data from 16 clean-ice glaciers in Manaslu exhibited a neutral elevation change (0.00 m $a^{-1}$) between 2000 and 2013, compared to 13 debris-covered glaciers with a negative elevation change (−0.29 m $a^{-1}$) indicating that debris-covered glaciers are losing more mass than clean-ice glaciers in the region highlighting the complexity of mass loss in relation to local and glacier dependent factors.

This research highlights the need for continued monitoring of debris-covered glaciers to further understand the processes and controls on the dynamics and response to future climatic change. Despite similarities and homogeneity in terms of global negative mass balance and reduced surface velocity, this research supports previous studies, which highlighted high levels of variability and complexity in glacier response to climatic warming. Understanding these variations and reasons for such, is important to enable future research to adequately model climatic response, quantify and aid water resource management, especially for those in regions such as high-mountain Asia where such resources are vital to livelihoods, and to mitigate against the development of potentially hazardous proglacial lakes.

Although glacial lakes at Miage Glacier are unlikely to reach the hydrological base and pose a GLOF risk, the presence of increased ponding affects water storage and glacier runoff. The proglacial river from Miage Glacier delivers meltwater into the river Dora di Veny, which consequently flows into the River Po, the longest river in Italy. Thus, although water storage does not pose an imminent risk at Miage Glacier, future water resources and seasonal fluctuations may be affected downstream. Glacial hazards have substantial implications in this region as Val Veny is a well populated region as highlighted by the events at the nearby Brenva Glacier in 1997 when a large avalanche caused significant damage and killed two skiers (Giani et al., 2001), and the risk of collapse at Planpincieux Glacier in September 2019 which resulted in evacuation of local residents (Giordan et al., 2020). In comparison to Miage Glacier, the glaciers in the Manaslu regions of the Himalaya provide seasonal runoff to the Buri Ghandaki River, along which many of the small villages along the Manaslu trekking circuit are situated. If the proglacial lakes at Punggen Glacier and supraglacial ponds begin to coalesce, the potential risk of large lakes forming, and risk of a GLOF event is heightened and thus, future monitoring should be considered. The monastery at the base of Hinang Glacier would also be at risk in the event of a GLOF event from higher up the valley. Risk management would require the Nepalese authorities and governments to monitor and if decided necessary, put in place drainage or monitoring systems as implemented at Belvedere Glacier (Haeberli et al., 2002; Diolaiuti et al., 2003) to control the safe drainage of potentially hazardous and rapidly growing lakes that may form in the future.

## 8.4. Limitations and future work

### 8.4.1. Methodological considerations for remote sensing techniques

There are several limitations to this research that need to be acknowledged and several further research tasks, which would be beneficial to aid our understanding of debris-covered glacier evolution and the processes involved. First, as highlighted in Chapter 6 and Chapter 8, the extraction of DEMs from SPOT and Pleiades imagery is dependent upon available, good quality imagery, which

is both clear of snow and cloud. Availability of imagery over Miage Glacier provided good temporal coverage, yet several extracted datasets (from 2000 and 2005) produced high errors and were not useable. In comparison, data coverage of the Manaslu region was limited with reduced satellite coverage. Pre-existing DEMs such as the HMA datasets provided by the NSIDC (Shean, 2017) were investigated but did not provide coverage of the study area other than the data from 2013. Furthermore, periods of snow free glaciers often coincided with heavy cloud cover associated with the monsoon and hence the data used in this study from 2016 represents the best available data despite the acknowledgement of potential errors associated with snow cover in the higher elevations. Therefore, further analysis using high-temporal data of Himal Chuli Glacier to further assess the dynamic flow behaviour will require requests for satellite acquisition data to cover this region. Additional sources of imagery such as the US archives for aerial could also be explored. Continued monitoring of overall mass balance and surface velocity at high-temporal resolution at Miage Glacier and the Manaslu glaciers to assess their continued evolution and trajectories in relation to Benn et al.'s (2012) model would be highly beneficial to unpick the complexities previously discussed especially those in recent periods.

DEM differencing analysis and geodetic mass balance calculations were based on the assumption that all surface elevation change is due to ice mass fluctuations. However, some of these fluxes are resultant from debris inputs such as rockfall or avalanche debris onto the glacier surface (Figure 5.3). Although larger events have the potential to be identified and accounted for (e.g. Figure 5.3), comparatively smaller events are not necessarily identifiable dependent upon timing and imagery resolution, especially when observation periods cover a long temporal period (e.g. 20+ years). It is often assumed that these impacts are negligible on the overall glacier mass balance; yet they are likely to have a bigger influence on higher-temporal assessments. Newly developed techniques such as GERALDINE (Smith et al., 2020) could be incorporated into future DEM assessments to account for supraglacial debris inputs and eliminated from ice mass calculations.

Quantification of the contribution of supraglacial ponds and ice cliffs to overall ablation rates also pose some methodological assumptions. By using a simple approach and only extracting the corresponding elevation changes within the extent of the ponds and cliffs, the attribution of distal ablation was excluded and thus likely to represent an underestimation. However, distal ablation is likely to be confined to englacial channels and accounting for this using a GIS based approach is difficult to assess. Thus, additional techniques including the use of ground penetrating radar (GPR) could be used to assess englacial conduits in the vicinity of supraglacial ponds could provide an ability to quantify additional subsurface ablation.

Assessment of the contribution of supraglacial ponds and ice cliffs to overall ablation rates also negates emergence velocity quantification. The development of a method for improving

quantification of emergence velocity using raster data for velocity, ice thickness and mass transfer would improve quantification of spatial and temporal variations in emergence velocity. Previous methods to calculate emergence velocity are based upon a theoretical line across the glacier surface to quantify ice flux through that line (e.g. Westoby et al., 2020). However, it is possible that an improved approach could be derived utilising the gridded raster layers for each of the required components (e.g. surface velocity, ice thickness etc.) to derive a higher resolution temporal assessment.

Mapping of surface features is also open to subjective bias, especially when using older panchromatic imagery. Segmentations and classifications were used to help remove an element of subjectivity but is difficult to eliminate entirely. Recently developed semi-automated approaches for mapping ponds and cliffs could help reduce this issue in future studies (Anderson et al., 2021; Kneib et al., 2021). In addition to the high spatial and temporal assessment of surface features on Miage Glacier, GPR data collected in March 2018 could be used to further assess englacial and subsurface structures in relation to debris entrainment, surface features and surface evolution.

Although statistical assessment here does not show any strong relationships (Table 8.1), a global assessment using a larger database to statistically assess the 'controls' on supraglacial pond size and location could help constrain a number of these potentially important factors. These future research plans could add to the wealth of data presented in this thesis and to the assessment of debris-covered glaciers in high-mountain regions around the world.

### 8.4.2. Logistical considerations with fieldwork

The first field visit to Miage Glacier in June/July 2017 and subsequent visit in June/July 2018 enabled a wealth of data to be collected. Comparatively, fieldwork in the Himalaya proved to be more complicated and costly. Despite our best plans and organisation with a local guide, we were unable to visit the Himal Chuli Glacier as we had initially planned due to the access path being blocked. Thus, we continued along the Manaslu trekking circuit to access Hinang Glacier. Due to the scale of the glacier, limited time available and time to recharge batteries with a generator, we were not able to access and survey as many ponds, which limited the use and analysis planned for the resulting dataset. It would also be beneficial to resurvey the ponds at both Miage Glacier and Hinang Glacier to continue monitoring their development and influence of glacier mass loss and evolution, but this was beyond the scope and budgets of this research.

Replication of the bathymetric surveys to asses future development of the ponds at Miage Glacier and Manaslu glaciers in comparison to the future prognoses and predictions provided in this thesis would provide high-resolution detail regarding the processes responsible for debris-covered glacier evolution and the important components for such.

An enlaps Tikee time-lapse camera was installed at Hinang Glacier in September 2019 (Figure 7.1) in the hope of using it for assessment of surface velocity and supraglacial pond dynamics including timings and mechanisms associated with drainage. Further analysis of temporal variations for supraglacial pond variability and evolution including drainage patterns could help provide high temporal and spatial details that could be applied to glaciers with highly dynamic flow behaviour in an attempt to constrain glacier dynamics.

# Chapter 9 : Conclusions

This study aimed to investigate temporal and spatial debris-covered glacier dynamics in the Alpine European Alps and the Himalayan Manaslu region using a range of *in situ* data collection methods and remotely sensed data, enabling comprehensive analysis of both glacier-scale dynamics and detailed glaciological processes. It has found broadly similar trends in debris-covered glacier response in both the Alps and Himalaya associated with sustained periods of negative mass balance, reduced surface velocity, flattening of the longitudinal profile and the development of surface features. However, individual glacier variability complicates the narrative and general trends. The results add to the current knowledge base and offer a unique and valuable insight into the variability of debris-covered glacier responses in two comparatively different environmental settings aiding our understanding of past and future debris-covered glacier evolution.

Structural analysis of Miage Glacier shows a transition from an active glacier in the 1950s to one of prolonged deterioration by 2018. Miage Glacier has transitioned from a period of active flow and limited surface water storage during the twentieth century, to one of downwasting ice since 1990 with continued thinning (−0.86 ± 0.27 m w.e. $a^{-1}$ between 1990 to 2018), increased surface water storage (>6000 $m^2$), expanded debris cover (+10%) and dramatic reduction in glacier surface velocity (-46%). A reduction and deceleration of thinning rates is attributed to an expanding and thickening debris cover; resulting in complex, nonlinear changes over time. Quantification of the mass loss associated with the presence of supraglacial ponds and ice cliffs support the importance of such features as localised regions of enhanced ablation despite their relative small size, which have previously been disregarded and highlight the importance for inclusion in glacier-wide assessments. Yet the surface features observed appear to have not passed a threshold in which they outweigh sub-debris ice loss and are likely to play a significant role in future positive feedbacks promoting further glacier ablation through increased absorption of solar radiation and transmission to the glacier ice. Furthermore, potential tipping points in glacier evolution can be identified from the dataset from Miage Glacier with a substantial increase in the number and area of supraglacial ponds across the glacier surface since 2004. The timing indicates a lagged glacier response to warming temperatures since 1990 of approximately 14 years in the Alps. The co-evolution of pond and ice cliffs highlight the importance of understanding the simultaneous development and glaciological processes. In the future, it is possible that positive feedbacks between ponding, ice cliff backwasting and surface topography will enhance ice loss associated with surface features promoting further growth and thus have further implications for glacier-wide mass balance and glacier dynamics.

Glaciers in the Manaslu region experienced long-term negative mass balance (mean −0.29 ± 0.05 m w.e. $a^{-1}$), overall reduced surface velocity and increased presence of supraglacial ponding between 1970 and 1990, yet show distinct individual variability despite similarities in environmental setting.

Such variability is partly attributed to dynamic flow behaviour of Himal Chuli Glacier as assessed by glacier hypsometry promoting fluctuations in mass flux and surface velocity. Ice mass loss is likely to be influenced by glacier hypsometry with glaciers with a top-heavy hypsometry likely to be able to sustain longer response times and withstand short-term climate fluctuations. However, glacier response is also likely to be influenced by the altitudinal range and future glacier response will be affected by altitudinal variations in precipitation and temperature. Thus, glacier hypsometry and altitudinal range are likely to be key controls on glacier response and have significant influences on short term glacier behaviour, which are often overlooked by assessing long-term change and regional trends. The variability observed within the Himalaya dataset highlight the importance of individual glacier response and thus regional response commonly discussed within the literature will invariably negate glacier- or catchment-scale variability, which could have significant implications for local water resources.

Observations of changes in glacier evolution over periods of negative glacier mass balance indicate the relative importance of glaciological processes including ice cliff backwasting and supraglacial pond expansion at both locations. Such processes are both products of surface topographic change and further promote future glacier morphometric change. The presence and development of such features have importance implications for catchment hydrology and alter the energy budget at the glacier surface.

Despite two environmentally different regions of the Alps and Himalaya, and thus climatically influenced ablation and monsoonal regimes, debris-covered glacier evolution of the examples within this thesis indicate they are following similar trajectories in terms of their evolution and dynamics. Evolution of the Manaslu glaciers is perhaps at a slightly more advanced stage with the presence of increased area of ice cliffs, supraglacial ponds and proglacial ponding. However, no evidence of pond networks or coalescing ponds were observed. Thus, Miage Glacier appears to be following the trajectory of Himalayan debris-covered glaciers and supports the use of this Alpine glacier to aid our understanding of glaciological processes at a comparatively accessible location for application to less-accessible and less constrained regions of the Himalaya. Future assessment of debris-covered glaciers in regions such as New Zealand, Patagonia and the Andes will support the development of debris-covered glacier evolution more generally.

This research presented in this thesis illustrates the varied and complex response of debris-covered glaciers to global and local climatic change and importance for continued monitoring and assessment of surface features for inclusion in modelled attempts of debris-covered glacier evolution. This thesis has gathered a wealth of data to aid our understanding of both long- and short-term response in two climatically different regions and provides quantification which can be used to improve parameterisation and constrain numerical models for application to debris-

covered glaciers in the Alps and Himalaya and more widely. The complexity of the feedbacks associated with debris-covered glaciers mean it is difficult to accurately model climatic response and assess their present and future evolution, which require further research. The thresholds associated with glacier evolution and timings of such remain variable and uncertain and are dependent on a number of local factors. Further constraint is required to understand and quantify timings and controls on glacier evolution including thresholds and quantification of tipping points including the area of debris cover and surface features at which they have influence overall mass balance and thus glacier dynamics. This would aid both understanding and ability to develop more realistic numerical models with feedbacks and quantification of important glaciological processes associated with debris-covered glaciers.

# References


Anderson, B., and Mackintosh, A. (2012). Controls on mass balance sensitivity of maritime glaciers in the Southern Alps, New Zealand: The role of debris cover. *Journal of Geophysical Research: Earth Surface* 117. doi:10.1029/2011JF002064.

Anderson, L.S., and Anderson, R.S. (2016). Modeling debris-covered glaciers: response to steady debris deposition. *The Cryosphere* 10, 1105–1124. doi:10.5194/tc-10-1105-2016.

Anderson, L.S., and Anderson, R.S. (2018). Debris thickness patterns on debris-covered glaciers. *Geomorphology* 311, 1–12. doi:10.1016/j.geomorph.2018.03.014.

Anderson, L.S., Armstrong, W.H., Anderson, R.S., and Buri, P. (2021). Debris cover and the thinning of Kennicott Glacier, Alaska: in situ measurements, automated ice cliff delineation and distributed melt estimates. *The Cryosphere* 15, 265–282. doi:https://doi.org/10.5194/tc-15-265-2021.

Appleby, J.R., Brook, M.S., Vale, S.S., and Macdonald-Creevey, A.M. (2010). Structural Glaciology of a Temperate Maritime Glacier: Lower Fox Glacier, New Zealand. *Geografiska Annaler: Series A, Physical Geography* 92, 451–467. doi:10.1111/j.1468-0459.2010.00407.x.

Atherton, D. (1963). Comparisons of Ogive Systems Under Various Regimes. *Journal of Glaciology* 4, 547–557. doi:10.3189/S0022143000028082.

Azam, M.F., Wagnon, P., Berthier, E., Vincent, C., Fujita, K., and Kargel, J.S. (2018). Review of the status and mass changes of Himalayan-Karakoram glaciers. *Journal of Glaciology* 64, 61–74. doi:10.1017/jog.2017.86.

Azzoni, R.S., Fugazza, D., Zennaro, M., Zucali, M., D'Agata, C., Maragno, D., Cernuschi, M., Smiraglia, C., and Diolaiuti, G.A. (2017). Recent structural evolution of Forni Glacier tongue (Ortles-Cevedale Group, Central Italian Alps). *Journal of Maps* 13, 870–878. doi:10.1080/17445647.2017.1394227.

Azzoni, R.S., Fugazza, D., Zerboni, A., Senese, A., D'Agata, C., Maragno, D., Carzaniga, A., Cernuschi, M., and Diolaiuti, G.A. (2018). Evaluating high-resolution remote sensing data for reconstructing the recent evolution of supra glacial debris: A study in the Central Alps (Stelvio Park, Italy). *Progress in Physical Geography: Earth and Environment* 42, 3–23. doi:10.1177/0309133317749434.

Baltsavias, E., Kocaman, S., Akca, D., and Wolff, K. (2007). Geometric and radiometric investigations of Cartosat-1 data. in *ISPRS Workshop" High Resolution Earth Imaging for Geospatial Information"* (ISPRS).

Bamber, J.L., and Rivera, A. (2007). A review of remote sensing methods for glacier mass balance determination. *Global and Planetary Change* 59, 138–148. doi:10.1016/j.gloplacha.2006.11.031.

Bartlett, O.T., Ng, F.S.L., and Rowan, A.V. (2021). Morphology and evolution of supraglacial hummocks on debris-covered Himalayan glaciers. *Earth Surface Processes and Landforms* 46, 525–539. doi:https://doi.org/10.1002/esp.5043.

Bash, E.A., Moorman, B.J., and Gunther, A. (2018). Detecting Short-Term Surface Melt on an Arctic Glacier Using UAV Surveys. *Remote Sensing* 10, 1547. doi:10.3390/rs10101547.

Benn, D., and Evans, D.J.A. (2010). *Glaciers and Glaciation, 2nd Edition*. Routledge.

Benn, D.I., Bolch, T., Hands, K., Gulley, J., Luckman, A., Nicholson, L.I., Quincey, D., Thompson, S., Toumi, R., and Wiseman, S. (2012). Response of debris-covered glaciers in the Mount Everest

region to recent warming, and implications for outburst flood hazards. *Earth-Science Reviews* 114, 156–174. doi:10.1016/j.earscirev.2012.03.008.

Benn, D.I., and Lehmkuhl, F. (2000). Mass balance and equilibrium-line altitudes of glaciers in high-mountain environments. *Quaternary International* 65–66, 15–29. doi:10.1016/S1040-6182(99)00034-8.

Benn, D.I., Thompson, S., Gulley, J., Mertes, J., Luckman, A., and Nicholson, L. (2017). Structure and evolution of the drainage system of a Himalayan debris-covered glacier, and its relationship with patterns of mass loss. *The Cryosphere* 11, 2247–2264. doi:10.5194/tc-11-2247-2017.

Benn, D.I., Wiseman, S., and Hands, K.A. (2001). Growth and drainage of supraglacial lakes on debris mantled Ngozumpa Glacier, Khumbu Himal, Nepal. *Journal of Glaciology* 47, 626–638. doi:10.3189/172756501781831729.

Bennett, M.R., Huddart, D., Hambrey, M.J., and Ghienne, J.F. (1996). Moraine Development at the High-Arctic Valley Glacier Pedersenbreen, Svalbard. *Geografiska Annaler: Series A, Physical Geography* 78, 209–222. doi:10.1080/04353676.1996.11880468.

Berthier, E., Cabot, V., Vincent, C., and Six, D. (2016). Decadal Region-Wide and Glacier-Wide Mass Balances Derived from Multi-Temporal ASTER Satellite Digital Elevation Models. Validation over the Mont-Blanc Area. *Frontiers in Earth Science* 4. doi:10.3389/feart.2016.00063.

Berthier, E., Vincent, C., Magnússon, E., Gunnlaugsson, Á., Pitte, P., Le Meur, E., Masiokas, M., Ruiz, L., Pálsson, F., and Belart, J.M.C. (2014). Glacier topography and elevation changes derived from Pléiades sub-meter stereo images. *Cryosphere* 8, 2275–2291. doi:10.5194/tc-8-2275-2014.

Biemans, H., Siderius, C., Lutz, A.F., Nepal, S., Ahmad, B., Hassan, T., von Bloh, W., Wijngaard, R.R., Wester, P., Shrestha, A.B., and Immerzeel, W.W. (2019). Importance of snow and glacier meltwater for agriculture on the Indo-Gangetic Plain. *Nature Sustainability* 2, 594–601. doi:10.1038/s41893-019-0305-3.

Bolch, T., Buchroithner, M.F., Peters, J., Baessler, M., and Bajracharya, S. (2008). Identification of glacier motion and potentially dangerous glacial lakes in the Mt. Everest region/Nepal using spaceborne imagery. *Natural Hazards and Earth System Sciences* 8, 1329–1340. doi:10.5194/nhess-8-1329-2008.

Bolch, T., Kulkarni, A., Kaab, A., Huggel, C., Paul, F., Cogley, J.G., Frey, H., Kargel, J.S., Fujita, K., Scheel, M., Bajracharya, S., and Stoffel, M. (2012). The State and Fate of Himalayan Glaciers. *Science* 336, 310–314. doi:10.1126/science.1215828.

Bolch, T., Pieczonka, T., and Benn, D.I. (2011). Multi-decadal mass loss of glaciers in the Everest area (Nepal Himalaya) derived from stereo imagery. *The Cryosphere* 5, 349–358. doi:10.5194/tc-5-349-2011.

Bolch, T., Shea, J.M., Liu, S., Azam, F.M., Gao, Y., Gruber, S., Immerzeel, W.W., Kulkarni, A., Li, H., Tahir, A.A., Zhang, G., and Zhang, Y. (2019). "Status and Change of the Cryosphere in the Extended Hindu Kush Himalaya Region," in *The Hindu Kush Himalaya Assessment: Mountains, Climate Change, Sustainability and People*, eds. P. Wester, A. Mishra, A. Mukherji, and A. B. Shrestha (Cham: Springer International Publishing), 209–255. doi:10.1007/978-3-319-92288-1_7.

Bookhagen, B., and Burbank, D.W. (2010). Toward a complete Himalayan hydrological budget: Spatiotemporal distribution of snowmelt and rainfall and their impact on river discharge. *Journal of Geophysical Research: Earth Surface* 115. doi:https://doi.org/10.1029/2009JF001426.

Brock, B.W., Mihalcea, C., Kirkbride, M.P., Diolaiuti, G., Cutler, M.E.J., and Smiraglia, C. (2010). Meteorology and surface energy fluxes in the 2005–2007 ablation seasons at the Miage debris-covered glacier, Mont Blanc Massif, Italian Alps. *Journal of Geophysical Research: Atmospheres* 115, D09106. doi:10.1029/2009JD013224.

Brun, F., Berthier, E., Wagnon, P., Kääb, A., and Treichler, D. (2017). A spatially resolved estimate of High Mountain Asia glacier mass balances from 2000 to 2016. *Nature Geoscience* 10, 668–673. doi:10.1038/ngeo2999.

Brun, F., Buri, P., Miles, E.S., Wagnon, P., Steiner, J., Berthier, E., Ragettli, S., Kraaijenbrink, P., Immerzeel, W.W., and Pellicciotti, F. (2016). Quantifying volume loss from ice cliffs on debris-covered glaciers using high-resolution terrestrial and aerial photogrammetry. *Journal of Glaciology* 62, 684–695. doi:10.1017/jog.2016.54.

Brun, F., Wagnon, P., Berthier, E., Jomelli, V., Maharjan, S.B., Shrestha, F., and Kraaijenbrink, P.D.A. (2019). Heterogeneous Influence of Glacier Morphology on the Mass Balance Variability in High Mountain Asia. *Journal of Geophysical Research: Earth Surface* 124, 1331–1345. doi:10.1029/2018JF004838.

Brun, F., Wagnon, P., Berthier, E., Shea, J.M., Immerzeel, W.W., Kraaijenbrink, P.D.A., Vincent, C., Reverchon, C., Shrestha, D., and Arnaud, Y. (2018). Ice cliff contribution to the tongue-wide ablation of Changri Nup Glacier, Nepal, central Himalaya. *The Cryosphere* 12, 3439–3457. doi:https://doi.org/10.5194/tc-12-3439-2018.

Buckel, J., Otto, J.C., Prasicek, G., and Keuschnig, M. (2018). Glacial lakes in Austria - Distribution and formation since the Little Ice Age. *Global and Planetary Change* 164, 39–51. doi:10.1016/j.gloplacha.2018.03.003.

Burger, F., Ayala, A., Farias, D., Shaw, T.E., MacDonell, S., Brock, B., McPhee, J., and Pellicciotti, F. (2019). Interannual variability in glacier contribution to runoff from a high-elevation Andean catchment: understanding the role of debris cover in glacier hydrology. *Hydrological Processes* 33, 214–229. doi:10.1002/hyp.13354.

Buri, P., Miles, E., Steiner, J., Immerzeel, W., Wagnon, P., and Pellicciotti, F. (2016a). A physically based 3-D model of ice cliff evolution over debris-covered glaciers. *Journal of Geophysical Research: Earth Surface* 121, 2471–2493.

Buri, P., Pellicciotti, F., Steiner, J.F., Miles, E.S., and Immerzeel, W.W. (2016b). A grid-based model of backwasting of supraglacial ice cliffs on debris-covered glaciers. *Annals of Glaciology* 57, 199–211. doi:10.3189/2016AoG71A059.

Capt, M., Bosson, J.-B., Fischer, M., Micheletti, N., and Lambiel, C. (2016). Decadal evolution of a very small heavily debris-covered glacier in an Alpine permafrost environment. *Journal of Glaciology* FirstView, 1–17. doi:10.1017/jog.2016.56.

Carrivick, J.L., and Tweed, F.S. (2013). Proglacial lakes: character, behaviour and geological importance. *Quaternary Science Reviews* 78, 34–52. doi:10.1016/j.quascirev.2013.07.028.

Carrivick, J.L., and Tweed, F.S. (2016). A global assessment of the societal impacts of glacier outburst floods. *Global and Planetary Change* 144, 1–16. doi:10.1016/j.gloplacha.2016.07.001.

Chen, C., Fine, R.A., and Millero, F.J. (1977). The equation of state of pure water determined from sound speeds. *Journal of Chemical Physics* 66, 2142–2144. doi:10.1063/1.434179.

Cheng, P. (2015). Pan-Sharpening, DEM Extraction and Geometric Correction - Spot-6 and Spot-7 Satellites. *GeoInformatics* 18, 24.

Chikita, K., Jha, J., and Yamada, T. (1999). Hydrodynamics of a Supraglacial Lake and Its Effect on the Basin Expansion: Tsho Rolpa, Rolwaling Valley, Nepal Himalaya. *Arctic, Antarctic, and Alpine Research* 31, 58–70. doi:10.2307/1552623.

Chikita, K., Jha, J., and Yamada, T. (2001). Sedimentary effects on the expansion of a Himalayan supraglacial lake. *Global and Planetary Change* 28, 23–34. doi:10.1016/S0921-8181(00)00062-X.

Chikita, K., Joshi, S.P., Jha, J., and Hasegawa, H. (2000). Hydrological and thermal regimes in a supra-glacial lake: Imja, Khumbu, Nepal Himalaya. *Hydrological Sciences Journal* 45, 507–521. doi:10.1080/02626660009492353.

Cogley, J.G. (2011). "Himalayan Glaciers in 2010 and 2035," in *Encyclopedia of Snow, Ice and Glaciers*, eds. V. P. Singh, P. Singh, and U. K. Haritashya (Dordrecht: Springer Netherlands), 520–523. doi:10.1007/978-90-481-2642-2_673.

Cogley, J.G., Kargel, J.S., Kaser, G., and Van der Veen, C.J. (2010). Tracking the source of glacier misinformation. *Science* 327, 522. doi:10.1126/science.327.5965.522-a.

Conforti, D., Deline, P., Mortara, G., and Tamburini, A. (2005). Terrestrial scanning LiDAR technology applied to study the evolution of the ice-contact Miage lake (Mont Blanc, Italy). in *Proceedings of the 9th Alpine Glaciological Meeting* (Milan, Italy). doi:10.1.1.503.4137.

Cook, S.J., and Quincey, D.J. (2015). Estimating the volume of Alpine glacial lakes. *Earth Surface Dynamics* 3, 559–575. doi:10.5194/esurf-3-559-2015.

Cruz, R.V., Harasawa, H., Lal, M., Wu, S., Anokhin, Y., Punsalmaa, B., Honda, Y., Jafari, M., Li, C., and Ninh, N.H. (2007). *Climate Change 2007: Impacts, Adaptation and Vulnerability, Chapter 10: Asia. Contribution of Working Group II to the Fourth Assessment Report of the Intergovernmental Panel on Climate Change*. Cambridge University Press, Cambridge, UK and New York, NY.

Cuffey, K.M., and Paterson, W.S.B. (2010). *The physics of glaciers*. Academic Press.

Dehecq, A., Gourmelen, N., Gardner, A.S., Brun, F., Goldberg, D., Nienow, P.W., Berthier, E., Vincent, C., Wagnon, P., and Trouvé, E. (2019). Twenty-first century glacier slowdown driven by mass loss in High Mountain Asia. *Nature Geoscience* 12, 22–27. doi:10.1038/s41561-018-0271-9.

Deline, P. (2005). Change in surface debris cover on Mont Blanc massif glaciers after the 'Little Ice Age' termination. *The Holocene* 15, 302–309. doi:10.1191/0959683605hl809rr.

Deline, P. (2009). Interactions between rock avalanches and glaciers in the Mont Blanc massif during the late Holocene. *Quaternary Science Reviews* 28, 1070–1083. doi:10.1016/j.quascirev.2008.09.025.

Deline, P., Diolaiuti, G., Kirkbride, M., Mortara, G., Pavan, M., Smiraglia, C., and Tamburini, A. (2004). Drainage of ice-contact Miage Lake (Mont Blanc Massif, Italy) in September 2004. *Geografia Fisica e Dinamica Quaternaria* 27, 113–119.

Deline, P., Gardent, M., Magnin, F., and Ravanel, L. (2012). The Morphodynamics of the Mont Blanc Massif in a Changing Cryosphere: A Comprehensive Review. *Geografiska Annaler: Series A, Physical Geography* 94, 265–283. doi:10.1111/j.1468-0459.2012.00467.x.

Deline, P., and Ravanel, L. (2014). "On the Roof of Europe: High-Altitude Morphodynamics in the Mont Blanc Massif," in *Landscapes and Landforms of France* World Geomorphological Landscapes., eds. M. Fort and M.-F. André (Dordrecht: Springer Netherlands), 171–181. doi:10.1007/978-94-007-7022-5_17.

Diolaiuti, G., Citterio, M., Carnielli, T., D'Agata, C., Kirkbride, M., and Smiraglia, C. (2006). Rates, processes and morphology of freshwater calving at Miage Glacier (Italian Alps). *Hydrological Processes* 20, 2233–2244. doi:10.1002/hyp.6198.

Diolaiuti, G., D'Agata, C., Meazza, A., Zanutta, A., and Smiraglia, C. (2009). Recent (1975–2003) changes in the Miage debris-covered glacier tongue (Mont Blanc, Italy) from analysis of aerial photos and maps. *Geografia Fisica e Dinamica Quaternaria* 32, 117–127.

Diolaiuti, G., D'Agata, C., and Smiraglia, C. (2003). Belvedere Glacier, Monte Rosa, Italian Alps: Tongue Thickness and Volume Variations in the Second Half of the 20th Century. *Arctic, Antarctic, and Alpine Research* 35, 255–263. doi:10.1657/1523-0430(2003)035[0255:BGMRIA]2.0.CO;2.

Diolaiuti, G., Kirkbride, M.P., Smiraglia, C., Benn, D.I., D'Agata, C., and Nicholson, L. (2005). Calving processes and lake evolution at Miage glacier, Mont Blanc, Italian Alps. *Annals of Glaciology* 40, 207–214. doi:10.3189/172756405781813690.

Dunning, S.A., Rosser, N.J., McColl, S.T., and Reznichenko, N.V. (2015). Rapid sequestration of rock avalanche deposits within glaciers. *Nature Communications* 6, 7964. doi:10.1038/ncomms8964.

Emmer, A., Merkl, S., and Mergili, M. (2015). Spatiotemporal patterns of high-mountain lakes and related hazards in western Austria. *Geomorphology* 246, 602–616. doi:10.1016/j.geomorph.2015.06.032.

European Environment Agency (2009). Regional climate change and adaptation; The Alps facing the challenge of changing water resrouces. *EEA, Copenhagen* Report 8. doi:10.2800/12552.

Evans, D.J.A., Ewertowski, M., and Orton, C. (2017). Skaftafellsjökull, Iceland: glacial geomorphology recording glacier recession since the Little Ice Age. *Journal of Maps* 13, 358–368. doi:10.1080/17445647.2017.1310676.

Evatt, G.W., Abrahams, I.D., Heil, M., Mayer, C., Kingslake, J., Mitchell, S.L., Fowler, A.C., and Clark, C.D. (2015). Glacial melt under a porous debris layer. *Journal of Glaciology* 61, 825–836. doi:10.3189/2015JoG14J235.

Falaschi, D., Lenzano, M.G., Villalba, R., Bolch, T., Rivera, A., and Lo Vecchio, A. (2019). Six Decades (1958–2018) of Geodetic Glacier Mass Balance in Monte San Lorenzo, Patagonian Andes. *Frontiers in Earth Science* 7. doi:10.3389/feart.2019.00326.

Farinotti, D., Huss, M., Fürst, J.J., Landmann, J., Machguth, H., Maussion, F., and Pandit, A. (2019). A consensus estimate for the ice thickness distribution of all glaciers on Earth. *Nature Geoscience* 12, 168–173. doi:10.1038/s41561-019-0300-3.

Farinotti, D., Immerzeel, W.W., de Kok, R.J., Quincey, D.J., and Dehecq, A. (2020). Manifestations and mechanisms of the Karakoram glacier Anomaly. *Nature Geoscience* 13, 8–16. doi:10.1038/s41561-019-0513-5.

Fisher, J.E. (1962). Ogives of the Forbes Type on Alpine Glaciers and a Study of their Origins. *Journal of Glaciology* 4, 53–61. doi:10.3189/S0022143000018207.

Foster, L.A., Brock, B.W., Cutler, M.E.J., and Diotri, F. (2012). A physically based method for estimating supraglacial debris thickness from thermal band remote-sensing data. *Journal of Glaciology* 58, 677–691. doi:10.3189/2012JoG11J194.

Fujita, K., and Nuimura, T. (2011). Spatially heterogeneous wastage of Himalayan glaciers. *PNAS* 108, 14011–14014. doi:10.1073/pnas.1106242108.

Fushimi, H. (1977). Structural Studies of Glaciers in the Khumbu Region. *Journal of the Japanese Society of Snow and Ice* 39, 30–39. doi:10.5331/seppyo.39.Special_30.

Fyffe, C., Reid, T., Brock, B., Kirkbride, M., Diolaiuti, G., Smiraglia, C., and Diotri, F. (2014). A distributed energy-balance melt model of an alpine debris-covered glacier. *Journal of Glaciology* 60, 587–602. doi:10.3189/2014JoG13J148.

Fyffe, C.L., Brock, B.W., Kirkbride, M.P., Mair, D.W.F., Arnold, N.S., Smiraglia, C., Diolaiuti, G., and Diotri, F. (2019). Do debris-covered glaciers demonstrate distinctive hydrological behaviour compared to clean glaciers? *Journal of Hydrology* 570, 584–597. doi:10.1016/j.jhydrol.2018.12.069.

Fyffe, C.L., Brock, B.W., Kirkbride, M.P., Mair, D.W.F., and Diotri, F. (2012). The hydrology of a debris-covered glacier, the Miage Glacier, Italy. in *BHS Eleventh National Symposium, Hydrology for a changing world. British Hydrological Society, Dundee*, 1–5.

Fyffe, C.L., Woodget, A.S., Kirkbride, M.P., Deline, P., Westoby, M.J., and Brock, B.W. (2020). Processes at the margins of supraglacial debris cover: quantifying dirty ice ablation and debris redistribution. *Earth Surface Processes and Landforms* 45, 2272–2290. doi:10.1002/esp.4879.

Gardelle, J., Arnaud, Y., and Berthier, E. (2011). Contrasted evolution of glacial lakes along the Hindu Kush Himalaya mountain range between 1990 and 2009. *Global and Planetary Change* 75, 47–55. doi:10.1016/j.gloplacha.2010.10.003.

Gardelle, J., Berthier, E., and Arnaud, Y. (2012). Slight mass gain of Karakoram glaciers in the early twenty-first century. *Nature Geoscience* 5, 322–325. doi:10.1038/ngeo1450.

Gardelle, J., Berthier, E., Arnaud, Y., and Kaab, A. (2013). Region-wide glacier mass balances over the Pamir-Karakoram-Himalaya during 1999-2011. *The Cryosphere* 7, 1885–1886. doi:10.5194/tc-7-1885-2013.

Giani, G.P., Silvano, S., and Zanon, G. (2001). Avalanche of 18 January 1997 on Brenva glacier, Mont Blanc Group, Western Italian Alps: an unusual process of formation. *Annals of Glaciology* 32, 333–338. doi:10.3189/172756401781819157.

Gibson, M.J., Glasser, N.F., Quincey, D.J., Mayer, C., Rowan, A.V., and Irvine-Fynn, T.D.L. (2017a). Temporal variations in supraglacial debris distribution on Baltoro Glacier, Karakoram between 2001 and 2012. *Geomorphology* 295, 572–585. doi:10.1016/j.geomorph.2017.08.012.

Gibson, M.J., Glasser, N.F., Quincey, D.J., Rowan, A.V., and Irvine-Fynn, T.D. (2017b). Changes in glacier surface cover on Baltoro glacier, Karakoram, north Pakistan, 2001–2012. *Journal of Maps* 13, 100–108. doi:10.1080/17445647.2016.1264319.

Giordan, D., Dematteis, N., Allasia, P., and Motta, E. (2020). Classification and kinematics of the Planpincieux Glacier break-offs using photographic time-lapse analysis. *Journal of Glaciology* 66, 188–202. doi:10.1017/jog.2019.99.

Glasser, N.F., Hambrey, M.J., Etienne, J.L., Jansson, P., and Pettersson, R. (2003). The Origin and Significance of Debris-charged Ridges at the Surface of Storglaciären, Northern Sweden. *Geografiska Annaler: Series A, Physical Geography* 85, 127–147. doi:10.1111/1468-0459.00194.

Glasser, N.F., Holt, T.O., Evans, Z.D., Davies, B.J., Pelto, M., and Harrison, S. (2016). Recent spatial and temporal variations in debris cover on Patagonian glaciers. *Geomorphology* 273, 202–216. doi:10.1016/j.geomorph.2016.07.036.

Glasser, N.F., and Scambos, T.A. (2008). A structural glaciological analysis of the 2002 Larsen B ice-shelf collapse. *Journal of Glaciology* 54, 3–16. doi:10.3189/002214308784409017.

Gobiet, A., Kotlarski, S., Beniston, M., Heinrich, G., Rajczak, J., and Stoffel, M. (2014). 21st century climate change in the European Alps—A review. *Science of The Total Environment* 493, 1138–1151. doi:10.1016/j.scitotenv.2013.07.050.

Goodsell, B., Hambrey, M.J., and Glasser, N.F. (2002). Formation of band ogives and associated structures at Bas Glacier d'Arolla, Valais, Switzerland. *Journal of Glaciology* 48, 287–300. doi:10.3189/172756502781831494.

Goodsell, B., Hambrey, M.J., and Glasser, N.F. (2005a). Debris transport in a temperate valley glacier: Haut Glacier d'Arolla, Valais, Switzerland. *Journal of Glaciology* 51, 139–146. doi:10.3189/172756505781829647.

Goodsell, B., Hambrey, M.J., Glasser, N.F., Nienow, P., and Mair, D. (2005b). The Structural Glaciology of a Temperate Valley Glacier: Haut Glacier d'Arolla, Valais, Switzerland. *Arctic, Antarctic, and Alpine Research* 37, 218–232.

Gulley, J., and Benn, D.I. (2007). Structural control of englacial drainage systems in Himalayan debris-covered glaciers. *Journal of Glaciology* 53, 399–412. doi:10.3189/002214307783258378.

Haeberli, W., Buetler, M., Huggel, C., Friedli, T.L., Schaub, Y., and Schleiss, A.J. (2016). New lakes in deglaciating high-mountain regions – opportunities and risks. *Climatic Change* 139, 201–214. doi:10.1007/s10584-016-1771-5.

Haeberli, W., Kääb, A., Paul, F., Chiarle, M., Mortara, G., Mazza, A., Deline, P., and Richardson, S. (2002). A surge-type movement at Ghiacciaio del Belvedere and a developing slope instability in the east face of Monte Rosa, Macugnaga, Italian Alps. *Norsk Geografisk Tidsskrift - Norwegian Journal of Geography* 56, 104–111. doi:10.1080/002919502760056422.

Hall, D.K., Bayr, K.J., Schöner, W., Bindschadler, R.A., and Chien, J.Y.L. (2003). Consideration of the errors inherent in mapping historical glacier positions in Austria from the ground and space (1893–2001). *Remote Sensing of Environment* 86, 566–577. doi:10.1016/S0034-4257(03)00134-2.

Hambrey, M.J., and Clarke, G.K.C. (2019). Structural Evolution During Cyclic Glacier Surges: 1. Structural Glaciology of Trapridge Glacier, Yukon, Canada. *Journal of Geophysical Research: Earth Surface* 124, 464–494. doi:https://doi.org/10.1029/2018JF004869.

Hambrey, M.J., and Lawson, W. (2000). Structural styles and deformation fields in glaciers: a review. *Geological Society, London, Special Publications* 176, 59–83.

Hambrey, M.J., and Milnes, AG. (1977). Structural Geology of an Alpine Glacier (Griesgletcher, Valais, Switzerland). *Eclogae Geologicae Helvetiae* 70, 667–684.

Hambrey, M.J., Murray, T., Glasser, N.F., Hubbard, A., Hubbard, B., Stuart, G., Hansen, S., and Kohler, J. (2005). Structure and changing dynamics of a polythermal valley glacier on a centennial timescale: Midre Lovénbreen, Svalbard. *Journal of Geophysical Research: Earth Surface* 110. doi:10.1029/2004JF000128.

Hambrey, M.J., Quincey, D.J., Glasser, N.F., Reynolds, J.M., Richardson, S.J., and Clemmens, S. (2008). Sedimentological, geomorphological and dynamic context of debris-mantled glaciers, Mount Everest (Sagarmatha) region, Nepal. *Quaternary Science Reviews* 27, 2361–2389. doi:10.1016/j.quascirev.2008.08.010.

Han, H., Wang, J., Wei, J., and Liu, S. (2010). Backwasting rate on debris-covered Koxkar glacier, Tuomuer mountain, China. *Journal of Glaciology* 56, 287–296. doi:10.3189/002214310791968430.

Haritashya, U.K., Kargel, J.S., Shugar, D.H., Leonard, G.J., Strattman, K., Watson, C.S., Shean, D., Harrison, S., Mandli, K.T., and Regmi, D. (2018). Evolution and controls of large glacial lakes in the Nepal Himalaya. *Remote Sensing* 10. doi:10.3390/rs10050798.

Haritashya, U.K., Pleasants, M.S., and Copland, L. (2015). Assessment of the Evolution in Velocity of Two Debris-Covered Valley Glaciers in Nepal and New Zealand. *Geografiska Annaler: Series A, Physical Geography* 97, 737–751. doi:10.1111/geoa.12112.

Heid, T., and Kääb, A. (2012). Evaluation of existing image matching methods for deriving glacier surface displacements globally from optical satellite imagery. *Remote Sensing of Environment* 118, 339–355. doi:10.1016/j.rse.2011.11.024.

Herbst, P., Neubauer, F., and Schöpfer, M.P. (2006). The development of brittle structures in an alpine valley glacier: Pasterzenkees, Austria, 1887–1997. *Journal of Glaciology* 52, 128–136. doi:10.3189/172756506781828872.

Herreid, S., and Pellicciotti, F. (2020). The state of rock debris covering Earth's glaciers. *Nature Geoscience* 13, 621–627. doi:10.1038/s41561-020-0615-0.

Hersbach, H., Bell, B., Berrisford, P., Biavati, G., Horányi, A., Muñoz Sabater, J., Nicolas, J., Peubey, C., Radu, R., and Rozum, I. (2018). *ERA5 hourly data on single levels from 1979 to present, Copernicus Climate Change Service (C3S) Climate Data Store (CDS)*.

Hewitt, K. (2005). The Karakoram Anomaly? Glacier Expansion and the 'Elevation Effect,' Karakoram Himalaya. *mred* 25, 332–340. doi:10.1659/0276-4741(2005)025[0332:TKAGEA]2.0.CO;2.

Hock, R., Rasul, G., Adler, C., Caceres, B., Gruber, S., Hirabayashi, Y., Jackson, M., Kääb, A., Kang, S., and Kutuzov, S. (2019). *High Mountain Areas: In: IPCC Special Report on the Ocean and Cryosphere in a Changing Climate*.

Howat, I.M., Negrete, A., and Smith, B.E. (2014). The Greenland Ice Mapping Project (GIMP) land classification and surface elevation data sets. *The Cryosphere* 8, 1509–1518. doi:10.5194/tc-8-1509-2014.

Hudleston, P.J., and Hooke, R.LeB. (1980). Cumulative deformation in the barnes ice cap and implications for the development of foliation. *Tectonophysics* 66, 127–146. doi:10.1016/0040-1951(80)90042-6.

Huggel, C., Kääb, A., Haeberli, W., Teysseire, P., and Paul, F. (2002). Remote sensing based assessment of hazards from glacier lake outbursts: a case study in the Swiss Alps. *Canadian Geotechnical Journal* 39, 316–330. doi:10.1139/t01-099.

Huss, M. (2012). Extrapolating glacier mass balance to the mountain-range scale: the European Alps 1900–2100. *The Cryosphere* 6, 713–727. doi:https://doi.org/10.5194/tc-6-713-2012.

Huss, M. (2013). Density assumptions for converting geodetic glacier volume change to mass change. *The Cryosphere* 7, 877–887. doi:10.5194/tc-7-877-2013.

Huss, M., Dhulst, L., and Bauder, A. (2015). New long-term mass-balance series for the Swiss Alps. *Journal of Glaciology* 61, 551–562. doi:10.3189/2015JoG15J015.

Huss, M., and Hock, R. (2018). Global-scale hydrological response to future glacier mass loss. *Nature Climate Change* 8, 135. doi:10.1038/s41558-017-0049-x.

Immerzeel, W.W., Kraaijenbrink, P.D.A., Shea, J.M., Shrestha, A.B., Pellicciotti, F., Bierkens, M.F.P., and de Jong, S.M. (2014). High-resolution monitoring of Himalayan glacier dynamics using unmanned aerial vehicles. *Remote Sensing of Environment* 150, 93–103. doi:10.1016/j.rse.2014.04.025.

Immerzeel, W.W., Lutz, A.F., Andrade, M., Bahl, A., Biemans, H., Bolch, T., Hyde, S., Brumby, S., Davies, B.J., Elmore, A.C., Emmer, A., Feng, M., Fernández, A., Haritashya, U., Kargel, J.S., Koppes, M., Kraaijenbrink, P.D.A., Kulkarni, A.V., Mayewski, P.A., Nepal, S., Pacheco, P., Painter, T.H., Pellicciotti, F., Rajaram, H., Rupper, S., Sinisalo, A., Shrestha, A.B., Viviroli, D., Wada, Y., Xiao, C., Yao, T., and Baillie, J.E.M. (2019). Importance and vulnerability of the world's water towers. *Nature*, 1–6. doi:10.1038/s41586-019-1822-y.

Immerzeel, W.W., Van Beek, L.P., and Bierkens, M.F. (2010). Climate change will affect the Asian water towers. *Science* 328, 1382–1385. doi:10.1126/science.1183188.

Immerzeel, W.W., van Beek, L.P.H., Konz, M., Shrestha, A.B., and Bierkens, M.F.P. (2012). Hydrological response to climate change in a glacierized catchment in the Himalayas. *Climatic Change* 110, 721–736. doi:10.1007/s10584-011-0143-4.

Irvine-Fynn, T.D.L., Porter, P.R., Rowan, A.V., Quincey, D.J., Gibson, M.J., Bridge, J.W., Watson, C.S., Hubbard, A., and Glasser, N.F. (2017). Supraglacial ponds regulate runoff from Himalayan debris-covered glaciers. *Geophysical Research Letters*, 2017GL075398. doi:10.1002/2017GL075398.

Iwata, S., Watanabe, O., and Fushimi, H. (1980). Surface Morphology in the Ablation Area of the Khumbu Glacier. *Journal of the Japanese Society of Snow and Ice* 41, 9–17. doi:10.5331/seppyo.41.Special_9.

Jennings, S.J.A., Hambrey, M.J., Glasser, N.F., James, T.D., and Hubbard, B. (2016). Structural glaciology of Austre Brøggerbreen, northwest Svalbard. *Journal of Maps* 12, 790–796. doi:10.1080/17445647.2015.1076744.

Juen, M., Mayer, C., Lambrecht, A., Han, H., and Liu, S. (2014). Impact of varying debris cover thickness on ablation: a case study for Koxkar Glacier in the Tien Shan. *The Cryosphere* 8, 377–386. doi:10.5194/tc-8-377-2014.

Kääb, A. (2005). Combination of SRTM3 and repeat ASTER data for deriving alpine glacier flow velocities in the Bhutan Himalaya. *Remote Sensing of Environment* 94, 463–474. doi:10.1016/j.rse.2004.11.003.

Kääb, A., Berthier, E., Nuth, C., Gardelle, J., and Arnaud, Y. (2012). Contrasting patterns of early twenty-first-century glacier mass change in the Himalayas. *Nature* 488, 495–498. doi:10.1038/nature11324.

Kääb, A., and Vollmer, M. (2000). Surface Geometry, Thickness Changes and Flow Fields on Creeping Mountain Permafrost: Automatic Extraction by Digital Image Analysis. *Permafrost and Periglacial Processes* 11, 315–326. doi:10.1002/1099-1530(200012)11:4<315::AID-PPP365>3.0.CO;2-J.

Kargel, J.S., Leonard, G.J., Shugar, D.H., Haritashya, U.K., Bevington, A., Fielding, E.J., Fujita, K., Geertsema, M., Miles, E.S., Steiner, J., Anderson, E., Bajracharya, S., Bawden, G.W., Breashears, D.F., Byers, A., Collins, B., Dhital, M.R., Donnellan, A., Evans, T.L., Geai, M.L., Glasscoe, M.T., Green, D., Gurung, D.R., Heijenk, R., Hilborn, A., Hudnut, K., Huyck, C., Immerzeel, W.W., Liming,

J., Jibson, R., Kääb, A., Khanal, N.R., Kirschbaum, D., Kraaijenbrink, P.D.A., Lamsal, D., Shiyin, L., Mingyang, L., McKinney, D., Nahirnick, N.K., Zhuotong, N., Ojha, S., Olsenholler, J., Painter, T.H., Pleasants, M., Pratima, K.C., Yuan, Q.I., Raup, B.H., Regmi, D., Rounce, D.R., Sakai, A., Donghui, S., Shea, J.M., Shrestha, A.B., Shukla, A., Stumm, D., Kooij, M. van der, Voss, K., Xin, W., Weihs, B., Wolfe, D., Lizong, W., Xiaojun, Y., Yoder, M.R., and Young, N. (2016). Geomorphic and geologic controls of geohazards induced by Nepal's 2015 Gorkha earthquake. *Science* 351. doi:10.1126/science.aac8353.

Kattel, D.B., and Yao, T. (2013). Recent temperature trends at mountain stations on the southern slope of the central Himalayas. *J Earth Syst Sci* 122, 215–227. doi:10.1007/s12040-012-0257-8.

Kellerer-Pirklbauer, A., and Kulmer, B. (2019). The evolution of brittle and ductile structures at the surface of a partly debris-covered, rapidly thinning and slowly moving glacier in 1998–2012 (Pasterze Glacier, Austria). *Earth Surface Processes and Landforms* 44, 1034–1049. doi:10.1002/esp.4552.

Kellerer-Pirklbauer, A., Lieb, G.K., Avian, M., and Gspurning, J. (2008). The Response of Partially Debris-Covered Valley Glaciers to Climate Change: The Example of the Pasterze Glacier (austria) in the Period 1964 to 2006. *Geografiska Annaler: Series A, Physical Geography* 90, 269–285. doi:10.1111/j.1468-0459.2008.00345.x.

King, C. a. M., and Lewis, W.V. (1961). A Tentative Theory of Ogive Formation. *Journal of Glaciology* 3, 912–939. doi:10.3189/S0022143000027283.

King, O., Bhattacharya, A., Bhambri, R., and Bolch, T. (2019). Glacial lakes exacerbate Himalayan glacier mass loss. *Scientific Reports* 9, 1–9. doi:10.1038/s41598-019-53733-x.

King, O., Bhattacharya, A., Ghuffar, S., Tait, A., Guilford, S., Elmore, A.C., and Bolch, T. (2020a). Six Decades of Glacier Mass Changes around Mt. Everest Are Revealed by Historical and Contemporary Images. *One Earth* 3, 608–620. doi:10.1016/j.oneear.2020.10.019.

King, O., Dehecq, A., Quincey, D., and Carrivick, J. (2018). Contrasting geometric and dynamic evolution of lake and land-terminating glaciers in the central Himalaya. *Global and Planetary Change* 167, 46–60. doi:10.1016/j.gloplacha.2018.05.006.

King, O., Quincey, D.J., Carrivick, J.L., and Rowan, A.V. (2017). Spatial variability in mass loss of glaciers in the Everest region, central Himalayas, between 2000 and 2015. *The Cryosphere* 11, 407–426. doi:10.5194/tc-11-407-2017.

King, O., Turner, A.G.D., Quincey, D.J., and Carrivick, J.L. (2020b). Morphometric evolution of Everest region debris-covered glaciers. *Geomorphology* 371, 107422. doi:10.1016/j.geomorph.2020.107422.

Kirkbride, M.P. (1993). The temporal significance of transitions from melting to calving termini at glaciers in the central Southern Alps of New Zealand. *The Holocene* 3, 232–240. doi:10.1177/095968369300300305.

Kirkbride, M.P. (2000). Ice marginal geomorphology and Holocene expansion of debris-covered Tasman Glacier, New Zealand. *IAHS PUBLICATION*, 211–218.

Kirkbride, M.P., and Deline, P. (2013). The formation of supraglacial debris covers by primary dispersal from transverse englacial debris bands. *Earth Surface Processes and Landforms* 38, 1779–1792. doi:10.1002/esp.3416.

Kirkbride, M.P., and Dugmore, A.J. (2003). Glaciological response to distal tephra fallout from the 1947 eruption of Hekla, south Iceland. *Journal of Glaciology* 49, 420–428. doi:10.3189/172756503781830575.

Kirkbride, M.P., and Warren, C.R. (1997). Calving processes at a grounded ice cliff. *Annals of Glaciology* 24, 116–121.

Kneib, M., Miles, E.S., Jola, S., Buri, P., Herreid, S., Bhattacharya, A., Watson, C.S., Bolch, T., Quincey, D., and Pellicciotti, F. (2021). Mapping ice cliffs on debris-covered glaciers using multispectral satellite images. *Remote Sensing of Environment*, 112201. doi:10.1016/j.rse.2020.112201.

Kraaijenbrink, P., Meijer, S.W., Shea, J.M., Pellicciotti, F., De Jong, S.M., and Immerzeel, W.W. (2016a). Seasonal surface velocities of a Himalayan glacier derived by automated correlation of unmanned aerial vehicle imagery. *Annals of Glaciology* 57, 103–113. doi:10.3189/2016AoG71A072.

Kraaijenbrink, P.D.A., Shea, J.M., Pellicciotti, F., Jong, S.M. de, and Immerzeel, W.W. (2016b). Object-based analysis of unmanned aerial vehicle imagery to map and characterise surface features on a debris-covered glacier. *Remote Sensing of Environment* 186, 581–595. doi:10.1016/j.rse.2016.09.013.

Lague, D., Brodu, N., and Leroux, J. (2013). Accurate 3D comparison of complex topography with terrestrial laser scanner: Application to the Rangitikei canyon (N-Z). *ISPRS Journal of Photogrammetry and Remote Sensing* 82, 10–26. doi:10.1016/j.isprsjprs.2013.04.009.

Lawson, W.J., Sharp, M.J., and Hambrey, M.J. (1994). The structural geology of a surge-type glacier. *Journal of Structural Geology* 16, 1447–1462. doi:10.1016/0191-8141(94)90008-6.

Leighton, F.B. (1951). Ogives of the East Twin Glacier, Alaska Their Nature and Origin. *The Journal of Geology* 59, 578–589. doi:10.1086/625913.

Linsbauer, A., Frey, H., Haeberli, W., Machguth, H., Azam, M.F., and Allen, S. (2016). Modelling glacier-bed overdeepenings and possible future lakes for the glaciers in the Himalaya—Karakoram region. *Annals of Glaciology* 57, 119–130. doi:10.3189/2016AoG71A627.

Liu, Q., Mayer, C., and Liu, S. (2015). Distribution and interannual variability of supraglacial lakes on debris-covered glaciers in the Khan Tengri-Tumor Mountains, Central Asia. *Environmental Research Letters* 10, 014014. doi:10.1088/1748-9326/10/1/014014.

Lovell, A.M., Carr, J.R., and Stokes, C.R. (2018). Topographic controls on the surging behaviour of Sabche Glacier, Nepal (1967 to 2017). *Remote Sensing of Environment* 210, 434–443. doi:10.1016/j.rse.2018.03.036.

Lovell, A.M., Carr, J.R., and Stokes, C.R. (2019). Spatially Variable Glacier Changes in the Annapurna Conservation Area, Nepal, 2000 to 2016. *Remote Sensing* 11, 1452. doi:10.3390/rs11121452.

Luckman, A., Quincey, D., and Bevan, S. (2007). The potential of satellite radar interferometry and feature tracking for monitoring flow rates of Himalayan glaciers. *Remote Sensing of Environment* 111, 172–181. doi:10.1016/j.rse.2007.05.019.

Magnin, F., Haeberli, W., Linsbauer, A., Deline, P., and Ravanel, L. (2020). Estimating glacier-bed overdeepenings as possible sites of future lakes in the de-glaciating Mont Blanc massif (Western European Alps). *Geomorphology* 350, 106913. doi:10.1016/j.geomorph.2019.106913.

Masetti, M., Diolaiuti, G., D'Agata, C., and Smiraglia, C. (2010). Hydrological Characterization of an Ice-Contact Lake: Miage Lake (Monte Bianco, Italy). *Water Resources Management* 24, 1677–1696. doi:10.1007/s11269-009-9519-x.

Mattson, L.E., Gardner, J.S., and Young, G.J. (1993). "Ablation on debris covered glaciers: an example from the Rakhiot Glacier, Punjab, Himalaya," in *Snow and glacier hydrology*, ed. G. J. Young (Wallingford: IAHS-IASH Publication 218), 289–296.

Mazué, R., Deline, P., and Kirkbride, M.P. (2009). "Suivi de l'évolution de la couverture détritique d'un glacier noir par photo-comparaison: le glacier d'Estelette (Massif du Mont Blanc)," in *Neige et glace de montagne : Reconstitution, dynamique, pratiques* (Collection EDYTEM - Cahiers de Géographie, n°8), 171–178.

McNabb, R., Nuth, C., Kääb, A., and Girod, L. (2019). Sensitivity of glacier volume change estimation to DEM void interpolation. *The Cryosphere* 13, 895–910. doi:https://doi.org/10.5194/tc-13-895-2019.

Mertes, J.R., Thompson, S.S., Booth, A.D., Gulley, J.D., and Benn, D.I. (2017). A conceptual model of supra-glacial lake formation on debris-covered glaciers based on GPR facies analysis. *Earth Surface Processes and Landforms* 42, 903–914. doi:10.1002/esp.4068.

Midgley, N.G., and Tonkin, T.N. (2017). Reconstruction of former glacier surface topography from archive oblique aerial images. *Geomorphology* 282, 18–26. doi:10.1016/j.geomorph.2017.01.008.

Mihalcea, C., Brock, B.W., Diolaiuti, G., D'Agata, C., Citterio, M., Kirkbride, M.P., Cutler, M.E.J., and Smiraglia, C. (2008). Using ASTER satellite and ground-based surface temperature measurements to derive supraglacial debris cover and thickness patterns on Miage Glacier (Mont Blanc Massif, Italy). *Cold Regions Science and Technology* 52, 341–354. doi:10.1016/j.coldregions.2007.03.004.

Mihalcea, C., Brock, B.W., Diolaiuti, G.C., D'Agata, C., Citterio, M., Kirkbride, M.P., Smiraglia, C., and Cutler, M.E.J. (2007). Comparison of ground based and ASTER derived measurements of surface temperature and supraglacial debris thickness on Miage Glacier, Mont Blanc Massif, Italy. in *Geophysical Research Abstracts*, 03765.

Miles, E.S., Pellicciotti, F., Willis, I.C., Steiner, J.F., Buri, P., and Arnold, N.S. (2016). Refined energy-balance modelling of a supraglacial pond, Langtang Khola, Nepal. *Annals of Glaciology* 57, 29. doi:10.3189/2016AoG71A421.

Miles, E.S., Steiner, J., Willis, I., Buri, P., Immerzeel, W.W., Chesnokova, A., and Pellicciotti, F. (2017a). Pond dynamics and supraglacial-englacial connectivity on debris-covered Lirung Glacier, Nepal. *Frontiers in Earth Science* 5, 69. doi:10.3389/feart.2017.00069.

Miles, E.S., Willis, I., Buri, P., Steiner, J.F., Arnold, N.S., and Pellicciotti, F. (2018). Surface Pond Energy Absorption Across Four Himalayan Glaciers Accounts for 1/8 of Total Catchment Ice Loss. *Geophysical Research Letters* 0. doi:10.1029/2018GL079678.

Miles, E.S., Willis, I.C., Arnold, N.S., Steiner, J.F., and Pellicciotti, F. (2017b). Spatial, seasonal and interannual variability of supraglacial ponds in the Langtang Valley of Nepal, 1999–2013. *Journal of Glaciology* 63, 88–105. doi:10.1017/jog.2016.120.

Miles, K.E., Hubbard, B., Irvine-Fynn, T.D.L., Miles, E.S., Quincey, D.J., and Rowan, A.V. (2020). Hydrology of debris-covered glaciers in High Mountain Asia. *Earth-Science Reviews* 207, 103212. doi:10.1016/j.earscirev.2020.103212.

Mölg, N., Bolch, T., Rastner, P., Strozzi, T., and Paul, F. (2018). A consistent glacier inventory for Karakoram and Pamir derived from Landsat data: distribution of debris cover and mapping challenges. *Earth System Science Data* 10, 1807–1827. doi:10.5194/essd-10-1807-2018.

Mölg, N., Bolch, T., Walter, A., and Vieli, A. (2019). Unravelling the evolution of Zmuttgletscher and its debris cover since the end of the Little Ice Age. *The Cryosphere* 13, 1889–1909. doi:10.5194/tc-13-1889-2019.

Mölg, N., Ferguson, J., Bolch, T., and Vieli, A. (2020). On the influence of debris cover on glacier morphology: How high-relief structures evolve from smooth surfaces. *Geomorphology* 357, 107092. doi:10.1016/j.geomorph.2020.107092.

Mölg, T., Maussion, F., and Scherer, D. (2014). Mid-latitude westerlies as a driver of glacier variability in monsoonal High Asia. *Nature Climate Change* 4, 68–73. doi:10.1038/nclimate2055.

Mool, P.K., Bajracharya, S.R., and Joshi, S. (2001). Inventory of Glaciers, Glacial Lakes and Glacial Lake Outburst Floods: Monitoring and Early Warning Systems in the Hindu Kush-Himalayan Region - Nepal - HIMALDOC. Available at: http://lib.icimod.org/record/7511.

Mool, P.K., Maskey, P.R., Koirala, A., Joshi, S.P., Lizong, W., Shrestha, A.B., Eriksson, M., Gurung, S., Pokharel, B., Khanal, N.R., Panthi, S., Adhikari, T., Kayastha, K.B., Ghimire, P., Thapa, R., Shrestha, B., Shrestha, S., and Shrestha, R.B. (2011). Glacial Lakes and Glacial Lake Outburst Fllods in Nepal, International Centre for Integrated Mountain Development, Kathmandu, Nepal. Available at: http://www.icimod.org/dvds/201104_GLOF/reports/final_report.pdf.

Mukherjee, K., Bhattacharya, A., Pieczonka, T., Ghosh, S., and Bolch, T. (2018). Glacier mass budget and climate reanalysis data indicate a climatic shift around 2000 in Lahaul-Spiti, western Himalaya. *Climatic Change* 148, 219–233. doi:10.1007/s10584-018-2185-3.

Murray, T., Strozzi, T., Luckman, A., Jiskoot, H., and Christakos, P. (2003). Is there a single surge mechanism? Contrasts in dynamics between glacier surges in Svalbard and other regions. *Journal of Geophysical Research: Solid Earth* 108. doi:10.1029/2002JB001906.

Nakawo, M., and Rana, B. (1999). Estimate of Ablation Rate of Glacier Ice under a Supraglacial Debris Layer. *Geografiska Annaler: Series A, Physical Geography* 81, 695–701. doi:10.1111/1468-0459.00097.

Nakawo, M., Yabuki, H., and Sakai, A. (1999). Characteristics of Khumbu Glacier, Nepal Himalaya: recent change in the debris-covered area. *Annals of Glaciology* 28, 118–122. doi:10.3189/172756499781821788.

Narama, C., Daiyrov, M., Tadono, T., Yamamoto, M., Kääb, A., Morita, R., and Ukita, J. (2017). Seasonal drainage of supraglacial lakes on debris-covered glaciers in the Tien Shan Mountains, Central Asia. *Geomorphology* 286, 133–142. doi:10.1016/j.geomorph.2017.03.002.

Neckel, N., Loibl, D., and Rankl, M. (2017). Recent slowdown and thinning of debris-covered glaciers in south-eastern Tibet. *Earth and Planetary Science Letters* 464, 95–102. doi:10.1016/j.epsl.2017.02.008.

Nicholson, L., and Benn, D.I. (2006). Calculating ice melt beneath a debris layer using meteorological data. *Journal of Glaciology* 52, 463–470. doi:10.3189/172756506781828584.

Nie, Y., Liu, Q., and Liu, S. (2013). Glacial Lake Expansion in the Central Himalayas by Landsat Images, 1990–2010. *PLOS ONE* 8, e83973. doi:10.1371/journal.pone.0083973.

Nie, Y., Sheng, Y., Liu, Q., Liu, L., Liu, S., Zhang, Y., and Song, C. (2017). A regional-scale assessment of Himalayan glacial lake changes using satellite observations from 1990 to 2015. *Remote Sensing of Environment* 189, 1–13. doi:10.1016/j.rse.2016.11.008.

Nuimura, T., Fujita, K., Yamaguchi, S., and Sharma, R.R. (2012). Elevation changes of glaciers revealed by multitemporal digital elevation models calibrated by GPS survey in the Khumbu region, Nepal Himalaya, 1992–2008. *Journal of Glaciology* 58, 648–656. doi:10.3189/2012JoG11J061.

Nuth, C., and Kääb, A. (2011). Co-registration and bias corrections of satellite elevation data sets for quantifying glacier thickness change. *The Cryosphere* 5, 271. doi:10.5194/tc-5-271-2011.

Nye, J.F. (1952). The Mechanics of Glacier Flow. *Journal of Glaciology* 2, 82–93. doi:10.3189/S0022143000033967.

Nye, J.F. (1958). A theory of wave formation in glaciers. *International Association of Hydrological Sciences* 47, 139–154.

Østrem, G. (1959). Ice melting under a thin layer of moraine, and the existence of ice cores in moraine ridges. *Geografiska Annaler* 41, 228–230. doi:10.1080/20014422.1959.11907953.

Pachauri, R.K., Allen, M.R., Barros, V.R., Broome, J., Cramer, W., Christ, R., Church, J.A., Clarke, L., Dahe, Q., Dasgupta, P., Dubash, N.K., Edenhofer, O., Elgizouli, I., Field, C.B., Forster, P., Friedlingstein, P., Fuglestvedt, J., Gomez-Echeverri, L., Hallegatte, S., Hegerl, G., Howden, M., Jiang, K., Jimenez Cisneroz, B., Kattsov, V., Lee, H., Mach, K.J., Marotzke, J., Mastrandrea, M.D., Meyer, L., Minx, J., Mulugetta, Y., O'Brien, K., Oppenheimer, M., Pereira, J.J., Pichs-Madruga, R., Plattner, G.-K., Pörtner, H.-O., Power, S.B., Preston, B., Ravindranath, N.H., Reisinger, A., Riahi, K., Rusticucci, M., Scholes, R., Seyboth, K., Sokona, Y., Stavins, R., Stocker, T.F., Tschakert, P., van Vuuren, D., and van Ypserle, J.-P. (2014). *Climate Change 2014: Synthesis Report. Contribution of Working Groups I, II and III to the Fifth Assessment Report of the Intergovernmental Panel on Climate Change*. , eds. R. K. Pachauri and L. Meyer Geneva, Switzerland: IPCC Available at: https://epic.awi.de/id/eprint/37530/.

Panthi, J., Dahal, P., Shrestha, M.L., Aryal, S., Krakauer, N.Y., Pradhanang, S.M., Lakhankar, T., Jha, A.K., Sharma, M., and Karki, R. (2015). Spatial and Temporal Variability of Rainfall in the Gandaki River Basin of Nepal Himalaya. *Climate* 3, 210–226. doi:10.3390/cli3010210.

Paul, F., Barrand, N.E., Baumann, S., Berthier, E., Bolch, T., Casey, K., Frey, H., Joshi, S.P., Konovalov, V., Bris, R.L., Mölg, N., Nosenko, G., Nuth, C., Pope, A., Racoviteanu, A., Rastner, P., Raup, B., Scharrer, K., Steffen, S., and Winsvold, S. (2013). On the accuracy of glacier outlines derived from remote-sensing data. *Annals of Glaciology* 54, 171–182. doi:10.3189/2013AoG63A296.

Paul, F., Bolch, T., Briggs, K., Kääb, A., McMillan, M., McNabb, R., Nagler, T., Nuth, C., Rastner, P., Strozzi, T., and Wuite, J. (2017). Error sources and guidelines for quality assessment of glacier area, elevation change, and velocity products derived from satellite data in the Glaciers_cci project. *Remote Sensing of Environment* 203, 256–275. doi:10.1016/j.rse.2017.08.038.

Paul, F., Frey, H., and Bris, R.L. (2011). A new glacier inventory for the European Alps from Landsat TM scenes of 2003: challenges and results. *Annals of Glaciology* 52, 144–152. doi:10.3189/172756411799096295.

Paul, F., Kääb, A., and Haeberli, W. (2007). Recent glacier changes in the Alps observed by satellite: Consequences for future monitoring strategies. *Global and Planetary Change* 56, 111–122. doi:10.1016/j.gloplacha.2006.07.007.

Pellicciotti, F., Stephan, C., Miles, E., Herreid, S., Immerzeel, W.W., and Bolch, T. (2015). Mass-balance changes of the debris-covered glaciers in the Langtang Himal, Nepal, from 1974 to 1999. *Journal of Glaciology* 61, 373–386. doi:10.3189/2015JoG13J237.

Pfeffer, W.T., Arendt, A.A., Bliss, A., Bolch, T., Cogley, J.G., Gardner, A.S., Hagen, J.-O., Hock, R., Kaser, G., Kienholz, C., Miles, E.S., Moholdt, G., Mölg, N., Paul, F., Radić, V., Rastner, P., Raup, B.H., Rich, J., and Sharp, M.J. (2014). The Randolph Glacier Inventory: a globally complete inventory of glaciers. *Journal of Glaciology* 60, 537–552. doi:10.3189/2014JoG13J176.

Phillips, E., Everest, J., Evans, D.J.A., Finlayson, A., Ewertowski, M., Guild, A., and Jones, L. (2017). Concentrated, 'pulsed' axial glacier flow: structural glaciological evidence from Kvíárjökull in SE Iceland. *Earth Surface Processes and Landforms* 42, 1901–1922. doi:10.1002/esp.4145.

Purdie, H., Bealing, P., Tidey, E., Gomez, C., and Harrison, J. (2016). Bathymetric evolution of Tasman Glacier terminal lake, New Zealand, as determined by remote surveying techniques. *Global and Planetary Change* 147, 1–11. doi:10.1016/j.gloplacha.2016.10.010.

Qiu, J. (2008). China: The third pole. *Nature*. doi:10.1038/454393a.

Quincey, D.J., Luckman, A., and Benn, D. (2009). Quantification of Everest region glacier velocities between 1992 and 2002, using satellite radar interferometry and feature tracking. *Journal of Glaciology* 55, 596–606. doi:10.3189/002214309789470987.

Quincey, D.J., Richardson, S.D., Luckman, A., Lucas, R.M., Reynolds, J.M., Hambrey, M.J., and Glasser, N.F. (2007). Early recognition of glacial lake hazards in the Himalaya using remote sensing datasets. *Global and Planetary Change* 56, 137–152. doi:10.1016/j.gloplacha.2006.07.013.

Rabatel, A., Dedieu, J.P., and Vincent, C. (2016). Spatio-temporal changes in glacier-wide mass balance quantified by optical remote sensing on 30 glaciers in the French Alps for the period 1983–2014. *Journal of Glaciology* 62, 1153–1166. doi:10.1017/jog.2016.113.

Radić, V., Bliss, A., Beedlow, A.C., Hock, R., Miles, E., and Cogley, J.G. (2014). Regional and global projections of twenty-first century glacier mass changes in response to climate scenarios from global climate models. *Climate Dynamics* 42, 37–58. doi:10.1007/s00382-013-1719-7.

Ragettli, S., Bolch, T., and Pellicciotti, F. (2016). Heterogeneous glacier thinning patterns over the last 40 years in Langtang Himal, Nepal. *Cryosphere* 10, 2075–2097. doi:10.5194/tc-10-2075-2016.

Ragettli, S., Pellicciotti, F., Immerzeel, W.W., Miles, E.S., Petersen, L., Heynen, M., Shea, J.M., Stumm, D., Joshi, S., and Shrestha, A. (2015). Unraveling the hydrology of a Himalayan catchment through integration of high resolution in situ data and remote sensing with an advanced simulation model. *Advances in Water Resources* 78, 94–111. doi:10.1016/j.advwatres.2015.01.013.

Rana, G. (2003). The International Centre for Integrated Mountain Development (ICIMOD). *mred* 23, 288–289. doi:10.1659/0276-4741(2003)023[0288:TICFIM]2.0.CO;2.

Ravanel, L., Magnin, F., and Deline, P. (2017). Impacts of the 2003 and 2015 summer heatwaves on permafrost-affected rock-walls in the Mont Blanc massif. *Science of The Total Environment* 609, 132–143. doi:10.1016/j.scitotenv.2017.07.055.

Reid, T.D., and Brock, B.W. (2010). An energy-balance model for debris-covered glaciers including heat conduction through the debris layer. *Journal of Glaciology* 56, 903–916. doi:10.3189/002214310794457218.

Reid, T.D., and Brock, B.W. (2014). Assessing ice-cliff backwasting and its contribution to total ablation of debris-covered Miage glacier, Mont Blanc massif, Italy. *Journal of Glaciology* 60, 3–13. doi:10.3189/2014JoG13J045.

Reynolds, J.M. (1992). "The identification and mitigation of glacier-related hazards: examples from the Cordillera Blanca, Peru," in *Geohazards* AGID Report Series., eds. G. J. H. McCall, D. J. C. Laming, and S. C. Scott (Springer Netherlands), 143–157. doi:10.1007/978-94-009-0381-4_13.

Reynolds, J.M. (1998). Managing the risks of glacial flooding at hydro plants. *Hydro Review Worldwide* 6, 18–22.

Reynolds, J.M. (2000). On the formation of supraglacial lakes on debris-covered glaciers. *IAHS publication*, 153–164.

RGI Consortium (2017). Randolph Glacier Inventory - A Datatset of Global Glacier Outlines: Version 6.0: Technical Report, Global Land Ice Measurements from Space, Colarado, USA. Digital Media. doi:10.7265/N5-RGI-60.

Richardson, S.D., and Reynolds, J.M. (2000). An overview of glacial hazards in the Himalayas. *Quaternary International* 65–66, 31–47. doi:10.1016/S1040-6182(99)00035-X.

Roberson, S. (2008). Structural composition and sediment transfer in a composite cirque glacier: Glacier de St. Sorlin, France. *Earth Surface Processes and Landforms* 33, 1931–1947. doi:10.1002/esp.1635.

Robson, B.A., Nuth, C., Dahl, S.O., Hölbling, D., Strozzi, T., and Nielsen, P.R. (2015). Automated classification of debris-covered glaciers combining optical, SAR and topographic data in an object-based environment. *Remote Sensing of Environment* 170, 372–387. doi:10.1016/j.rse.2015.10.001.

Robson, B.A., Nuth, C., Nielsen, P.R., Girod, L., Hendrickx, M., and Dahl, S.O. (2018). Spatial Variability in Patterns of Glacier Change across the Manaslu Range, Central Himalaya. *Frontiers in Earth Science* 6. doi:10.3389/feart.2018.00012.

Röhl, K. (2006). Thermo-erosional notch development at fresh-water-calving Tasman Glacier, New Zealand. *Journal of Glaciology* 52, 203–213. doi:10.3189/172756506781828773.

Röhl, K. (2008). Characteristics and evolution of supraglacial ponds on debris-covered Tasman Glacier, New Zealand. *Journal of Glaciology* 54, 867–880. doi:10.3189/002214308787779861.

Rounce, D.R., Quincey, D.J., and McKinney, D.C. (2015). Debris-covered glacier energy balance model for Imja–Lhotse Shar Glacier in the Everest region of Nepal. *The Cryosphere* 9, 2295–2310. doi:10.5194/tc-9-2295-2015.

Rowan, A.V. (2017). The 'Little Ice Age' in the Himalaya: A review of glacier advance driven by Northern Hemisphere temperature change. *The Holocene* 27, 292–308. doi:10.1177/0959683616658530.

Rowan, A.V., Egholm, D.L., Quincey, D.J., and Glasser, N.F. (2015). Modelling the feedbacks between mass balance, ice flow and debris transport to predict the response to climate change of debris-covered glaciers in the Himalaya. *Earth and Planetary Science Letters* 430, 427–438. doi:10.1016/j.epsl.2015.09.004.

Rowan, A.V., Nicholson, L.I., Quincey, D.J., Gibson, M.J., Irvine-Fynn, T.D.L., Watson, C.S., Wagnon, P., Rounce, D.R., Thompson, S.S., Porter, P.R., and Glasser, N.F. (2021). Seasonally stable

temperature gradients through supraglacial debris in the Everest region of Nepal, Central Himalaya. *Journal of Glaciology* 67, 170–181. doi:10.1017/jog.2020.100.

Sakai, A., and Fujita, K. (2010). Formation conditions of supraglacial lakes on debris-covered glaciers in the Himalaya. *Journal of Glaciology*, 177–181.

Sakai, A., Fujita, K., and Yamada, T. (2003). Volume change of Imja Glacial Lake in the Nepal Himalayas. *Disaster Mitigation and Water Management, ISDB.*

Sakai, A., Nakawo, M., and Fujita, K. (1998). Melt rate of ice cliffs on the Lirung Glacier, Nepal Himalayas, 1996. *Bulletin of Glacier Research* 16, 57–66.

Sakai, A., Nakawo, M., and Fujita, K. (2002). Distribution Characteristics and Energy Balance of Ice Cliffs on Debris-Covered Glaciers, Nepal Himalaya. *Arctic, Antarctic, and Alpine Research* 34, 12–19. doi:10.2307/1552503.

Sakai, A., Nishimura, K., Kadota, T., and Takeuchi, N. (2009). Onset of calving at supraglacial lakes on debris-covered glaciers of the Nepal Himalaya. *Journal of Glaciology* 55, 909–917.

Sakai, A., Takeuchi, N., Fujita, K., and Nakawo, M. (2000). Role of supraglacial ponds in the ablation process of a debris-covered glacier in the Nepal Himalayas. *IAHS PUBLICATION*, 119–132.

Salerno, F., Gambelli, S., Viviano, G., Thakuri, S., Guyennon, N., D'Agata, C., Diolaiuti, G., Smiraglia, C., Stefani, F., Bocchiola, D., and Tartari, G. (2014). High alpine ponds shift upwards as average temperatures increase: A case study of the Ortles–Cevedale mountain group (Southern Alps, Italy) over the last 50years. *Global and Planetary Change* 120, 81–91. doi:10.1016/j.gloplacha.2014.06.003.

Salerno, F., Thakuri, S., Tartari, G., Nuimura, T., Sunako, S., Sakai, A., and Fujita, K. (2017). Debris-covered glacier anomaly? Morphological factors controlling changes in the mass balance, surface area, terminus position, and snow line altitude of Himalayan glaciers. *Earth and Planetary Science Letters* 471, 19–31. doi:10.1016/j.epsl.2017.04.039.

Sam, L., Bhardwaj, A., Singh, S., and Kumar, R. (2016). Remote sensing flow velocity of debris-covered glaciers using Landsat 8 data. *Progress in Physical Geography* 40, 305–321. doi:10.1177/0309133315593894.

Scherler, D., Bookhagen, B., and Strecker, M.R. (2011). Spatially variable response of Himalayan glaciers to climate change affected by debris cover. *Nature Geoscience* 4, 156–159. doi:10.1038/ngeo1068.

Scherler, D., Wulf, H., and Gorelick, N. (2018). Global Assessment of Supraglacial Debris-Cover Extents. *Geophysical Research Letters* 45, 11,798-11,805. doi:10.1029/2018GL080158.

Senese, A., Diolaiuti, G., Mihalcea, C., and Smiraglia, C. (2012). Energy and Mass Balance of Forni Glacier (Stelvio National Park, Italian Alps) from a Four-Year Meteorological Data Record. *Arctic, Antarctic, and Alpine Research* 44, 122–134. doi:10.1657/1938-4246-44.1.122.

Sevestre, H., and Benn, D.I. (2015). Climatic and geometric controls on the global distribution of surge-type glaciers: Implications for a unifying model of surging. *Journal of Glaciology* 61, 646–662. doi:10.3189/2015JoG14J136.

Sharp, M. (1988). Surging glaciers: behaviour and mechanisms. *Progress in Physical Geography: Earth and Environment* 12, 349–370. doi:10.1177/030913338801200302.

Shaw, T.E., Brock, B.W., Fyffe, C.L., Pellicciotti, F., Rutter, N., and Diotri, F. (2016). Air temperature distribution and energy-balance modelling of a debris-covered glacier. *Journal of Glaciology* 62, 185–198. doi:10.1017//jog.2016.31.

Shea, J.M., Immerzeel, W.W., Wagnon, P., Vincent, C., and Bajracharya, S. (2015). Modelling glacier change in the Everest region, Nepal Himalaya. *The Cryosphere* 9, 1105–1128. doi:10.5194/tc-9-1105-2015.

Shean, D. (2017). High Mountain Asia 8-meter DEMs Derived from Along-track Optical Imagery, Version 1. doi:10.5067/GSACB044M4PK.

Shean, D.E., Bhushan, S., Montesano, P., Rounce, D.R., Arendt, A., and Osmanoglu, B. (2020). A Systematic, Regional Assessment of High Mountain Asia Glacier Mass Balance. *Frontiers in Earth Science* 7. doi:10.3389/feart.2019.00363.

Sherwood, S., Webb, M.J., Annan, J.D., Armour, K.C., Forster, P.M., Hargreaves, J.C., Hegerl, G., Klein, S.A., Marvel, K.D., Rohling, E.J., Watanabe, M., Andrews, T., Braconnot, P., Bretherton, C.S., Foster, G.L., Hausfather, Z., Heydt, A.S. von der, Knutti, R., Mauritsen, T., Norris, J.R., Proistosescu, C., Rugenstein, M., Schmidt, G.A., Tokarska, K.B., and Zelinka, M.D. (2020). An assessment of Earth's climate sensitivity using multiple lines of evidence. *Reviews of Geophysics* 58. doi:10.1029/2019RG000678.

Shugar, D.H., Burr, A., Haritashya, U.K., Kargel, J.S., Watson, C.S., Kennedy, M.C., Bevington, A.R., Betts, R.A., Harrison, S., and Strattman, K. (2020). Rapid worldwide growth of glacial lakes since 1990. *Nature Climate Change*, 1–7. doi:10.1038/s41558-020-0855-4.

Shukla, A., and Garg, P.K. (2019). Evolution of a debris-covered glacier in the western Himalaya during the last four decades (1971–2016): A multiparametric assessment using remote sensing and field observations. *Geomorphology* 341, 1–14. doi:10.1016/j.geomorph.2019.05.009.

Shukla, A., Garg, P.K., and Srivastava, S. (2018). Evolution of Glacial and High-Altitude Lakes in the Sikkim, Eastern Himalaya Over the Past Four Decades (1975–2017). *Frontiers in Environmental Science* 6. doi:10.3389/fenvs.2018.00081.

Silverio, W., and Jaquet, J.-M. (2005). Glacial cover mapping (1987–1996) of the Cordillera Blanca (Peru) using satellite imagery. *Remote Sensing of Environment* 95, 342–350. doi:10.1016/j.rse.2004.12.012.

Smiraglia, C., Diolaiuti, G., Casati, D., and Kirkbride, M.P. (2000). Recent areal and altimetric variations of Miage Glacier (Monte Bianco massif, Italian Alps). *IAHS PUBLICATION 264*, 227–233.

Smith, W.D., Dunning, S.A., Brough, S., Ross, N., and Telling, J. (2020). GERALDINE (Google Earth Engine supRaglAciaL Debris INput dEtector): a new tool for identifying and monitoring supraglacial landslide inputs. *Earth Surface Dynamics* 8, 1053–1065. doi:https://doi.org/10.5194/esurf-8-1053-2020.

Song, C., Sheng, Y., Wang, J., Ke, L., Madson, A., and Nie, Y. (2017). Heterogeneous glacial lake changes and links of lake expansions to the rapid thinning of adjacent glacier termini in the Himalayas. *Geomorphology* 280, 30–38. doi:10.1016/j.geomorph.2016.12.002.

Stefaniak, A.M., Robson, B.A., Cook, S.J., Clutterbuck, B., Midgley, N.G., and Labadz, J.C. (2021). Mass balance and surface evolution of the debris-covered Miage Glacier, 1990–2018. *Geomorphology* 373, 107474. doi:10.1016/j.geomorph.2020.107474.

Steiner, J.F., Buri, P., Miles, E.S., Ragettli, S., and Pellicciotti, F. (2019). Supraglacial ice cliffs and ponds on debris-covered glaciers: spatio-temporal distribution and characteristics. *Journal of Glaciology*, 1–16. doi:10.1017/jog.2019.40.

Steiner, J.F., Pellicciotti, F., Buri, P., Miles, E.S., Immerzeel, W.W., and Reid, T.D. (2015). Modelling ice-cliff backwasting on a debris-covered glacier in the Nepalese Himalaya. *Journal of Glaciology* 61, 889–907. doi:10.3189/2015JoG14J194.

Stewart, R.L., Westoby, M., Pellicciotti, F., Rowan, A., Swift, D., Brock, B., and Woodward, J. (2021). Using climate reanalysis data in conjunction with multi-temporal satellite thermal imagery to derive supraglacial debris thickness changes from energy-balance modelling. *Journal of Glaciology*, 1–19. doi:10.1017/jog.2020.111.

Stokes, C.R., Popovnin, V., Aleynikov, A., Gurney, S.D., and Shahgedanova, M. (2007). Recent glacier retreat in the Caucasus Mountains, Russia, and associated increase in supraglacial debris cover and supra-/proglacial lake development. *Annals of Glaciology* 46, 195–203. doi:10.3189/172756407782871468.

Strozzi, T., Wiesmann, A., Kääb, A., Joshi, S., Mool, P., and Mergili, M. (2012). Glacial lake mapping with very high resolution satellite SAR data. *Natural Hazards & Earth System Sciences* 12.

Thakuri, S., Salerno, F., Smiraglia, C., Bolch, T., D'Agata, C., Viviano, G., and Tartari, G. (2014). Tracing glacier changes since the 1960s on the south slope of Mt. Everest (central Southern Himalaya) using optical satellite imagery. *The Cryosphere* 8, 1297–1315. doi:10.5194/tc-8-1297-2014.

Thompson, S., Benn, D.I., Mertes, J., and Luckman, A. (2016). Stagnation and mass loss on a Himalayan debris-covered glacier: processes, patterns and rates. *Journal of Glaciology* 62, 467–485. doi:10.1017/jog.2016.37.

Thompson, S.S., Benn, D.I., Dennis, K., and Luckman, A. (2012). A rapidly growing moraine-dammed glacial lake on Ngozumpa Glacier, Nepal. *Geomorphology* 145–146, 1–11. doi:10.1016/j.geomorph.2011.08.015.

Thomson, M.H., Kirkbride, M.P., and Brock, B.W. (2000). Twentieth century surface elevation change of the Miage Glacier, Italian Alps. *IAHS PUBLICATION 264*, 219–226.

Tinti, S., Maramai, A., and Cerutti, A.V. (1999). The Miage Glacier in the Valley of Aosta (Western Alps, Italy) and the extraordinary detachment which occurred on August 9, 1996. *Physics and Chemistry of the Earth, Part A: Solid Earth and Geodesy* 24, 157–161. doi:10.1016/S1464-1895(99)00012-5.

Tonkin, T.N., and Midgley, N.G. (2016). Ground-Control Networks for Image Based Surface Reconstruction: An Investigation of Optimum Survey Designs Using UAV Derived Imagery and Structure-from-Motion Photogrammetry. *Remote Sensing* 8, 786. doi:10.3390/rs8090786.

van Woerkom, T., Steiner, J.F., Kraaijenbrink, P.D.A., Miles, E.S., and Immerzeel, W.W. (2019). Sediment supply from lateral moraines to a debris-covered glacier in the Himalaya. *Earth Surface Dynamics* 7, 411–427. doi:10.5194/esurf-7-411-2019.

Vaughan, D.G., Comiso, J.C., Allison, I., Carrasco, J., Kaser, G., Kwok, R., Mote, P., Murray, T., Paul, F., and Ren, J. (2013). "Observations: Cryosphere," in *Climate change 2013: The Physical Science Basis. Contribution of Working Group I to the Fifth Assessment Report on the Intergovenmental Panel on Climate Change. [Stocker, T.F., D. Qin, G.-K. Plattner, M. Tignor, S.K. Allen, J. Boschung, A. Nauels, Y. Xia, V. Bex and P.M. Midgley (eds.)]* (Cambridge, United Kingdom and New York, NY, USA: Cambridge University Press), 317–382. Available at: doi:10.1017/CBO9781107415324.012.

Viani, C., Machguth, H., Huggel, C., Godio, A., Franco, D., Perotti, L., and Giardino, M. (2020). Potential future lakes from continued glacier shrinkage in the Aosta Valley Region (Western Alps, Italy). *Geomorphology* 355, 107068. doi:10.1016/j.geomorph.2020.107068.

Vincent, C., Dumont, M., Six, D., Brun, F., Picard, G., and Arnaud, L. (2018). Why do the dark and light ogives of Forbes bands have similar surface mass balances? *Journal of Glaciology* 64, 236–246. doi:10.1017/jog.2018.12.

Vincent, C., Fischer, A., Mayer, C., Bauder, A., Galos, S.P., Funk, M., Thibert, E., Six, D., Braun, L., and Huss, M. (2017). Common climatic signal from glaciers in the European Alps over the last 50 years. *Geophysical Research Letters* 44, 1376–1383. doi:10.1002/2016GL072094.

Vincent, C., Garambois, S., Thibert, E., Lefèbvre, E., Le Meur, and Six, D. (2010). Origin of the outburst flood from Glacier de Tête Rousse in 1892 (Mont Blanc area, France). *Journal of Glaciology* 56, 688–698. doi:10.3189/002214310793146188.

Vincent, C., Soruco, A., Six, D., and Meur, E.L. (2009). Glacier thickening and decay analysis from 50 years of glaciological observations performed on Glacier d'Argentière, Mont Blanc area, France. *Annals of Glaciology* 50, 73–79. doi:10.3189/172756409787769500.

Vincent, C., Wagnon, P., Shea, J.M., Immerzeel, W.W., Kraaijenbrink, P., Shrestha, D., Soruco, A., Arnaud, Y., Brun, F., Berthier, E., and Sherpa, S.F. (2016). Reduced melt on debris-covered glaciers: investigations from Changri Nup Glacier, Nepal. *The Cryosphere* 10, 1845–1858. doi:10.5194/tc-10-1845-2016.

Watanabe, T., Ives, J.D., and Hammond, J.E. (1994). Rapid Growth of a Glacial Lake in Khumbu Himal, Himalaya: Prospects for a Catastrophic Flood. *Mountain Research and Development* 14, 329–340. doi:10.2307/3673729.

Watson, C.S., King, O., Miles, E.S., and Quincey, D.J. (2018a). Optimising NDWI supraglacial pond classification on Himalayan debris-covered glaciers. *Remote Sensing of Environment* 217, 414–425. doi:10.1016/j.rse.2018.08.020.

Watson, C.S., Quincey, D.J., Carrivick, J.L., and Smith, M.W. (2016). The dynamics of supraglacial ponds in the Everest region, central Himalaya. *Global and Planetary Change* 142, 14–27. doi:10.1016/j.gloplacha.2016.04.008.

Watson, C.S., Quincey, D.J., Carrivick, J.L., and Smith, M.W. (2017a). Ice cliff dynamics in the Everest region of the Central Himalaya. *Geomorphology* 278, 238–251. doi:10.1016/j.geomorph.2016.11.017.

Watson, C.S., Quincey, D.J., Carrivick, J.L., Smith, M.W., Rowan, A.V., and Richardson, R. (2018b). Heterogeneous water storage and thermal regime of supraglacial ponds on debris-covered glaciers. *Earth Surface Processes and Landforms* 43, 229–241. doi:10.1002/esp.4236.

Watson, C.S., Quincey, D.J., Smith, M.W., Carrivick, J.L., Rowan, A.V., and James, M.R. (2017b). Quantifying ice cliff evolution with multi-temporal point clouds on the debris-covered Khumbu Glacier, Nepal. *Journal of Glaciology* 63, 823–837. doi:10.1017/jog.2017.47.

Westoby, M.J., Brasington, J., Glasser, N.F., Hambrey, M.J., and Reynolds, J.M. (2012). 'Structure-from-Motion' photogrammetry: A low-cost, effective tool for geoscience applications. *Geomorphology* 179, 300–314. doi:10.1016/j.geomorph.2012.08.021.

Westoby, M.J., Dunning, S.A., Woodward, J., Hein, A.S., Marrero, S.M., Winter, K., and Sugden, D.E. (2016). Interannual surface evolution of an Antarctic blue-ice moraine using multi-temporal DEMs. *Earth Surface Dynamics* 4, 515–529. doi:10.5194/esurf-4-515-2016.

Westoby, M.J., Glasser, N.F., Hambrey, M.J., Brasington, J., Reynolds, J.M., and Hassan, M.A.A.M. (2014). Reconstructing historic Glacial Lake Outburst Floods through numerical modelling and geomorphological assessment: Extreme events in the Himalaya. *Earth Surface Processes and Landforms* 39, 1675–1692. doi:10.1002/esp.3617.

Westoby, M.J., Rounce, D.R., Shaw, T.E., Fyffe, C.L., Moore, P.L., Stewart, R.L., and Brock, B.W. (2020). Geomorphological evolution of a debris-covered glacier surface. *Earth Surface Processes and Landforms* 45, 3431–3448. doi:10.1002/esp.4973.

WGMS (2019). *Fluctuations of Glaciers Database*. World Glacier Monitoring Service, Zurich, Switzerland Available at: doi.org/10.5904/wgms-fog-2018-11.

Wood, L.R., Neumann, K., Nicholson, K.N., Bird, B.W., Dowling, C.B., and Sharma, S. (2020). Melting Himalayan Glaciers Threaten Domestic Water Resources in the Mount Everest Region, Nepal. *Frontiers in Earth Science* 8. doi:10.3389/feart.2020.00128.

Woodward, J., Murray, T., and McCaig, A. (2002). Formation and reorientation of structure in the surge-type glacier Kongsvegen, Svalbard. *Journal of Quaternary Science* 17, 201–209. doi:10.1002/jqs.673.

Yamada, T. (1998). Glacier lake and its outburst flood in the Nepal Himalaya. Tokyo, Japanese Society of Snow and Ice. *Data Center for Glacier Research. (Monograph 1.)*.

Yang, K., Smith, L.C., Chu, V.W., Gleason, C.J., and Li, M. (2015). A Caution on the Use of Surface Digital Elevation Models to Simulate Supraglacial Hydrology of the Greenland Ice Sheet. *IEEE Journal of Selected Topics in Applied Earth Observations and Remote Sensing* 8, 5212–5224. doi:10.1109/JSTARS.2015.2483483.

Yao, T., Thompson, L., Yang, W., Yu, W., Gao, Y., Guo, X., Yang, X., Duan, K., Zhao, H., Xu, B., Pu, J., Lu, A., Xiang, Y., Kattel, D.B., and Joswiak, D. (2012a). Different glacier status with atmospheric circulations in Tibetan Plateau and surroundings. *Nature Climate Change* 2, 663–667. doi:10.1038/nclimate1580.

Yao, X., Liu, S., Sun, M., Wei, J., and Guo, W. (2012b). Volume calculation and analysis of the changes in moraine-dammed lakes in the north Himalaya: a case study of Longbasaba lake. *Journal of Glaciology* 58, 753–760. doi:10.3189/2012JoG11J048.

Zekollari, H., Huss, M., and Farinotti, D. (2020). On the Imbalance and Response Time of Glaciers in the European Alps. *Geophysical Research Letters* 47, e2019GL085578. doi:10.1029/2019GL085578.

Zemp, M., Frey, H., Gärtner-Roer, I., Nussbaumer, S.U., Hoelzle, M., Paul, F., Haeberli, W., Denzinger, F., Ahlstrøm, A.P., Anderson, B., Bajracharya, S., Baroni, C., Braun, L.N., Cáceres, B.E., Casassa, G., Cobos, G., Dávila, L.R., Delgado Granados, H., Demuth, M.N., Espizua, L., Fischer, A., Fujita, K., Gadek, B., Ghazanfar, A., Hagen, J.O., Holmlund, P., Karimi, N., Li, Z., Pelto, M., Pitte, P., Popovnin, V.V., Portocarrero, C.A., Prinz, R., Sangewar, C.V., Severskiy, I., Sigurðsson, O., Soruco, A., Usubaliev, R., and Vincent, C. (2015). Historically unprecedented global glacier decline in the early 21st century. *Journal of Glaciology* 61, 745–762. doi:10.3189/2015JoG15J017.

Zemp, M., Huss, M., Thibert, E., Eckert, N., McNabb, R., Huber, J., Barandun, M., Machguth, H., Nussbaumer, S.U., Gärtner-Roer, I., Thomson, L., Paul, F., Maussion, F., Kutuzov, S., and Cogley, J.G. (2019). Global glacier mass changes and their contributions to sea-level rise from 1961 to 2016. *Nature* 568, 382–386. doi:10.1038/s41586-019-1071-0.

Zhang, G., Bolch, T., Allen, S., Linsbauer, A., Chen, W., and Wang, W. (2019). Glacial lake evolution and glacier–lake interactions in the Poiqu River basin, central Himalaya, 1964–2017. *Journal of Glaciology*, 1–19. doi:10.1017/jog.2019.13.

Zhang, G., Yao, T., Xie, H., Wang, W., and Yang, W. (2015). An inventory of glacial lakes in the Third Pole region and their changes in response to global warming. *Global and Planetary Change* 131, 148–157. doi:10.1016/j.gloplacha.2015.05.013.

Zhang, Y., Fujita, K., Liu, S., Liu, Q., and Nuimura, T. (2011). Distribution of debris thickness and its effect on ice melt at Hailuogou glacier, southeastern Tibetan Plateau, using in situ surveys and ASTER imagery. *Journal of Glaciology* 57, 1147–1157. doi:10.3189/002214311798843331.

# Appendix

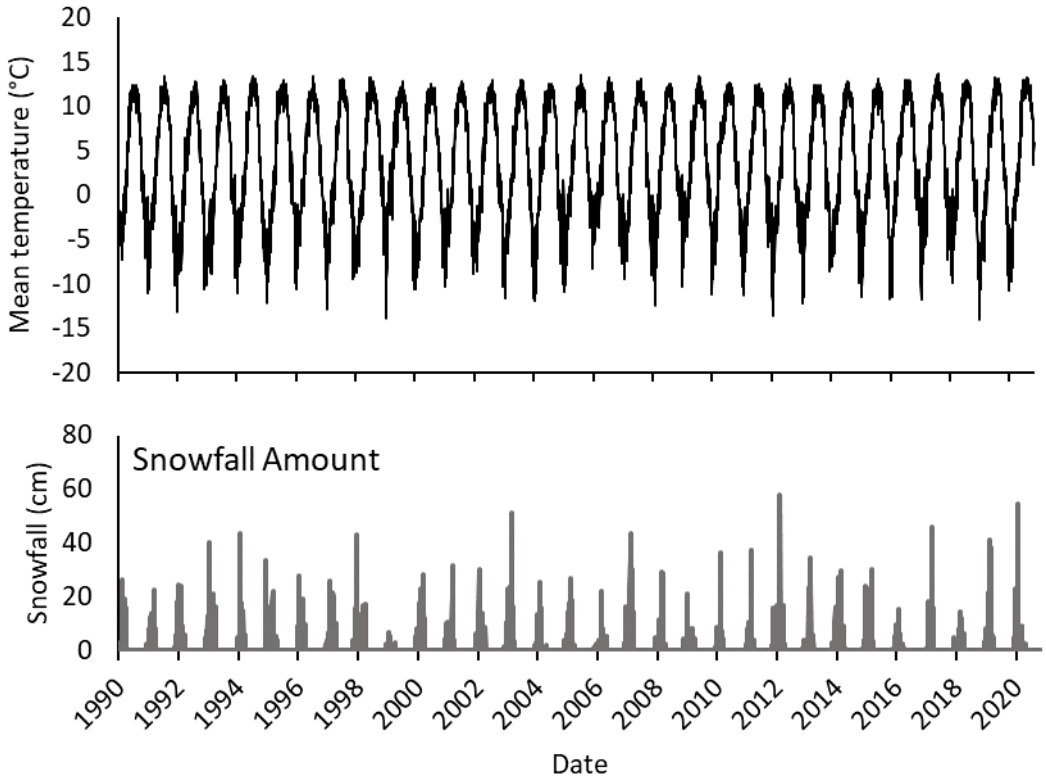


**Appendix 1:** ERA5 Climate data of Himal Chuli Glacier showing mean temperature (top) and snowfall (bottom). Data provided by MeteoBlue.